

Stellingen bij het proefschrift van J. Westerweel

1. Het bepalen van de wrijvingssnelheid voor een turbulente wandstroming bij een laag Reynolds-getal uit het logaritmische snelheids-profiel gaat er ten onrechte van uit dat dit verband ook werkelijk aanwezig is.
(J. Kim, P. Moin & R. Moser *J. Fluid Mech.* 177 (1987) 133-166; dit proefschrift)
2. De relaties tussen de parameters voor metingen met Particle Image Velocimetry (belichting, tracer-dichtheid, etc.) lijken een volledig bepaald stelsel van vergelijkingen te vormen; door één van de parameters te kiezen liggen de optimale waarden van alle andere vast.
3. De afmetingen van de meeste bestaande experimentele faciliteiten voor turbulentie-onderzoek zijn gemaximaliseerd om de relatieve invloed van de meet-probes (Pitot-buis en hitte-draad) te minimaliseren. Deze faciliteiten zijn dan ook ontoereikend voor metingen met Particle Image Velocimetry, omdat daarbij de beschikbare licht-intensiteit efficiënter benut kan worden naarmate de afmetingen van de faciliteit kleiner zijn.
(R.J. Adrian, *Annu. Rev. Fluid Mech.* 22 (1991) 261-304)
4. Digitale beeld-opname zal in Particle Image Velocimetry uiteindelijk de gangbare fotografische technieken vervangen.
(dit proefschrift)
5. De gekozen waarde van het Smagorinsky-getal in large-eddy simulatie zal voor iedere niet-triviale geometrie aan de hand van meet-resultaten moeten worden geverifieerd; dit houdt in dat large-eddy simulaties niet zonder meer de rol van experimenten kunnen overnemen.
(Contactdag Turbulentie, 29 april 1992)
6. Bij het combineren van onderzoeks-resultaten uit verschillende disciplines is het vrijwel onmogelijk om een consistente notatie aan te houden.
(dit proefschrift)
7. De gevolgde gedachtengang in een wetenschappelijke artikel wordt in sommige gevallen pas duidelijk indien het van achteren naar voren wordt gelezen.
8. Het is paradoxaal en opportunistisch dat een AIO zich gezien de tijdelijke duur van het arbeidscontract wel particulier voor ziektekosten dient te verzekeren, maar aan de andere kant weer niet als tijdelijk werknemer wordt gezien met betrekking tot een vergoeding in de reiskosten tussen woon- en werkadres.
9. Een evenredige taakverdeling tussen twee of drie sessie-voorzitters bij conferenties doet meestal het "Kwik, Kwek & Kwak"-effect ontstaan.
10. Als werkgevers werkelijk willen bijdragen aan de emancipatie kunnen zij beter hun (vrouwelijke en mannelijke) medewerkers gelegenheid geven om gebruik te maken van kinderopvang en deeltijd-werk, dan in hun personeels-advertenties positieve discriminatie van vrouwen te benadrukken.

scanned
by
ms

**TR diss
2240**

Digital Particle Image Velocimetry

– Theory and Application –

Digital Particle Image Velocimetry

– Theory and Application –

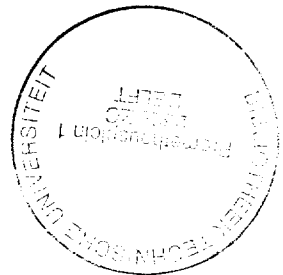
PROEFSCHRIFT

ter verkrijging van de graad van doctor aan de Technische Universiteit Delft, op gezag van de Rector Magnificus, prof. drs. P.A. Schenck, in het openbaar te verdedigen ten overstaan van een commissie aangewezen door het College van Dekanen op vrijdag 25 juni 1993 om 14.00 uur

door

Jerry Westerweel

natuurkundig ingenieur,
geboren te Rotterdam



Delft University Press / 1993

Dit proefschrift is goedgekeurd door de promotor
Prof. dr. ir. F.T.M. Nieuwstadt

CIP-DATA KONINKLIJKE BIBLIOTHEEK, DEN HAAG

Westerweel, Jerry

Digital particle image velocimetry : theory and
application / Jerry Westerweel. - Delft : Delftse
Universitaire Pers. - Ill.

Thesis Technische Universiteit Delft. - With ref.
ISBN 90-6275-881-9

NUGI 841

Subject headings: fluid dynamics / digital image
processing.

Published and distributed by:

Delft University Press
Stevinweg 1
2628 CN Delft, the Netherlands
Telephone +31 15 783254
Fax +31 15 781661

Copyright ©1993 by J. Westerweel

All rights reserved.

No part of the material protected by this copyright notice may be reproduced or utilized
in any form or by any means, electronic or mechanical, including photocopying, recording
or by any information storage and retrieval system, without permission from the publisher.

Printed in the Netherlands.

*I was dreaming I was awake.
And then I woke up,
and found myself asleep.*

Stan Laurel
in "Oliver the Eighth" (1934)

Contents

1	Introduction	5
1.1	Background	6
1.1.1	changing views on turbulence	6
1.1.2	near-wall turbulent flow in a pipe	8
1.1.3	coherent structures in near-wall turbulent flow	9
1.1.4	new measurement techniques	12
1.2	Quantitative visualization with tracer particles	13
1.2.1	image modes: PTV, PIV and LSV	13
1.2.2	analysis of PIV/LSV images	15
1.2.3	applications	20
1.2.4	alternative implementations	21
1.3	Digital particle image velocimetry	22
1.3.1	principle	22
1.3.2	vortex street behind a cylinder	24
1.3.3	context	25
1.4	Outline of this thesis	27
I	theory	29
2	Statistics of PIV Images	31
2.1	Introduction	31
2.2	Ideal tracer particles	32
2.3	The displacement field	33
2.4	The tracer pattern	34
2.5	Optical system	38
2.6	Images from seeded flows	40
2.7	Ensemble statistics of PIV images	42
2.8	Multiple-exposure images	46
2.9	Annotations	48
3	Digital Analysis	51
3.1	Introduction	51

3.2	Image sampling	52
3.3	Quantization	54
3.4	Intensity statistics	55
3.5	Bandwidth of PIV images	57
3.6	Estimation of the mean and cross-covariance	61
3.6.1	estimation of the mean image intensity	62
3.6.2	estimation of the cross-covariance	63
3.6.3	weight kernels	67
3.6.4	valid-data yield	68
3.7	Estimation of the displacement	69
3.8	Estimation of the fractional displacement	75
3.8.1	three-point estimators	76
3.9	Statistics of fractional-displacement estimators	78
3.9.1	expectation	79
3.9.2	variance	83
3.9.3	non-zero fractional displacements	89
3.10	Experimental verification	92
3.10.1	experimental set-up	92
3.10.2	results	94
3.11	Summary and conclusions	100
4	Data Validation: Detection of Spurious Vectors	107
4.1	Introduction	107
4.2	The PIV signal	109
4.3	Detection methods	112
4.3.1	global-mean test	115
4.3.2	local-mean test	115
4.3.3	local-median test	117
4.4	Performance tests	119
4.5	Conclusions	122
5	Estimation of Vorticity and Deformation	124
5.1	Introduction	124
5.2	Vorticity	125
5.3	Deformation	129
5.4	Conclusion	131
II	application	133
6	Application of Digital Particle Image Velocimetry to Turbulent Flow	135
6.1	Introduction	135
6.2	Experimental set-up	136
6.3	Digital analysis	137

6.4	Vorticity and deformation	138
6.5	Conclusions	142
7	Measurements with Particle Image Velocimetry of Fully Developed Turbulent Pipe Flow at Low Reynolds Number	143
7.1	Introduction	143
7.2	Experiments	145
7.2.1	pipe flow facility	145
7.2.2	seeding	145
7.2.3	LDA measurements	146
7.2.4	PIV measurements	147
7.2.5	interrogation of the PIV photographs	147
7.3	Results	150
7.3.1	fully developed flow	150
7.3.2	turbulence statistics	152
7.3.3	vortical structures	156
7.4	Summary and conclusions	159
8	Comparison of Vortical Flow Structures in DNS and PIV Studies of Turbulent Pipe Flow	162
8.1	Introduction	162
8.2	Computational technique and results	163
8.2.1	Introduction	163
8.2.2	Computation of near-wall structure properties	164
8.2.3	Computation of mean shape-parameter	166
8.3	Conditionally sampled flow statistics	167
8.4	Summary and discussion	169
9	Application of Digital Particle Image Velocimetry to a Turbulent Pipe Flow	172
9.1	Introduction	172
9.2	Experimental set-up	174
9.3	Results	176
9.4	Conclusions	185
10	Conclusions	186
10.1	Theory (Part I)	187
10.2	Application (Part II)	192
10.3	Future developments	194
10.4	Concluding remarks	198
A		199
A.1	Linear system analysis	199
A.2	The tracer ensemble	200

4 *Contents*

A.3	Ensemble statistics of the tracer pattern	202
A.4	Diffraction limited spot of an optical system	202
A.5	Relevant properties of Gaussian curves	203
B		205
B.1	Image enhancement	205
B.1.1	correction for non-uniform illumination	205
B.2	Computation of the cross-covariance	210
B.2.1	zero-padding	211
B.2.2	window functions	212
C		214
C.1	Non-homogeneous random fields	214
C.2	The pdf of the mean and the median	215
References		216
List of Symbols		223
List of Abbreviations		228
Summary		229
Samenvatting		232
Acknowledgements		235
Curriculum Vitae		236

Chapter 1

Introduction

Abstract. *Flow visualizations clearly show that turbulence is not a random process, but consists of coherent flow structures. An interpretation in terms of coherent structures plays an important role in many complicated turbulent phenomena. With visualization we only obtain a qualitative picture of these structures. Traditional instruments like the hot-wire and laser-Doppler anemometer are one-point measurement techniques, and therefore not able to reveal the instantaneous spatial structure of a flow. With the aid of a new observation technique, called "particle image velocimetry" (PIV), quantitative, two-dimensional information of the flow velocity field is obtained. These data enable us to compute other flow quantities, such as vorticity or deformation; these quantities are directly related to the dynamics of coherent flow structures. The original method for PIV image analysis yields accurate results with a high spatial resolution, but is very time-consuming. This is a major problem in the application of PIV to study the dynamics of coherent structures in turbulent flows, which requires the analysis of a large number of images. A digital implementation of the PIV method considerably reduces the processing time, at the cost of a slight reduction in measurement accuracy. This provides a feasible solution to process large quantities of PIV images.*

The main aim of the work described in this thesis is the development and application of the digital counterpart of a measurement technique called *particle image velocimetry* (PIV). This technique yields the instantaneous, spatial measurement of the velocity observed in a planar cross section of a flow. This is a considerable improvement with conventional measurement techniques that yield velocity measurements from a single point only, and makes the technique ideally suited for the investigation of coherent structures in turbulent flows.

In this introductory chapter we review some of the background and history of turbulent flow research in relation to particle image velocimetry (Sect. 1.1). We subsequently describe the basic principles of PIV, and discuss its shortcomings with respect to the investigation of coherent structures in turbulent flows (Sect. 1.2). The digital implementation of the PIV technique presented here provides a feasible solution to these shortcomings (Sect. 1.3). We conclude this chapter with an outline of the topics treated in the remainder

of this thesis.

1.1 Background

Turbulent flow is so much a part of our daily life that we hardly realize the complexity of the underlying processes. In fact, turbulence is still lacking a satisfactory theoretical explanation. In general turbulence is described as a chaotically fluctuating state of a flow that occurs when a characteristic flow parameter such as the Reynolds number, defined as $Re = \mathcal{U}\mathcal{L}/\nu$, where \mathcal{U} and \mathcal{L} are characteristic velocity and length scales and ν is the kinematic viscosity, exceeds a certain critical value. It is beyond the scope of this thesis to give a detailed description of turbulence, but instead a brief outline of some relevant aspects is given below. For further details refer to Tennekes & Lumley (1972) or Hinze (1975).

Fully developed turbulence at sufficiently large Re is characterized by the existence of two scaling regimes, denoted as the *macrostructure* and the *microstructure*. The classical picture is that turbulent kinetic energy is produced at the macrostructure, where it is extracted from the mean flow by instability processes. This energy is transferred from the macrostructure to the microstructure by the so-called *energy cascade*: large-scale eddies break up into smaller eddies, by which energy is transferred from larger scales to smaller scales. This process of eddy break-up repeats itself until the microstructure is reached where the energy is finally dissipated by molecular viscosity. The scaling of the macrostructure is determined by the geometry of the flow; the scaling of the microstructure is determined by the viscosity of the fluid and the amount of energy transferred along the cascade (*Kolmogorov scale*). As a result of assuming these two separate scaling regimes the ratio of the length scales of the macrostructure (\mathcal{L}) and the microstructure (η) is given by

$$\mathcal{L}/\eta \sim Re^{3/4}. \quad (1.1)$$

In laboratory-type flows with $Re \sim 10^4$ and $\mathcal{L} \sim 0.1$ m, the Kolmogorov length given by (1.1) is about 0.1 mm.

In the cascade process smaller eddies are deformed by larger eddies. The deformation is coupled with the *vorticity*, which is defined as the rotation of the velocity field. As a result of this interaction energy is transferred from the larger eddies to the smaller eddies, which further increases the vorticity of the smaller eddies. This mechanism is referred to as *vortex stretching*.

1.1.1 changing views on turbulence

The "classical" notion of a turbulent flow is that of a stochastic process, described by its statistical moments. This view was based on laboratory experiments with traditional single-point measurement probes such as the hot-wire anemometer (HWA) and the laser-

Doppler anemometer (LDA)¹. This classical notion of turbulence was maintained until the mid 50's, when nonrandom phenomena were discovered by means of flow visualization² in turbulent flows (Townsend 1956; Kim *et al.* 1971). These flow visualizations revealed that turbulent flow is not completely disorganized, but contains large-scale so-called *coherent structures*. Brown & Roshko (1974) demonstrated that the *instantaneous* spatial structure of the flow can *not* be described by the turbulence statistics obtained from the single-point probes.

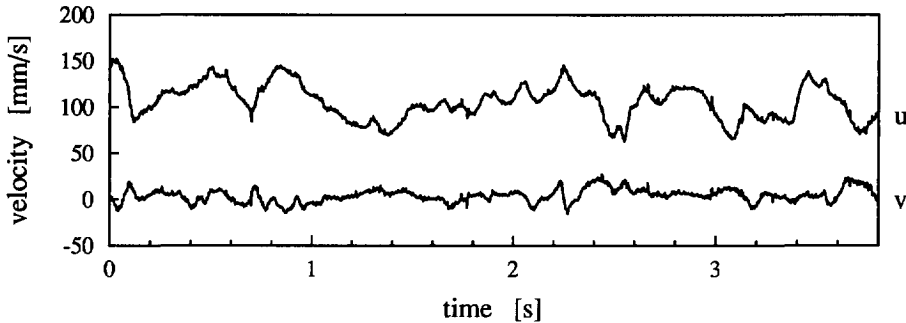


Figure 1.1: A single-point measurement (by laser-Doppler anemometry) of the streamwise (u) and vertical (v) velocity signals as function of time in a turbulent boundary layer over a flat plate. The measurement was taken at 20 viscous wall-units above the plate. (Courtesy A.D. Schwarz-van Manen.)

The occurrence of organized motion or coherent structures in turbulent flows is (apparently) in contradiction with the conventional statistical description of a turbulent flow. This is illustrated by Figures 1.1 and 1.2, which show a section of a LDA signal and a hydrogen-bubble time-line visualization in the near-wall region of a turbulent boundary layer. Whereas the appearance of the LDA signal suggests that it was generated by a random process, the visualization reveals large-scale elongated structures. Obviously the classical view of turbulence as a random process is no longer valid and new concepts of turbulence had to be found. This is still a topic of theoretical, numerical and experimental research.

The presence of “organized structures” in an apparently random signal shows similarities to what is known as “deterministic chaos” of non-linear dynamical systems (Bergé *et al.* 1987). Aubry *et al.* (1988) attempt to describe turbulent flow as a non-linear dynamical system in which they apply a mathematical approach of coherent structures in terms

¹These techniques measure the flow velocity as function of the time in a single point. Descriptions of these techniques are given by Fingerson & Freymuth (1983) and Adrian (1983) respectively.

²This is a collective terminology for observation methods that visualize the motion, structure or density distribution of a fluid, either in a planar cross section or integrated along the line-of-sight (Merzkirch 1987). The motion of a fluid can be visualized by adding small particles or dye to the fluid. A set of beautiful examples has been collected by Van Dyke (1982).

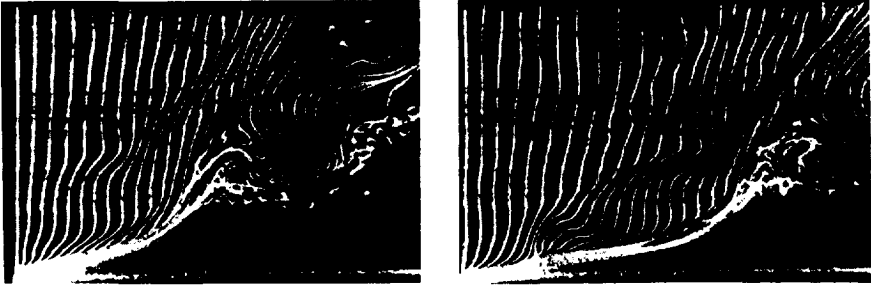


Figure 1.2: Photographs of hydrogen bubble time lines, showing typical large scale vortex motion in turbulent boundary layer flow near a smooth wall. From: Kim *et al.* (1971)

of eigenfunctions. Other innovative work has been carried out by Vassilicos (1992) who proposes a “multispiral” vortical structure that accounts for the spectral density distribution that is commonly associated with the energy cascade mentioned before. However, these theories still lack feedback from experiments.

A large part of the research on coherent structures is concentrated on incompressible turbulent flow near a solid wall, the so-called *boundary layer*. Let us therefore briefly review some of the aspects related to this type of flow.

1.1.2 near-wall turbulent flow in a pipe

A flow geometry of specific interest is that of a wall-bounded turbulent flow, like e.g. the turbulent boundary layer and turbulent channel and pipe flows. Here we will restrict ourselves to a pipe flow. For a detailed treatment of this flow type refer to Schlichting (1979). The velocity of the flow near the wall scales with the *friction velocity* u_* , given by the wall shear stress τ_* , i.e.

$$u_* = \sqrt{\tau_*/\rho} \quad (1.2)$$

where ρ is the density of the fluid.

The turbulent pipe flow consists of an *outer* region, that scales with the pipe diameter (D), and an *inner* region that scales ν/u_* . Usually the flow velocity (u) and the distance (y) from the wall are made dimensionless by u_* and ν , viz.

$$u^+ = u/u_* \quad \text{and} \quad y^+ = yu_*/\nu. \quad (1.3)$$

The turbulent pipe flow can be divided into four layers:

wake region ($y/D \gtrsim 0.1$)

In the wake region the eddies scale with the flow geometry, i.e. $\mathcal{L} \sim D$. In this region the total shear stress is dominated by the turbulent shear stress (the mean product of the axial and radial fluctuating velocities).

logarithmic wall layer ($y^+ > 30...40$, $y/D \lesssim 0.1$)

In the logarithmic wall layer the size of the eddies is determined by their distance from the wall, i.e. $\mathcal{L} \sim \kappa y$, where κ is the Von-Kármán “constant” which has an empirical value of 0.4. The velocity profile in this region is given by

$$u^+ = \frac{1}{\kappa} \ln y^+ + \Pi \quad (1.4)$$

with $\Pi \sim 5.5$ for a smooth wall. The logarithmic shape of the velocity profile in this region is a direct consequence of the fact that the wall-bounded flow consists of an inner and outer region.

buffer layer ($5...10 < y^+ < 30...40$)

The buffer layer is the transition region between the viscous sublayer (see below) and the logarithmic wall layer. Both viscous and turbulent stresses play an equal part in this layer.

viscous sublayer ($y^+ < 5...10$)

Very close to the wall the viscous stress dominates the flow, and turbulence can no longer exist. The mean axial velocity is directly proportional to the distance from the wall, i.e.

$$u^+ = y^+. \quad (1.5)$$

The highest energy production and turbulent shear stress is found in the buffer layer (Mansour *et al.* 1988). A great deal of turbulent flow research is dedicated to the mechanisms and the processes in this layer, which cannot be comprehended or explained by contemporary statistical models. This applies in particular to the recently observed drag reduction for flows with certain polymer additives (Harder & Tiederman 1991) and for flows over grooved surfaces or “riblets” (Walsh & Lindemann 1984). It has been conjectured that this drag reduction can be explained in terms of the dynamical behaviour of coherent structures in the buffer layer (Luchini *et al.* 1991; Schwarz-van Manen 1992). Furthermore it is believed that coherent structures play an important role in all kinds of transport processes (such as heat transfer, the deposition/resuspension of particles or chemical reactions).

1.1.3 coherent structures in near-wall turbulent flow

Most of the experimental information of coherent flow structures has been obtained through flow visualization. Their interpretation is very subjective, and as a result there is a wide variety of definitions and models of coherent flow structure. Reviews of the structures that have been identified in near-wall turbulent flow are given by Cantwell (1981), Robinson (1991b) and Brand (1992). In this subsection a brief description is given of the so-called “burst process” which may account for the production of turbulent kinetic energy and turbulent shear stress in the buffer layer. It should be noted however that the bursting process as such is ill-defined in the literature. The description given below

is extracted from the reviews mentioned above.

The flow very close to the wall consists of long elongated regions in which the fluid velocity is lower than average fluid velocity. These regions are called *low-speed streaks*. Instability processes cause that small disturbances of the vortex sheet surrounding the low-speed streak grow and develop into a so-called *hairpin* vortex. This is illustrated in Figure 1.3. The tip of the vortex moves away from the wall by self-induction. The legs of the vortex stretch and thus extract energy from the mean flow. Finally, the hairpin vortex becomes unstable and breaks up into smaller structures ("burst"). During the self-induction stage of the vortex low-momentum fluid is "pumped" away from the wall between the legs of the vortex. This motion is called *ejection*, which strongly contributes to the Reynolds stress. After the burst event high-momentum fluid moves towards the wall, which is called a *sweep*, and interacts with the low-speed fluid near the wall. The sweep may disturb another low-speed streak, and initiate another burst cycle. The time scale of this cycle in a boundary layer is given by $T_B \sim 5...7\delta/U_c$, where δ is the boundary-layer thickness (for pipe flow $\delta \sim \frac{1}{2}D$). Note that T_B scales with the *outer* flow parameters³. This is rather surprising since a process that takes place in the buffer layer is supposed to scale with inner parameters.

The coherent structures related to the bursting process have been identified in flow visualization studies; see Kline *et al.* (1967), Kim *et al.* (1971) and Head & Bandyopadhyay (1981). It was mentioned before that these visualizations provide only a *qualitative* picture of these structures and related flow processes. Therefore the interpretation of these visualization experiments are somewhat subjective.

Recently, Robinson (1991a) demonstrated the presence of these coherent flow structures in a direct numerical simulation⁴ (DNS) of a turbulent boundary layer by Spalart (1988). The DNS allows a detailed *quantitative* investigation of these structures, but a drawback is that one has to solve the *entire* flow field, even if one is only interested in studying a small section of the flow (e.g. the buffer layer). Thus, direct numerical simulation can only be applied to simple flow geometries (like e.g. channel flow between smooth walls) and to flows with relatively low Reynolds numbers ($Re \sim 3-7,000$). Nonetheless, based on DNS data Robinson (1991a) proposes detection criteria for hairpin vortices with respect to the (spanwise component of the) vorticity, the fluctuating pressure and the deformation of the flow field.

Hence, quantitative experimental data are necessary to make further substantial progress in the investigation of coherent flow structures in turbulent flows. The traditional measurement techniques, like HWA and LDA, only provide information from a single point in the flow and therefore—by principle—can neither reveal the instantaneous spatial

³This is still a subject of discussion.

⁴In a direct numerical simulation the equations of motion of a fluid (viz., the Navier-Stokes equations) are solved numerically, in which all flow scales from the macrostructure to the microstructure are resolved, thus without relying to any turbulence modeling.

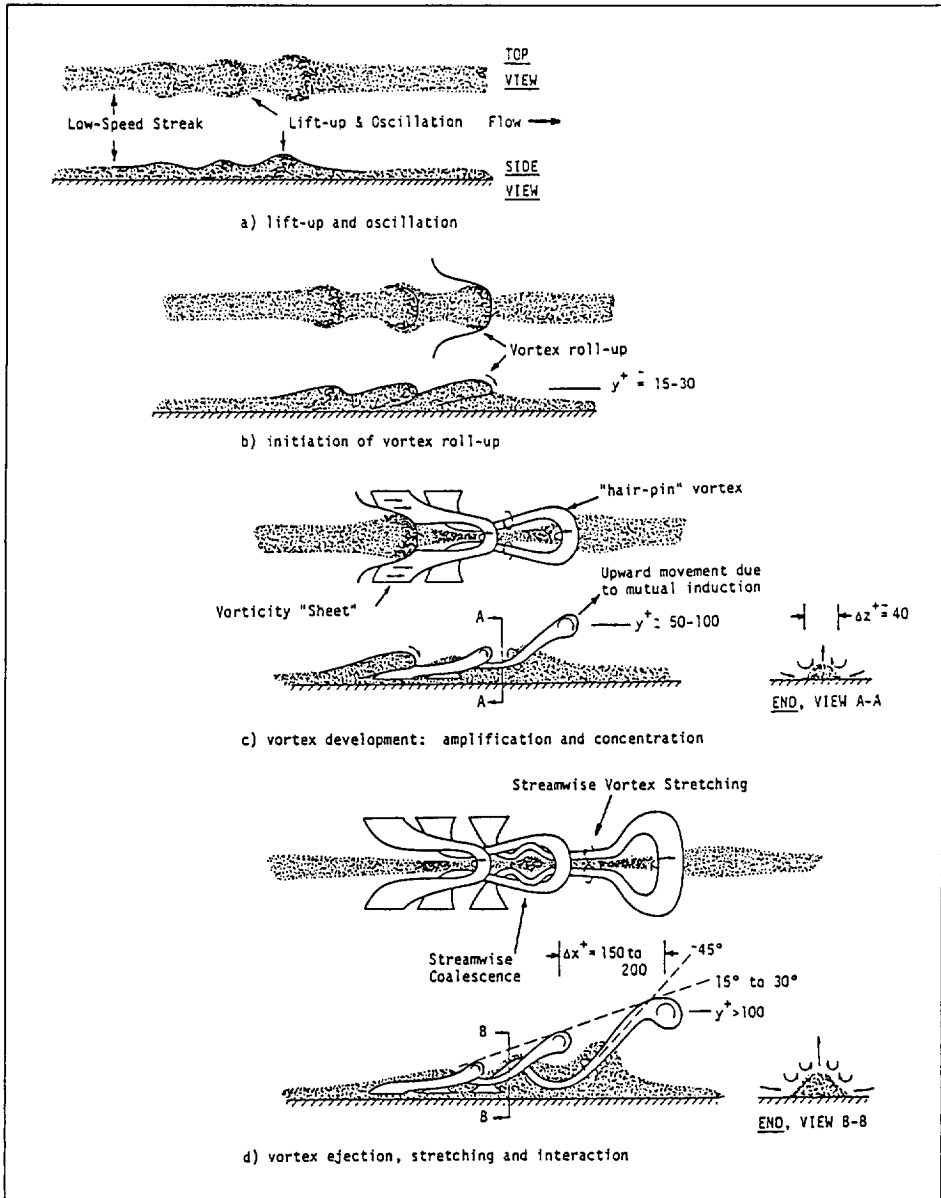


Figure 1.3: Representation of the "bursting" process in which a low-speed streak develops into a hairpin vortex. From: Smith (1984)

structure of the flow nor its dynamics (Kline 1978). Attempts to yield the instantaneous spatial structure with single-point probes was done by conditional sampling, in which the velocity signal is accepted when a predefined condition is met; e.g. the VITA (Gupta *et al.* 1971; Blackwelder & Kaplan 1976) and quadrant (Wallace *et al.* 1972; Willmarth & Lu 1972) methods. The large amount of somewhat conflicting views obtained from these one-point observations shows that it is difficult to relate the conditional events to the structures observed in flow visualization. The choice of detection criteria is not well defined, which gives the results and their interpretation again a subjective nature. Another disadvantage is that one can only study one event at the time. This makes it very difficult to investigate the relationship—in time and space—between different events. Therefore new measurement techniques that yield the instantaneous structure of the flow need to be developed. This conclusion was the point of departure for the investigation described in this thesis.

1.1.4 new measurement techniques

A breakthrough was achieved by the application of digital image processing to flow visualization, which enabled a quantitative and automated analysis of flow pictures. These techniques are collectively known as *quantitative visualization*. A general review of optical flow diagnostics applying digital image processing is given by Hesselink (1988). One of the categories of these new measurement methods visualizes the motion of the fluid by small tracer particles added to the fluid. By measurement of the displacement of the tracers in a given time interval the velocity field can be constructed. By subsequent differentiation of the velocity data one can infer additional flow quantities such as the vorticity and the deformation of the flow.

The vorticity and deformation are crucial quantities in understanding the dynamics of coherent flow structures (Hussain 1986; Hunt *et al.* 1988). To yield useful results we have to meet the following demands:

- The strongest vorticity occurs at the smallest scales in the flow (i.e. microstructure), and thus the method should have a sufficient spatial resolution in order to resolve both the macrostructure and microstructure. The required ratio between the smallest and largest attainable length scales is given by (1.1).
- To investigate also the temporal evolution of coherent structures, e.g. the development of a low-speed streak into a hairpin vortex, we should have a temporal resolution that matches the time scale of the flow.
- Differentiation increases the noise. Since vorticity is obtained by differentiation of the measured velocity field, the accuracy of the measured data should be sufficiently high in order to yield significant results for the vorticity (Hesselink 1988).

Note that the requirements for the spatial and temporal resolution are equivalent to those for numerical simulation. (In that respect it should also be noted that it will not always

be necessary to resolve all scales and yet obtain a feasible representation of the flow, like in large-eddy simulation.)

In the next section we will discuss quantitative visualization with tracer particles in more detail. For an extensive review refer to Adrian (1991).

1.2 Quantitative visualization with tracer particles

Consider a flow that has been seeded with small tracer particles. These particles are supposed to accurately follow the motions of the fluid. With a light sheet a planar cross section of the flow is illuminated, and an image is formed of the tracer particles that are located inside the light sheet. The measurement principle of velocity is now based on the displacement of the tracer particles in a given time interval. The most widespread method to record the displacement of the particles is by taking a *double-exposure* picture of the tracer particles in the light sheet. We will first discuss the appearance of these images as function of the tracer density, and after that discuss the analysis method.

1.2.1 image modes: PTV, PIV and LSV

The appearance and information content of the recorded image is described by two dimensionless numbers, denoted as the *source density* (N_S) and the *image density* (N_I), introduced by Adrian & Yao (1984). The source density indicates whether the image consists of individual particle images (i.e. $N_S \ll 1$), or that particle images overlap and—for coherent illumination—interference of light comes into play (i.e. $N_S \gg 1$). The other dimensionless number, the image density, represents the number of particle images within a particular area around a point at which we would like to determine the flow velocity. This area is referred to as the *interrogation area*. (The exact definitions for N_S and N_I are given later in Sects. 2.6 and 3.6.4 respectively.)

Depending on the values of N_S and N_I we can distinguish between three different *modes* of the recorded image, illustrated in Figure 1.4 (where an interrogation area is indicated by a circle):

particle tracking velocimetry (PTV): $N_S \ll 1$, $N_I \ll 1$

In this mode we observe individual particle images ($N_S \ll 1$). The average distance between distinct particle images is much larger than the mean displacement, so that the expected number of particle image in the interrogation area is low ($N_I \ll 1$); see Fig. 1.4a. Because of the large distance between distinct particle images with respect to the mean displacement it is fairly easy to identify particle-image pairs that correspond to the same tracer particle in the flow, and thus obtain the local flow velocity. However, since the image density is low we cannot determine the velocity in any arbitrary position, but only at positions where a tracer particle happens to be present. The result is a random sampling of the flow field. We will see later (Sect. 2.3) that the sampling is in general not optimal. Because the velocity field is

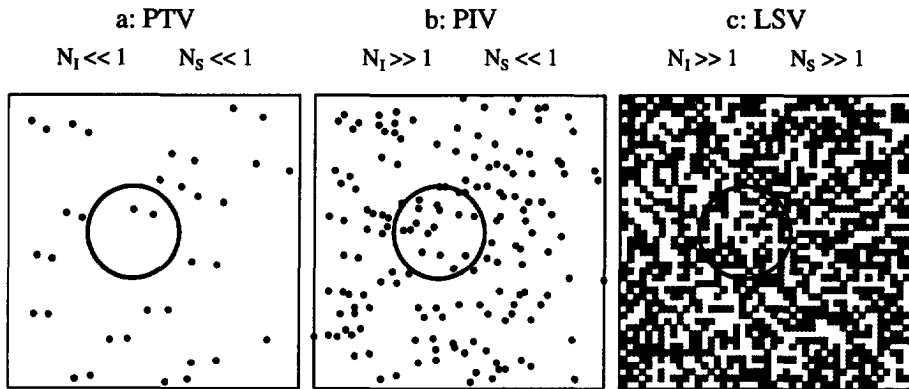


Figure 1.4: The image types in: (a) particle tracking velocimetry (PTV), (b) particle image velocimetry (PIV) and (c) laser speckle velocimetry (LSV). The information content (viz., N_I) and appearance (viz., N_S) are determined by the tracer density. The circle indicates an interrogation area. (The parameters N_I and N_S are further explained in the text.)

obtained from the displacement of individual tracer particles this analysis is referred to as *particle tracking velocimetry* (PTV).

particle image velocimetry (PIV): $N_S \ll 1$, $N_I \gg 1$

To yield a greater density of information of the flow field we have to increase the density of the tracer particles. In Fig. 1.4b the situation for $N_I \gg 1$ is shown. We can still distinguish individual particle images ($N_S \ll 1$). Now the interrogation region contains practically always a sufficient number of particle images to determine the (local average) flow velocity in any position. However it is no longer possible to identify individual particle-image pairs unambiguously. We therefore have to use a statistical method, that will be described in the next subsection, to determine the most probable displacement. The measurement technique that deals with this type of images is referred to as *particle image velocimetry* (PIV).

laser speckle velocimetry (LSV): $N_S \gg 1$, $N_I \gg 1$

If we further increase the density of tracer particles in the flow, the particle images will tend to overlap ($N_S \gg 1$). For illumination with a coherent light source (viz., a laser) the resultant image is that of a random interference pattern, better known as *speckle*; see Fig. 1.4c. The speckle pattern moves along with the tracer particles in the flow. By measurement of the displacement of the speckle pattern we can determine the displacement of the particles in the flow. In principle the displacement of the speckle pattern is measured in the same manner as in PIV, but since the observed image consists of speckle it is referred to as *laser speckle velocimetry* (LSV).

There are two points that have to be made here. First, Adrian (1984) demonstrated that

Table 1.1: Synonyms for *particle image velocimetry* (PIV).

digital image velocimetry
double-pulsed velocimetry
particle imaging velocimetry
laser speckle velocimetry
pulsed laser velocimetry
pulsed light velocimetry
particle image displacement velocimetry
whole field velocimetry
image processing velocimetry
...

the observation of “true” speckle in flow visualization requires such high tracer density that other undesired effects—like e.g. two-phase flow effects or multiple scattering—come into play. It may be that pictures considered to show speckle actually consisted of a dense packing of individual particle images (these two image types are hard to distinguish). Secondly, images in PIV and LSV are analyzed in the same way (see Sect. 1.2.2). So there is no real need for using different names to describe the measurement technique. However, some authors refer to particle tracking velocimetry as particle-image velocimetry. This considerably confuses what PIV stands for. In reaction, some refer to PIV/LSV consistently as LSV, even though no speckle is observed at all. Even worse is the continuous inflation of new names, each with its own three or four letter abbreviation; a literature scan (Meynart 1991) may add up to twenty (!) proposed names all referring to the same basic measurement principle; see Table 1.1.

1.2.2 analysis of PIV/LSV images

We still have to explain how we determine the displacement for the cases with $N_I \gg 1$. Note that we actually want to determine the displacement of a *random pattern*. For a double-exposure image the displaced pattern is superimposed on the original pattern. Fig. 1.5a represents a double-exposure PIV record. One may see that the displacement of the particle-image pairs changes its magnitude and direction throughout the image. Now consider a small interrogation area that is sufficiently small to assume that the particle-image displacement is uniform over this area. The interrogation image in Fig. 1.5b corresponds to the sub-image in the rectangle in Fig. 1.5a. It is not possible in Fig. 1.5b to pair images unambiguously. The interrogation image is analyzed through its spatial (auto-)covariance function (Adrian 1988). For a double-exposure image we obtain a covariance function with *three* dominant peaks, depicted in Fig. 1.5c: a central *self-correlation peak* that is due to the correlation of each particle image with itself, and

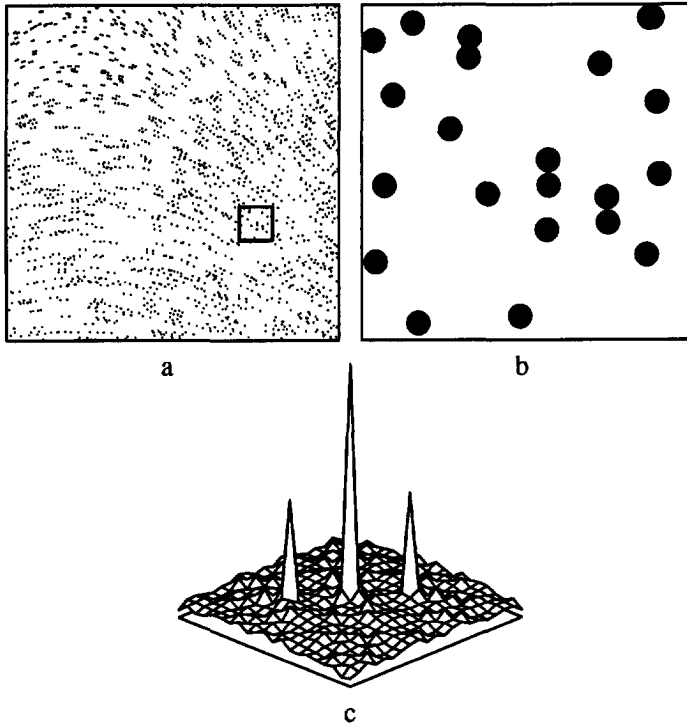


Figure 1.5: A schematic representation of the image analysis in PIV: (a) double-exposure PIV image (the small square indicates the interrogation area); (b) interrogation image, with nearly uniform displacement of particle-image pairs, and (c) two dimensional covariance with a central self-correlation peak and two displacement correlation peaks (embedded in random correlation peaks).

two *displacement-correlation peaks* on opposite sides of the self-correlation peak that are due to the correlation of the particle-images in the first exposure with their corresponding images in the second exposure and *vice versa*. The width of these peaks is mainly determined by the particle-image diameter. Obviously, we can only distinguish three peaks for a displacement that is larger than this particle-image diameter. These three peaks are embedded in a background noise due to the random correlation between distinct particle-image pairs. Provided that sufficient particle-image pairs are present within the interrogation region, the displacement-correlation peaks will rise above the random noise peaks. Hence, we can identify the displacement-correlation peaks as the highest non-central peaks in the auto-covariance function. The centroid of the displacement-correlation peak yields the local-average, in-plane displacement of the particles in the

interrogation region. The same principle applies to speckle images. The only difference is that the width of the covariance peaks is determined by the average size of the speckle, instead of the particle-image diameter.

For double-exposure images we should realize that we cannot distinguish between the two correlation peaks (the auto-covariance is a symmetric function), and therefore we determine the direction of the displacement with a 180° directional ambiguity. In this thesis we only consider *uni-directional* turbulent flows, so that the sign of the displacement is known *a priori*. In the case of a flow that is *not* uni-directional we have to use techniques that resolve the directional ambiguity during the image recording; see also Sect. 2.8. Another way to avoid the directional ambiguity is to record each exposure on a different frame, and subsequently use a *cross-covariance* analysis to determine the particle-image displacement for corresponding interrogation areas in the two frames (Cho 1989). We now find only one displacement-correlation peak (the self-correlation peak will not appear). A disadvantage of recording successive exposures on separate frames is that frame rate determines the temporal resolution of the measurement.

criteria for optimal analysis

Keane & Adrian (1990) carried out Monte-Carlo simulations to determine the requirements for the experimental parameters to yield optimal performance of the PIV analysis. They recommended the following criteria:

- the number of particle images per interrogation area should be at least 15;
- the particle-image displacement in the direction perpendicular to the light sheet ("out-of-plane" displacement) should be less than $1/4$;
- the in-plane displacement of the particle images should be about or less than $1/4$ of the diameter of the interrogation area;
- the velocity gradient over the interrogation area should be at the most 5% of the mean velocity.

We will refer to these criteria throughout this thesis.

Young's fringe analysis

Let us now have a look at how the analysis of double-exposure photographs is implemented. The analysis method that is employed most commonly is identical to the analysis of double-exposure images in speckle metrology (Burch & Tokarski 1968). After development the film negative is mounted on a xy-translation stage. A schematic drawing of the interrogation set-up is given in Figure 1.6. A small area in the negative (*viz.*, the interrogation area) is illuminated with a laser beam (usually a HeNe-laser). The transmitted beam is observed in the back focal plane of a lens. In this optical arrangement the observed image is the optical Fourier transform of the transmitted light field in the

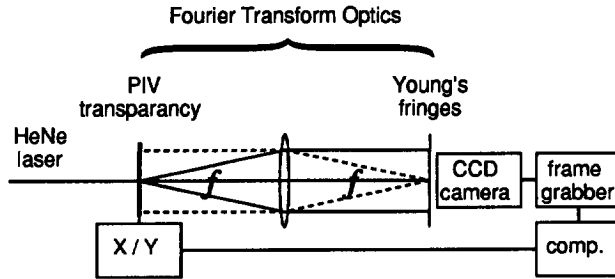


Figure 1.6: Interrogation of a PIV photograph using the Young's fringe method. The PIV photo is mounted on a computer controlled XY-translation stage. The lens performs an optical Fourier transform of the interrogation image. The fringe pattern is digitized and subsequently analyzed by a computer.

object plane (Goodman 1968). The double-exposure PIV negative acts as a diffraction grating that yields an image in the back focal plane of the lens that consists of alternating light and dark bands, better known as *Young's fringes*. The direction of these fringes is perpendicular to the direction of the particle-image displacement, and the spacing of the fringes is inversely proportional to the magnitude of the displacement. (Again we have a 180° directional ambiguity.) The Fourier transform of the Young's fringe pattern is formally equivalent to the auto-covariance of the image in the interrogated region on the PIV negative (Keane & Adrian 1990). The fringe pattern is digitized (using an electronic imaging device, like a CCD array, connected to a "frame grabber") and is subsequently evaluated with a digital computer. After the analysis of the fringe pattern the negative is translated to the next interrogation position. This procedure is repeated until the entire negative is analyzed.

Since all the above methods employ an *optical* read-out system for PIV transparencies we henceforth refer to these methods collectively as *optical particle image velocimetry* (OPIV).

The elegance of the Young's fringe method is that the information in the interrogation spot is transformed optically into a pattern that can be readily analyzed, by direct measurement of the direction and spacing of the fringes. However, in practice the fringe visibility or contrast appears to be rather low (Landreth & Adrian 1990b), and as a result the direct analysis of the fringes is not very robust. The direct analysis of the fringe pattern was subsequently replaced by discrete Fourier analysis, which is capable of detecting the regular fringe pattern under less ideal circumstances. (The discrete Fourier transform of the fringe pattern is commonly computed with the efficient Fast Fourier Transform (FFT) algorithm.) The reason why it is difficult to detect the orientation and spacing of the fringe pattern directly is that it is a *global* image feature. Some thought reveals that the Fourier transform of the fringe pattern concentrates the signal energy in a peak,

which is now a *local* feature and therefore easier to detect.

The discrete Fourier analysis is usually carried out with a high resolution of 256×256 or 512×512 pixels. This yields an estimated accuracy of about 0.3 pixel units (px). Hence, for a nominal displacement that is 1/4 of the diameter of the interrogation area the relative measurement accuracy is better than 1% (Prasad *et al.* 1992). However, the analysis is very time consuming; at such high pixel resolution it takes at least a few seconds to compute the Fourier transform. Taking into account that a PIV photograph is interrogated in 1,000 to 10,000 interrogation positions, then the total time required to analyze a single PIV negative is usually expressed in *hours* (Adrian 1986b; Lourenço & Krothapalli 1988a). This is clearly a disadvantage for applications that require the analysis of a large number of PIV pictures.

direct correlation

By performing a numerical analysis of the fringe pattern the actual advantage of the fast optical processing is somewhat lost. We therefore might just as well compute the image auto-correlation *directly*. This is illustrated in Figure 1.7; now *two* digital Fourier transformations are necessary to yield the image covariance function. This slows down the analysis by a factor two, but in return the direct computation also has advantages. For example, the illumination of the interrogation region by a *coherent* light source is no longer required. Incoherent illumination considerably reduces the effect of scattering by the carrier material of the film negative, which improves the image contrast. Direct correlation has been applied to PIV image analysis successfully (Reuss *et al.* 1989; Landreth & Adrian 1990a).

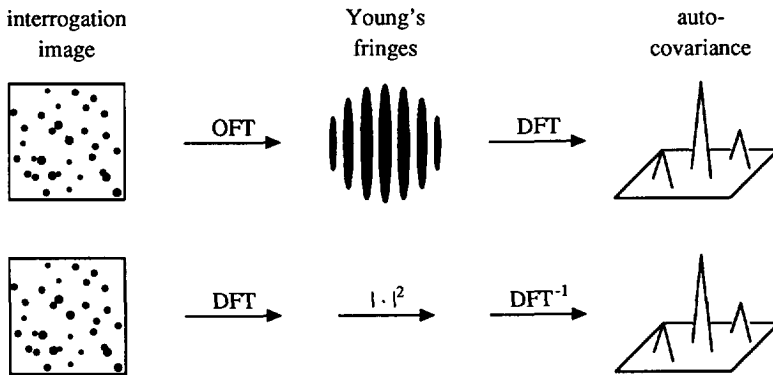


Figure 1.7: The analogy of Young's fringe analysis (top) and direct correlation analysis (bottom). The abbreviations refer to: optical Fourier transformation (OFT) and discrete Fourier transformation (DFT). The operation denoted by $|\cdot|^2$ denotes the squared norm of a complex field.

1.2.3 applications

Some of the earliest reported applications of PIV/LSV concerned Bénard convection (Simpkins & Dudderar 1978) and jet flow (Meynart 1983). Since then most of the work has been devoted to improvement of the technique. Since the analysis of a single image takes several hours (see previous paragraph) most applications of PIV to study coherent structures in (turbulent) flows have been limited to a few individual realizations (up to 11) of the instantaneous flow field, see e.g. Lourenço & Krothapalli (1988a), Landreth & Adrian (1990a) and Liu *et al.* (1992). Although this number may be sufficient to estimate first and second order statistics of the velocity field (Liu *et al.* 1992), it is insufficient to determine the relevant properties of coherent structures; a single realization of a PIV measurement reveals the spatial coherence present in the flow but it does not provide any information on the evolution or statistics of the structures. This requires the analysis of a sequence of images. Measurements that study the evolution of flow structures were carried out on vortex pairing (Meynart 1983), on temporal evolution of the flow past a circular cylinder (Lourenço & Krothapalli 1988b), and on the flow under water waves (Gray & Greated 1988). In fact, these experiments concern reproducible flow phenomena, which relaxes the need for (fast) cinematographic recording and analysis of large amounts of images to yield a satisfactory result. This is, however, not the case for turbulent flows.

This was about the situation at the beginning of the study described in this thesis. We have seen that the PIV yields quantitative measurements of the instantaneous velocity field in a planar cross section of the flow. This is the type of measurement that we need for the investigation of coherent flow structures. However, the conventional PIV method is very slow, which makes it impractical to analyze large sets of flow pictures. Let us illustrate with an example that it is *essential* to have a very fast analysis method for the application of PIV to study the dynamics of coherent flow structures in turbulent flows.

Example 1 (*The PIV bottleneck in turbulent flow measurements*)

Say we want to study a particular structure or event in a turbulent flow. Suppose that we have a 10% probability to record this structure. To obtain reliable estimates of the *statistics* of this structure we need a sample of say 100 events. Hence, we have to process about 1,000 pictures to obtain a satisfactory result. For a spatial resolution of 1,000 interrogations per picture this yields a total of about 10^6 interrogations. Even a larger number of pictures would be required if we would also like to determine the *dynamics* of this structure, i.e. through the analysis of time-resolved picture sequences, not to mention the total number of pictures that would be needed if we also would like to study the structure or event under different flow conditions. If we assume an analysis time of one second per interrogation—which is representative for the Young's fringe analysis—then the total analysis of 10^6 interrogations would take about *two weeks*. In practice this would not even be enough time because we should also include the time that is required for film development, mounting the negatives in the interrogation system and post-processing the data.

It should be clear by now that we cannot use a method that requires several *hours* to analyze a single picture; the total time that is required to process all the images would have to be expressed in *weeks* or even *months*. Hence, *the current implementations of the PIV method are not adequate for the investigation of coherent flow structures in turbulent flows*. This was the situation that we faced at the start of the study described in this thesis. The solution to this problem is the introduction of the digital counterpart of the conventional PIV method, which is the main topic of this thesis. The basic idea is explained in the next section.

1.2.4 alternative implementations

The time-consuming digital analysis of the fringe pattern does not only nullify the elegance of the optical processing, but also creates a bottleneck in PIV applications that require the analysis of a large number of PIV images. Therefore alternative analysis methods were developed with the aim to reduce the processing time of PIV images.

image compression

Yao & Adrian (1984) proposed a one-dimensional orthogonal compression technique, in which the fringe pattern is integrated along two orthogonal directions (using cylindrical lenses). Now only two one-dimensional FFT computations are required to analyze the fringe pattern. A disadvantage of this method is that the random noise peaks increase considerably, which enhances the probability of a spurious identification of the displacement-correlation peak (Adrian 1986b). In addition, we now have a *fourfold* directional ambiguity instead of a twofold directional ambiguity. Despite some of the obvious advantages this method has not become very popular.

optical correlators

Another approach followed by several researchers (Coupland & Halliwell 1988) was to develop a fully *optical correlator*. The basic idea is to implement the two Fourier transformations that are required to obtain the covariance function *optically*. A fully optical correlator is described by Coupland & Halliwell (1988). In this device the fringe pattern is first recorded in a photorefractive⁵ bismuth-silicon-oxide (BSO) crystal, while being illuminated with a reference beam. Subsequently the reference beam is switched off, and by the principles of holographic reconstruction (Goodman 1968) the auto-correlation of the image written in the BSO crystal appears in the back focal plane of a second lens. In theory, this correlator is capable to yield the auto-correlation associated with the fringe pattern almost instantaneously. In practice however the limiting factor is the time that is required to "write" the photorefractive crystal. With a 0.1 W Ar⁺ laser the typical response time is 1 second. Although optical correlators yield the image covariance function

⁵Photorefractives are reusable materials that store phase information through the mechanism of the linear electrooptic effect.

without any numerical calculation, they have yet not been able to reduce the processing speed within the order of a few minutes per PIV image.

These alternative implementation only aim to speed up the analysis time. However, one should realize that the *total* processing time is not determined by the acquisition of the covariance function alone; the traversing of the negative along the interrogation optics, but also the evaluation of the auto-covariance function (i.e. estimation of the centroid of the displacement-correlation peak) tend to determine the total processing time as the time required to process the interrogation image is reduced. Besides that we should also take into account the time that is required for film development, and mounting the negative to the interrogation system.

1.3 Digital particle image velocimetry

What we have seen from the discussion above is that the bottleneck-problem is twofold: (a) we have to find a way how to reduce the computational effort in the PIV image analysis; and (b) we must also avoid the processing of photographic film and the mechanical manipulation, which are inherent to OPIV. An alternative approach that would provide a feasible solution is to implement the PIV method *digitally*. The key principle of the digitally implemented PIV method, referred to as *digital* particle image velocimetry (DPIV), will be explained first. We will then describe a simple test experiment that was carried out to assess the feasibility of this alternative implementation. Finally we will place the method in its historical context.

1.3.1 principle

Let us first tackle the first part of the bottleneck-problem. The time that is required to compute the two-dimensional discrete Fourier transform of a $N \times N$ -pixel image is proportional to $N^2 \log N$. Thus, we can reduce the processing time considerably by reducing the pixel resolution of the interrogation image. However, a reduction of resolution also affects the accuracy of the measured displacement. At first thought one would expect that the relative measurement error for the displacement for a $N \times N$ -pixel interrogation area is proportional to $1/N$ (Adrian 1986b). Suppose we would reduce the pixel resolution from 256×256 to 32×32 . Though the relative error is then increased by a factor of 8, the processing time is reduced by more than a factor of 100! Referring to the performance quoted for Young's fringe analysis, the typical processing time required to analyze a 32×32 -pixel interrogation area is 5–10 milliseconds, with an expected relative measurement accuracy of less than 4%. (As we will see later (Sect. 3.10), in practice it appears that the accuracy of DPIV is *better*, namely about 1–2%.) Provided that the turbulence intensity is significantly larger than the relative measurement error⁶ then the proposed reduction in

⁶in the near-wall region of a turbulent boundary-layer flow the turbulence intensity is 10–20%; Hinze (1975)

pixel resolution may still yield useful results.

We have argued in the last paragraph of the previous section that we can only take full benefit of the reduction in FFT processing time if we can also tackle the second part of the bottleneck problem. Namely, we must avoid the overhead of processing photographic materials and mechanical manipulation of a PIV transparency in some interrogation system. This can be achieved by recording the PIV image *directly* with an electronic imaging device and store it in digital memory. An additional advantage is that the total image is available in the memory of the computer we can apply various (global) image-processing operations (e.g. make corrections for perspective distortion, subtract a background image or align successive frames). The principle of the analysis is the same way as for the direct correlation method, described in Sect. 1.2.2; instead of subsequent optical interrogation we now digitally subdivide the complete image in small interrogation regions. These are subsequently analyzed by computation of an image auto-correlation (using a FFT-algorithm). The spatial resolution of this type of analysis depends on the pixel resolution of the digital image. Typical resolutions for solid-state arrays are 512×512 or 1024×1024 pixels⁷. Although the *spatial* resolution of most electronic imaging devices several orders of magnitude lower than that of photographic film (see Table 1.2), the *interrogation* resolution differs only by an order of magnitude. However, the reduction of pixel resolution in the interrogation analysis would still allow us to retrieve a satisfactory amount of data from a digital PIV image. For example, suppose we have a 1024×1024 -pixel digital image that is interrogated with 32×32 -pixel interrogation areas, in which we allow a 50% area overlap for subsequent interrogation positions. This would still yield a resolution of about 4,000 interrogations per image.

The overall performance of PIV analysis is characterized by spatial resolution, accuracy and processing speed. In Table 1.2 we compare the (estimated) performances of OPIV and DPIV. It is the author's belief that the distribution of performance over resolution,

Table 1.2: Comparison of the performances for OPIV and DPIV.

		OPIV	DPIV
image resolution	px	10^7 – 10^9	$\sim 10^6$
interrogations/image	$\times 10^3$	4–40	1–4
relative accuracy	%	< 1	1–4
processing time ^a	s	>500	10

^aper 1,000 interrogations

accuracy and speed in DPIV is more suitable for the investigation of large sequences of

⁷arrays with 2048×2048 or even 4096×4096 pixels are currently being developed.

data than in OPIV. This conjecture was the point of departure for the work described in this thesis.

1.3.2 vortex street behind a cylinder

To show the feasibility of the digital implementation of the PIV method described above we have carried out a simple test experiment. In this experiment a sequence of 13 double-exposure images of a vortex street in water behind a cylinder were analyzed. The vortex street can be considered as a simple, incompressible two-dimensional flow consisting of vortical structures which remain constant in strength and move at constant velocity (Lamb 1932; Roshko 1954; Kaufmann 1963). This appeared to be an ideal test flow, with well-defined vortical structures and with predictable dynamical behaviour.

Here we only briefly describe the experimental conditions of the test experiment; for more details refer to Westerweel *et al.* (1992). A cross section of the flow behind the cylinder was illuminated with a light sheet. Seeding of the flow was accomplished by introducing small air bubbles. The mean fluid velocity was 16 mm/s, and the diameter of the cylinder was 20 mm, yielding a Reynolds number of 320. The motions of the bubbles in the light sheet were observed with a CCD-video camera, and recorded on a VHS video-tape. The video images were digitized with a 512×512-pixel, 8-bit frame grabber. Every fourth video frame was captured, with a total of 14 frames. The images were re-sampled at 256×192 pixels (extracting only the even scanlines from the interlaced video signal). The size of the images correspond to an area of 60×120 mm² in the light sheet. The frames were added pairwise, yielding 13 double-exposure images with an exposure time-delay of 0.16 s. The average particle-image displacement was 5–6 pixel units.

The images were analyzed using overlapping 32×32-pixel interrogation sub-images, with a shift of 16 pixels between successive interrogations. Each image yielded a data set of 15×11 velocity vectors with an estimated rms error of 1 mm/s. To reveal the vortical structures the vorticity from the experimental data was computed. The results are shown in Figure 1.8. At $Re=320$ the vortex street is outside the stable range, and the large-scale structures are perturbed by small-scale instabilities (Roshko 1954). However, in Fig. 1.8 the typical structure of a vortex street can be recognized. The theory predicts that the vortices move with a constant advection velocity of 0.7 times the mean flow velocity, and that the vorticity of these structures remains constant (Lamb 1932; Kaufmann 1963). The position and the average vorticity of a vortex structure were determined from the vorticity data. The results are given in Figure 1.9. The measured advection velocity and strength of the vortices agreed with the theoretical predictions within the statistical accuracy of the results. In addition it should be noted that since the advection velocity of the vortices (in the experiment) is about 0.7 times the mean flow velocity, the vortices move *significantly slower* than the tracer particles themselves. This implies that the pattern we see in Fig. 1.8 is not tied to the tracer particles in the flow. *This is an important difference with respect to traditional visualization, in which structures are only visible if the tracer is applied inhomogeneously or is tied to the observed structure.*

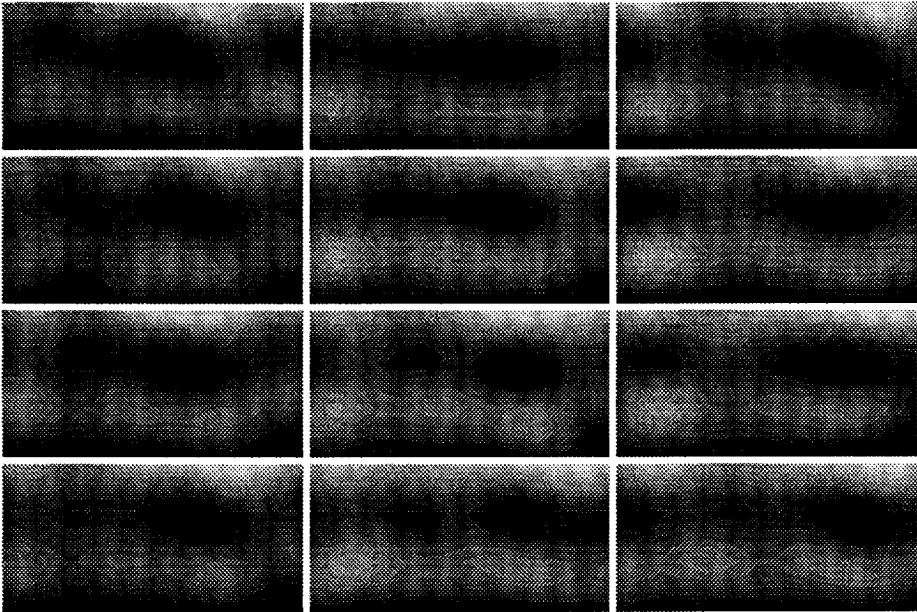


Figure 1.8: Grey-scale maps of the vorticity component perpendicular to the image plane of a vortex street behind a cylinder determined from 12 double-exposure images after PIV analysis. Light regions indicate positive values, dark regions negative values. The sequence of the maps is according to the diagram. The flow is from left to right.

1	5	9
2	6	10
3	7	11
4	8	12

1.3.3 context

The first digital PIV application at high image density known to the author was by He *et al.* (1984). They took direct digital images from a densely seeded, steady laminar flow in a rectangular tube. Subsequent images were analyzed using a template-matching approach: subimages of the first image were cross-correlated with the entire second image. Kimura & Takamori (1986) applied the same template-matching method to PIV images of the wake region behind a circular cylinder. These precursive developments to digital PIV were limited to simple flows, in which demands for high spatial and temporal resolution and accuracy were not essential.

Independent of the development of digital PIV by the author, Willert & Gharib (1991) developed a similar digital PIV method. Their aim was to come up with a method *without the directional ambiguity* that is inherent to PIV applications with double-exposure images, whereas the aim of the author of this thesis was to come up with an essentially *faster* method. Instead of an auto-correlation method Willert & Gharib implemented

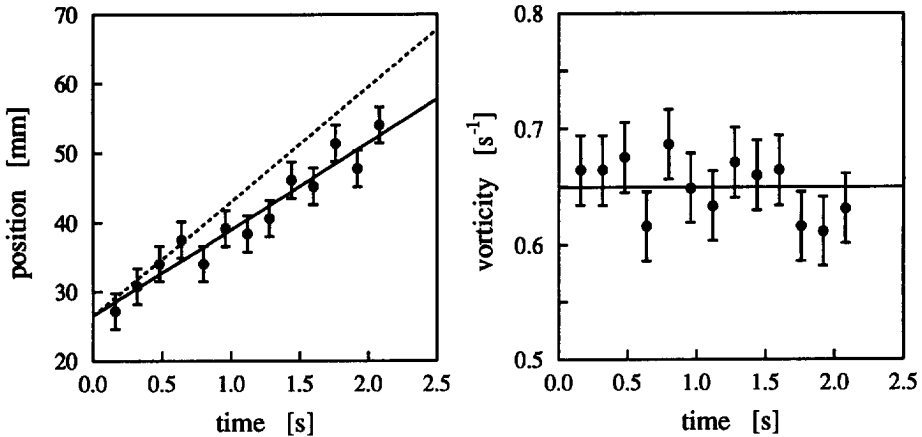


Figure 1.9: The position (left) and strength (right) of a vortex structure in Fig. 1.8. The solid lines are linear least-squares fits to the experimental data. The dashed line in the left graph would represent the position of an object that moves with the mean flow velocity.

a cross-correlation method between two single-exposure frames as was suggested by Cho (1989); see Sect. 1.2.2. They subsequently applied their method to the temporal evolution of a vortex ring. The time scale of this low-speed flow could easily be resolved by the frame rate (30 Hz) of their video system. An interesting aspect of their work was that they introduced a new type of estimator for the centroid of the displacement-correlation peak, namely the Gaussian peak-fit estimator. They demonstrated that this estimator yielded an *absolute* measurement accuracy *better* than 0.1 px, whereas the conventional estimation method (i.e. center-of-mass estimator) yields an accuracy of only 0.3–0.4 px (Prasad *et al.* 1992). This was quite remarkable, and showed that earlier estimates of the expected measurement accuracy for DPIV (i.e. interrogation with low pixel resolution), based on the assumption that the relative measurement error is inversely proportional to the pixel resolution, were too pessimistic. Obviously interrogation with low pixel resolution requires a different type of estimator than interrogation with high pixel resolution. The accuracy claimed by Willert & Gharib implied that measurements of the displacement with interrogation regions of only 32×32 pixels could yield a *relative* accuracy close to 1%, which is also found in interrogation analysis with high pixel resolution in OPIV (Prasad *et al.* 1992). The conclusion that a reduction in pixel resolution by a factor 8^2 practically does not affect the measurement accuracy was generally received with scepticism. Although it was welcomed by those who believe in digital PIV, it is necessary to solve this *controversy* in order to accept digital PIV as a feasible alternative for OPIV. This is one of the problems that will be addressed in this thesis.

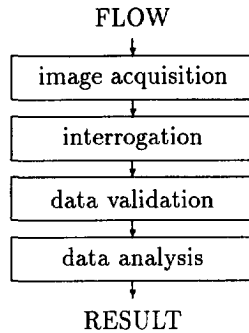


Figure 1.10: The four stages in image and data analysis in (digital) PIV.

1.4 Outline of this thesis

In this chapter we have seen that particle image velocimetry is a new experimental technique that reveals the instantaneous spatial structures in turbulent flows. However, the conventional implementation of PIV is not suited to investigate large sequences of data which would be required to investigate also the *dynamics* or *statistics* of coherent structures. An alternative implementation, denoted as *digital* particle image velocimetry, was developed, which is expected to meet this requirement. So, the main aim of this thesis can be more specifically defined as *to establish the necessary theoretical basis and practical verification to justify this expectation*.

The remainder of this thesis is divided in two parts. The first part consists of four chapters, which describe the four stages in image and data analysis in (digital) PIV as shown in Figure 1.10. In Chapter 2 we review the relation between tracer particles in a flow and their respective images, and how a statistical analysis yields the velocity field. This theory is extended in Chapter 3 to include the aspect that we are actually dealing with digital images. We will use this theory to investigate different estimators to yield optimal results as function of the digital resolution. Chapter 4 describes the validation procedure that is required to remove spurious data from PIV results. In Chapter 5 it is described how we can extract information from this data that is related to coherent flow structures.

Part II consists of applications of PIV to turbulent flows. In Chapter 6 a test measurement in grid turbulence with digital PIV is described. The remainder of Part II (Chapters 7, 8 and 9) consists of three papers describing a comparative study of fully developed turbulent pipe flow carried out with direct numerical simulation and both OPIV and DPIV.

This thesis concludes in Chapter 10 with a summary of the main results and conclu-

sions from the preceding chapters. In addition we focus on the (expected) future developments with respect to digital particle image velocimetry and its further application to the investigation of coherent flow structures in turbulent flows.

Part I
theory

Chapter 2

Statistics of PIV Images

Abstract. *In PIV a flow is seeded with small tracer particles that are illuminated by a thin light sheet. The in-plane fluid velocity in a planar cross-section of the seeded flow can be obtained from the cross-covariance of two subsequent images recorded with a given time delay. A relation between the statistics of the tracer particles and the statistics of PIV pictures is established for the case of an incompressible flow that is seeded homogeneously with ideal tracer particles. It is shown that the displacement field for the tracer particles in a certain time interval can be regarded as a low-pass filtered representation of the flow velocity field.*

2.1 Introduction

Optical flow diagnostics are based on the interaction, i.e. refraction, absorption or scattering, of (visible) light with inhomogeneous media. In this thesis we restrict ourselves to incompressible flow of constant density fluids, which are effectively homogeneous at the scale of the wavelength of light. Hence there is no significant interaction of the incident light with the fluid, such as refraction by density variations, by which we can retrieve information of the flow velocity field (except for molecular scattering which is very weak under normal conditions, viz., at room temperature and atmospheric pressure). We are therefore forced to add small tracer particles to the fluid that act as scattering sites for the incident light field. Provided that these tracer particles are *ideal* (see Section 2.2) the local flow velocity is obtained from the displacement of the tracer particle in a given time period. We may regard this as the basic principle of velocity measurement by the technique of quantitative flow visualization with tracer particles.

In this chapter we discuss and review some of the basic principles of this technique, as shown in Figure 2.1. In Section 2.3 we take a closer look at the relation between the displacement of the tracer particles and the underlying flow field. The tracer particles can in fact be viewed as an observable pattern that is tied to the fluid (Section 2.4). The tracer particles are randomly distributed over the flow, so that the tracer pattern is also a random quantity. In Section 2.4 we discuss the *ensemble* of all realizations of the tracer pattern for a given flow field, and evaluate the statistics of this tracer pattern. The tracer

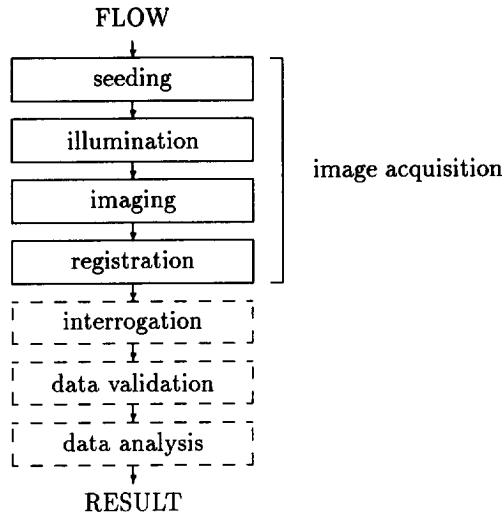


Figure 2.1: The subsequent stages of image acquisition in PIV.

pattern is observed in a planar cross section of the flow by illumination of the tracers with a thin light sheet. Pictures of the tracer particles are observed in the image plane of the lens; in Section 2.5 we review some relevant aspects of the optical system, and in Sections 2.7 and 2.8 we relate the statistical properties of the observed particle images to the statistics of the tracer pattern. We conclude this chapter with a discussion of this theoretical analysis of the measurement of flow velocity fields from flow visualization with tracer particles (Section 2.9).

2.2 Ideal tracer particles

The tracer particles that are added to the fluid (or that may already be present in the fluid) should follow the motion of the fluid exactly. In addition they should not alter the flow, and also should not interact with each other. In that case the tracer particles are said to be *ideal*. In a practical situation we can only *approximate* this ideal situation. We should not only consider the dynamical response of the tracer particles with respect to the fluid motion, but also their light scattering characteristics. These two aspects impose somewhat conflicting demands on the tracer particles; small particles cause a smaller distortion of the flow than large particles, while on the other hand large particles scatter light more efficiently.

There is an abundance of literature that deals with the behaviour of particles in fluids and that deals with the scattering of light by (small) particles (Mie scattering). Emrich

(1981) gives an overview of the dynamical response of particles in fluids, and see Kerker (1969) for further details with respect to the scattering of light. For practical computations of light scattering properties of particles (with respect to PIV applications) see Adrian & Yao (1985) and Smallwood (1992). Practical information on a choice of seeding materials is given by Emrich (1981) and Oertel & Oertel (1989). Let us here briefly review some general considerations that are important when one selects the seeding for an experiment.

The efficiency of the light scattering is determined by the difference in index of refraction for the fluid and the particles. In gas flows seeded with solid or liquid particles, or in liquid flows seeded with gas bubbles, we have efficient scattering of light. However, the large relative difference in density between the fluid and tracer particles (about a factor 10^3) requires that the diameter of the particles must be very small ($\sim 1 \mu\text{m}$) to assure a proper tracking of the fluid motion. This cancels the favourable scattering properties of the particles. Buoyancy effects can be neglected when the response time of a particle to a sudden change of the fluid velocity (Emrich 1981) is smaller than the smallest time scale of the flow.

On the other hand, in liquid flows we can use solid particles that are almost neutrally buoyant. In general this assures good tracking performance of the particles. However, the difference between the refractive indices of liquids and solids are generally quite small, so that relatively large particles ($\sim 10 \mu\text{m}$) are required to yield sufficient scattering. Large particles have a stronger mutual interaction or a stronger influence on the flow dynamics. Obviously, the dynamics of turbulent flows is altered when seed particles have a diameter that is comparable with the Kolmogorov length scale. We have seen in Sect. 1.1 that this scale in laboratory-type flows is about $100 \mu\text{m}$.

In general it should be possible to keep the non-ideal behaviour of tracer particles with respect to the fluid motion within acceptable limits, i.e. within the experimental error for the measurement of the displacement (see Table 1.2). We therefore will consider the tracer particles as *ideal* for the remainder of this thesis.

2.3 The displacement field

The displacement field $\vec{D}(\vec{X}; t', t'')$ is defined as the distance traveled by a tracer particle initially located in \vec{X} in a time interval $\Delta t = t'' - t'$ by the flow velocity field $\vec{v}(\vec{X}, t)$, and is given by

$$\vec{D}(\vec{X}; t', t'') = \int_{t'}^{t''} \vec{v}[\vec{X}(t), t] dt \quad (2.1)$$

for *ideal* tracer particles. Note that from the displacement field one can only obtain information about the *average* velocity field along trajectories traversed in a time Δt . Thus, \vec{D} can *not* lead to an exact representation of \vec{v} , but approximates it within an

error ε :

$$\|\vec{D}(\vec{X}; t', t'') - \vec{v}(\vec{X}, t)\Delta t\| < \varepsilon, \quad \text{with } t' \leq t \leq t''. \quad (2.2)$$

Effectively, \vec{D} may be regarded as a low-pass filtered representation of \vec{v} , by which we can only observe phenomena that occur over a time interval which is longer than Δt and a that have a spatial extent that is larger than the absolute displacement $\|\vec{D}\|$.

We only obtain information from those positions at which tracer particles are located. In other words, displacements of individual tracer particles constitute a random sampling of the displacement field. Since the particles are randomly distributed over the flow, different realizations yield different estimates of \vec{D} . Obviously we can neglect these differences as long as the reconstructed displacement field satisfies Eq. (2.2). This implies that we should sample the displacement field at a density that matches with the smallest length scale of the spatial variations in \vec{D} , which is proportional to $\|\vec{D}\|$. In other words, the average distance between tracer particles should be smaller than the particle displacement. Recall from Sect. 1.2 that this corresponds to situation with high image density. Hence it is demonstrated that particle tracking velocimetry (in which the average distance between distinct particle images is usually *larger* than the displacement) in general cannot fully resolve the displacement field.

2.4 The tracer pattern

We have seen in Section 1.2 that it is not possible to identify corresponding particle-image pairs unambiguously in double-exposure PIV images at high image density. Instead we use a statistical analysis to yield the displacement field.

Let us consider the tracer particles as a *pattern* that is “tied” to the fluid; the motion of the flow is visible through the motion of the tracer pattern. We define the tracer pattern in \vec{X} at time t as

$$G(\vec{X}, t) = \sum_{i=1}^{\mathcal{N}} \delta[\vec{X} - \vec{X}_i(t)] \quad (2.3)$$

where \mathcal{N} is the total number of particles in the flow, $\delta(\vec{X})$ denotes the Dirac δ -function and $\vec{X}_i(t)$ the position vector of the particle with index i at time t . The integration of $G(\vec{X}, t)$ over a volume yields the number of particles in that volume.

Since the tracer particles are randomly distributed over the flow $G(\vec{X}, t)$ is a random field. This implies that each realization of the tracer pattern yields a different sampling of the displacement field. Following Adrian (1988) we consider the ensemble of all possible realizations of the tracer pattern for a given flow field, and evaluate the statistical properties of the tracer pattern. The tracer ensemble and the statistical properties of the tracer pattern are discussed in more detail in Appendix A.2. There we show that a homogeneous distribution of tracer particles in the case of an incompressible flow remains homogeneous (in space and time). This allows us to determine the statistics of the tracer

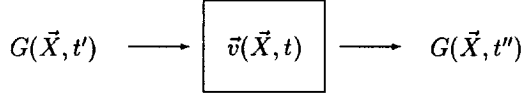


Figure 2.2: The velocity field $\vec{v}(\vec{X}, t)$ is viewed as a black-box system that acts on the tracer pattern $G(\vec{X}, t')$ at the input to yield the tracer pattern $G(\vec{X}, t'')$ at the output.

pattern in a straightforward way. We will now show how these statistics are related to the velocity field.

Consider a particular realization of the tracer pattern at times t' and t'' , with $t' < t''$, denoted by $G'(\vec{X})$ and $G''(\vec{X})$ respectively. For a given flow field the displacement of an (ideal) tracer particle in a time interval $t'' - t'$ located in a position \vec{X} at time t' is given by the displacement field $\vec{D}(\vec{X}; t', t'')$, defined in (2.1). Hence, the relation between $G'(\vec{X})$ and $G''(\vec{X})$ under action of $\vec{v}(\vec{X}, t)$ is a *shift* over $\vec{D}(\vec{X}; t', t'')$. In a sense we can consider the flow as a “black-box” system that acts on a random field $G'(\vec{X})$ at the “input” to yield the random field $G''(\vec{X})$ at the “output”. This is depicted in Figure 2.2. We previously assumed that the tracer particles are *ideal* (see Sect. 2.2), which implies that they do not influence the flow and do not interact with each other. In other words, including or deleting a particle from $G(\vec{X}, t)$ has no effect on the other particles. This implies that we can consider the “system” in Fig. 2.2 as *linear* in $G(\vec{X}, t)$. By analogy with linear systems analysis (see Appendix A.1) we can determine the displacement field that corresponds to the observed flow field by evaluation of the *cross-covariance function* of the random fields $G'(\vec{X})$ and $G''(\vec{X})$. This function is defined as

$$R_{GG}(\vec{X}', \vec{X}'') = \langle G'(\vec{X}')G''(\vec{X}'') \rangle - \langle G'(\vec{X}') \rangle \langle G''(\vec{X}'') \rangle \quad (2.4)$$

where $\langle \dots \rangle$ denotes the ensemble average. In Appendix A.3 we use the statistics of the tracer particles in an incompressible flow, derived in Appendix A.2, to evaluate the first and second order statistics in (2.4):

$$\langle G(\vec{X}') \rangle = \langle G(\vec{X}'') \rangle = C \quad (2.5)$$

$$\langle G'(\vec{X}')G''(\vec{X}'') \rangle = C\delta[\vec{X}'' - \vec{X}' - \vec{D}(\vec{X}'; t', t'')] + C^2. \quad (2.6)$$

where C is the number density of the tracer particles in the fluid. If we substitute these results in (2.4) we obtain

$$R_{GG}(\vec{X}', \vec{X}'') = C\delta[\vec{X}'' - \vec{X}' - \vec{D}(\vec{X}'; t', t'')]. \quad (2.7)$$

Note that the displacement field appears as a *shift* in R_{GG} . The displacement field in (2.7) disappears for $t' = t''$. In that case R_{GG} is shift-invariant, which implies that the tracer pattern is a spatially homogeneous random field. The cross-covariance function for

$G(\vec{X}, t')$ and $G(\vec{X}, t'')$ on the other hand is *not* necessarily shift-invariant, due to the spatial variation of the displacement field. We could proceed with our analysis, taking into account that the displacement field depends on \vec{X}' explicitly. However, we can simplify the analysis considerably in case of a “locally” homogeneous displacement field. Let us have a closer look at the effect of a (weak) spatial variation of the displacement field over a small volume.

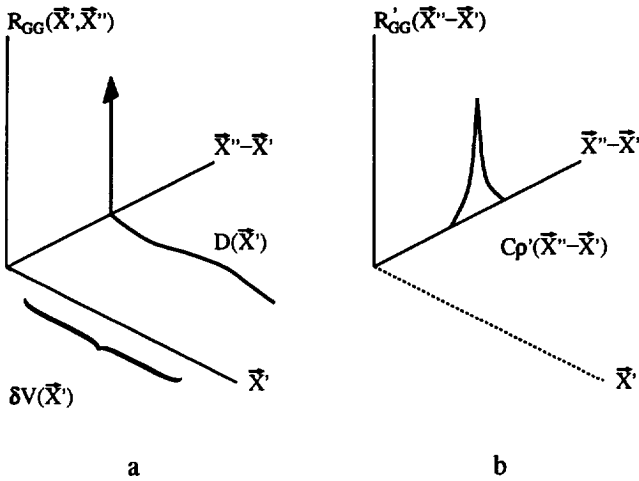


Figure 2.3: (a) Schematic representation of the integration of the cross-covariance (R_{GG}) of the tracer pattern over a small volume $\delta V(\vec{X}')$. (b) Due to the spatial variation of the displacement field ($\vec{D}(\vec{X}; t', t'')$) the δ -function in R_{GG} is replaced by the distribution function ($\rho'(\vec{X}'' - \vec{X}')$) of the local displacement field; see text.

The integration of $R_{GG}(\vec{X}', t'; \vec{X}'', t'')$ over a small volume $\delta V(\vec{X}')$ is depicted in Figure 2.3. (Note that the axes \vec{X}' and $\vec{X}'' - \vec{X}'$ actually represent three-dimensional spaces.) The peak in the covariance function is broadened due to the spatial fluctuations of the displacement field over the integration volume; see Fig. 2.3b. In practice, the spatial distribution function of $\vec{D}(\vec{X}'; t', t'')$ over $\delta V(\vec{X}')$, indicated by $\rho'(\vec{X}')$, replaces the δ -impulse in (2.7), i.e.

$$R'_{GG}(\vec{X}'' - \vec{X}') = C\rho'(\vec{X}'' - \vec{X}') \tag{2.8}$$

where the prime for R_{GG} and ρ indicates the averaging over $\delta V(\vec{X}')$. The local mean displacement, denoted by \vec{D}' , is given by

$$\vec{D}' = \int_{\delta V(\vec{X}')} \vec{D}(\vec{X}'; t', t'')\rho'(\vec{X}'' - \vec{X}')d(\vec{X}'' - \vec{X}') \tag{2.9}$$

(again the prime refers to a spatial averaging over $\delta V(\vec{X}')$). We now associate $\delta V(\vec{X}')$ with the measurement volume for which we want to measure the flow velocity (viz., tracer displacement). Again consider the relation between the velocity field $\vec{v}(\vec{X}, t)$ and the displacement field $\vec{D}(\vec{X}; t', t'')$ given in (2.1). There we noted that the displacement field is a low-pass filtered representation of the corresponding velocity field. As a direct consequence the displacement field is strongly correlated over a length scale that is proportional to the magnitude of the displacement; see Figure 2.4. This implies that the spatial vari-

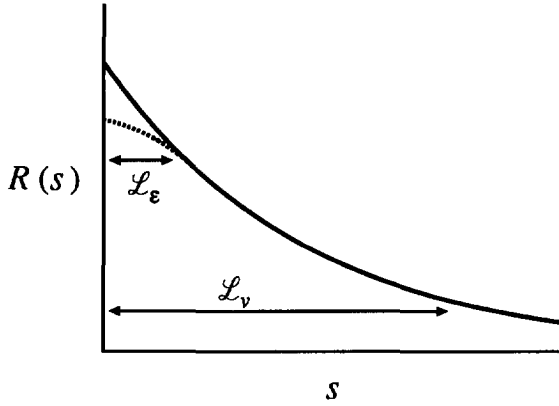


Figure 2.4: The (one-dimensional) auto-covariance of a turbulent velocity field (solid line) as function of the separation s . The dashed line represents the auto-covariance of the corresponding displacement field. The arrows represent the integral length scale of the velocity field (L_v) and the filter length (L_ϵ) associated with the displacement field; see Eq. (2.2).

ation of $\vec{D}(\vec{X}'; t', t'')$ over $\delta V(\vec{X}')$ is negligible provided that $\delta V^{1/3} = \mathcal{O}(\|\vec{D}\|)^1$. For a (nearly) uniform displacement we have

$$\rho'(\vec{X}'' - \vec{X}') \sim \delta(\vec{X}'' - \vec{X}' - \vec{D}'). \quad (2.10)$$

(If we substitute this in (2.9) then we find $\vec{D}' \sim \vec{D}(\vec{X}'; t', t'')$; in other words, ρ' can be viewed as a *pseudo* δ -function (Priestley 1992) with respect to the displacement field.) In the following sections we will therefore consider R_{GG} for $t'' \neq t'$ as a shift-invariant function that consists of a δ -impulse shifted over \vec{D}' , viz.

$$R_{GG}(\vec{X}', \vec{X}'') \approx R'_{GG}(\vec{X}'' - \vec{X}') = C\delta[\vec{X}'' - \vec{X}' - \vec{D}']. \quad (2.11)$$

In the remainder of this thesis we assume that we are dealing with a displacement field that can be considered as locally *uniform*; see also Sect. 2.9. In that situation we can

¹Here we have implicitly assumed that the displacement field is also isotropic, which is not the case where we have a strong velocity gradient perpendicular to the flow direction, like e.g. in the near-wall region of a boundary layer flow. We will return to this situation in Sect. 2.9.

use the expression in (2.11) for the cross-covariance function of the tracer pattern, and consider the cross-covariance as *homogeneous*.

2.5 Optical system

In Figure 2.5 is shown a schematic representation of the light sheet and optical system for imaging tracer particles in a planar cross section of a flow. We assume that the system consists of an aberration-free, thin circular lens with a focal length f and a diameter D . The object distance Z_0 and image distance z_0 satisfy the geometrical lens law:

$$\frac{1}{Z_0} + \frac{1}{z_0} - \frac{1}{f} = 0. \quad (2.12)$$

with the *image magnification* defined as:

$$M = \frac{z_0}{Z_0}. \quad (2.13)$$

The particles in the object plane are illuminated with a thin light sheet of thickness ΔZ_0 from a coherent light source (viz., a laser) with wavelength λ . We assume that all observed particles are in focus. This condition is satisfied for ΔZ_0 less than the object focal depth δZ , given by (Adrian 1991):

$$\delta Z \approx 4 \left(1 + \frac{1}{M}\right)^2 \frac{f^2 \lambda}{D^2}. \quad (2.14)$$

The intensity $I_o(X, Y, Z)$ of the light sheet is assumed uniform in the X and Y directions within the observed area. Hence, we may write

$$I_o(X, Y, Z) = I_o(Z) \quad (2.15)$$

where $I_o(Z)$ is the light-sheet intensity profile perpendicular to the object plane. For a laser light sheet $I_o(Z)$ is typically a Gaussian profile

$$I_o(Z) = I_Z \exp[-8(Z - Z_0)^2 / \Delta Z_0^2] \quad (2.16)$$

where I_Z is the maximum intensity along the Z -direction. Note that ΔZ_0 for the Gaussian profile is defined by the $1/e^2$ intensity.

In the optical system described here the relation between the complex amplitude field $U_o(X, Y)$ in the object plane and the complex amplitude field $U_i(x, y)$ in the image plane for coherent illumination is (Goodman 1968):

$$U_i(x, y) = h(x, y) * U_o(x, y) \quad (2.17)$$

with

$$U_g(x, y) = \frac{1}{M} U_o \left(-\frac{x}{M}, -\frac{y}{M} \right) \quad (2.18)$$

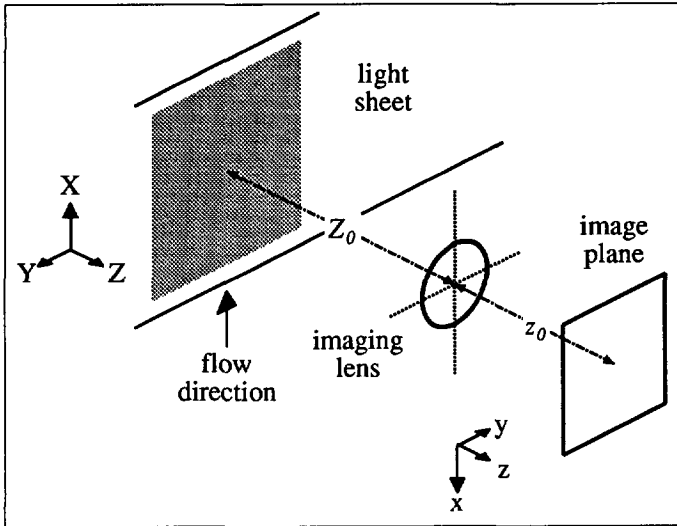


Figure 2.5: Schematic representation of the imaging set-up in PIV.

where $h(x, y)$ is the diffraction limited (amplitude) impulse response of the optical system, the symbol $*$ represents the convolution integral and $U_o(x, y)$ is the geometrical optics prediction in the paraxial approximation for the complex amplitude in the image plane. The signal field $f(x, y)$, i.e. the optical density of a film negative or the electric charge collected with a CCD sensor, is proportional to the image intensity field $I(x, y)$, viz.

$$f(x, y) \sim I(x, y) = |U_i(x, y)|^2. \quad (2.19)$$

For CCD's the collected charge is directly proportional to the incident light intensity; for photographic material this relationship is that of a power-law (Oertel & Oertel 1989). In both cases the conversion from f to I , and *vice versa*, is trivial. We therefore deal directly with the image intensity for the remainder of this thesis.

In the Gaussian approximation of $h(x, y)$ (see Appendix A.4) the image diameter d_i of a small circular object with diameter d_p is given by

$$d_i^2 \approx M^2 d_p^2 + d_s^2. \quad (2.20)$$

where d_s is the diameter of the Airy pattern (see Appendix A.4), given by:

$$d_s \approx 2.44 \frac{\lambda z_0}{D}. \quad (2.21)$$

In Figure 2.6 is given the diameter of the diffraction limited image of a disc with diameter d_p as function of Md_p (its geometrical image diameter). For comparison we also plotted the image diameter predicted according to the Gaussian approximation in (2.20).

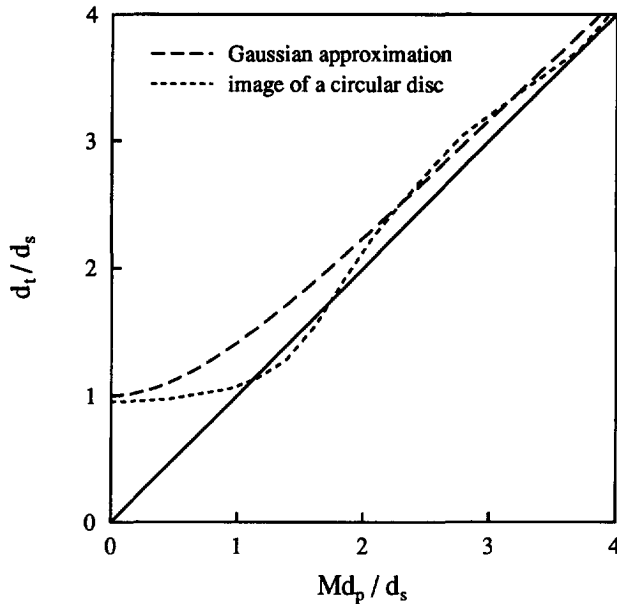


Figure 2.6: The image diameter (d_i) as function of the geometrical-optics diameter (Md_p) normalized by the diffraction-limited spot diameter (d_s). The dotted line represents the actual image diameter, and the dashed line the diameter according to a Gaussian approximation.

2.6 Images from seeded flows

The optical system described in the previous section is linear in the (complex) amplitude field. Thus, we may write the complex amplitude field $U_i(x, y)$ in the image plane as:

$$U_i(x, y) = \sum_k A_k(x, y). \tag{2.22}$$

where $A_k(x, y)$ is the amplitude field due to a particle with index k . We assume that the tracer particles in the flow are identical, with a diameter d_p that is small with respect to ΔZ_0 . The absolute amplitude of $A_k(x, y)$ is then proportional to $I_o^{1/2}(Z_k)$, given the position $\vec{X}_k = (X_k, Y_k, Z_k)$ of the particle. It is clear that only particles with $|Z_k - Z_0| < \Delta Z_0$ make a significant contribution to $U_i(x, y)$. Also, we may consider these particles in focus (provided that $\delta Z > \Delta Z_0$) which implies (in the paraxial approximation) that their corresponding images all have equal diameter, independent of their position. As a result we may write Eq. (2.22) as:

$$U_i(x, y) = \sum_k I_o^{1/2}(Z_k) a(x - MX_k, y - MY_k) e^{i\phi_k(x, y)} \tag{2.23}$$

where $a(x, y)$ normalized amplitude field of a tracer particle ((ampfld)) is the (normalized) amplitude field of a tracer particle given by Eqs. (2.17–2.18), and $\phi_k(x, y)$ an additional phase term that depends explicitly on k (viz. \vec{X}_k). The image intensity field $I(x, y)$ is according to Eq. (2.19) given by:

$$I(x, y) = \sum_k \sum_l I_o^{1/2}(Z_k) I_o^{1/2}(Z_l) a_k a_l^* \cos[\phi_k(x, y) - \phi_l(x, y)] \quad (2.24)$$

with $a_i = a(x - MX_i, y - MY_i)$ and where a_j^* denotes the complex conjugate of a_j .

The appearance of $I(x, y)$ depends on the concentration of tracer particles in the light sheet. The *source density* N_S , due to Adrian (1984), is a dimensionless quantity defined as

$$N_S = C \Delta Z_0 \frac{\pi}{4} \frac{d_t^2}{M^2} \quad (2.25)$$

where C is the number of tracer particles per unit volume, and d_t the particle-image diameter. A distinction is made between two image modes, determined by the value of N_S : At low source density ($N_S \ll 1$) the average distance between particles is much larger than the particle-image diameter, and thus the image consists of *isolated* particle images. On the other hand, at high source density ($N_S \gg 1$) particle images overlap; For coherent illumination the resultant image is a random interference pattern, better known as *speckle*. These modes are commonly referred to as the *particle-image mode* and the *laser-speckle mode* respectively. For the analysis of the images discussed here we will only consider the particle-image mode. This restriction is merely practical, and for two reasons: First, the particle-image mode is most common, since true speckle images require high concentrations (which may lead to undesired effects, like e.g. two-phase flow effects; see Adrian 1984). Secondly, restriction to low source density allows us to find a straightforward relation between the tracer pattern $G(\vec{X}, t)$ and particle-image pattern, that will be given below. However, for an analysis that applies to speckle images refer to Goodman (1984).

At low source density ($N_S \ll 1$) particle images do not overlap. Hence all cross terms in (2.24) vanish, viz., $a_k a_l^* \sim 0$ for $k \neq l$ and (2.24) reduces to

$$I(x, y) = \sum_k I_o(Z_k) t(x - MX_k, y - MY_k) \quad (2.26)$$

with $t(x, y) = |a(x, y)|^2$. This result is identical to the image field that would be obtained for *incoherent* illumination (Goodman 1968). We may write Eq. (2.26) alternatively as

$$I(x, y) = I_Z t(x, y) * g(x, y) \quad (2.27)$$

with

$$g(x, y) = \frac{1}{I_Z} \sum_k I_o(Z_k) \delta(x - MX_k, y - MY_k) \quad (2.28)$$

where $g(x, y)$ is referred to as the *particle-image pattern*. The relation between $g(x, y)$ and $G(\vec{X})$ is obviously given by

$$g(x, y) = \frac{1}{I_Z} \frac{1}{M^2} \int I_o(Z) G\left(\frac{x}{M}, \frac{y}{M}, Z\right) dZ. \tag{2.29}$$

Note, by analogy with $G(X, Y, Z)$, that the integral of $g(x, y)$ over a given area yields the (non-integer) number of particle-images in that area.

2.7 Ensemble statistics of PIV images

With the relation between the particle-image pattern g and the tracer pattern G given in (2.29) we may now find the first and second order statistics of the image field $I(x, y)$, given the first and second order statistics of the tracer pattern. We first consider the ensemble average and ensemble auto-covariance function of $I(x, y)$. Then we consider the ensemble cross-covariance of two realizations $I'(x, y)$ and $I''(x, y)$ at times t' and t'' respectively.

average

Using (2.27), we can simply express the ensemble average of $I(x, y)$ in terms of the ensemble average $\langle g(x, y) \rangle$ of the particle-image pattern:

$$\langle I(x, y) \rangle = \langle I_Z t(x, y) * g(x, y) \rangle = I_Z t(x, y) * \langle g(x, y) \rangle. \tag{2.30}$$

The ensemble average of $g(x, y)$, defined in (2.28), is easily found:

$$\begin{aligned} \langle g(x, y) \rangle &= \left\langle \frac{1}{M^2} \int \frac{I_o(Z)}{I_Z} G\left(\frac{x}{M}, \frac{y}{M}, Z\right) dZ \right\rangle \\ &= \frac{1}{M^2} \int \frac{I_o(Z)}{I_Z} \left\langle G\left(\frac{x}{M}, \frac{y}{M}, Z\right) \right\rangle dZ \\ &= \frac{1}{M^2} \left\langle G\left(\frac{x}{M}, \frac{y}{M}, Z\right) \right\rangle \int \frac{I_o(Z)}{I_Z} dZ \\ &= \frac{1}{M^2} C \Delta Z' \end{aligned} \tag{2.31}$$

with

$$\Delta Z' = \frac{1}{I_Z} \int I_o(Z) dZ. \tag{2.32}$$

For the Gaussian profile in (2.16) we have $\Delta Z' = 0.63 \Delta Z_0$. Substitution of (2.31) in (2.30) yields

$$\langle I(x, y) \rangle = \frac{1}{M^2} I_Z t_0 C \Delta Z' \tag{2.33}$$

with

$$t_0 = \iint t(x, y) dx dy \tag{2.34}$$

cf. Adrian (1988). Note that $\langle I(x, y) \rangle$ is space and time invariant.

auto-covariance

The ensemble auto-covariance of $I(x, y)$ is defined as

$$R_I(x', y'; x'', y'') = \langle I(x', y')I(x'', y'') \rangle - \langle I(x', y') \rangle \langle I(x'', y'') \rangle. \tag{2.35}$$

Use (2.33) to rewrite the second term on the right-hand side as

$$\langle I(x', y') \rangle \langle I(x'', y'') \rangle = \left[\frac{1}{M^2} I_Z t_0 C \Delta Z' \right]^2 \tag{2.36}$$

and hence the second order statistics $\langle I(x', y')I(x'', y'') \rangle$ remains to be found. Substitution of (2.27) yields

$$\begin{aligned} \langle I(x', y')I(x'', y'') \rangle &= I_Z^2 \langle t(x', y') * g(x', y') \cdot t(x'', y'') * g(x'', y'') \rangle = \\ &I_Z^2 \iint t(x' - u', y' - v') \iint t(x'' - u'', y'' - v'') \langle g(u', v')g(u'', v'') \rangle du' dv' du'' dv'' \end{aligned} \tag{2.37}$$

We first consider the second order statistics of $g(x, y)$:

$$\begin{aligned} &\langle g(u', v')g(u'', v'') \rangle \\ &= \left\langle \frac{1}{M^4 I_Z^2} \iint I_o(Z') I_o(Z'') G\left(\frac{u'}{M}, \frac{v'}{M}, Z'\right) G\left(\frac{u''}{M}, \frac{v''}{M}, Z''\right) \right\rangle dZ' dZ'' \\ &= \frac{1}{M^4 I_Z^2} \iint I_o(Z') I_o(Z'') \left\langle G\left(\frac{u'}{M}, \frac{v'}{M}, Z'\right) G\left(\frac{u''}{M}, \frac{v''}{M}, Z''\right) \right\rangle dZ' dZ'' \\ &= \frac{1}{M^4 I_Z^2} \iint I_o(Z') I_o(Z'') \left\{ C \delta\left[\frac{u'' - u'}{M}, \frac{v'' - v'}{M}, Z'' - Z'\right] + C^2 \right\} dZ' dZ'' \\ &= \frac{1}{M^4 I_Z^2} \left[\int I_o^2(Z) dZ \right] C \delta(u'' - u', v'' - v') + \frac{1}{M^4 I_Z^2} \left[\int I_o(Z) dZ \right]^2 C^2 \\ &= \frac{1}{M^4} \Delta Z'' C \delta(u'' - u', v'' - v') + \frac{1}{M^4} C^2 (\Delta Z')^2 \end{aligned} \tag{2.38}$$

with

$$\Delta Z'' = \frac{1}{I_Z^2} \int I_o^2(Z) dZ \tag{2.39}$$

cf. Adrian (1988). The value of $\Delta Z''$ for (2.16) is equal to $0.44 \Delta Z_0$. Now substitute (2.38) in (2.37):

$$\begin{aligned} &\langle I(x', y')I(x'', y'') \rangle = \\ &= \frac{I_Z^2}{M^4} \iint t(x' - u', y' - v') \iint t(x'' - u'', y'' - v'') \cdot \\ &\quad \left\{ \Delta Z'' C \delta(u'' - u', v'' - v') + C^2 (\Delta Z')^2 \right\} du' dv' du'' dv'' \\ &= \frac{I_Z^2}{M^4} \left[\iint t(x' - u', y' - v') t(x'' - u'', y'' - v'') du' dv' \right] C \Delta Z'' + \\ &\quad + \frac{I_Z^2}{M^4} \left[\iint t(u, v) du dv \right]^2 C^2 \\ &= \frac{I_Z^2}{M^4} C \Delta Z'' t_0^2 F_t(x'' - x', y'' - y') + \left[\frac{1}{M^2} I_Z t_0 C \Delta Z' \right]^2 \end{aligned} \tag{2.40}$$

with

$$F_t(x, y) = \frac{1}{t_0^2} \iint t(u, v)t(u+x, v+y)du dv. \tag{2.41}$$

In the Gaussian approximation $F_t(x, y)$ has a $1/e^2$ diameter equal to $d_t\sqrt{2}$, and a peak value $F_t(0, 0)=4/\pi d_t^2$. After substitution the second term in (2.40) cancels out with the second term in (2.35), and what finally remains is:

$$R_I(x', y'; x'', y'') = I_Z^2 C \Delta Z'' t_0^2 F_t(x'' - x', y'' - y'). \tag{2.42}$$

Note that the autocovariance of $I(x, y)$, like its average, is shift and time invariant. In other words, $I(x, y)$ is also *homogeneous* in its second order statistics.

cross-covariance

We now evaluate the cross-covariance function between two realizations of $I(x, y)$ at times t' and t'' , indicated as $I'(x, y)$ and $I''(x, y)$ respectively. The ensemble cross-covariance function of $I'(x, y)$ and $I''(x, y)$ is defined as

$$R_{II}(x', y'; x'', y'') = \langle I'(x', y')I''(x'', y'') \rangle - \langle I'(x', y') \rangle \langle I''(x'', y'') \rangle. \tag{2.43}$$

Note the similarity of this expression with that of the image auto-covariance given in (2.35). Hence, the first part of the analysis is practically identical, i.e.:

$$\langle I(x', y') \rangle \langle I(x'', y'') \rangle = \left[\frac{1}{M^2} I_Z t_0 C \Delta Z' \right]^2$$

and by analogy with (2.37):

$$\begin{aligned} \langle I'(x', y')I''(x'', y'') \rangle &= I_Z^2 \langle \{t(x', y') * g'(x', y')\} \cdot \{t(x'', y'') * g''(x'', y'')\} \rangle = \\ &I_Z^2 \iint \iint t(x' - u', y' - v') \iint t(x'' - u'', y'' - v'') \langle g'(u', v')g''(u'', v'') \rangle du' dv' du'' dv''. \end{aligned} \tag{2.44}$$

Consider the second order joint statistics of $g'(x, y)$ and $g''(x, y)$:

$$\begin{aligned} &\langle g'(u', v')g''(u'', v'') \rangle \\ &= \frac{1}{M^4 I_Z^2} \iint I_o(Z') I_o(Z'') \left\langle G' \left(\frac{u'}{M}, \frac{v'}{M}, Z' \right) G'' \left(\frac{u''}{M}, \frac{v''}{M}, Z'' \right) \right\rangle dZ' dZ'' \\ &= \frac{1}{M^4 I_Z^2} \iint I_o(Z') I_o(Z'') \cdot \\ &\quad \left\{ C \delta \left[\frac{u'' - u'}{M} - D'_X, \frac{v'' - v'}{M} - D'_Y, Z'' - Z' - D'_Z \right] + C^2 \right\} dZ' dZ'' \end{aligned} \tag{2.45}$$

with $\vec{D}' = (D'_X, D'_Y, D'_Z)$. Formally \vec{D}' is a function of u', v' and Z' . In Sect. 2.4 we saw that \vec{D} may effectively be regarded as (almost) constant, which allows us to reduce (2.45)

further to:

$$\begin{aligned}
 & \langle g'(u', v')g''(u'', v'') \rangle \\
 &= \frac{1}{M^4 I_Z^2} \left[\int I_o(Z') I_o(Z' + D'_Z) dZ' \right] C \delta \left[\frac{u'' - u'}{M} - D_X, \frac{v'' - v'}{M} - D_Y \right] + \\
 & \quad + \frac{1}{M^4 I_Z^2} C^2 \left[\int I_o(Z) dZ \right]^2 \\
 &= \frac{1}{M^4} C \Delta Z'' F_O(D'_Z) \delta \left[\frac{u'' - u'}{M} - D'_X, \frac{v'' - v'}{M} - D'_Y \right] + \frac{1}{M^4} C^2 \Delta Z'^2 \quad (2.46)
 \end{aligned}$$

with

$$F_O(D'_Z) = \int I_o(Z) I_o(Z + D'_Z) dZ \bigg/ \int I_o^2(Z) dZ \quad (2.47)$$

cf. Adrian (1988). The function (2.47) is interpreted as the loss of particle-image pairs due to motion *perpendicular* to the plane of the light sheet ("out-of-plane motion"). We subsequently substitute (2.46) in (2.44):

$$\begin{aligned}
 & \langle I'(x', y') I''(x'', y'') \rangle \\
 &= \frac{I_Z^2}{M^4} \iint t(x' - u', y' - v') \iint t(x'' - u'', y'' - v'') \cdot \\
 & \quad \left\{ C \Delta Z'' F_O(D'_Z) \delta \left[\frac{u'' - u'}{M} - D'_X, \frac{v'' - v'}{M} - D'_Y \right] + C^2 \Delta Z'^2 \right\} du' dv' du'' dv'' \\
 &= \frac{I_Z^2}{M^4} C \Delta Z'' F_O(D'_Z) \iint t(x' - u', y' - v') t(x'' - u' - M D'_X, y'' - v' - M D'_Y) du' dv' \\
 & \quad + \frac{I_Z^2}{M^4} C^2 \Delta Z'^2 \left[\iint t(u, v) du dv \right]^2. \quad (2.48)
 \end{aligned}$$

Again it should be mentioned here that D'_X and D'_Y are actually functions of u' , v' and Z_0 , but are considered here as constants. Then (2.48) further reduces to:

$$\begin{aligned}
 & \langle I'(x', y') I''(x'', y'') \rangle \\
 &= \frac{I_Z^2}{M^4} C \Delta Z'' F_O(D_Z) t_0^2 F_t(x'' - x' - M D'_X, y'' - y' - M D'_Y) + \frac{I_Z^2}{M^4} C^2 \Delta Z'^2 t_0^2.
 \end{aligned}$$

If we substitute this result in (2.43) then again the second term in (2.49) cancels with the second term on the right-hand side in (2.43):

$$\begin{aligned}
 R_{II}(x', y'; x'', y'') &= \frac{I_Z^2}{M^4} C \Delta Z'' F_O(D'_Z) t_0^2 F_t(x'' - x' - M D'_X, y'' - y' - M D'_Y) \\
 &= F_O(D'_Z) R_I(x'' - x' - M D'_X, y'' - y' - M D'_Y). \quad (2.49)
 \end{aligned}$$

Thus the cross-covariance is (approximately) equal to the image auto-covariance, shifted over a distance directly proportional to the in-plane displacement of the tracer particles and with an amplitude proportional to F_O . This result shows that the in-plane displacement of tracer particles in the light sheet is found by locating the centroid of R_{II} .

2.8 Multiple-exposure images

So far we have only considered the ensemble statistics of *single-exposure* images. In general however it is not always possible to record two (or more) subsequent images on separate frames. This would require a frame rate of at least Δt^{-1} . Practical values for Δt are typically about a millisecond. In addition, recording images in individual frames is only feasible provided that the relative positions of the subsequent frames match exactly. Although equipment (both photographic and electronic) with sufficiently high frame rate is available, single-exposure multiple-frame recording is not necessarily a desirable implementation. Instead successive exposures are recorded on a *single* frame. We thus implicitly assure a proper matching of the images, and reduce the need for a very high frame rate. Actually, double-exposure single-frame (photographic) recording is presently the most common implementation. Consider a double-exposure frame $f(x, y)$:

$$f(x, y) = I'(x, y) + I''(x, y). \quad (2.50)$$

Provided that the statistics of I' and I'' are identical the average of $f(x, y)$ is equal to

$$\langle f(x, y) \rangle = 2\langle I \rangle. \quad (2.51)$$

The auto-covariance and cross-covariance functions of $I'(x, y)$ and $I''(x, y)$ appear in the auto-covariance function of $f(x, y)$:

$$\begin{aligned} R_f(x', y'; x'', y'') &= \langle \{I'(x', y') + I''(x', y')\} \{I'(x'', y'') + I''(x'', y'')\} \rangle \\ &\quad - \langle I'(x', y') + I''(x', y') \rangle \langle I'(x'', y'') + I''(x'', y'') \rangle \\ &= 2R_I(x'' - x', y'' - y') + R_{II}(x', y'; x'', y'') + R_{II}(x'', y''; x', y') \end{aligned} \quad (2.52)$$

Substitution of (2.49) for R_{II} , and subsequently s for $x'' - x'$ and t for $y'' - y'$ in (2.52) yields

$$R_f(s, t) \approx R_I(s, t) * \{2\delta(s, t) + F_O(D'_Z) [\delta(s - s_D, t - t_D) + \delta(s + s_D, t + t_D)]\}. \quad (2.53)$$

This last expression is exact for a uniform displacement field. Note that $R_f(s, t)$ is symmetric with respect to the origin. It has two displacement correlation peaks in opposite locations with respect to a central self-correlation peak. We can not determine the *sign* of the displacement. This is usually referred to as the *directional ambiguity*. This may only be a real problem for flows that are not *unidirectional*. Also, the presence of the central peak prevents the measurement of small displacements, which may be a problem in applications where the mean velocity is small with respect to the rms fluctuating displacement. In both cases we can overcome these problems by pre-shifting the first image relative to the second image such that the images of the particle in the second exposure is always on the same side with respect to the images in the first exposure. For more details on applications of image-shifting techniques refer to Adrian (1986a), Coupland *et al.* (1987) and Landreth & Adrian (1988).

The average and covariance function for frames in which more than two exposures have been recorded is obtained in the same way as shown in Eqs. (2.50–2.53) for double-exposure frames. Generalization of the expression for double-exposure frames from a uniform displacement field given in (2.53) to P -fold exposure frames, with identical time delays between successive exposures, yield

$$\langle f^{(P)}(x, y) \rangle = P \langle I(x, y) \rangle \tag{2.54}$$

and

$$R_f^{(P)}(s, t) = \sum_{p=-P+1}^{P-1} (P - |p|) F_O(pD'_z) R_I(s-ps_D, t-pt_D) \tag{2.55}$$

with $P > 1$. The main advantage of multiple exposure frames is that the number of particle-image pairs is $(P - 1)$ times the number of tracer particles in the light sheet. We therefore can use a lower concentration of tracer particles, while still yielding the same density of particle-images on the PIV record. The different exposure sequences are depicted schematically in Figure 2.7. However, for multiple-exposure frames the total

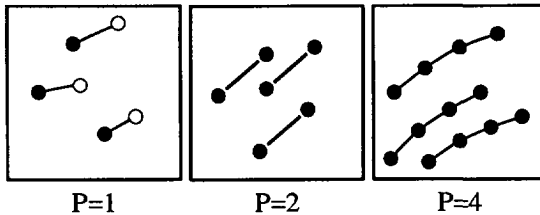


Figure 2.7: Schematic representation of single-exposure/multiple-frame recording ($P = 1$; left), double-exposure/single-frame recording ($P = 2$; middle) and multiple-exposure/single-frame recording ($P = 4$; right).

“integration” time is equal to $(P - 1)\Delta t$, which implies an additional smoothing of the displacement field with respect to the velocity flow field; see the discussion following Eq. (2.1). Keane & Adrian (1993) carried out an extensive study, using Monte Carlo simulation, in which they compared the performances of the image analysis of single, double and multiple exposure frames. Their study showed that single-exposure/multiple-frame recording has the best performance² as function of the number of particle-images, while double-exposure/single-frame has, in a relative sense, the worst performance. The performance of multiple-exposure/single-frame recording with more than two exposures has a better performance compared to double-exposure recording, but here the advantage (viz., improved data-yield) should be weighed against the disadvantages (viz., extended integration time).

²Here the performance refers to the valid-data yield; this quantity will be further explained in Sect. 3.6.4 and in Chapter 4.

2.9 Annotations

In the preceding sections we have established the relation between the statistics of the PIV images and the tracer particles in the flow. We have made several assumptions and idealizations of the situation. In this final section of this chapter we review these assumptions and idealizations, and take into consideration the scope of their validity. Besides, we compare the present results with those obtained by Adrian (1988).

- The result in Eq. (2.49) is valid for *ideal* tracer particles in *incompressible* flows. We have subsequently assumed that the displacement of the tracer particles is *locally uniform*. This implies that the velocity gradients and the motion of the fluid at the scale of the measurement volume must be negligible.
- In the case of non-ideal behaviour of the tracer particles the fluid motion is not exactly followed. This implies that the distribution of the tracer particles is not homogeneous, but depends on the underlying flow field (see Appendix A.2). For example, the inertia of particles with a density that is higher than that of the density of the fluid will expel these particles from vortex cores, while particles with a lower density (e.g. tiny air bubbles in water) are caught in low-pressure regions, such as occurs in vortex cores. In these situations the velocity field is no longer sampled independently from the flow field; regions with a high local concentration of tracer particles will make a larger contribution to the measured displacement than regions with a low local concentration. As a result the measurement is biased towards velocity regions with a high density of tracer particles. The same effect applies to *compressible* flows, in which the fluid density is related to the velocity field. Besides that, many compressible flows (i.e. transonic flows) contain strong and abrupt changes in the velocity and density fields (shock waves) which imply strong demands on the tracer particles.

In general the effects as a result of non-ideal behaviour of tracer particles in compressible flows are small and can be neglected as long as the deviations from ideal behaviour are small with respect to the measurement error for estimating the centroid of the displacement correlation peak. This error will be estimated at about one percent (see Table 1.2), and will be discussed in more detail in the next chapter.

- In Sect. 2.3 it has been made plausible that the local variations of the displacement field under general conditions are negligible, because of the spatial filtering that is implied when the velocity field is obtained from the measurement of the displacement in a finite time interval. Strong local variations of the displacement field can occur when (a) the integration time and displacement are large compared to the Kolmogorov time and length scales of the turbulent flow, or when (b) there is a strong velocity gradient perpendicular to the streamwise direction of the flow. As a result the displacement distribution function over the measurement volume, introduced in (2.8), may have non-negligible width and may also change its shape. This

can be neglected provided that the width of the distribution function is small compared to the width of the displacement-correlation peak. Let us illustrate this with an example. Suppose that we have particle images with a diameter of $25 \mu\text{m}$, and a particle-image displacement of $250 \mu\text{m}$. In the Gaussian approximation the width of the displacement-correlation peak is about $35 \mu\text{m}$. Hence, local fluctuations of the displacement that are less than about 15% ($\sim 35/250$) of the (local) mean displacement are negligible with respect to the width of the displacement-correlation peak. Let us evaluate the effects of local variations of the velocity field mentioned above under (a) and (b) respectively.

Turbulent fluctuations of the velocity field over short distances are usually very small, and at the most only a few percent of the local mean displacement (see also Chapter 4). The effect of the low-pass filtering is that part of the turbulent fluctuations are not resolved; see Fig. 2.4. This can be neglected if the defect is smaller than the measurement error for the estimation of the centroid of the displacement-correlation peak.

For near-wall turbulent flows strong variations in the displacement field due to spatial velocity gradients are evidently the strongest in the viscous sublayer and buffer region (see Sect. 1.1.2). Let us consider a numerical example to determine the extent of the region where we can expect serious deviations from the idealized behaviour. Consider a measurement volume (viz., interrogation area) with a diameter ΔY . In the viscous sublayer and buffer layer of a turbulent pipe flow the variation of the mean axial velocity (\bar{u}) over a distance ΔY along the radial direction (Y) is approximately given by (for $\bar{u}/Y \sim \text{constant}$)

$$\frac{\partial \bar{u}}{\partial Y} \frac{\Delta Y}{\bar{u}} \sim \frac{\Delta Y}{Y}.$$

Suppose that we measure the velocity with a spatial resolution of $\Delta Y^+ = 4$ (see Part II) then the variation of the mean velocity gradient can be neglected (i.e. $\Delta Y/Y < 15\%$) for radial distances $Y^+ > 25$. Thus only very close to the wall we can expect serious deviations from the expected behaviour as a result of velocity gradients in a near-wall turbulent flow. (Thus for measurements in the viscous sublayer and buffer layer it would be necessary to have a spatial resolution $\Delta Y \ll 4$.)

Even with relatively strong velocity gradients it may still be possible to detect a displacement-correlation peak. It appears that for a finite size of the interrogation region the measured velocity is biased towards low velocity. (For more details see Adrian (1988); this is also discussed in the next chapter.) Hence, *qualitatively* the measured displacement from regions with *strong* velocity gradients can be considered as a low-pass filtered representation of the observed flow field; the problem however is how to interpret the measured displacement *quantitatively*. This aspect is left untouched here (we only deal with *weak* velocity gradients), but further investigation is required.

- At the beginning of this chapter we mentioned that the relation between the statistics of PIV images and the velocity of the flow has been derived previously by Adrian (1988) for double-exposure images; see also Keane & Adrian (1990). Later this work was further extended to include also multiple-exposure images (Keane & Adrian 1991), and single-exposure/multiple-frame images (Keane & Adrian 1993). Let us compare our results with these previously obtained results.

For double-exposure PIV images Adrian finds that the mean covariance function consists of *four* terms: a self-correlation peak (R_P), two displacement-correlation peaks (R_{D+} and R_{D-} respectively) on opposite sides of R_P and a term R_C due to the mean image intensity. Obviously the term R_P corresponds to $R_I(x, y)$ (2.42), and the terms R_{D+} and R_{D-} correspond to $R_{II}(x, y)$ and $R_{II}(-x, -y)$ respectively. The term R_C does not occur in our final results for the image auto-covariance and cross-covariance, but appears to correspond to Eq. (2.36); the estimator for the image covariance considered by Adrian only involves the second-order statistics of the image intensity. This has an obvious reason: in Young's fringe analysis the non-diffracted interrogation beam is superimposed on the fringe pattern. As a result there appears an extra term in the image covariance function.

The main difference with the approach followed here and that by Adrian is that Adrian departs from a particular estimator for the image covariance and relates its statistics to that of the tracer particles, whereas our point of departure in this thesis is the tracer pattern from which we deduce the statistics of PIV images. Hence Adrian describes the ensemble statistics for a spatial average, while here the result is expressed as a two-point ensemble average. These two descriptions are closely related. However, it appeared that the latter approach (described in this chapter) is a more convenient point of departure for including the discretization of the PIV images. After that, a spatial-average estimator, based on discrete image samples (viz., pixels) will be introduced. These latter points will be further dealt with in the next chapter.

Chapter 3

Digital Analysis

Abstract. *A relation is derived between the statistics of continuous PIV images and digital PIV images. In conventional PIV analysis the sampling rate in the interrogation area matches the optical bandwidth of the PIV imaging system. It is demonstrated that the minimum required sampling rate for PIV images is a factor 3–4 lower than the optical bandwidth. This explains why a reduction in pixel resolution as applied in digital PIV has little effect on the relative measurement accuracy. The performance of different estimators for the particle-image displacement is investigated. It is found that the finite size of the interrogation area yields a biased estimate for the displacement. The proposed correction adequately compensates for this bias. It is demonstrated that interrogation with high pixel resolution (conventional PIV) and with low pixel resolution (digital PIV) need different optimal estimators for the particle-image displacement. The analytical predictions are in good quantitative agreement with measurement results obtained from a linearly displaced test image.*

3.1 Introduction

In the previous section we have derived the relation between the statistics of PIV images and that of the tracer particles in the flow. It was shown that the displacement field can be obtained from the cross-covariance function of two subsequent images, usually recorded in a single frame, with a time delay Δt . This function can be assessed indirectly through the (optical) Fourier transform of the recorded images in the interrogation area (viz., Young's fringe analysis). Nowadays it is more common to digitize the images (either directly, or from photographic records) and process the data numerically. As long as the sampling rate is sufficiently high we may still use the continuous expressions for the second order statistics given in the previous section. (Refer to Adrian (1988) for an analysis of the statistics of PIV interrogation in the continuous domain.) However, the interrogation analysis with high pixel resolution is relatively slow; to improve the processing speed we have to use a lower pixel resolution. In a situation where we do not fully resolve the bandwidth we can no longer disregard the influence of discretization on the statistics.

In this chapter we discuss the aspects related to the analysis of digital PIV images,

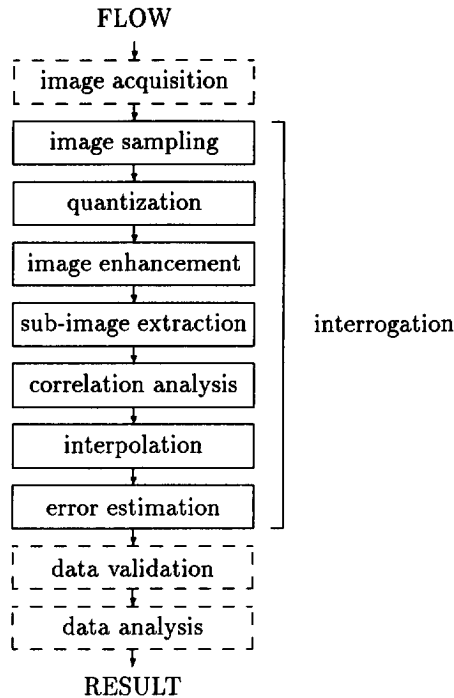


Figure 3.1: The subsequent stages in the interrogation analysis of (digital) PIV analysis.

as shown in Figure 3.1. We first determine the relation between the (ensemble) statistics in the continuous domain and those in the discrete domain (Sects. 3.2 and 3.3), and then discuss the choice of the sampling rate (Sect. 3.5). We then introduce an estimator for the (discrete) image covariance (Sect. 3.6), and derive the statistics of this estimator. This result is subsequently used to investigate the behaviour of estimators for the centroid of the displacement-correlation peak (Sects. 3.7–3.9). In Sect. 3.10 our analytical results are compared with those from a test experiment, and in Sect. 3.11 we summarize the main conclusions from this chapter.

3.2 Image sampling

The image $I(x, y)$ is commonly discretized with an electronic imaging device (usually a CCD) that “integrates” the light intensity over a small area, usually referred to as a *pixel*. We assume that the device has a linear response with respect to light intensity (see Sect. 2.5), and is made of square and contiguous pixels with area Δ^2 . Then the relation

between the discrete image $I_{i,j}$ and the continuous image $I(x, y)$ is given by:

$$I_{i,j} = \iint p(x-i\Delta, y-j\Delta) I(x, y) dx dy \quad (3.1)$$

where $p(x, y)$ is the sampling function:

$$p(x, y) = \begin{cases} 1/\Delta^2 & |x| < \Delta/2, |y| < \Delta/2 \\ 0 & \text{elsewhere} \end{cases} \quad (3.2)$$

Note that $p(x, y)$ is symmetric in x and y (viz., $p(x, y) = p(-x, -y)$) and that $\iint p(x, y) dx dy = 1$. We may now determine the statistics of the discrete PIV images, given the statistics of the continuous PIV images.

$$\begin{aligned} \langle I_{i,j} \rangle &= \left\langle \iint p(x-i\Delta, y-j\Delta) I(x, y) dx dy \right\rangle \\ &= \iint p(x-i\Delta, y-j\Delta) \langle I(x, y) \rangle dx dy \\ &= \langle I(x, y) \rangle \iint p(x-i\Delta, y-j\Delta) dx dy = \langle I(x, y) \rangle \end{aligned} \quad (3.3)$$

Thus, the average intensity of the discrete image field is equal to the average of the continuous image field.

Following a similar procedure for the auto-covariance of the discrete image field, we obtain

$$\begin{aligned} R_I[i, j; k, l] &= \langle I_{i,j} I_{k,l} \rangle - \langle I_{i,j} \rangle \langle I_{k,l} \rangle = \\ &= \iint \iint p(x'-i\Delta, y'-j\Delta) \iint p(x''-k\Delta, y''-l\Delta) R_I(x', y'; x'', y'') dx' dy' dx'' dy'' \end{aligned} \quad (3.4)$$

The auto-covariance function of $I(x, y)$ is shift-invariant, so we can rewrite $R_I(x', y'; x'', y'')$ as $R_I(x''-x', y''-y')$. If we subsequently substitute $s = x''-x'$ and $t = y''-y'$, and use the symmetry property of $p(x, y)$, (3.4) reduces to:

$$R_I[i, j; k, l] = \{ \Phi_{pp} * R_I \} (k\Delta - i\Delta, l\Delta - j\Delta) \quad (3.5)$$

with

$$\Phi_{pp}(s, t) = \iint p(x, y) p(s-x, t-y) dx dy. \quad (3.6)$$

If we substitute (3.2) in (3.6) then $\Phi_{pp}(s, t)$ is a quadrilateral pyramid with a base of 2Δ . Note that $R_I[i, j; k, l]$ is also a shift-invariant, which implies that the discrete image, like the continuous image, is a homogeneous random field. For $d_i/\Delta = 0$ the image covariance $R_I[r, s]$ is given by $\Phi_{pp}(s, t)$, i.e. the values of $R_I[r, s]$ directly adjacent to $[0, 0]$ become just equal to zero. But for all non-zero values of d_i/Δ , like we have in practice, $R_I[r, s]$ covers *more than one pixel*. This property makes it possible to estimate the centroid of the displacement at sub-pixel accuracy.

The discrete cross-covariance function of two (discrete) images $I'_{i,j}$ and $I''_{k,l}$ is defined as:

$$R_{II}[i, j; k, l] = \langle I'_{i,j} I''_{k,l} \rangle - \langle I'_{i,j} \rangle \langle I''_{k,l} \rangle. \quad (3.7)$$

The relation between $R_{II}[i, j; k, l]$ and $R_{II}(x', y'; x'', y'')$ is practically identical to that between the discrete and continuous auto-covariance function given in (3.4):

$$R_{II}[i, j; k, l] = \iint p(x' - i\Delta, y' - j\Delta) \iint p(x'' - k\Delta, y'' - l\Delta) R_{II}(x', y'; x'', y'') dx' dy' dx'' dy''. \quad (3.8)$$

The main difference with (3.4) is that $R_{II}(x', y'; x'', y'')$ is in principle *not* shift-invariant. However, like we have done before in our analysis, $R_{II}(x', y'; x'', y'')$ is considered approximately as shift-invariant. We therefore replace the cross-covariance in (3.9) by (2.49), and rewrite the integration variables:

$$R_{II}[i, j; k, l] = \iint p(x', y') \iint p(x'', y'') F_I(D_Z) \cdot R_I(k\Delta - i\Delta - x'' + x' + MD_X, l\Delta - j\Delta - y'' + y' + MD_Y) dx' dy' dx'' dy'' \quad (3.9)$$

As a result, the integration variables in (3.10) only appear as differences, which allows us to express $R_{II}[i, j; k, l]$ in a form similar to that of $R_I[i, j; k, l]$ in (3.5). Hence,

$$R_{II}[i, j; k, l] = F_I(D_Z) \{ \Phi_{pp} * R_I \} (k\Delta - i\Delta - MD_X, l\Delta - j\Delta - MD_Y). \quad (3.10)$$

Note however that the displacements MD_X and MD_Y are in general *not* integer multiples of Δ , and therefore, unlike (2.49), we cannot simply express $R_{II}[i, j; k, l]$ as a copy of $R_I[i, j; k, l]$, multiplied by $F_O(D_Z)$ and shifted over $(MD_X/\Delta, MD_Y/\Delta)$.

The expression in (3.10) is an important result that we will use frequently in the remainder of this chapter. The (ensemble) cross-covariance between the images I' and I'' represents the *signal* in our analysis. This quantity can be directly evaluated if we record the images I' and I'' in separate frames, and subsequently apply a cross-covariance analysis between corresponding interrogation areas in the two frames. We have seen in Sect. 2.8 that multiple-exposure imaging in a single frame is a more common implementation. Provided that the displacement is large compared to the particle-image diameter (so that the displacement-correlation peaks are well separated from the central self-correlation peaks) we can easily identify and isolate the displacement-correlation peak. We therefore only consider here the image cross-covariance.

3.3 Quantization

The step subsequent to image sampling is *quantization*, by which the image intensity I is mapped onto a discrete variable I^* that takes values from a finite set of numbers. The most commonly used quantizer for digitization of images is an 8-bit uniform quantizer, with zero memory (the quantizer output depends on the current sample at the input

only). Let us briefly consider some aspects of quantization. For a review of quantizer designs and their properties refer to Jain (1989).

Quantization is irreversible, and therefore introduces a distortion. The relation between the quantizer input and output can be written as

$$I = I^\bullet + \zeta \quad (3.11)$$

where ζ denotes the quantizer noise. Consider a uniform quantizer, i.e. with equidistant quantization levels. Provided that the number of levels is large with respect to the range of the input signal, ζ has (approximately) a uniform distribution, with the following statistics

$$E\{\zeta\} = 0 \quad \text{var}\{\zeta\} = \frac{1}{12}q^2 \quad E\{I\zeta\} = 0 \quad (3.12)$$

(Jain 1989) where q is the difference between two consecutive quantization levels. This implies that I^\bullet is an *unbiased* estimate of I , with

$$\text{var}\{I^\bullet\} < \text{var}\{I\}$$

by an amount given by $\text{var}\{\zeta\}$. Furthermore, (3.12) implies that the quantizer noise is uncorrelated with I .

For an 8-bit quantizer the number of quantization levels is 256. Suppose that this range is equal to 5 times the standard deviation of the image intensity (so that only a tiny fraction of the pixels in the input image falls outside the quantizer range). Hence the signal-to-noise ratio, defined as $\text{var}\{I\}/\text{var}\{\zeta\}$ (Jain 1989), for the quantizer noise is approximately 45 dB. From this estimate we conclude that the quantizer noise for an 8-bit digitizer is negligible in practice.

3.4 Intensity statistics

In Section 2.6 we deliberately limited ourselves to low source-density images in order to derive a relationship between the statistics of the tracer pattern in the flow and its corresponding image. In this section we consider the probability density function of the intensity. It will be made clear that, despite our earlier limitation, our results for the statistics of the image from the previous sections also apply to high source-density images.

Goodman (1984) analyzed the intensity statistics of coherent light scattered from a rough surface (viz., speckle patterns). Let us briefly review his results.

Consider a rough surface that is illuminated with coherent light. The surface is subdivided in small surface elements, that each scatter light. The amplitude at a given point in the image plane consists of the superposition of contributions from different surface

elements in the rough surface. If the surface roughness is large with respect to the wavelength of the light, then the phase of the (complex) light amplitude from a surface element is a random variable with a uniform distribution between 0 and 2π . The superposition of complex amplitudes of all scattered light waves can be considered as a random walk in the complex plane. By the central limit theorem it is found that the light amplitude is a circular (complex) Gaussian random variable. From this it immediately follows that the light *intensity*, which is the square of the amplitude, is a random variable with a *negative exponential* probability density function. This analytical result was verified experimentally (Goodman 1984).

Now consider a pixel in the discrete PIV image. The equivalent area of a pixel in the object plane is $(\Delta/M)^2$. In the paraxial approximation all tracer particles in a rectangular tube of "infinite" length (viz., a length $\gg \Delta Z_0$, that is large enough to include all illuminated tracer particles) contribute to the light intensity in the pixel. Note that for any *finite* Δ the number of scattering sites in this tube is infinite (or at least $\gg 1$), although the tracer particles do not contribute to the total (pixel) intensity by an equal amount; see Eq. (2.26). The tracer particles are distributed randomly over the flow. Hence, the distance between tracer particles is also a random quantity, which implies that the phases of the light amplitudes from different scattering sites are uncorrelated on average and in general much larger than the light wavelength (implying phase excursions of many times 2π). These are the same conditions from which Goodman (1984) starts his analysis. Therefore we may deal with the tracer pattern in the fluid as a "rough surface", and accordingly expect that the pdf for the light intensity at low source-density is also that of a *negative exponential* distribution.

In Figure 3.2 is shown the histogram of the count of pixels per grey level as function of the grey level (between 0 and 255) of a low source-density image (for more details refer to Sect. 3.10.1). The solid line in this figure represents a negative exponential curve fit to the histogram for the grey levels between 20 and 170. Below a grey level of 20 the histogram deviates from the fitted curve, which is most likely due to instrumental noise; above a grey level of 170 the histogram no longer follows the exponential curve and drops to zero. The upper limit for the grey level in the histogram is determined by the amount of light scattered by a particle located at $Z = Z_0$ (i.e. where the light-sheet intensity profile has a maximum).

We conclude that the conditions for Goodman's analysis of the intensity distribution of a high source-density image (viz., speckle image) also apply (to a certain extent) to low source-density images. In his subsequent analysis, Goodman (1984) obtains results for the average and auto-covariance function of speckle patterns. Although his results strictly apply to the speckle pattern obtain from laser light scattered by a rough surface, his final results appear to be similar to Eqs. (2.33) and (2.42). Therefore we now conclude that the statistical properties of PIV images and LSV images, obtained from homogeneously seeded, incompressible flows have the *same* statistical properties. Thus,

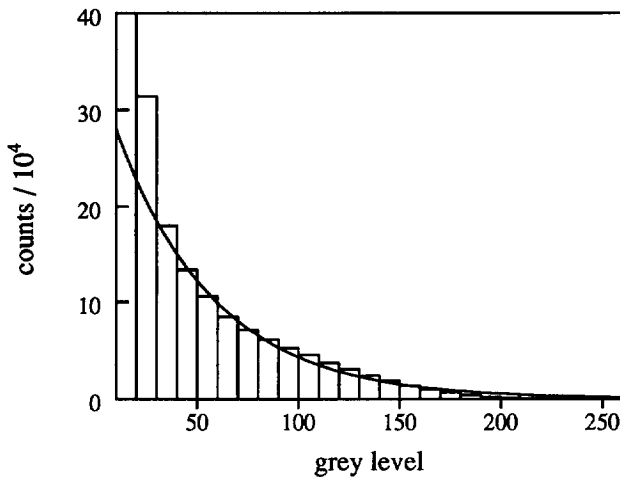


Figure 3.2: Histogram of the intensity or grey level distribution of a digital PIV image. The solid line is a negative-exponential curve fit to the histogram.

the analysis of discrete images from seeded flows that follows will apply to images in both the particle-image mode and the laser-speckle mode (i.e. independent of the image and source densities).

In fact, the only thing that counts is that the images are described by a homogeneous, negative-exponential random field, with a narrow covariance function. The purpose of the analysis is to find the displacement field that maps one image into a second image, by evaluating the cross-correlation of the two images. The underlying physical principle by which the image is created is of secondary importance¹.

3.5 Bandwidth of PIV images

So far we have not discussed the most important aspect of digitization, and that is the choice of the *sampling rate* that is required for the digital image to yield a fair representation of the original continuous image. In other words, what is the *bandwidth* of a PIV image? This is a very important consideration, since it will give us the lower bound for the pixel resolution that we can use in digital PIV.

A signal is said to be *bandlimited* if its Fourier transform $F(\chi, \psi)$ is nonzero over only

¹To the author's opinion this again demonstrates that there is no real need to make a distinction between LSV and PIV with respect to the image analysis.

a finite region in the frequency domain:

$$F(\chi, \psi) = 0, \text{ for } |\chi| > \chi_0, |\psi| > \psi_0. \quad (3.13)$$

The *bandwidth* W of $F(\chi, \psi)$ is defined as the maximum of χ_0 and ψ_0 . The *sampling theorem* (Oppenheim *et al.* 1983) states that a bandlimited continuous signal can be reconstructed *exactly* provided that the sampling rate (for an infinite number of samples) on a square grid is (at least) *twice* the bandwidth. The minimum sampling rate (viz., $2\chi_0, 2\psi_0$) is commonly referred to as the *Nyquist rate*.

Consider the optical system shown in Fig. 2.5. For a thin spherical lens with a focal length f and an aperture D , the bandwidth of the image intensity field for coherent light with a wavelength λ is equal to (Goodman 1968):

$$W = \frac{D}{\lambda z_0} = \frac{D}{\lambda f(M+1)} \quad (3.14)$$

with: $z_0 = f(M+1)$; see (2.12-2.13). Let us estimate the required pixel resolution to correctly sample a PIV image formed by this optical system.

Example 2 (*Optical bandwidth of the PIV imaging system*)

According to the sampling theorem mentioned above the image has to be sampled at a rate $2W$. For an optical system with $f/D=8$ and $M=1$, and coherent light with $\lambda=0.5 \mu\text{m}$, Eq. (3.14) yields a sampling rate ($2W$) of at least 250 mm^{-1} . For photographic PIV this is not a problem; Most of the commonly available photographic films (e.g. ASA100) have sufficient spatial resolution. This result also indicates that the digital analysis of a $1 \times 1 \text{ mm}^2$ area on film requires a 256×256 -pixel digitizer. On the other hand, for CCD arrays the spatial resolution in general does not exceed 100 mm^{-1} , and one is therefore inclined to conclude that direct electronic imaging cannot be used for PIV image recording. However, as will be made clear below, it is not necessary to resolve the optical bandwidth in order to obtain a fairly accurate result from interrogation analysis.

However, the considerations for the sampling rate given above apply to the exact *reconstruction* of a PIV image. The aim of the interrogation analysis is *not* image reconstruction, but to obtain the position of the displacement covariance peak; see Eq. (2.49). In other words, we are not interested in the exact shape of the particle images, but only in their *positions* (i.e. only the low wave-number range is of interest). Thus, instead of the bandwidth of the optical system, we should consider the bandwidth of the spectral density $S(\chi, \psi)$ of the random field that describes the statistics of the PIV image. Since we are not interested in the exact reconstruction of the image we will use a generalized approach to the concept of bandwidth.

Ignoring its detailed shape, the covariance function of a PIV image rapidly decays to zero, at a rate that is characterized by its second moment, and has a spectral density

function that vanishes (but not necessarily becomes equal to zero) for sufficiently large (χ, ψ) , viz.

$$S(\chi, \psi) \sim 0, \text{ for } |\chi| > \chi_0, |\psi| > \psi_0. \tag{3.15}$$

This is a generalization of the definition in (3.13), and defines a signal type that is called “nearly bandlimited”. Many different definitions of the bandwidth for this type of signal exist, but for random processes they all conceptually relate the spectral bandwidth to the maximum rate of decay of the covariance function (Priestley 1992). Here we use a definition that is a two-dimensional generalization of Parzen’s definition (1957) for a one-dimensional signal: the bandwidth W_P of a process with a circularly symmetric spectral

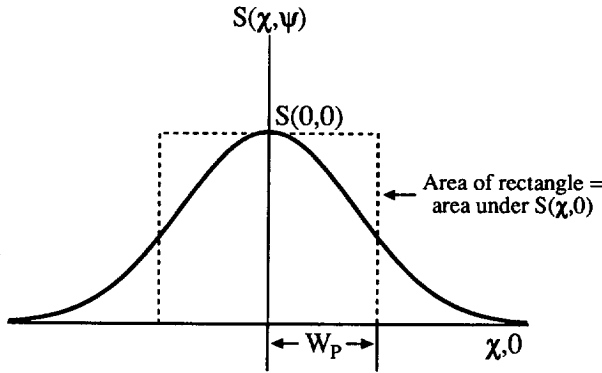


Figure 3.3: The bandwidth according to the definition by Parzen; after Oppenheim *et al.* (1983).

density $S(\chi, \psi)$ is defined as the width of a cylinder which has the same volume as $S(\chi, \psi)$ (viz., unity) and the same height as $S(\chi, \psi)$ at $(\chi, \psi) = (0, 0)$. Thus,

$$W_P = \sqrt{\frac{1/\pi}{S(0, 0)}} \tag{3.16}$$

This is illustrated in Figure 3.3. The result for W_P applies to a circularly symmetric spectral density function, but we have to take into account that the sampling is done on a square grid. In Figure 3.4 are given three possibilities for relating W_P to the sampling rate: the numbers represent the ratio of the sampling rate and the bandwidth. The ones on the left and right represent the “extreme” situations; for the one in the middle the disc and the square have equal areas.

Now, let us apply this to the optical system in Fig. 2.5 for the case of particle images that have a size of approximately d_s . We assume that the particle images are Gaussian curves, i.e. $h(x, y) \propto \mathcal{G}(x, y; \sigma_h)$ with $\sigma_h = \frac{d_s \sqrt{2}}{2.44\pi}$; see Eq. (A.23). The image auto-covariance

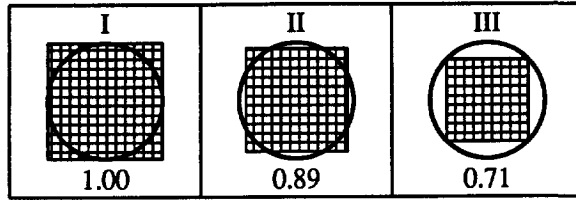


Figure 3.4: Three possibilities to relate the bandwidth of a circularly symmetric spectral density function to the sampling rates on a rectangular grid. The numbers represent the ratio of the side of the square and the diameter of the disc.

function R_I is found by convolution of $h(x, y)$ with itself; see Eq. (2.41). The Wiener-Khintchine theorem (Priestley 1992; Rosenfeld & Kak 1982) states that the Fourier transform of R_I yields the spectral density function of the PIV image². By using the properties for Gaussian curves in Appendix A.5 we thus obtain:

$$\begin{aligned}
 h(x, y) &\propto \mathcal{G}(x, y; \sigma_h) \text{ with } \sigma_h = \frac{d_s \sqrt{2}}{2.44\pi} \\
 &\downarrow \\
 R_I(x, y) &\propto \mathcal{G}(x, y; \sigma_h \sqrt{2}) \\
 &\downarrow \\
 S_P(\chi, \psi) &\propto \mathcal{G}(\chi, \psi; \Sigma_h) \text{ with } \Sigma_h = \frac{1}{2\pi\sigma_h^2} \\
 &\downarrow \\
 S(0, 0) &\propto \frac{1}{2\pi\Sigma_h^2} = 4\pi\sigma_h^2
 \end{aligned}$$

Thus, (3.16) yields a bandwidth

$$W_P = 1/2\pi\sigma_h. \tag{3.17}$$

Let us again consider the bandwidth with the same values for λ , f/D and M as for the evaluation of the optical bandwidth.

Example 3 (the bandwidth of a PIV image)

We assume that $d_p \rightarrow 0$, so that the particle-image diameter is given by d_s ; see Eqs. (2.20–2.21). For the optical parameters given above we find $d_s = 20 \mu\text{m}$, which yields a value of $3.7 \mu\text{m}$ for $\sigma_h (= d_s \sqrt{2}/2.44\pi)$; see Eq. (A.23). By (3.17) and Fig. 3.4 we thus find that the minimum sampling rate ($2W_P$) should be between 61 and 86 mm^{-1} . *This is a factor 3–4 less than the optical bandwidth!* We now find that a CCD array has sufficient spatial resolution for direct recording. Thus, a pixel resolution of 64^2 pixels for the analysis of a $1 \times 1 \text{ mm}^2$ interrogation area should be sufficient.

²For multiple exposure pictures the Fourier transform of R_I yields the “envelope” of the spectral density function; see Eq. (2.53).

Finally, it should be noted that the particle-image diameter d_t in a practical situation is usually larger than d_s . This is not only due to the fact that Md_p is not negligible with respect to d_s , but also because optical aberrations (e.g. out-of-focus effects) and other imperfections in general increase d_t . As a result, the bandwidth W_P and corresponding minimum required sampling rate in a practical situation will be even smaller. For example, if we would use tracer particles with $d_p=15 \mu\text{m}$ in an experimental setup with the parameters for the optical system given above, Eq. (2.20) yields $d_t \approx 28 \mu\text{m}$. Following the discussion in this section we find that in this case a sampling rate of about 32^2 may already suffice.

From the discussion in this section we may conclude that in photographic PIV using a high pixel-resolution for interrogation analysis *oversamples* the image covariance function. This partially explains why a reduction of pixel resolution from 256^2 to 32^2 yields little effect on analysis performance. In Section 3.7 we will take a closer look at the information content of a PIV image as function of the resolution.

3.6 Estimation of the mean and cross-covariance

So far the expressions for the mean and covariance of the image intensity have been *ensemble averages* with respect to *all* possible realizations of PIV images for a given flow field. In practice the flow field is not reproducible (i.e. turbulent flow), and we have available only a *single* realization of $I'_{i,j}$ and $I''_{i,j}$ (either as a pair of single-exposure frames, or as a single multiple-exposure frame). The basic strategy in such a situation is to replace the *ensemble averages* by their corresponding *spatial averages*. A necessary condition is that the random field is *ergodic* with respect to the mean and covariance. This condition implies that the spatial average over $N \times N$ samples converges to the *ensemble average* for $N \rightarrow \infty$. For further details refer to Rosenfeld & Kak (1982) or Priestley (1992). In this section we introduce spatial-average estimators for the mean and covariance of the image intensity. We assume that the first and second order (ensemble) statistics of $I'_{i,j}$ and $I''_{i,j}$ are *identical* and given by Eqs. (3.3), (3.5) and (3.10). We subsequently determine the statistical properties of these estimators, i.e. their expectation and (co)variance. This is closely related to the analysis by Priestley (1992) of the statistical properties of one-dimensional time-averaging estimators for the mean and auto-covariance of a stationary random process. In Appendix B.2 we go into more detail about the computation of the estimated covariance by means of discrete Fourier transformations.

Our point of departure is the ensemble image cross-covariance, defined in (3.7),

$$R_{II}[r, s] = \langle I'_{i,j} I''_{i+r,j+s} \rangle - \langle I \rangle^2 \tag{3.18}$$

with

$$\langle I'_{i,j} \rangle = \langle I''_{i,j} \rangle = \langle I \rangle \quad \forall_{i,j} \tag{3.19}$$

cf. (3.3). Alternatively (3.18) can be expressed as

$$R_{II}[r, s] = \langle \Delta I'_{i,j} \Delta I''_{i+r,j+s} \rangle \tag{3.20}$$

with

$$\Delta I'_{i,j} = I'_{i,j} - \langle I \rangle \quad \text{and} \quad \Delta I''_{i,j} = I''_{i,j} - \langle I \rangle. \tag{3.21}$$

In the following subsections we introduce the spatial-average estimators for (3.19) and (3.20), and derive the first and second order statistics of these estimators. In Appendix B.2 it is shown how to compute the estimator for $\hat{R}_{II}[r, s]$ by means of discrete Fourier transformation (viz., the fast Fourier transform or FFT algorithm).

3.6.1 estimation of the mean image intensity

Let us first deal with the spatial average of $I_{i,j}$ over a square region of $N \times N$ pixels, defined as

$$\bar{I} = \frac{1}{N^2} \sum_{i=1}^N \sum_{j=1}^N I_{i,j}. \tag{3.22}$$

The expectation value of \bar{I} is given by

$$E[\bar{I}] = \frac{1}{N^2} \sum_{i=1}^N \sum_{j=1}^N E[I_{i,j}] = \langle I \rangle \tag{3.23}$$

and its variance by

$$\begin{aligned} \text{var}[\bar{I}] &= E[(\bar{I} - \langle I \rangle)^2] \\ &= \frac{1}{N^4} \sum_{i=1}^N \sum_{j=1}^N \sum_{k=1}^N \sum_{l=1}^N R_I[k-i, l-j] \\ &= \frac{1}{N^2} \sum_{r=-(N-1)}^{N-1} \sum_{s=-(N-1)}^{N-1} \left(1 - \frac{|r|}{N}\right) \left(1 - \frac{|s|}{N}\right) R_I[r, s] \end{aligned} \tag{3.24}$$

cf. Priestley (1992). For finite sample size (viz., N) $I_{i,j}$ and \bar{I} are correlated; their covariance is given by

$$\text{cov}[I_{i,j}, \bar{I}] = \frac{1}{N^2} \sum_{k=1}^N \sum_{l=1}^N R_I[k-i, l-j]. \tag{3.25}$$

For PIV images with small particle images, i.e. $d_t/\Delta \sim 1$ (see Sect. 3.7), $R_I[s, t]$ is practically negligible for all $[s, t] \neq [0, 0]$. In that situation (3.24) and (3.25) are approximately equal to

$$\text{var}[\bar{I}] \sim \frac{1}{N^2} R_I[0, 0] \quad \text{and} \quad \text{cov}[I_{i,j}, \bar{I}] \sim \frac{1}{N^2} R_I[0, 0]. \tag{3.26}$$

From Eqs. (3.23) and (3.26) we conclude that \bar{I} is an *unbiased* and *consistent* estimator of the average image intensity.

3.6.2 estimation of the cross-covariance

The image cross-covariance for two $N \times N$ -pixel (interrogation) images, $\Delta I'_{i,j}$ and $\Delta I''_{i,j}$, for a shift over $[r, s]$ is estimated by (see also Appendix B.2):

$$\hat{R}_{II}[r, s] = \frac{1}{N^2} \sum_i^{N-|r|} \sum_j^{N-|s|} \Delta I'_{i,j} \Delta I''_{i+r, j+s} \tag{3.27}$$

with

$$\sum_i^{N-|r|} = \begin{cases} \sum_{i=1}^{N-r} & \text{for } r \geq 0 \\ \sum_{i=1-r}^N & \text{for } r < 0 \end{cases} \tag{3.28}$$

(i.e. the subscript in the summation symbol indicates the summation variable and the superscript the number of summation terms). Since we have in general no *a priori* knowledge of $\langle I \rangle$, we have to estimate it from the same record that we use for $\hat{R}_{II}[r, s]$. This implies that the estimate $\hat{R}_{II}[r, s]$ is correlated with \bar{I} . Let us have a closer look at this.

The image mean can be estimated from the entire image, while the cross-covariance is estimated at each interrogation position from the pixels in a small sub-image (viz., the interrogation region). If we have an image of $M \times M$ pixels with $M \gg N$, say $M=N^2$, then by (3.26) we have that

$$\text{var}[\bar{I}] \sim \mathcal{O}(1/M^2) \quad \text{and} \quad \text{cov}[\Delta I_{i,j}, \bar{I}] \sim \mathcal{O}(1/M^2). \tag{3.29}$$

As we will see later (Eqs. (3.40-3.41)) the noise in $\hat{R}_{II}[r, s]$ is $\mathcal{O}(1/N^2)$. Since $1/M^2 \ll 1/N^2$ we may regard \bar{I} *effectively* as an exact estimate of $\langle I \rangle$, and henceforth neglect the correlation between $\hat{R}_{II}[r, s]$ and \bar{I} .

We will now determine the expectation value and covariance for the estimator defined in (3.27). First consider the expectation value:

$$\begin{aligned} E \{ \hat{R}_{II}[r, s] \} &= \frac{1}{N^2} \sum_i^{N-|r|} \sum_j^{N-|s|} E \{ \Delta I'_{i,j} \Delta I''_{i+r, j+s} \} \\ &= \frac{1}{N^2} \sum_i^{N-|r|} \sum_j^{N-|s|} R_{II}[r, s] \\ &= \left(1 - \frac{|r|}{N} \right) \left(1 - \frac{|s|}{N} \right) R_{II}[r, s] \end{aligned} \tag{3.30}$$

Thus the estimator in (3.27) is *not* unbiased, although the bias vanishes for $N \rightarrow \infty$. The bias is the result of the fact that for a shift over $[r, s]$ only part of the signal in $\Delta I'_{i,j}$ and $\Delta I''_{i,j}$ contributes to the estimate for $R_{II}[r, s]$. This is depicted in Figure 3.5. In Sect. 2.4 we have seen that the measurement of the displacement over a finite measurement volume (viz., interrogation area) implies a spatial filtering of the displacement field. Now we have obtained the “signature” of this spatial filter, i.e. a quadrilateral pyramid with a base

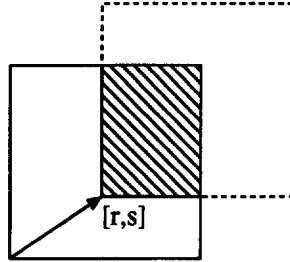


Figure 3.5: For a shift over $[r, s]$ only the shaded part of the signal in the interrogation area contributes to the estimated covariance.

that is twice the size of the interrogation area. The shape of this filter implies that large displacements make a smaller contribution to the mean than small displacements. As a result the measured displacement over a flow region with a strong velocity gradient is biased towards lower velocity. Adrian (1988) was the first who reported this bias. He also gave the following, perhaps more comprehensive explanation of the velocity bias. Consider an interrogation region of given size, denoted by the square with the solid lines in Figure 3.5. For a particle-image displacement over a vector $[r, s]$ only the particle-images within the shaded region remain in the interrogation area and thus contribute to the displacement-correlation peak in the image covariance. This is referred to as the *in-plane loss-of-pairs*, by analogy with the out-of-plane loss-of-pairs; see Eq. (2.47). For measurements over a region with a strong velocity gradient the interrogation region contains a larger number of particle-image pairs with a small displacement than with a large displacement. So, small displacements make a larger contribution to the local mean displacement than large displacements. This biases the measurement towards the lowest velocity in the measurement volume. This effect makes it difficult to interpret the measured displacements in regions with strong velocity gradients. It is therefore important to verify that the expected variation of the displacement over the interrogation area is within acceptable limits; see Sect. 2.9.

We now direct our attention to the covariance of $\hat{R}_{II}[r, s]$, given by

$$\begin{aligned} & \text{cov} \{ \hat{R}_{II}[r, s], \hat{R}_{II}[r+t, s+u] \} \\ &= E \{ \hat{R}_{II}[r, s] \hat{R}_{II}[r+t, s+u] \} - E \{ \hat{R}_{II}[r, s] \} E \{ \hat{R}_{II}[r+t, s+u] \}. \end{aligned} \quad (3.31)$$

Note that this expression is *even* in t and u . Let us first consider the first term at the right hand side of (3.31):

$$\begin{aligned} & E \{ \hat{R}_{II}[r, s] \hat{R}_{II}[r+t, s+u] \} \\ &= \frac{1}{N^4} \sum_v^{N-|r|} \sum_x^{N-|r+t|} \sum_w^{N-|s|} \sum_y^{N-|s+u|} E \{ \Delta I'_{v,w} \Delta I''_{v+r,w+s} \Delta I'_{x,y} \Delta I''_{x+r+t,y+s+u} \} \end{aligned}$$

$$\begin{aligned}
 &= \frac{1}{N^4} \sum_v^{N-|r|} \sum_x^{N-|r+t|} \sum_w^{N-|s|} \sum_y^{N-|s+u|} \left[E \left\{ \Delta I'_{v,w} \Delta I''_{v+r,w+s} \right\} E \left\{ \Delta I'_{x,y} \Delta I''_{x+r+t,y+s+u} \right\} + \right. \\
 &\quad E \left\{ \Delta I'_{v,w} \Delta I'_{x,y} \right\} E \left\{ \Delta I''_{v+r,w+s} \Delta I''_{x+r+t,y+s+u} \right\} + \\
 &\quad \left. E \left\{ \Delta I'_{v,w} \Delta I''_{x+r+t,y+s+u} \right\} E \left\{ \Delta I'_{x,y} \Delta I''_{v+r,w+s} \right\} + \kappa_4 \right] \\
 &= \frac{1}{N^4} \sum_v^{N-|r|} \sum_x^{N-|r+t|} \sum_w^{N-|s|} \sum_y^{N-|s+u|} \{ R_{II}[r, s] R_{II}[r+t, s+u] + \\
 &\quad R_I[x-v, u-w] R_I[x+t-v, y+u-w] + \\
 &\quad R_{II}[x+r+t-v, y+s+u-w] R_{II}[v+r-x, w+s-y] + \kappa_4 \} \quad (3.32)
 \end{aligned}$$

where κ_4 is a fourth order cumulant of the joint distribution function of $\Delta I'$ and $\Delta I''$. For a Gaussian process $\kappa_4 \equiv 0$ (Priestley 1992; Isserlis 1918). We have seen in Sect. 3.4 that I is not Gaussian, but negative-exponential, and not necessarily equal to zero. Nonetheless, as a higher order term, κ_4 is not expected to play a dominant role in (3.32). Therefore, in the subsequent analysis κ_4 is left out. A justification for this simplification will be found in the experimental verification in Sect. 3.10. An analytical proof should be provided in a future study. The first term in (3.32) cancels with the second term in (3.31), so that we remain with

$$\begin{aligned}
 &\text{cov} \left\{ \hat{R}_{II}[r, s], \hat{R}_{II}[r+t, s+u] \right\} \\
 &= \frac{1}{N^4} \sum_v^{N-|r|} \sum_x^{N-|r+t|} \sum_w^{N-|s|} \sum_y^{N-|s+u|} \{ R_I[x-v, u-w] R_I[x+t-v, y+u-w] + \\
 &\quad R_{II}[x+r+t-v, y+s+u-w] R_{II}[v+r-x, w+s-y] \} \quad (3.33)
 \end{aligned}$$

Note that the variables v, w, x and y in (3.33) only occur as $x-v$ and $y-w$. We may therefore simplify the expression given above by substitution of $m=x-v$ and $n=y-w$. However, it is then not possible to give an expression with the generalized notation given in (3.28). We therefore consider here only the case that $r, s, t, u \geq 0$ (for the other cases analogous results can be obtained):

$$\begin{aligned}
 &\text{cov} \left\{ \hat{R}_{II}[r, s], \hat{R}_{II}[r+t, s+u] \right\} \\
 &= \frac{1}{N^2} \sum_{m=-(N-r)+1}^{N-r-t-1} \sum_{n=-(N-s)+1}^{N-s-u-1} \left(1 - \frac{\eta[m]+r+t}{N} \right) \left(1 - \frac{\eta[n]+s+u}{N} \right) \cdot \\
 &\quad \cdot \{ R_I[m, n] R_I[m+t, n+u] + R_{II}[m+r+t, n+s+u] R_{II}[r-m, s-n] \} \quad (3.34)
 \end{aligned}$$

with

$$\eta[m] = \begin{cases} m & m > 0 \\ 0 & -t \leq m \leq 0 \\ -m-t & -(N-r)+1 \leq m \leq -t \end{cases} \quad (3.35)$$

(for $\eta[n]$ substitute s for r and u for t). The expression in (3.34) gives the covariance of the estimated cross-covariance of a homogeneous random field that satisfies the description

given in Sect. 2.7. This result is an extension of the expression for the covariance of the estimated auto-covariance of a stationary random process, given by Priestley (1992). For $t=0$ and $u=0$ we obtain the expression for the variance of $\hat{R}_{II}[r, s]$, viz.

$$\text{var} \{ \hat{R}_{II}[r, s] \} = \frac{1}{N^2} \sum_{m=-(N-r)+1}^{N-r-1} \sum_{n=-(N-s)+1}^{N-s-1} \left(1 - \frac{|m|+r}{N} \right) \left(1 - \frac{|n|+s}{N} \right) \cdot \{ R_I^2[m, n] + R_{II}[r+m, s+n]R_{II}[r-m, s-n] \} \quad (3.36)$$

The expressions (3.34) and (3.36) are rather complicated, but reduce to much simpler equations for large N , i.e.

$$\text{cov} \{ \hat{R}_{II}[r, s], \hat{R}_{II}[r+t, s+u] \} \sim \frac{1}{N^2} \sum_{m=-\infty}^{\infty} \sum_{n=-\infty}^{\infty} \{ R_I[m, n]R_I[m+t, n+u] + R_{II}[m+r+t, n+s+u]R_{II}[r-m, s-n] \} \quad (3.37)$$

and

$$\text{var} \{ \hat{R}_{II}[r, s] \} \sim \frac{1}{N^2} \sum_{m=-\infty}^{\infty} \sum_{n=-\infty}^{\infty} \{ R_I^2[m, n] + R_{II}[r+m, s+n]R_{II}[r-m, s-n] \}. \quad (3.38)$$

(The expressions in (3.37-3.38) are valid for all r, s, t and u .) The conditions for which we may consider N as large are

$$N \gg d_t/\Delta \quad \text{and} \quad |r|, |s| \ll N. \quad (3.39)$$

The first condition implies that the particle images should be small with respect to the interrogation area. This condition is generally satisfied for PIV images. The second condition implies that Eqs. (3.37-3.38) are only valid for displacements that are small with respect to N . To our interest are only those values of r and s that are close to the location of the displacement-correlation peak. If we follow the recommendations given by Keane & Adrian (1990), then the in-plane particle-image displacements are less than 1/4 of the diameter of the interrogation region. This implies that we only consider Eqs. (3.37-3.38) for $|r|, |s| < N/4$. Let us assume that this is sufficient to consider N as "large." So, in most practical situations we also satisfy the second condition in (3.39).

The first condition in (3.39) implies that we are dealing with a narrow displacement-correlation peak. Let us evaluate Eqs. (3.37-3.38) for the case of a narrow peak, i.e. $R_I[r, s] \sim 0$ for $r \neq 0, s \neq 0$. For reasons of simplicity we assume that $F_O \sim 1$ and that the particle-image displacement is exactly an integer multiple of pixels, so that $\hat{R}_{II}[r, s]$ is a shifted copy of $\hat{R}_I[r, s]$. Hence, we obtain

$$\text{cov} \{ \hat{R}_{II}[r, s], \hat{R}_{II}[r+t, s+u] \} \sim 0 \quad (3.40)$$

(for $t \neq 0, u \neq 0$), and

$$\text{var} \{ \hat{R}_{II}[r, s] \} \sim \frac{1}{N^2} R_I^2[0, 0] \quad (3.41)$$

cf. Priestley (1992). These results show that the noise in the estimate for $R_{II}[r, s]$ is uncorrelated and proportional to $1/N^2$. In other words, the result for $\hat{R}_{II}[r, s]$ consists of a dominant correlation peak, i.e.

$$E \{ \hat{R}_{II}[r, s] \} \gg \text{var} \{ \hat{R}_{II}[r, s] \}^{1/2} \tag{3.42}$$

that is associated with the displacement peak $R_{II}[r, s]$, embedded in background noise that has the properties of a white random field (for $d_t/\Delta \rightarrow 0$; in Section 3.7 we will investigate the situation for finite peak width). For increasing particle-image displacement the amplitude of the displacement-correlation peak in $\hat{R}_{II}[r, s]$ decreases; see Eq. (3.30). This means that for increasing displacement we have an increasing probability that the displacement-correlation peak becomes smaller than one of the random noise peaks. In that case the identification of the highest correlation peak as the displacement-correlation peak yields an erroneous measurement of the displacement. In Section 3.6.4 we go into more detail.

Let us summarize the results we have obtained so far. The expressions (3.30) and (3.37) show that $\hat{R}_{II}[r, s]$, defined in (3.27), yields an asymptotically unbiased and consistent estimate for $R_{II}[r, s]$. However, for finite values of N the estimate is biased, proportional to the magnitude of the displacement. The noise in $\hat{R}_{II}[r, s]$, due to random particle-image correlations, is approximately a white random field. The probability that the displacement-correlation peak is smaller than highest noise peak is proportional to the magnitude of the displacement.

3.6.3 weight kernels

In the previous analysis each pixel $\Delta I_{i,j}$ contributed by an equal amount to the estimated covariance. However, in some situations it is desirable to put a different weight to each pixel; see Appendix B.2.2. Let us investigate the effect of an arbitrary weight kernel on the expectation of $\hat{R}_{II}[r, s]$.

Suppose we multiply $\Delta I'_{i,j}$ and $\Delta I''_{i,j}$ with a weight kernel denoted by $W_{i,j}$. Note that we multiply only the *fluctuating* image intensity with the weight kernel. The generalized expression for the estimator of the discrete image cross-covariance that includes the weight kernel reads

$$\hat{R}_{II}[r, s] = \frac{1}{N^2} \sum_m^{N-|r|} \sum_n^{N-|s|} W_{m,n} \Delta I'_{m,n} W_{m+r,n+s} \Delta I''_{m+s,n+s} \tag{3.43}$$

cf. (3.27). Provided that $\Delta I'$ and $\Delta I''$ are homogeneous, zero-mean random fields the expectation for (3.43) is subsequently given by

$$E \{ \hat{R}_{II}[r, s] \} = F_I[r, s] R_{II}[r, s] \tag{3.44}$$

with

$$F_I[r, s] = \frac{1}{N^2} \sum_m \sum_n W_{m,n} W_{m+r,n+s} \tag{3.45}$$

cf. Adrian (1988). In Appendix B.2.2 we discuss the effect of weight kernels with respect to the computation of $\hat{R}_{II}[r, s]$ by the FFT algorithm (i.e. "windowing").

For an *uniform* weight kernel $W_{i,j}$ is given by

$$W_{i,j} = \begin{cases} 1 & \text{for } 1 \leq i \leq N, 1 \leq j \leq N \\ 0 & \text{elsewhere} \end{cases} \quad (3.46)$$

By (3.45) we obtain

$$F_I[r, s] = \left(1 - \frac{|r|}{N}\right) \left(1 - \frac{|s|}{N}\right). \quad (3.47)$$

Note that this expression is exactly the prefix of $R_{II}[r, s]$ in (3.30). Adrian (1988) refers to F_I as the *in-plane loss-of-pairs* function; see also the discussion following Eq. (3.30).

In this thesis we will consider, besides the uniform weight kernel given in (3.46), also a *Gaussian* weight kernel, given by

$$W_{i,j} = \exp \left[-8 \frac{(i - \frac{1}{2}N)^2 + (j - \frac{1}{2}N)^2}{N^2} \right] \quad (3.48)$$

(The characteristic width of this kernel, based on the e^{-2} "intensity," is equal to N .) A Gaussian weight kernel would occur "naturally" in Young's fringe analysis (the interrogation laser beam in Fig. 1.6 has a Gaussian intensity distribution). The corresponding in-plane "loss of pairs" function is approximately given by

$$F_I[r, s] \sim \exp \left[-4 \frac{r^2 + s^2}{N^2} \right]. \quad (3.49)$$

(Here we implicitly assumed that the indices m and n in (3.45) are not bounded, and that N is sufficiently large to deal with (3.48) as a continuous function.)

3.6.4 valid-data yield

We have seen in Sect. 3.6.2 that for a finite sample size (viz., $N \times N$) there is a finite probability that one of the peaks in the background noise is larger than the displacement correlation peak. This may lead to an erroneous measurement of the displacement. The likelihood of such an event is determined by the expected height of the estimated displacement-correlation peak, given by the maximum of (3.30), with respect to the level of noise in $\hat{R}_{II}[r, s]$; see (3.41). We have seen in (3.30) that the estimated correlation peak is biased, proportional to the magnitude of the displacement. Hence, the larger the displacement the more likely a noise peak rises above the signal peak.

It has been suggested by several authors (Lourenço 1988, Coupland & Pickering 1988) that at least four particle-image pairs are required to find a reliable measurement of the displacement. The average number of particle-images in a $N \times N$ -pixel interrogation area is given by

$$N_I = \frac{C}{M^2} (\Delta \cdot N)^2 \Delta Z_0. \quad (3.50)$$

Adrian & Yao (1984) refer to N_I as the *image density*. The number n of particle-images in a given area is assumed to have a Poisson distribution (Adrian 1991), viz.

$$P(n) = e^{-\mu} \frac{\mu^n}{n!} \quad (3.51)$$

where $P(n)$ is the probability to find exactly n particle-images, and μ the average number of particle-image pairs. Given μ we can determine by (3.51) the probability to find a sufficient number of particle-image pairs in the interrogation area. This probability is generally referred to as the valid-data yield, denoted by Γ . The average μ depends on the displacement, i.e. for a displacement $[r, s]$ the *effective* average number of particle-image pairs that remains inside the interrogation area is given by:

$$\mu = N_I F_I F_O \quad (3.52)$$

where F_I , defined in (3.45), accounts for the *in-plane* "loss of pairs" (see Fig. 3.5), while F_O , defined in (2.47), accounts for the *out-of-plane* "loss of pairs." For given μ the valid-data yield (viz., the probability to find more than four particle-image pairs) is given by $P(n \geq 5) = 1 - P(n \leq 4)$, i.e.

$$\Gamma \sim 1 - \left(1 + \mu + \frac{1}{2!}\mu^2 + \frac{1}{3!}\mu^3 + \frac{1}{4!}\mu^4 \right) e^{-\mu}. \quad (3.53)$$

In Section 3.10 we compare this model with the actual data-yield for experimental data.

3.7 Estimation of the displacement

In Sect. 3.6 we evaluated the statistical properties of the estimator $\hat{R}_{II}[r, s]$. For a displacement-correlation peak that is narrow with respect to the size of the interrogation area we have obtained the expressions (3.30) and (3.37) for the expectation and covariance of $\hat{R}_{II}[r, s]$. The maximum of $\hat{R}_{II}[r, s]$ corresponds with the displacement-correlation peak. But the position of the maximum itself yields only the displacement with a resolution of 1 px. We have seen in Sect. 3.2 that the peak always has a finite width, i.e. the peak always covers more than one pixel. By including the values of the covariance adjacent to the maximum of $\hat{R}_{II}[r, s]$ the centroid of the displacement-correlation peak can be estimated at sub-pixel level. Obviously, the accuracy of the estimation of the peak centroid is determined by the number of pixels that is covered by the peak. Like in Sect. 3.5 we face the question of how densely we should sample the interrogation area to yield an accurate estimate of the displacement? In this section we provide an answer by evaluating Eqs. (3.37–3.38). Of course, one may solve these equations numerically, given the expressions for $R_I[r, s]$ and $R_{II}[r, s]$ in (3.5) and (3.10) respectively. However, presently we prefer an *analytical* result. We therefore introduce a simple model that allows a straightforward evaluation of (3.37) and (3.38).

a simple model for the image covariance

Considering the structure of Eqs. (3.37) and (3.38) it is convenient to use a model for $R_I[r, s]$ that has a trivial solution for the double summation over (r, s) . We therefore model the image auto-covariance with

$$R_I[m, n] = \sigma_I^2 a^{|m|+|n|}, \quad 0 < a < 1 \tag{3.54}$$

with $\sigma_I^2 = \text{var}\{I\}$. Note that this model is *separable* in m and n , which allows us to evaluate the sums over m and n separately. Summation of the exponential term in (3.54) over $[m, n]$ yields

$$\sum_{m=-\infty}^{\infty} \sum_{n=-\infty}^{\infty} a^{|m|+|n|} = \left(\frac{1+a}{1-a}\right)^2. \tag{3.55}$$

We assume that the particle-image displacement is exactly an integer multiple of Δ , i.e.

$$MD_X = m_o\Delta \quad \text{and} \quad MD_Y = n_o\Delta \tag{3.56}$$

cf. Eq. (3.10), and that the displacement of the particles perpendicular to the plane of the light sheet is negligible with respect to the thickness of the light sheet, viz.

$$F_O(D'_Z) \sim 1$$

cf. Eqs. (2.47) and (3.10). In that case we can write

$$R_{II}[m, n] = R_I[m-m_o, n-n_o] \tag{3.57}$$

Finally, to complete our model we have to establish a relation between the particle-image diameter d_i and the model parameter a . We will do this by making the total sum of $R_I[m, n]$ in (3.54) equal to the total sum of $R_I[r, s]$ in (3.5). The expression given in (3.5) shows that $R_I[r, s]$ is the convolution of the continuous-image covariance with Φ_{pp} , which has the shape of a quadrilateral pyramid with a base of 2Δ . Let us approximate $\{\Phi_{pp} * R_{II}\}(x, y)$ with a Gaussian curve (see Appendix A.5), viz.

$$\{\Phi_{pp} * R_{II}\}(x, y) \sim \sigma_I^2 \mathcal{G}(x, y; d_R/4) \tag{3.58}$$

where d_R is given by (Gaussian approximation)

$$d_R^2 \approx 2d_i^2 + 4\Delta^2. \tag{3.59}$$

cf. Eq. (2.20). The total volume under $\mathcal{G}(x, y; d_R/4)$ is equal to $\pi d_R^2/8$; see Eq. A.25. The value for the parameter a is given by

$$\left(\frac{1+a}{1-a}\right)^2 = \frac{\pi d_R^2}{8}$$

which can be rewritten as

$$a = \frac{c-1}{c+1} \quad \text{with} \quad c = \sqrt{2\pi} d_R/4 \tag{3.60}$$

with d_R given by (3.59). Note that $d_R/\Delta \rightarrow 2$ for $d_i/\Delta \rightarrow 0$, i.e. $R_I[r, s]$ always has finite width in practice. This implies that $a > 0.11$ for all Δ . In Figure 3.6 the model in (3.54) is compared with a Gaussian function.

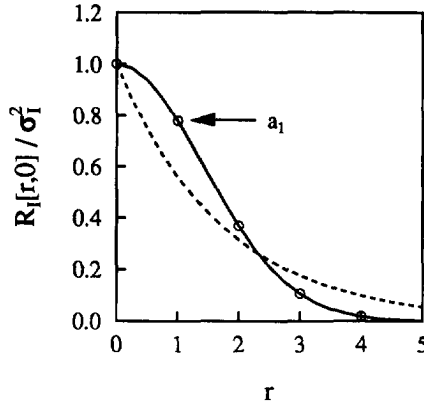


Figure 3.6: Comparison of the exponential model in (3.54) (dashed line) and Gaussian curve (solid line) for $R_I[r, s]$. The arrow indicates a_1 , defined in (3.75).

integral length scale of the cross-covariance

We can now straightforwardly solve the expression for the covariance of $\hat{R}_{II}[r, s]$ in (3.37). Let us have a closer look at the result for covariance between $\hat{R}_{II}[m_o, n_o]$ and $\hat{R}_{II}[m_o+t, n_o+u]$, given in (3.37). Given (3.57) we obtain

$$\begin{aligned}
 & \text{cov} \{ \hat{R}_{II}[m_o, n_o], \hat{R}_{II}[m_o+t, n_o+u] \} \\
 & \sim \frac{1}{N^2} \sum_{m=-\infty}^{\infty} \sum_{n=-\infty}^{\infty} \{ R_I[m, n] R_I[m+t, n+u] + R_{II}[m+m_o+t, n+n_o+u] R_{II}[m_o-m, n_o-n] \} \\
 & \sim \frac{2}{N^2} \sum_{m=-\infty}^{\infty} \sum_{n=-\infty}^{\infty} R_I[m, n] R_I[m+t, n+u]. \tag{3.61}
 \end{aligned}$$

Consider the double summation, and substitute (3.54):

$$\begin{aligned}
 \sum_{m=-\infty}^{\infty} \sum_{n=-\infty}^{\infty} R_I[m, n] R_I[m+t, n+u] &= \sum_{m=-\infty}^{\infty} \sum_{n=-\infty}^{\infty} a^{|m|+|n|+|m+t|+|n+u|} \\
 &= \left\{ \sum_{m=-\infty}^{\infty} a^{|m|+|m+t|} \right\} \left\{ \sum_{n=-\infty}^{\infty} a^{|n|+|n+u|} \right\}. \tag{3.62}
 \end{aligned}$$

Note that the terms between the braces are identical. We continue with the first term. Assume that $t \geq 0$ and split the summation in three parts:

$$\{ \dots \} = \sum_{m=-\infty}^{-t} a^{|m|+|m+t|} + \sum_{m=-t+1}^0 a^{|m|+|m+t|} + \sum_{m=1}^{\infty} a^{|m|+|m+t|}$$

$$\begin{aligned}
&= \sum_{m=t}^{\infty} a^{|m|+|m-t|} + \sum_{m=0}^{t-1} a^{|m|+|m-t|} + \sum_{m=1}^{\infty} a^{|m|+|m+t|} \\
&= \sum_{m=t}^{\infty} a^{2m-t} + \sum_{m=0}^{t-1} a^{m-m+t} + \sum_{m=1}^{\infty} a^{2m+t} \\
&= a^t \frac{1}{1-a^2} + a^t t + a^t \left(\frac{1}{1-a^2} - 1 \right) \\
&= a^t \left(\frac{1+a^2}{1-a^2} + t \right) \tag{3.63}
\end{aligned}$$

The result for $t < 0$ is obtained in a similar way, but with t in (3.63) replaced by $-t$. The same procedure is followed for the second term in (3.62), so we finally obtain

$$\text{cov} \left\{ \hat{R}_{II}[m_o, n_o], \hat{R}_{II}[m_o+t, n_o+u] \right\} = \frac{2\sigma_I^4}{N^2} a^{|t|+|u|} \left(\frac{1+a^2}{1-a^2} + |t| \right) \left(\frac{1+a^2}{1-a^2} + |u| \right). \tag{3.64}$$

We divide this expression by the variance of $\hat{R}_{II}[m_o, n_o]$, given by

$$\text{var} \left\{ \hat{R}_{II}[m_o, n_o] \right\} = \text{cov} \left\{ \hat{R}_{II}[m_o, n_o], \hat{R}_{II}[m_o, n_o] \right\}$$

and thus obtain the correlation $\rho[t, u]$ of the estimated covariance in $[m_o, n_o]$ with that in a position $[t, u]$ relative to $[m_o, n_o]$, i.e.

$$\rho[t, u] = a^{|t|+|u|} \left(1 + |t| \frac{1-a^2}{1+a^2} \right) \left(1 + |u| \frac{1-a^2}{1+a^2} \right). \tag{3.65}$$

This result points out that the estimated cross-covariance is correlated over a finite range. By analogy with the integral length scale in a one-dimensional random process, we may estimate an integral length scale \mathcal{L}_ρ associated with the signal peak by taking the square root of the double sum of $\rho[t, u]$ over all t, u . For the correlation in (3.65) we find

$$\mathcal{L}_\rho^2 = \sum_{t=-\infty}^{\infty} \sum_{u=-\infty}^{\infty} \rho[t, u] = \left[\frac{(1-a^2)(1+a)^2}{(1+a^2)(1-a)^2} \right]^2. \tag{3.66}$$

We may interpret \mathcal{L}_ρ^2 as the number of *correlated* samples, or reversely, consider $N^2 - \mathcal{L}_\rho^2$ as the number of *independent* samples for a sample size of $N \times N$ pixels. We regard $(N^2 - \mathcal{L}_\rho^2)/N^2$ as a measure for the information content of an interrogation area with respect to the estimation of the covariance. Let us apply this result in an example.

Example 4 (The integral length scale of the estimated signal peak)

Consider an interrogation region with an area of $1 \times 1 \text{ mm}^2$. The particle-image diameter d_t is $25 \mu\text{m}$, so that the peak in the image covariance has a e^{-2} diameter of $d_t\sqrt{2}$; see Sect. 3.5. For this situation we now evaluate the integral length scale \mathcal{L}_ρ in (3.65) as function of the

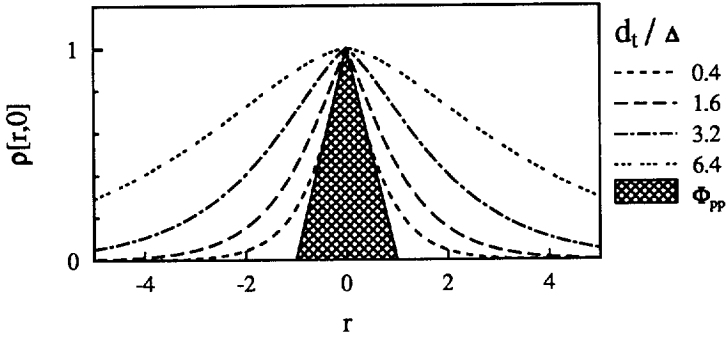


Figure 3.7: The self-correlation $\rho[r, 0]$ of the estimated image covariance given in Eq. (3.65), for four different values of the particle-image diameter (d_t) with respect to the pixel size (Δ). The shaded triangle represents Φ_{pp} ; see Eq. (3.6).

pixel resolution. For $N \times N$ pixels the side of a single (square and contiguous) pixel is equal to $\Delta = 1/N$ mm. The model parameter a is found by Eqs. (3.59) and (3.60). In Figure 3.7 $\rho[r, 0]$ is shown (as a continuous function of t) for four different values of d_t/Δ , i.e. 0.4, 1.6, 3.2 and 6.4, which correspond to pixel resolutions of $N \times N$ pixels, with $N=16, 64, 128$ and 256 respectively. In Table 3.1 are given the values of relevant parameters and results from Eqs. (3.66–3.60) for different values of N between 16 and 512. The result for \mathcal{L}_ρ as

Table 3.1: The integral length scale \mathcal{L}_ρ of the covariance of $\hat{R}_{II}[s, t]$ and values of relevant parameters in Example 4, for different values of the number of samples $N \times N$ per interrogation area.

N	Δ (μm)	d_t/Δ	d_R/Δ	c	a	\mathcal{L}_ρ	\mathcal{L}_ρ/N
16	62.5	0.4	2.08	1.303	0.132	1.64	0.10
32	31.3	0.8	2.30	1.441	0.181	1.95	0.061
64	16.6	1.6	3.02	1.892	0.309	2.96	0.046
128	7.8	3.2	4.95	3.102	0.512	5.62	0.044
256	3.9	6.4	9.27	5.809	0.706	11.3	0.044
512	2.0	12.8	18.2	11.41	0.839	22.6	0.044

function of d_t/Δ is plotted in Figure 3.8. This figure shows that \mathcal{L}_ρ for large Δ remains practically constant, up to a pixel resolution of about $N=32$. For $N < 32$ the particle-image diameter is less than a pixel. Hence, the width of $R_I[r, s]$ is determined mainly by Φ_{pp} (viz., $d_R \sim \Delta$). A constant value for \mathcal{L}_ρ implies that the information content of the interrogation area becomes larger with increasing N ; improving the resolution yields a better accuracy for the estimated displacement. However, above a resolution of $N=64$

we find that \mathcal{L}_q/N becomes constant. The value of this constant is proportional to the area covered by the particle-image and the interrogation area. This behaviour for \mathcal{L}_q now implies that the information content remains constant for increasing resolution. In other words, above $N=64$ the signal peak in the estimated covariance covers a larger number of pixels, but the estimated values are more strongly correlated, and do not yield more “information” as N increases. In effect, the observed behaviour for $N > 64$ is exactly what one would expect for the *oversampling* of a given signal, while the behaviour for $N < 32$ corresponds to an *undersampling* of the signal. This confirms our results for the estimated bandwidth of PIV images, discussed in Sect. 3.5.

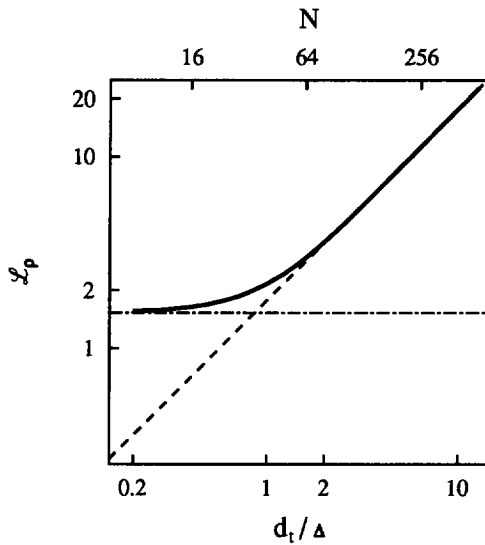


Figure 3.8: Correlation length \mathcal{L}_q of the estimated image covariance as function of the pixel resolution $N \times N$ for a $1 \times 1 \text{ mm}^2$ interrogation area and $25 \mu\text{m}$ particle-image diameter; see Example 4 on page 72. The straight lines represent the asymptotic behaviour of \mathcal{L}_q for $N \rightarrow 1$ and $N \rightarrow \infty$.

We have just learned from the preceding example that we should choose Δ in proportion to d_t . By (3.37) we know that the covariance of $\hat{R}_{II}[r, s] \sim \mathcal{O}(1/N^2)$. Therefore to improve the accuracy of $\hat{R}_{II}[r, s]$ we have to increase N relative to d_t/Δ . For “fixed” d_t (viz., $d_t/\Delta \sim 1$) this implies that we have to increase the interrogation area. We cannot make the interrogation area arbitrarily large, because of two (obvious) reasons. First, the total frame size is *fixed*, say $M \times M$ pixels. In order to preserve a certain degree of “spatial resolvability” in the measurement we should have that $N \ll M$, which limits the choice for N . Secondly, we cannot make the interrogation arbitrarily large without opposing the assumption that the displacement field over the interrogation area

is (approximately) uniform. Thus, in practice there is very little freedom to improve the accuracy of estimating the centroid of the displacement correlation peak by increasing the pixel resolution of the interrogation area. This partially explains why the accuracy of the PIV analysis changes very little with the pixel resolution of the interrogation area.

3.8 Estimation of the fractional displacement

The particle-image displacement is given by the location of the cross-covariance peak with respect to the origin; see Eq. (3.10). Provided that we have sufficient matching particle-image pairs (see Sect. 3.6.4) the cross-covariance peak is identified as the maximum of $\hat{R}_{II}[r, s]$, located in $[m_o, n_o]$. The actual displacement (r_D, s_D) can be written as

$$r_D = (m_o + \epsilon_m)\Delta \quad \text{and} \quad s_D = (n_o + \epsilon_n)\Delta \quad (3.67)$$

where m_o and n_o are now referred to as the *nearest-integer* displacements, and ϵ_m and ϵ_n as the *fractional* displacements, with

$$-0.5 < \epsilon_m \leq 0.5 \quad \text{and} \quad -0.5 < \epsilon_n \leq 0.5. \quad (3.68)$$

By itself the location of the maximum of $\hat{R}_{II}[r, s]$ is an estimate of the particle-image displacement, within an error $\pm\Delta/2$. At high pixel resolution (i.e. $d_t/\Delta \gg 1$) the difference between the displacement in integer pixel units and the actual displacement is very small with respect to the magnitude of the displacement; for example, the relative error for a displacement over 64 px in a 512×512 -pixel interrogation area would be $0.5/64$, which is less than 1%. This is not the case at low pixel resolution (i.e. $d_t/\Delta \sim 1$); for a 32×32 -pixel interrogation area the same relative displacement from the previous example now amounts to 8 px, which yields a relative error of $0.5/8$, which is more than 6%. In order to obtain an accuracy at *sub-pixel* level we make use of the fact that the displacement-correlation peak always covers more than one pixel (see Sect. 3.2), and *interpolate* the cross-covariance around the maximum in $\hat{R}_{II}[r, s]$.

Figure 3.9 illustrates the appearance of the covariance at low pixel resolution for different fractional displacements. Note that the strongest effect is found in the covariance adjacent to the maximum. The dashed line represents the corresponding noise level. This shows that at low pixel resolution only the nearest neighbours of the covariance maximum exceed the noise level, and implies that only the covariance maximum and its nearest-neighbours contain *significant* information with respect to the particle-image displacement. In this section we therefore only deal with estimators of the fractional displacement that use the covariance in $[m_o, n_o]$ and in its four-connected adjacent neighbours, shown in Figure 3.10. In our analysis we assume that $\hat{R}_{II}[r, s]$ is circularly symmetric and separable in r and s , and that ϵ_m and ϵ_n are statistically orthogonal, viz.

$$\text{cov}\{\hat{\epsilon}_m, \hat{\epsilon}_n\} = 0. \quad (3.69)$$

This allows us to deal with the fractional displacements in the two displacement directions as if they were independent. So we reduced the estimation of the fractional displacement

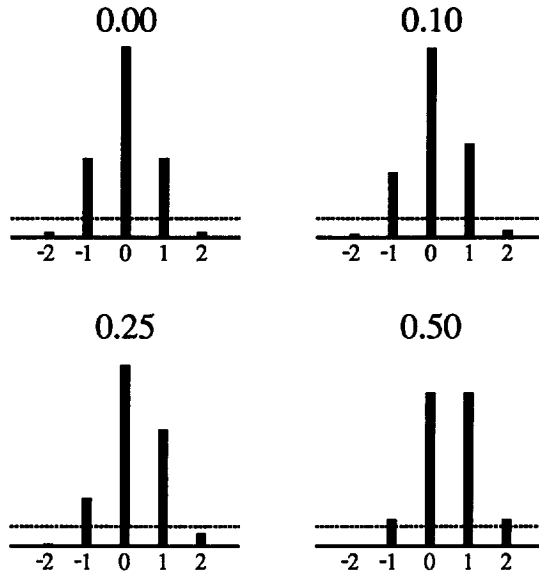


Figure 3.9: The discrete covariances for four different values of the fractional displacement. The situation shown here corresponds to $N=64$ in Table 3.1. The dashed line represents the 95% significance level of the background noise; see (3.41).

to a one-dimensional problem. We therefore only consider the estimation of the fractional displacement of r_D with $s_D = 0$. (The corresponding result for $s_D \neq 0$ is considered trivial.) We have seen in Fig. 3.9 that only three values of the image cross-covariance, i.e. $\hat{R}_{II}[m_o-1, n_o]$, $\hat{R}_{II}[m_o, n_o]$ and $\hat{R}_{II}[m_o+1, n_o]$ contain significant information with respect to the centroid of $\hat{R}_{II}[r, s]$; see also Sect. 3.7. We therefore refer to the estimators for ϵ that are introduced next as *three-point estimators* of the fractional displacement. We will subsequently use the following simplified notation:

$$R_m \equiv R_{II}[m_o+m, 0], \quad \hat{R}_m \equiv \hat{R}_{II}[m_o+m, 0], \quad F_m \equiv F_I[m_o+m, 0]. \quad (3.70)$$

3.8.1 three-point estimators

Here we introduce three different three-point estimators, denoted by $\hat{\epsilon}$, for the fractional displacement, given the location $[m_o, n_o]$ of the maximum in $\hat{R}_{II}[r, s]$. We limit ourselves to the three estimators that have also been studied by Willert (1989).

- **center-of-mass estimator**

Probably the most widely used method for estimation of a peak position is by the

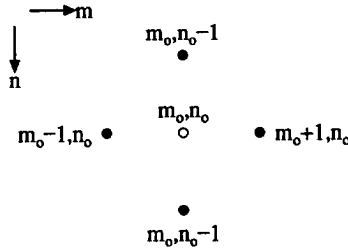


Figure 3.10: The four-connected neighbourhood (closed dots) of the covariance maximum in $[m_0, n_0]$ (open dot).

first moment of the peak. With only three points available this estimator becomes

$$\hat{\epsilon}_C = \frac{\hat{R}_{+1} - \hat{R}_{-1}}{\hat{R}_{-1} + \hat{R}_0 + \hat{R}_{+1}}. \tag{3.71}$$

In mechanics the first moment of a given mass distribution is denoted as the “center-of-mass” or “center-of-gravity”. We will therefore refer to the estimator in (3.71) as the center-of-mass estimator.

• **parabolic-fit estimator**

A more advanced estimator, in comparison with the center-of-mass estimator, is to fit a parabola. With three elements available we can exactly solve the three parameters of a parabolic curve. The position of the maximum of the parabola defines the parabolic-fit estimator:

$$\hat{\epsilon}_P = \frac{\hat{R}_{-1} - \hat{R}_{+1}}{2(\hat{R}_{-1} + \hat{R}_{+1} - 2\hat{R}_0)}. \tag{3.72}$$

The main difference with the center-of-mass estimator is that we now make explicit use of the fact that we are dealing with a *peak*, i.e. $\hat{R}_0 > \hat{R}_{\pm 1}$.

• **Gaussian-fit estimator**

An estimator that is very similar to the parabolic-fit estimator is the Gaussian-fit estimator. Here we do not only use the fact that we are dealing with a peak, but also use the fact that the image covariance function is (approximately) a Gaussian curve. The logarithm of a Gaussian curve is a parabolic curve, so by substitution of \hat{R}_m by $\ln \hat{R}_m$ in (3.72) we get

$$\hat{\epsilon}_G = \frac{\ln \hat{R}_{-1} - \ln \hat{R}_{+1}}{2(\ln \hat{R}_{-1} + \ln \hat{R}_{+1} - 2 \ln \hat{R}_0)}. \tag{3.73}$$

Note that, apart from $\hat{R}_0 > \hat{R}_{\pm 1}$, we should also have $\hat{R}_i > 0$ for $i = -1, 0, 1$.

In the next section we will further investigate the statistical properties of these three-point estimators. For now, let us make a *qualitative* comparison of these estimators with respect to their (expected) robustness and performance.

If we compare these three estimators we find that $\hat{\epsilon}_C$ will *always* yield a result, no matter what the actual shape for \hat{R}_m actually is. The parabolic-fit estimator requires that \hat{R}_0 is the *maximum* of the three elements. This requirement is always satisfied by the definition of $\{m_o, n_o\}$; see Eq. (3.67). For the Gaussian peak-fit estimator it is also required that the values of all three elements are positive. By (3.41) we know that $E\{\hat{R}_m\} \gg \text{var}\{\hat{R}_m\}^{1/2}$ so that this requirement is satisfied in general. Nonetheless, we may conclude that $\hat{\epsilon}_C$ has the highest *robustness* of these three estimators, while $\hat{\epsilon}_G$ has the lowest.

On the other hand, we have seen that $\hat{\epsilon}_C$ does *not* make use of any *a priori* knowledge with respect to \hat{R}_m , while $\hat{\epsilon}_P$ and $\hat{\epsilon}_G$ make use of the fact that \hat{R}_m has its maximum in m_o , and $\hat{\epsilon}_G$ even takes into account the approximate shape of $\{\Phi_{pp} * R_{II}\}(r, s)$. As a rule of thumb we know that the performance of an estimator improves as it makes more use of any *a priori* knowledge. We may therefore expect the best performance from $\hat{\epsilon}_G$ and the least from $\hat{\epsilon}_C$.

What should also be noted is that these three estimators have very similar form, despite their (expected) differences in robustness and performance. The numerator is only a function of \hat{R}_{-1} and \hat{R}_{+1} , while the denominator is a function of all three elements. In fact, \hat{R}_{-1} and \hat{R}_{+1} appear as a *difference* or *ratio* in the numerator. We therefore regard the numerator as a kind of balance, while the denominator is actually no more than a kind of normalization term. This reflects our initial observation at the beginning of this section that a fractional displacement most strongly affects R_{-1} and R_{+1} . Conversely, one may say that \hat{R}_{-1} and \hat{R}_{+1} hold most of the "information" with respect to the fractional displacement, and as a result we may expect them to play a dominant role in *all* three-point estimators for ϵ .

3.9 Statistics of fractional-displacement estimators

In this section we investigate the statistical properties of the fractional-displacement estimators introduced in the previous section. We have seen in (3.68) that the outcome of this estimator is between $-1/2$ and $+1/2$. Here we will analyze the situation for which the *actual* displacement is *exactly* an integer number of pixels. In other words, we will investigate the accuracy of the *estimated* fractional displacement given that the *actual* fractional displacement is zero (i.e. $\epsilon = 0$). This situation considerably simplifies the analysis, since we have for $\epsilon = 0$:

$$R_{-1} = R_{+1} = a_1 R_0 \quad \text{with} \quad 0 < a_1 < 1. \quad (3.74)$$

Note that a_1 gives the ratio of $R_{\pm 1}$ and R_0 , and is proportional to the width of the displacement-correlation peak. If we assume that this peak has a Gaussian shape then a_1

is given by

$$a_1 = \exp(-8/d_R^2) \tag{3.75}$$

with d_R given by (3.59). Note that $a_1 > a$; see Fig. 3.6.

3.9.1 expectation

To evaluate the expectation values for the three fractional displacement estimators defined in Sect. 3.8.1 we assume that we may deal with the numerators and denominators separately, viz.

$$E \left\{ \frac{A}{B} \right\} \approx \frac{E \{A\}}{E \{B\}}. \tag{3.76}$$

Let us evaluate the validity of this approximation. For the center-of-mass estimator in (3.71) we have

$$A = \hat{R}_{+1} - \hat{R}_{-1} \quad \text{and} \quad B = \hat{R}_{-1} + \hat{R}_0 + \hat{R}_{+1}. \tag{3.77}$$

For $\epsilon = 0$ we have

$$\text{var}\{\hat{R}_{-1}\} \approx \text{var}\{\hat{R}_{+1}\} \approx \text{cov}\{\hat{R}_{-1}, \hat{R}_{+1}\} \quad \text{and} \quad \text{cov}\{\hat{R}_{-1}, \hat{R}_0\} \approx \text{cov}\{\hat{R}_{+1}, \hat{R}_0\}$$

(see Eqs. (3.37–3.38)). Substitution in (3.77) yields (after some straightforward manipulation) that: $\text{cov}\{A, B\} \sim 0$, by which we may write

$$E \left\{ \frac{A}{B} \right\} \approx E \{A\} \cdot E \left\{ \frac{1}{B} \right\}. \tag{3.78}$$

The denominator B can be regarded as a normalization term (see previous section) that is proportional to the width of the covariance peak. For a *narrow* peak we have: $B \sim \hat{R}_0$, so that we may assume that $E\{B\} \gg \text{var}\{B\}^{1/2}$; see Eq. (3.42). Under this condition we may write

$$E \left\{ \frac{1}{B} \right\} \approx \frac{1}{E \{B\}}, \tag{3.79}$$

which completes the justification of the approximation in (3.76). (A similar approach can be followed to justify (3.76) for the peak-fit estimators.)

We use the result in (3.44), viz.

$$E \{ \hat{R}_m \} = F_m R_m$$

and substitute this with Eq. (3.74) in Eqs. (3.71–3.73) to obtain the following expressions for the expectations of $\hat{\epsilon}_C$, $\hat{\epsilon}_P$ and $\hat{\epsilon}_G$:

$$E \{ \hat{\epsilon}_C \} = \frac{F_{+1} - F_{-1}}{F_{-1} + F_{+1} + F_0/a_1} \tag{3.80}$$

$$E \{ \hat{\epsilon}_P \} = \frac{F_{-1} - F_{+1}}{2(F_{-1} + F_{+1} - 2F_0/a_1)} \tag{3.81}$$

$$E \{ \hat{\epsilon}_G \} = \frac{\ln F_{-1} - \ln F_{+1}}{2(\ln F_{-1} + \ln F_{+1} - 2 \ln F_0 + 2 \ln a_1)}. \tag{3.82}$$

The expression for $E\{\hat{\epsilon}_G\}$ was found by using the approximation

$$E\{\ln \hat{R}_m\} \approx \ln E\{\hat{R}_m\} \tag{3.83}$$

which is valid for $\text{var}\{\hat{R}_m\}^{1/2} \ll E\{\hat{R}_m\}$ (Priestley 1992). This condition is generally satisfied for PIV images; see (3.42). For an *unbiased* estimate of the fractional displacement, given that $\epsilon = 0$, one expects that the enumerators in Eqs. (3.80–3.82) are exactly equal to zero, i.e. $F_{-1} = F_{+1}$. However, we have seen in Sect. 3.6.3 that for a finite size of the interrogation area we have

$$F_{-1} > F_{+1} \tag{3.84}$$

(for $m_o > 0$). This implies that the enumerators in Eqs. (3.80–3.82) are not equal to zero for the case $\epsilon = 0$. Note that this bias is a direct consequence of (3.84), and therefore *not* a property of the estimators themselves. Hence, we expect that *all* estimates of the fractional displacement estimators are *biased* (except for the trivial case $m_o = 0$, when $F_{-1} = F_{+1}$).

Let us have a closer look at this bias for the uniform and Gaussian weight kernels introduced in Sect. 3.6.3. After substitution of the uniform weight kernel, given in (3.47), in Eqs. (3.80–3.82) we find (for $m_o > 0$)

$$E\{\hat{\epsilon}\} = -\frac{2}{N} \frac{N}{N - m_o} \cdot \begin{cases} \frac{a_1}{1 + 2a_1} & \text{for } \hat{\epsilon}_C \\ \frac{a_1}{4(1 - a_1)} & \text{for } \hat{\epsilon}_P \\ \frac{1}{4 \ln(1/a_1)} & \text{for } \hat{\epsilon}_G \end{cases} \tag{3.85}$$

The expression for $\hat{\epsilon}_G$ was found by using a first-order approximation for F_m , i.e.

$$F_m = \ln \left[1 - \frac{|m_o + m|}{N} \right] = -\frac{|m_o + m|}{N} + \mathcal{O}\left(\frac{1}{N^2}\right).$$

Let us subsequently evaluate the bias of the estimated fractional displacement for the Gaussian weight kernel, given by (3.48). Substitution in Eqs. (3.80–3.82) now yields:

$$E\{\hat{\epsilon}\} = -\frac{2}{N} \frac{8m_o}{N} \cdot \begin{cases} \frac{a_1}{1 + 2a_1} & \text{for } \hat{\epsilon}_C \\ \frac{a_1}{4(1 - a_1)} & \text{for } \hat{\epsilon}_P \\ \frac{1}{4 \ln(1/a_1)} & \text{for } \hat{\epsilon}_G \end{cases} \tag{3.86}$$

The expressions for $E\{\hat{\epsilon}_C\}$ and $E\{\hat{\epsilon}_P\}$ were found by a first-order approximation for F_m , i.e.

$$F_m = \exp \left[-8 \left(\frac{m_o + m}{N} \right)^2 \right] = 1 - 8 \left(\frac{m_o + m}{N} \right)^2 + \mathcal{O}\left(\frac{1}{N^4}\right).$$

Note that in (3.86) *only* the term in front of the brace has changed with respect to (3.85). Though not directly evident from Eqs. (3.80–3.82) it appears that the bias of the estimated fractional displacement for the three estimators considered in Eqs. (3.85–3.86) all show the same qualitative behaviour as function of the displacement. Obviously this behaviour is determined by the weight kernel; only the magnitude of the bias is determined by the estimator itself. In Figure 3.11 are shown the terms on the left-hand side of the brace

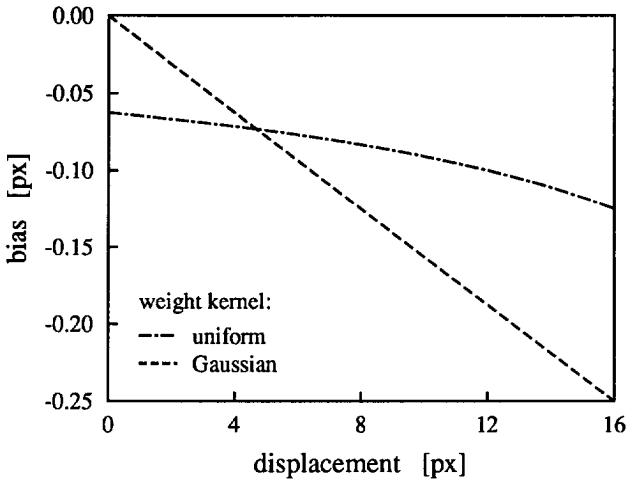


Figure 3.11: The bias in the estimated fractional displacement for the uniform and Gaussian weight kernels, viz. Eqs. (3.85) and (3.86) respectively, for the Gaussian peak-fit estimator, defined in (3.73), as function of the displacement, with $N=32$ and $a_1=0.6$ (viz., $4 \ln(1/a_1)=1$); see also text.

in (3.85) and (3.86) as function of m_o for $N=32$. Note that this term is approximately constant for the uniform weight kernel, while it is directly proportional to m_o for the Gaussian weight kernel. It is rather surprising that the use of a different weight kernel can cause such a change in behaviour. In Figure 3.12 are shown the terms on the right-hand side of the braces in (3.85) as function of a_1 . This figure shows the magnitude of the bias as function of the peak width. Note that for a_1 less than about 0.5 all these terms yield approximately the same value. But, for a_1 the value for the peak-fit estimators, $\hat{\epsilon}_P$ and $\hat{\epsilon}_G$, increases rapidly, while it remains practically constant for $\hat{\epsilon}_C$. A value of $a_1 < 0.5$ corresponds to a situation with $R_0 > 2R_{\pm 1}$. This indicates that the peak-fit estimators perform better if the displacement-correlation peak is *sharp*, whereas the performance of the center-of-mass estimator is not very sensitive to the shape of the peak. This conclusion corresponds with the discussion of the (expected) performance and robustness at the end of Sect. 3.8.1.

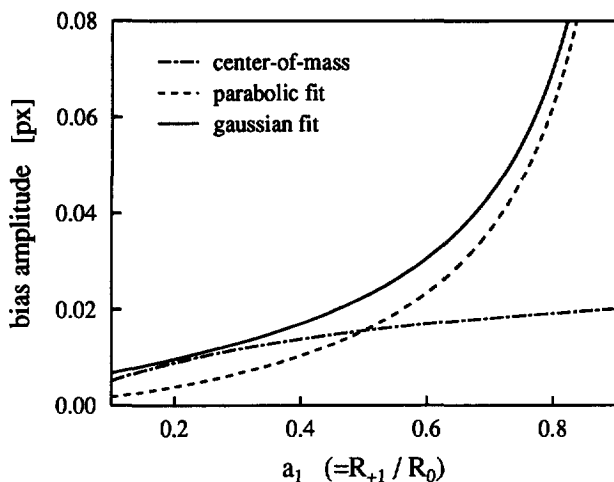


Figure 3.12: The magnitude of the bias in the estimated fractional displacement by (3.85) for three different estimators as function of $a_1 (= R_{\pm 1}/R_0)$; see (3.74). The curves are drawn for $N = 32$ and $m_o = 0$.

bias correction

A typical value of the bias for a 32×32 -pixel interrogation region, with $d_t = 5.6$ px (i.e. $4 \ln(1/a_1) = 1$), is about 0.06 px (see Fig. 3.11). Although it may seem negligible at first, it can lead to significant errors in the estimation of the flow velocity statistics, like the mean flow velocity, or in the computation of derived flow quantities, like the out-of-plane component of the vorticity. We therefore have to compensate for this bias.

We have seen that all three estimators show the same qualitative behaviour as function of the displacement, which is determined by the difference of F_{-1} and F_{+1} ; see (3.84). It is therefore proposed to apply the following correction to the estimated covariances *prior* to estimation of the fractional displacement:

$$R_{II}^*[r, s] = \frac{\hat{R}_{II}[r, s]}{F_I[r, s]} \tag{3.87}$$

(with: $R_m^* \equiv R_{II}^*[m_o + m, 0]$) where $R_{II}^*[r, s]$ is referred to as the *unbiased* estimate of the image cross-covariance. With this correction $E\{R_{-1}^*\}$ becomes equal to $E\{R_{+1}^*\}$ for $\epsilon = 0$. So now the expectation values for the numerators in all three fractional displacement estimators are zero (for all values of a_1), which implies that all three estimators are *unbiased*.

3.9.2 variance

We now turn to the *variance* of the estimated fractional displacement. Like in the previous subsection we consider the situation for which the *actual* displacement is an exact integer multiple of pixels (viz., $\epsilon = 0$), and evaluate the statistical properties of the estimators given in (3.71–3.73).

The variance of the estimated fractional displacement is approximated by

$$\text{var}\{\hat{\epsilon}\} \approx \sum_{i=-1}^{+1} \sum_{j=-1}^{+1} \frac{\partial \hat{\epsilon}}{\partial \hat{R}_i} \frac{\partial \hat{\epsilon}}{\partial \hat{R}_j} \text{cov}\{\hat{R}_i, \hat{R}_j\} \tag{3.88}$$

where $\partial \hat{\epsilon} / \partial \hat{R}_i$ denotes the partial derivative of $\hat{\epsilon}$ with respect to \hat{R}_i . The expression in (3.88) is valid provided that $\text{var}\{\hat{R}_m\} \ll E\{\hat{R}_m\}^2$, which is generally satisfied for $N \gg 1$; see (3.42). Like in the previous subsection, we consider the variance of the *estimated* fractional displacement in (3.88) given that the *actual* displacement is exactly an integer number of pixel units (i.e. $\epsilon=0$). In addition we apply the bias correction proposed in (3.87), so that

$$\frac{\partial \hat{\epsilon}}{\partial \hat{R}_i} = \frac{\partial \hat{\epsilon}}{\partial R_i^*} \frac{1}{F_i} \tag{3.89}$$

By $E\{R_{-1}^*\} = E\{R_{+1}^*\}$ we obtain for the partial derivatives in (3.89):

$$\frac{\partial \hat{\epsilon}}{\partial R_0^*} = 0 \quad \text{and} \quad \frac{\partial \hat{\epsilon}}{\partial R_{-1}^*} = -\frac{\partial \hat{\epsilon}}{\partial R_{+1}^*} \tag{3.90}$$

In the case of a *noise-free* image with $F_O(D_Z) = 1$ and $N \rightarrow \infty$ we have

$$\text{var}\{\hat{R}_{-1}\} = \text{var}\{\hat{R}_{+1}\} = \text{cov}\{\hat{R}_{-1}, \hat{R}_{+1}\} \tag{3.91}$$

see Eqs. (3.37–3.38). In practice it appears that the conditions for (3.91) are rarely met. Let us have a closer look at the consequences for (3.88). Suppose that the images are contaminated by *white* noise³. Some thought reveals that white noise mainly increases the *variances* of \hat{R} , while its influence on the covariances is negligible; see Eqs. (3.37–3.38). We therefore introduce a constant $K \geq 0$ that represents the *decorrelation* between \hat{R}_{-1} and \hat{R}_{+1} , i.e.

$$(1+K) \cdot \text{var}\{\hat{R}_{\pm 1}\} \geq \text{cov}\{\hat{R}_{-1}, \hat{R}_{+1}\} \tag{3.92}$$

Hence, we obtain for (3.88):

$$\text{var}\{\hat{\epsilon}\} \approx \left(\frac{\partial \hat{\epsilon}}{\partial R_{\pm 1}^*}\right)^2 \left[\frac{1+K}{F_{-1}^2} + \frac{1+K}{F_{+1}^2} - \frac{2}{F_{-1}F_{+1}} \right] \text{var}\{\hat{R}_{\pm 1}\} \tag{3.93}$$

This result shows that the variance of the estimated fractional displacement depends on three terms, of which each—as we will see later—appears to play an individual role with regard to the variance of $\hat{\epsilon}$. Namely:

³This is *additional* (instrumental) noise. Do not confuse this with the noise in the estimated covariance due to the finite sample size, described by (3.40–3.41).

- The partial-derivative term $(\partial\hat{\epsilon}/\partial R_{\pm 1}^*)^2$ directly depends on the applied fractional-displacement estimator; see Sect. 3.8.1. This term can be interpreted as the *sensitivity* of $\hat{\epsilon}$ to random errors in the estimated covariance.
- The term between brackets represents the effect due to in-plane loss-of-pairs as a result of the finite size of the interrogation area (see Sects. 3.6.2 and B.2). Because it depends on the (small) differences that exist between $\text{var}\{\hat{R}_{-1}\}$, $\text{var}\{\hat{R}_{+1}\}$ and $\text{cov}\{\hat{R}_{-1}, \hat{R}_{+1}\}$ we will refer to it as the *balance term*.
- The variance term $\text{var}\{\hat{R}_{\pm 1}\}$ given by Eq. (3.38) is directly related to the image covariance function, and subsequently depends on the bandwidth of the (continuous) PIV signal; see Sects. 3.5 and 3.7.

In the next three paragraphs we will evaluate these three terms, given the fractional-displacement estimators defined in Eqs. (3.71–3.73), the model for the image covariance in (3.54) and the in-plane loss-of-pairs function in (3.45).

But before proceeding we first reconsider the expression given in Eq. (3.93), but now for the case *without* applying the bias correction given in (3.87). In that case $1/F_m$ disappears as a prefix factor for the (co)variances of $\hat{R}_{II}[r, s]$, but re-appears in the partial derivatives. As a result (3.90) is no longer valid, and should be replaced by

$$\frac{\partial\hat{\epsilon}}{\partial\hat{R}_m} = \frac{1}{F_m} \frac{\partial\hat{\epsilon}}{\partial R_m^*} \tag{3.94}$$

cf. Eq. (3.89). Now it can be easily seen this would yield the same expression as in (3.93). Thus, the expression in (3.93) applies to both the corrected and uncorrected estimate image covariance.

partial derivatives

Consider the three fractional-displacement estimators defined in (3.71–3.73). For zero fractional displacement the squared partial-derivatives with respect to $R_{\pm 1}$ yield

$$\left(\frac{\partial\hat{\epsilon}_C}{\partial R_{\pm 1}^*}\right)^2 = \sigma_I^{-4} \left[\frac{2R_{\mp 1}^* + R_0^*}{(R_{-1}^* + R_0^* + R_{+1}^*)^2}\right]^2 \tag{3.95}$$

$$\left(\frac{\partial\hat{\epsilon}_P}{\partial R_{\pm 1}^*}\right)^2 = \sigma_I^{-4} \left[\frac{R_0^* - R_{\mp 1}^*}{(R_{-1}^* + R_{+1}^* - 2R_0^*)^2}\right]^2 \tag{3.96}$$

$$\left(\frac{\partial\hat{\epsilon}_G}{\partial R_{\pm 1}^*}\right)^2 = \sigma_I^{-4} \left[\frac{(\ln R_0^* - \ln R_{\mp 1}^*)/R_{\pm 1}^*}{(\ln R_{-1}^* + \ln R_{+1}^* - 2\ln R_0^*)^2}\right]^2 \tag{3.97}$$

Again note the similar form of the derivatives for the three different estimators. Since we consider integer displacements only we substitute 1 and a_1 for R_0^* and $R_{\pm 1}^*$ respectively.

We then find

$$\left(\frac{\partial \hat{\epsilon}}{\partial R_{\pm 1}^*}\right)^2 = \sigma_I^{-4} \cdot \begin{cases} \left[\frac{1}{1+2a_1}\right]^2 & \text{for } \hat{\epsilon}_C \\ \left[\frac{1}{4(1-a_1)}\right]^2 & \text{for } \hat{\epsilon}_P \\ \left[\frac{1}{4a_1 \ln a_1}\right]^2 & \text{for } \hat{\epsilon}_G \end{cases} \quad (3.98)$$

cf. Eqs. (3.85) and (3.86). In Figure 3.13 the partial derivatives are plotted as function of a_1 . Note that $(\partial \hat{\epsilon} / \partial R_{\pm 1}^*)^2$ for $\hat{\epsilon}_P$ and $\hat{\epsilon}_G$ strongly increases for a_1 larger than about 0.7, while it slowly decreases for $\hat{\epsilon}_C$. This shows that the peak-fit estimators are very sensitive to the width of the correlation peak; see also Fig. 3.12.

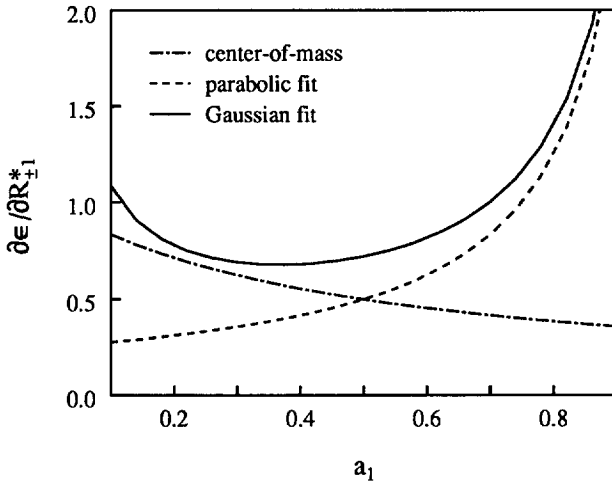


Figure 3.13: The partial derivatives of three fractional displacement estimators given by Eq. (3.98) as function of the model parameter a_1 . The parameter a_1 is proportional to the width of the displacement correlation peak; see Eq. (3.74).

balance term

The balance term in (3.93) depends only on F_m (viz., $F_I[m, n]$). Let us first consider the case for $K=0$. In that case the balance term in (3.93) can be written as:

$$\left[\frac{1}{F_{+1}} - \frac{1}{F_{-1}}\right]^2. \quad (3.99)$$

which is a function of m_0 ; see Eq. (3.70). The influence of the weight kernel on the variance of $\hat{\epsilon}$ is similar to that on the bias of $\hat{\epsilon}$; see Sect. 3.9.1. Substitution of (3.47) in (3.99) yields that the balance term is approximately constant, and $\mathcal{O}(4/N^2)$.

Now let us investigate the balance term for finite K . We first simplify the expression for the balance term by

$$F_{+1} \approx F_{-1} \approx F_0$$

so that the balance term reduces to

$$\left[\frac{1+K}{F_{-1}^2} + \frac{1+K}{F_{+1}^2} - \frac{2}{F_{-1}F_{+1}} \right] \approx \frac{2K}{F_0^2}. \tag{3.100}$$

We have $F_0 = 1 - \mathcal{O}(1/N^2)$ (see Sect. 3.6.3), so that the balance term for $K > 0$ is approximately constant, and $\mathcal{O}(2K)$. In principle it should be possible to find an expression for K from (3.37) and (3.38). However, our present aim is to investigate the performance of the fractional displacement estimators given in (3.8.1). The balance term depends on the weight kernel only, and its contribution to $\text{var}\{\hat{\epsilon}\}$ is equal for all three estimators. Hence the relative differences in performance between the three estimators is not determined by the balance term.

variance term

The variance term in (3.93) is given by (3.38). Like $\text{var}\{\hat{R}_0\}$ in Sect. 3.7 $\text{var}\{\hat{R}_{\pm 1}\}$ is easily evaluated through the model given in (3.54), which yields:

$$\begin{aligned} \text{var}\{\hat{R}_{\pm 1}\} &= \frac{1}{N^2} \sum_m \sum_n \left(R_I^2[m, n] + \hat{R}_{II}[1+m, n] \hat{R}_{II}[1-m, -n] \right) \\ &= \frac{\sigma_I^4}{N^2} \left[\left(\frac{1+a^2}{1-a^2} \right)^2 + \left(\frac{1+a^2}{1-a^2} \right) \left(\frac{2a^2}{1-a^2} + a^2 \right) \right] \\ &= \frac{\sigma_I^4}{N^2} \left(\frac{1+a^2}{1-a^2} \right) \left(\frac{1+3a^2}{1-a^2} + a^2 \right). \end{aligned} \tag{3.101}$$

In Figure 3.14 is plotted $\text{var}\{\hat{R}_{\pm 1}\}$ (normalized by σ_I^4) as function of a . In Example 4 we noted that the correlation length for fixed d_t increases proportional with N . In Fig. 3.14 we see that $\text{var}\{\hat{R}_{\pm 1}\}$ exhibits the same kind of behaviour, and that it remains practically constant for a larger than about 0.3.

We can now put together the results obtained in the three previous paragraphs. Note that the term σ_I^{-4} in (3.98) cancels with the term σ_I^4 in (3.101). Hence the variance of $\hat{\epsilon}$ does not depend on the σ_I^2 (viz., intensity variance). That implies that the accuracy of the estimated (uniform) displacement does not depend on the number of particle-image pairs in the interrogation area. This will be further discussed in Section 3.11.

In the following example we evaluate the variance of the fractional displacement estimators as function of the pixel resolution.

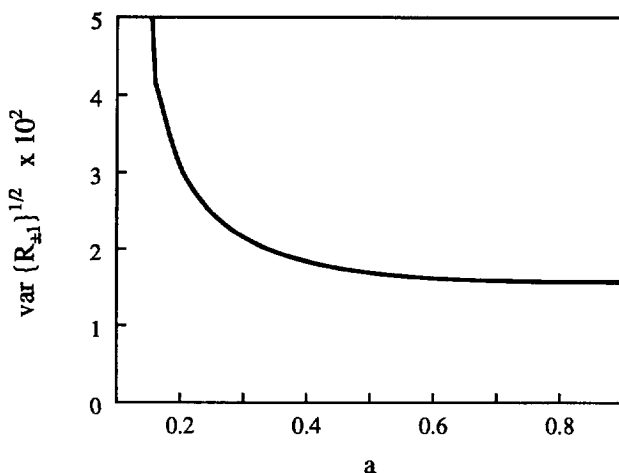


Figure 3.14: Square root of the variance of the estimated cross-covariance by Eq. (3.101) (adjacent to the peak maximum) as function of the model parameter a . The parameter a is proportional to the volume under the displacement correlation peak; see Eq. (3.54).

Example 5 (*The variance of the fractional displacement estimators*)

Again consider a 1×1 mm² interrogation area that has been digitized to a $N \times N$ -pixel image, with a particle-image diameter of 25 μm ; see also Example 4 on page 72. We evaluate Eqs. (3.98) and (3.101) to investigate the performances of the fractional displacement estimators \hat{e}_C , \hat{e}_P and \hat{e}_G as function of the pixel resolution. The model parameters a and a_1 are chosen according to (3.60) and (3.75) respectively. The random error of the estimated fractional displacement depends on the product of the partial-derivative term, the balance term and the variance term. We have seen that the balance term only describes the influence of the weight kernel. Hence, a measure for the random estimation error is given by the product of the partial-derivative term and the variance term. The partial derivatives for \hat{e}_C , \hat{e}_P and \hat{e}_G as function of a_1 are plotted in Figure 3.13. The variance term—which is equal for all three estimators—is plotted in Figure 3.14 as function of a . Table 3.2 contains the values for a $N \times N$ -pixel image, for several values of N between 16 and 512. In Figure 3.15 is given the product of the partial-derivative term and variance term as function of N . We see from this figure that the variance of \hat{e}_C is smallest of all three estimators for N larger than about 100. The parabolic and Gaussian peak-fit estimators appear to have an optimum, namely at $N \sim 40 \dots 80$ for \hat{e}_P and at $N \sim 60 \dots 100$ for \hat{e}_G .

It should be emphasized that these results apply to *integer* displacements only. Nonetheless, it demonstrates that the peak-fit estimators have optimal performance at *low*

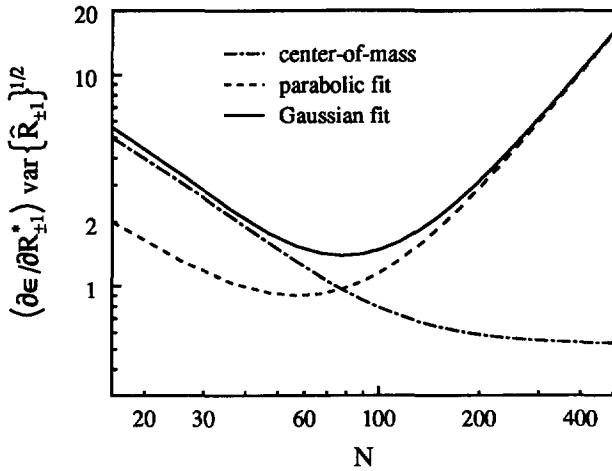


Figure 3.15: The product of the partial-derivative term $(\partial\epsilon/\partial R_{\pm 1}^*)$ and variance term $(\text{var}\{\hat{R}_{\pm 1}\})^{1/2}$ as function of the resolution for a $N \times N$ -pixel image; see Example 5.

Table 3.2: The partial derivatives for $\hat{\epsilon}_C$, $\hat{\epsilon}_P$ and $\hat{\epsilon}_G$ and $\text{var}\{\hat{R}_{\pm 1}\}$ for different values of the number of samples $N \times N$ per interrogation area for fixed $d_i=25 \mu\text{m}$. (The values in this table are given for $\sigma_I=1$.)

N	a	a ₁	var{R _{±1} } ^{1/2} 10 ⁻²	∂ε̂/∂R* _{±1}		
				C	P	G
16	0.132	0.157	6.63	0.76	0.30	0.86
32	0.181	0.220	3.49	0.69	0.32	0.75
64	0.309	0.416	2.12	0.55	0.42	0.69
128	0.512	0.721	1.67	0.41	0.89	1.06
256	0.706	0.911	1.58	0.36	2.81	2.94
512	0.839	0.976	1.57	0.35	> 10	> 10

pixel resolution, while the center-of-mass estimator has its optimal performance at *high* pixel resolution. However, to make a definite statement with respect to which of the three estimators has optimal performance at low pixel resolution we should first investigate their behaviour for non-zero fractional displacements. This is our subject of the next section.

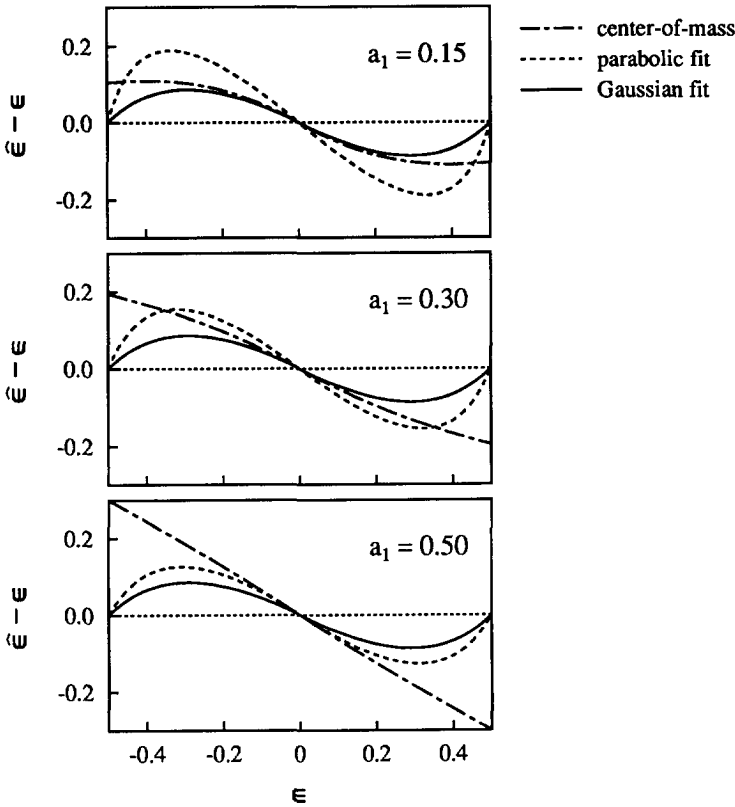


Figure 3.16: The tracking error for three different fractional-displacement estimators by Eqs. (3.104–3.106) as function of the fractional displacement for three values of the model parameter a_1 (proportional to the width of the displacement-correlation peak).

3.9.3 non-zero fractional displacements

So far we only considered integer displacements. In this section we will investigate the behaviour of the three fractional displacement estimators defined in Sect. 3.8.1 for non-zero fractional displacements. We do this by evaluating the *tracking error* of the estimators, which is the difference between the fractional displacement given by the estimator and the actual fractional displacement, viz.

$$\hat{\epsilon}_b = \hat{\epsilon} - \epsilon. \tag{3.102}$$

We will follow a procedure similar to Willert (1989); he did an analysis of the tracking error for three-point estimators of the fractional displacement.

To compare the outcome for each of the three estimators for a non-zero fractional displacement we model the image covariance by a small modification of (3.74), i.e.

$$R_{-1} = a_1^{1+\epsilon} \quad R_0 = a_1^\epsilon \quad R_{+1} = a_1^{1-\epsilon} \tag{3.103}$$

cf. (3.75). (We omitted here the term σ_I^2 , because it does not play any role in the evaluation of the tracking error.) We deliberately did *not* choose for a Gaussian form in (3.103), since that would certainly bias the tracking performances in favor of $\hat{\epsilon}_G$; see also Willert (1989). Substitution of (3.103) in (3.71–3.73) yields after some straightforward manipulation:

$$\hat{\epsilon}_C = \frac{\sinh(\epsilon \ln a_1)}{\cosh(\epsilon \ln a_1) + \frac{1}{2}a_1^{\epsilon-1}} \tag{3.104}$$

$$\hat{\epsilon}_P = \frac{\sinh(\epsilon \ln a_1)/2}{\cosh(\epsilon \ln a_1) - a_1^{\epsilon-1}} \tag{3.105}$$

$$\hat{\epsilon}_G = \frac{\epsilon}{2 - 2\epsilon} \tag{3.106}$$

Note that the fractional displacement for $\hat{\epsilon}_G$ does not depend on a_1 (i.e. the width of the correlation peak).

The result for the tracking error as function of ϵ is plotted in Figure 3.16 for three different values of a_1 . (In this figure the sign of the tracking error for $\hat{\epsilon}_C$ has been reversed to provide an easier mutual comparison of the three curves in each graph.) Since the tracking error for $\hat{\epsilon}_G$ is independent of a_1 , the three curves for $\hat{\epsilon}_G$ in Fig. 3.16 are identical. This is in contrast with the tracking errors for $\hat{\epsilon}_C$ and $\hat{\epsilon}_P$. The tracking error for $\hat{\epsilon}_P$ seems to approach that of $\hat{\epsilon}_G$ for large a_1 . The tracking error of $\hat{\epsilon}_C$ for small a_1 seems to approach that of $\hat{\epsilon}_G$. However, unlike the curves for $\hat{\epsilon}_P$ and $\hat{\epsilon}_G$, it appears that the tracking error for $\hat{\epsilon}_C$ is *discontinuous* at $\epsilon = \pm \frac{1}{2}$. The discontinuity increases with increasing a_1 . Effectively this means that $\hat{\epsilon}_C$ has a strong bias towards an integer value of the displacement, which explains why the variance of $\hat{\epsilon}_C$ for $\epsilon = 0$ is lower than that of $\hat{\epsilon}_P$ and $\hat{\epsilon}_G$ for large a_1 (see Example 5). But, for non-zero values of ϵ the estimation error of $\hat{\epsilon}_C$ can be much larger. The discontinuity is a direct result of the fact that the sample data (viz., estimated covariances) are not symmetrically distributed with respect to the peak centroid. Let us explain this with an example.

Suppose that we have a particle-image displacement of $m_o + \epsilon$, with $\epsilon = 0.5$ and where m_o is an integer number. In that case the covariances in m_o and $m_o + 1$ are equal; if we would only use the covariances in m_o and $m_o + 1$ then a center-of-mass estimator would yield $\hat{\epsilon} = \frac{1}{2}$. However, for a three-point estimator always a third covariance is included in $\hat{\epsilon}_C$. This is either the covariance in $m_o - 1$ or the covariance in $m_o + 2$, depending on which of the two central covariances is identified as the maximum⁴. Some thought shows that if

⁴Due to noise the two values will rarely be exactly equal; the identification of either m_o or $m_o + 1$ as the position of the maximum is then determined by chance.

we would use the covariances in m_o-1 , m_o and m_o+1 we find $\hat{\epsilon}_C < \frac{1}{2}$, while for m_o , m_o+1 and m_o+2 we find $\hat{\epsilon}_C > \frac{1}{2}$. This discontinuity does not appear in the peak-fit estimators.

In order to characterize the overall tracking performance of the fractional displacement estimators we now compute the rms tracking error, given by

$$\langle \hat{\epsilon}_b^2 \rangle = \int_{-1/2}^{1/2} (\hat{\epsilon} - \epsilon)^2 d\epsilon. \tag{3.107}$$

The results of (3.107) for $\hat{\epsilon}_C$, $\hat{\epsilon}_P$ and $\hat{\epsilon}_G$ are plotted in Figure 3.17 as function of a_1 . Note that $\langle \hat{\epsilon}_b^2 \rangle$ is constant is constant for the Gaussian peak-fit estimator, which reflects our earlier observation that the tracking error for $\hat{\epsilon}_G$ is independent from the model parameter in (3.103). This figure confirms the observation in Fig. 3.16 that the tracking error of $\hat{\epsilon}_G$ is a lower bound for the tracking errors of $\hat{\epsilon}_C$ for $a_1 \rightarrow 0$ and of $\hat{\epsilon}_P$ for $a_1 \rightarrow 1$. It is

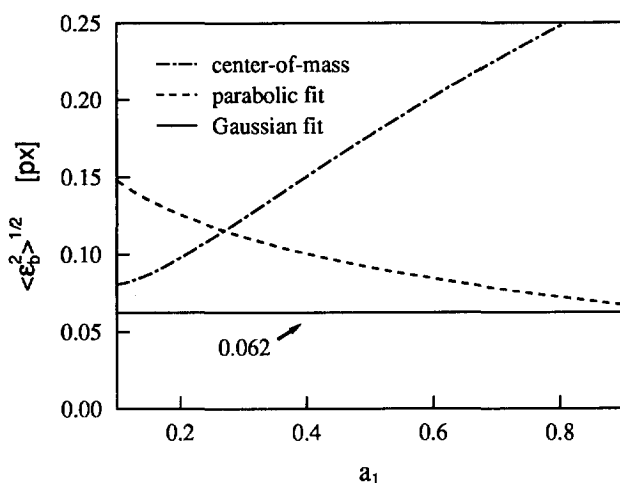


Figure 3.17: The rms tracking error $\langle \epsilon_b \rangle^{1/2}$ as function of the model parameter a_1 for three different fractional displacement estimators. The parameter a_1 is proportional to the width of the displacement correlation peak; see Eq. (3.74).

emphasized here that we deliberately used a model for the image covariance that is not Gaussian; see Eq. (3.103). Therefore it is quite possible that in reality the rms tracking error for $\hat{\epsilon}_G$ is smaller 0.06 px.

3.10 Experimental verification

In order to verify the analytical results from the previous sections a test experiment was carried out. In this experiment the measured displacement of a uniformly translated test object was compared with the actual displacement. From the results were determined the average and rms fluctuating displacements as function of the actual displacement. Also the effect of different weight kernels was tested.

3.10.1 experimental set-up

The optical arrangement in this test was similar to the schematic set-up shown in Fig. 2.5. In the object plane was put a test object that was mounted on a traversing stage, by which the test object could be accurately translated. In this way we could simulate uniform displacements along a given direction and over a given distance. The position of the test object was measured with a dial gauge, which had a smallest scale unit of $10\ \mu\text{m}$. The test object consisted of a photograph taken from a seeded flow with a known number density and particle size. The object area was illuminated with white light from a 60 W incandescent lamp. Because a fixed test object was used we have $F_O(D_Z \equiv 0) = 1$.

The object was observed by a CCD video camera (High Technology Holland - MX). The camera sensor (Philips NXA1011 frame transfer sensor) has an (effective) resolution of 604 (horizontal) by 576 (vertical) elements. The image area is 6.0 mm (horizontal) by 4.5 mm (vertical). The camera was equipped with a 28 mm focal length lens, with an aperture of $f/D=2$. The video signal from the camera was directly digitized by a high resolution frame grabber (Data Translation 2851) to a 512×512 -pixel, 8-bit digital image. The sample rate of the digitizer was not synchronized with the pixel clock of the camera. As a result the aspect ratio of a pixel in the digital image differs from that of a pixel in the camera sensor. The digital image consisted of rectangular pixels with an aspect ratio of 1.44. The equivalent area of the image in the object plane was $13.0 \times 9.1\ \text{cm}^2$. The image magnification was equal to 0.044.

A set of eight single-exposure frames were recorded at different positions of the test object over a displacement range of 1 mm in the direction perpendicular to the camera scan-lines. The frame recorded with the object in its initial position is referred to as the *reference* image. In the end, the object was repositioned at the initial position according to the dial gauge reading, and a second reference image was recorded. This would enable us to verify the reading and positioning errors of the translation stage. By shifting the reference image digitally, translations over a distances greater than 1 mm could be "simulated". The reference image and a digitally shifted pairing image were also used to examine the expectation and variance of the estimated cross-covariance and fractional displacement estimators for the case of a displacement of exactly an *integer* number of pixels. For this purpose the reference image was shifted over 6 px; for a 32×32 -pixel interrogation area a displacement of 6 px is approximately halfway the largest and smallest attainable absolute displacements. Thus, in total thirteen translated frames plus two reference frames we used for the image analysis. In Table 3.3 are listed the corresponding displacements.

Table 3.3: Positions of the test object for the recorded images, relative to the reference image (i.e. the image of the test object in its initial position). Frames 9–13 are “simulated” by shifting the digitized reference image.

frame	position		frame	position	
	mm	px		mm	px
1	0.05	0.28	8	1.00	5.65
2	0.10	0.57	9	–	7.13
3	0.15	0.85	10	–	8.26
4	0.20	1.13	11	–	9.39
5	0.40	2.26	12	–	10.52
6	0.60	3.39	13	–	11.65
7	0.80	4.52	(0)	0.00	0.00

The image contained a total of 3642 particle images of different intensities, with a particle-image diameter of 4.4 px (in the direction perpendicular to the scan-lines of the CCD sensor). In Table 3.4 an overview is given of the relevant statistical properties of the digital images and the model parameters a and a_1 .

Table 3.4: Relevant properties and related model parameters of the digital test images.

<i>grey value</i>			
– mean	\bar{I}	30.6	
– standard deviation	σ_I	34.7	
<i>particle-images</i>			
– image density	N_I	14.2	
– diameter	d_t	4.4	px
<i>model parameters</i>			
– global	a	0.592	
– local	a_1	0.813	

image analysis

For the analysis the images were sub-divided into 32×32 -pixel non-overlapping interrogation images. Corresponding sub-images in the translated image and reference image were analyzed by computation of the cross-covariance. The analysis was carried out with and without the correction for the displacement bias given in Eq. (3.87). Because there was no overlap between adjacent interrogation images, each pair of images yielded 256 sta-

tistically independent displacement vectors. Given the total number of particle-images, the average number of particle images in a 32×32 -pixel sub-image was equal to 14.2. This value is in accordance with the recommendation by Keane & Adrian (1990) for a valid-data yield of at least 95%. All measured integer displacements that deviated more than one pixel from the expected displacement were considered as spurious vectors due to insufficient particles image pairs, and were discarded from the data set. Such a strict test for spurious data can only be done if one has exact *a priori* knowledge of the displacement. From the remaining data were computed the displacement mean and standard deviation.

First, the observed mean and variance of the estimated cross-covariance and fractional displacement estimators for an integer displacement were determined for comparison with the analytically predicted results. Since only one test object was available, it was not possible to investigate the behaviour of the fractional displacement estimators as function of the particle-image diameter (viz., a_1). However, the main purpose of this experiment was to verify the predicted behaviour of the expected mean and rms displacements as function of the actual displacement. We have seen in Sect. 3.9 that the (qualitative) behaviour was mainly determined by the choice of the weight kernel. Here we tested the effect of the three different weight kernels: the 32×32 -pixel uniform and Gaussian weight kernels, and the 16×16 -pixel uniform weight kernel (with zero-padding).

Table 3.5: Results of the test measurements and analytical predictions for the mean and covariances of the estimated cross-covariances. The expectation values are normalized with respect to σ_f^2 (i.e. the variance of the image intensity), and the (co)variances with respect to σ_f^4/N^2 (with $N=32$).

	obs.	pred.		obs.	pred.
$E\{\hat{R}_0\}$	0.807	0.813	$\text{var}\{\hat{R}_0\}$	9.12	8.65
$E\{\hat{R}_{-1}\}$	0.748	0.686	$\text{var}\{\hat{R}_{-1}\}$	8.77	7.68
$E\{\hat{R}_{+1}\}$	0.706	0.635	$\text{var}\{\hat{R}_{+1}\}$	8.82	7.68
			$\text{cov}\{\hat{R}_{-1}, \hat{R}_{+1}\}$	7.37	7.68

3.10.2 results

We will first discuss the result of the cross-correlation analysis of the initial and the second reference image. The measured displacement between these two images was equal to (0.0013 ± 0.0013) mm (95% reliability interval). From this result we conclude that the reading and positioning errors are negligible with respect to the displacement.

The averages and (co)variances of \hat{R}_{-1} , \hat{R}_0 and \hat{R}_{+1} were determined from the analysis of the reference image and its pairing image that was shifted over 6 px. The results are given in Table 3.5. The values for the averages and (co)variances predicted according to Eqs. (3.30) and (3.37-3.38) for the model in (3.54) and the image parameters in Table 3.4

are also given in Table 3.5. The observed and predicted values agree within 10%. This may be attributed to the fact that the model for the covariance in (3.54) is somewhat coarse. The observed variances are systematically larger than the predicted values. However, note the close agreement of the observed and predicted values for $\text{cov}\{\hat{R}_{-1}, \hat{R}_{+1}\}$. This seems to support our earlier conjecture that in a practical situation white random noise mainly contributes to the variances of \hat{R}_m , while it leaves the covariance unaffected (see Sect. 3.9.2).

The image pair was analyzed with and without the bias correction proposed in (3.87). The results for the mean displacement for the three fractional displacement estimators taken over the entire image pair are given in Table 3.6. This table shows that the estimation of the fractional displacement *without* the bias correction yields a significant deviation from the actual mean displacement between 0.4 and 1.7%. If we apply the bias correction then the observed differences with the actual mean displacement are less than 0.05%, which is within the (estimated) reliability interval.

Table 3.6: Results for the mean displacement with (estimated) 95% reliability interval obtained from the reference image and its pairing image shifted over 6 px. The analysis was carried out for three different fractional displacement estimators, and with and without the bias correction in Eq. (3.87).

	without corr.	with corr.	rel. int. (95%)
$\hat{\epsilon}_C$	5.975	5.999	± 0.004
$\hat{\epsilon}_P$	5.917	5.998	± 0.005
$\hat{\epsilon}_G$	5.908	5.997	± 0.013

The *observed* variances and covariance of \hat{R}_{-1} and \hat{R}_{+1} given in Table 3.5 were used to determine the value of the constant K :

$$K = \frac{\text{var}\{\hat{R}_{-1}\} + \text{var}\{\hat{R}_{+1}\}}{2\text{cov}\{\hat{R}_{-1}, \hat{R}_{+1}\}} - 1 \tag{3.108}$$

cf. (3.92), which yields $K = 0.19$. This value will be used to predict the rms value of the estimated fractional displacement that will be discussed below.

Let us turn to the means and variances of the estimated fractional displacements. In Table 3.7 are given the partial derivatives for the center-of-mass, the parabolic peak-fit and Gaussian peak-fit estimators computed according to (3.98) with a_1 given in Table 3.4. If we multiply these numbers with the balance term given by (3.100) for $m_o = 6$ and $K = 0.19$, and with the variance term given by (3.101) (see also Table 3.5) we obtain the analytical predictions for the variance of the estimated fractional displacement. In Table 3.7 are given the standard deviations (viz. $\text{var}\{\hat{\epsilon}\}^{1/2}$) for the three fractional displacement

Table 3.7: Results of the analytical predictions and test measurements for the variance of the estimated fractional displacement for an integer displacement of 6 px. Also shown here are the partial derivative, balance and variance terms. (The term σ_I is omitted in the partial derivatives and variance terms.)

	partial derivative	balance term	variance term 10^{-3}	$\text{var}\{\hat{\epsilon}\}^{1/2}$	
				pred. px	obs. px
$\hat{\epsilon}_G$	0.145	0.596	7.12	0.025	0.021
$\hat{\epsilon}_P$	1.787	0.596	7.12	0.087	0.088
$\hat{\epsilon}_C$	2.206	0.596	7.12	0.097	0.094

estimators. Compare the predicted and observed values, which agree very well. This demonstrates that the analysis of the statistical properties of the fractional-displacement estimators in Sect. 3.9, for given values of R_{-1} , R_0 and R_{+1} , yields a correct prediction of the accuracy of the three fractional displacement estimators discussed in this thesis. The results also show that the displacement can be measured with an absolute accuracy that is better than 0.1 pixel (rms value). This implies that at low pixel resolution, say 32×32 pixels, the relative accuracy for a nominal displacement of $1/4$ of the interrogation-image diameter (i.e. 8 px) is about 1%.

The set of displaced images was used to investigate the mean and rms differences between the measured and actual displacements as function of the actual displacement. We only used the data that were obtained with the Gaussian peak-fit estimator (remember that we saw in Sect. 3.9 that the performance as function of the displacement is determined by the weight kernel, and not by the fractional displacement estimator). As was already explained in the previous paragraph, the images were analyzed with and without the bias correction in (3.87) and for three different weight kernels. The results are shown in Figure 3.18 as function of the displacement. The error bars represent the estimated 95% reliability intervals, based on the sample variance. The solid lines represent the displacement bias predicted by Eq. (3.82). From these results we conclude that the prediction for the displacement bias agrees very well with those observed in the experimental data. We can also see that the correction proposed in Eq. (3.87) adequately compensates for this bias. It should be emphasized here again that the correction is applied to the estimated (cross-)covariance, *prior* to estimation of the fractional displacement. In Fig. 3.18 are also given the rms differences between the measured and actual displacements. The rms difference for the uniform weight kernel is approximately constant over the displacement range. The dash-dotted lines in Fig. 3.18 are the predicted behaviour for the rms displacement error (viz., $\text{var}\{\hat{\epsilon}\}^{1/2}$) according to Eq. (3.93). For both the 32×32 -pixel and 16×16 -pixel uniform weight kernels the predicted behaviour agrees fairly well with the measured behaviour. On the other hand, for the Gaussian kernel the rms difference seems directly proportional to the displacement. This is *not* in correspondence with the pre-

dicted behaviour in (3.100). In fact, it appears as if the rms difference behaves according to the balance term for a noise-free system (i.e. $K = 0$), although the magnitude of the rms differences suggests that we have $K > 0$. This requires further investigation. Anyway, for the same test object the Gaussian kernel yields more accurate results than the uniform kernel. Suppose that the rms differences for the Gaussian kernel are indeed proportional to the displacement (thus the relative accuracy of the measured displacement is constant), then a linear fit to the rms differences in Fig. 3.18b yields a relative measurement error of the displacement in this experiment that is better than 1% (rms value)!

The results presented in Fig. 3.18 were found after first discarding spurious data. In Figure 3.19 is given the fraction of valid data as function of the displacement for the three different weight kernels. Note that the valid-data yield for the 16×16 -pixel zero-padded uniform kernel drops very rapidly. This is not surprising because in this case the effective image density (viz., the expected number of particle-images per interrogation region) is 3.6; only 1/4 of the image density for the 32×32 -pixel uniform kernel. This value is too low to expect a high valid-data yield. The 32×32 -pixel uniform and Gaussian kernels on the other hand have a valid-data yield that is very close to one over a wide displacement range. We have seen in the previous paragraph that the Gaussian weight kernel yields a more accurate estimate of the displacement than the uniform weight kernel. On the other hand, in Fig. 3.19 we find that the Gaussian weight kernel has a lower valid-data yield than the uniform weight kernel (for displacements that are larger than 9 px). So, the uniform weight kernel is more *robust* than the Gaussian weight kernel. This can be interpreted in terms of a difference in the *effective* number of particle-image pairs as function of the displacement, i.e. $N_I F_O(D_Z) F_I(m, n)$ given by (3.52). The lines in Fig. 3.19 represent the valid-data yield predicted by the model proposed in (3.53). Initially this model failed to predict the behaviour of the valid-data yield for the 16×16 -pixel uniform kernel, given an image density of 14.2 (see Table 3.4). The model in (3.53) was fitted to the observed valid-data yield for the 16×16 -pixel uniform kernel, with N_I as a free parameter. A good agreement was found when the original image density ($N_I = 14.2$) was multiplied by 0.7; see Fig. 3.19. In order to make an optimal design for a PIV experiment it is important to have a reliable model to predict the valid-data yield as function of the image density, the displacement and the weight kernel (see Chapter 4). Hence, further investigation is required to improve the model proposed in (3.53).

In Figure 3.20 the present result for the rms differences between the actual and observed displacements for the case of a 32×32 uniform weight kernel are compared with similar test experiments carried out by Willert & Gharib (1991) and Lourenço (1993). Willert & Gharib (1991) performed tests with artificially generated PIV images at various image densities, ranging from $N_I = 6$ to 74. They recorded and analyzed pairs of single-exposure images. They analyzed these images with the Gaussian peak-fit estimator and with a uniform weight kernel. In Fig. 3.20 are shown their data for $N_I = 11$, which is close to the image density in the present test. Lourenço (1993) carried out tests for multiple-exposure images (no quotations were made of the used image density, particle-

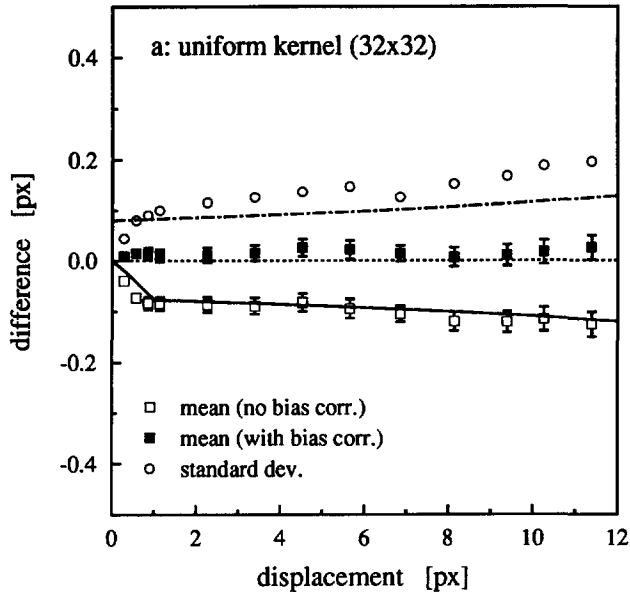
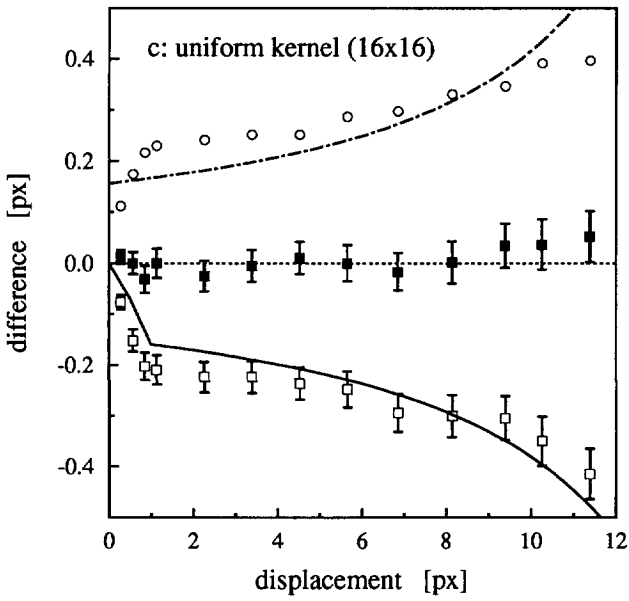
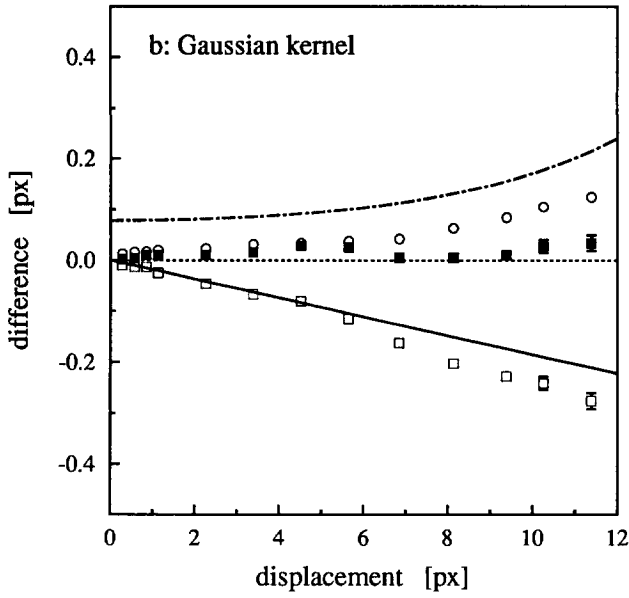


Figure 3.18: The mean (with and without bias correction) and rms differences between the actual and measured displacement as function of the displacement in pixels for the 32×32 uniform (a) and Gaussian (b), and 16×16 uniform (c) weight kernels. The lines represent the analytical predictions for the uncorrected mean (solid line) and rms (dash-dotted line) differences; see text.

image diameter, weight kernel and fractional-displacement estimator). In Fig. 3.20 are plotted his results for the double-exposure images. If we compare the results in Fig. 3.20 then we see that all three tests show the same qualitative behaviour, i.e. the rms measurement error changes very little over a considerable range of displacement. The differences in magnitude can be attributed to differences in the particle-image diameter; in the present tests we used a fairly large particle-image diameter (i.e. 4.4 px). So it seems that Willert & Gharib (1991) and Lourenço (1993) must have had smaller particle-image diameters. That implies that the accuracy of about 0.1 px found in the present test can be further improved by minimizing the particle-image diameter. However, it is remarkable that although both Willert & Gharib (1991) and Lourenço (1993) claim a measurement accuracy that is better than 0.1 px, neither of them report the bias found in the present results.



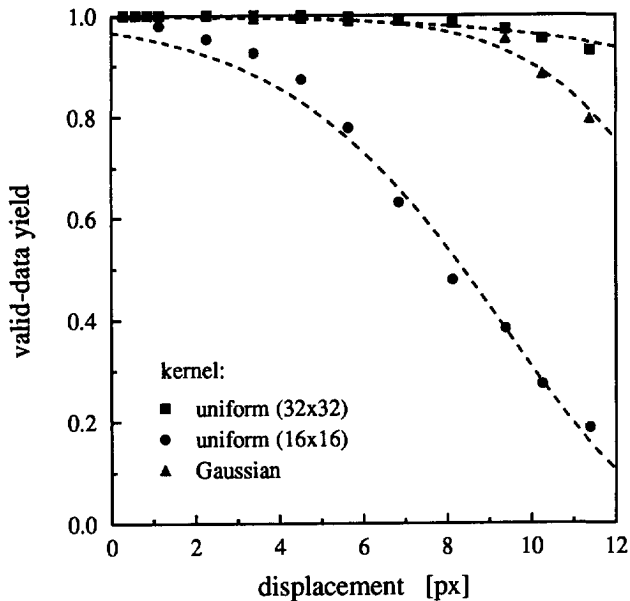


Figure 3.19: The fraction of valid displacement vectors for the data obtained in the test measurement as function of the displacement, for three different weight kernels. The dashed lines represent the predicted data yield according to (3.53)

3.11 Summary and conclusions

In this chapter we investigated the statistical properties and the analysis of digital PIV images. In this final section of this chapter a summary is given of the main conclusions of the preceding sections.

- It was shown that the digital images are unbiased estimates of the continuous images discussed in Chapter 2. Provided that the observed flow is incompressible and seeded homogeneously with ideal tracer particles, the digital PIV image can then be described in terms of a homogeneous, negative-exponential random field. This result was verified experimentally; see Fig. 3.2.
- One of the most important issues in digital image processing is the (minimum) required sampling rate of the continuous image field. We have seen that the PIV image is bandlimited by the finite aperture of the imaging lens. In general a high

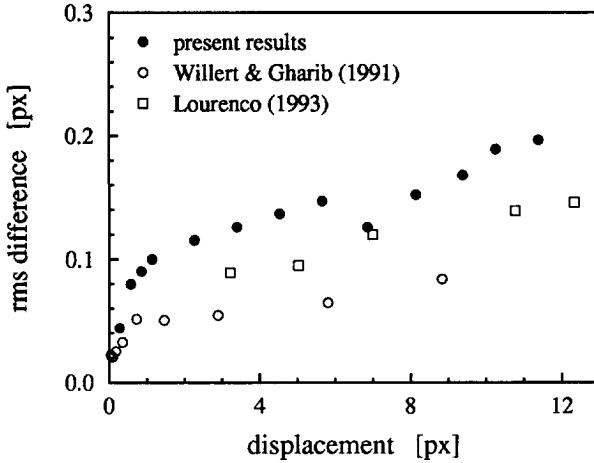


Figure 3.20: The rms measurement error as function of the displacement for uniformly translated test objects obtained by Willert & Gharib (1991) and Lourenço (1993) in comparison with the present results; see text.

sampling rate is necessary to resolve the optical bandwidth. In a practical situation this would correspond to a minimum resolution of 256×256 px/mm².

However, the measurement of the particle-image displacement does not require an exact reconstruction of the PIV image. So, there is no essential need to resolve the optical bandwidth. Instead, the bandwidth of the image spectral density, following Parzen's definition, is considered to give a more feasible measure for the required sampling rate. This yields a value that is about 1/4 of the optical bandwidth. In practice a resolution of 32×32 px/mm² or 64×64 px/mm² for the interrogation analysis is already sufficient. In fact, a resolution of 256×256 px/mm² that is conventionally used in OPIV oversamples the PIV image. This conclusion is confirmed by evaluation of the integral length scale of the estimated displacement-correlation peak as function of the pixel resolution; for a resolution of more than 64×64 px/mm² the number of independent samples that contribute to the variance of the estimate remains practically constant.

In the optimal situation, i.e. for a resolution that matches the Parzen bandwidth, the particle-images are about the size of a pixel ($d_t/\Delta \sim 1$; see Table 3.1).

- We introduced a spatial-average estimator for the image cross-covariance. The estimator can be computed efficiently by the fast Fourier transform (FFT) algorithm. (This subject is discussed separately in Appendix B.2.) For small particle images that are distributed homogeneously over the image (with zero background intensity) zero-padding and windowing of the interrogation image are not necessarily required.

The statistical properties of the estimator, based on a $N \times N$ -pixel interrogation image, were expressed in terms of the ensemble statistics of digital PIV images. Like its one-dimensional counterpart, the estimator appears to be asymptotically unbiased for $N \rightarrow \infty$. For a finite value of N the displacement-correlation peak is skewed towards the origin. This is the cause of a (small) bias in the estimated centroid of the displacement-correlation peak; see below.

- The particle-image displacement is given by the centroid of the displacement-correlation peak. This peak or "signal" is identified as the maximum of the (estimated) image cross-covariance. The amplitude of this "signal" with respect to the background noise (viz., the random correlation peaks) depends on the image density and the magnitudes of the in-plane and out-of-plane particle displacements, represented by F_I and F_O respectively. There is a finite probability that one of the noise peaks is higher than the signal peak. In that case we say that we have a *spurious* measurement of the displacement. The commonly accepted idea is that at least four or five particle-images are required to obtain an unambiguous (viz., valid) measurement of the displacement. A simple model, based on Poisson statistics, was proposed to predict the valid data yield as function of the displacement. The predictions from this model compared quite well with the observed valid-data yield in a test measurement.
- The maximum of the image cross-covariance yields only a rough estimate of the particle-image displacement (with a resolution of 1 px). By interpolation of the covariances near the peak maximum we obtain the location of the displacement-correlation peak at sub-pixel level, denoted as the fractional displacement. At low pixel resolution only the four-connected neighbourhood contains significant information. Hence the fractional displacement along each in orthogonal direction is estimated from only three points. We have investigated the statistics of three different interpolation methods, namely the center-of-mass estimator, the parabolic peak-fit estimator and the Gaussian peak-fit estimator.
- The skewness of the estimated cross-covariance is the cause of a small bias in the expected displacement towards the origin (i.e. zero displacement). The behaviour of the bias as function of the displacement is determined by the type of weight kernel. This kernel puts a different weight to each pixel in the interrogation image. Two types of kernels were introduced: a uniform kernel (all pixels contribute to the estimate by an equal amount) and a Gaussian kernel (the contribution of the pixels to the estimates gradually reduces towards the edges of the interrogation area). For a uniform weight kernel the bias is approximately constant up to 1/3 of the diameter of the interrogation image, while for a Gaussian weight kernel the bias is directly proportional to the displacement. A linear dependence of a bias as function of the displacement for a Gaussian weight kernel was reported by Keane & Adrian (1990) for the case of a continuous PIV image. The bias associated with the uniform weight kernel was not reported before. In a practical situation this bias is about 0.06 px

for a 32×32 pixel interrogation area. Though small, it significantly contributes to the measurement error at low pixel resolution where the random error is found to be about 0.08 px. Markedly, this bias was *not* reported by others that claim accurate measurement of displacement at low pixel resolution (Willert & Gharib 1991; Lourenço 1993). Adrian (1988) relates the magnitude of a displacement bias to the velocity gradient over the interrogation area; an interrogation area of given size can contain a higher number of particle-image pairs with a small displacement than pairs with a large displacement, which biases the measured displacement towards a value that is lower than the actual local mean displacement. Following this line of thought one would *not* expect to find a displacement bias for a uniform displacement. However, the present analysis revealed that the magnitude of the bias is directly determined by the width of the displacement-correlation peak with respect to the width of F_I . The width of this peak is not only determined by the particle-image size, but also by the variation of the displacement field over the interrogation area, for example due to a velocity gradient over the interrogation area or due to unresolved motion at scales smaller than the size of the interrogation area; see Sect. 2.4). Hence, we have given a more general explanation for the occurrence of a bias in the measured displacement.

The bias can be easily compensated for by dividing the covariance values with the in-plane loss-of-pairs function prior to the estimation of the fractional displacement; see (3.87). The elegance of this correction procedure is that it is non-parametric; it does not require any *a priori* knowledge of the particle-image size or local variation of the displacement field.

- The analysis pointed out that the random estimation error of the three-point fractional-displacement estimators can be expressed as the product of three terms, namely: one term that reflects the sensitivity of the estimator (*partial-derivative term*), one term that depends on the detailed balance between the two outer covariances (*balance term*) and one term that is determined by the bandwidth of the PIV image with respect to the sampling rate (*variance term*). The relative differences between the three estimators considered here are only determined by the partial derivative term. The balance term is determined by the size and shape of the weight kernel.
- The peak-fit estimators yield accurate results for *sharp* peaks, whereas the center-of-mass estimator is quite insensitive to the shape of the peak. It appeared that the peak-fit estimators perform optimally if the particle-images are approximately one pixel in diameter ($d_i/\Delta \sim 1$). If we only consider displacements that are exactly an integer number of pixel units then the center-of-mass estimator at high pixel resolution has the lowest absolute estimation error; see Fig. 3.15. However, the (three-point) center-of-mass estimator is strongly biased towards integer values of the displacement in pixel units, and it has a discontinuous behaviour for fractional displacements of $\pm \frac{1}{2}$ (i.e. displacement that lie exactly in the middle of two integer pixel values). As a result we have a tracking error of more than 0.2 px; see Figs. 3.16–3.17. This discontinuity can lead to large errors in the computation of flow quantities

that require the differentiation of the displacement (viz., velocity); see Chapter 5. At high pixel resolution this error is small in view of the nominal displacement (less than 1%), but it becomes relatively large at low pixel resolution (more than 4%). This makes the center-of-mass estimator unsuited for estimation of the displacement at low pixel resolution. This result corresponds to the conclusion by Prasad *et al.* (1992) who carried out test measurements to assess the measurement accuracy for a center-of-mass estimator as function of the pixel resolution.

On the other hand, the peak fit estimators can resolve the fractional displacement much better than the center-of-mass estimator, and are therefore better suited to estimate the displacement at low pixel resolution. The Gaussian peak-fit estimator has a random error that is somewhat larger than that of the parabolic peak-fit estimator, but has a much smaller bias error. We therefore conclude that the Gaussian peak-fit estimator has the best performance for estimating the particle-image displacement at low pixel resolution.

- Predictions from the theoretical analysis were compared with the observed values in a simple test experiment. The agreement between the observed and predicted values for the mean random error is fairly good. However, it was necessary to introduce an empirical constant $K > 0$ in the balance term of (3.93) to obtain a quantitative agreement of the predicted and observed rms error. The constant K accounts for a "unbalance" between the (co)variances of $\hat{R}_{\pm 1}$ (in addition to the effect due to the in-plane loss-of-pairs function F_I ; see Sect. 3.9.1). This additional unbalance may be due to the fact that in our analytical model the summations in Eqs. (3.34–3.38) were extended to infinity, while actually the summations include only a finite number of terms (proportional to $N \times N$). In our test experiment the particle-image diameter ($d_i/\Delta = 4.4$) was small in comparison with the size of the interrogation area ($N = 32$); under this condition Eq. (3.37) is a good approximation of Eq. (3.34)⁵. Therefore it is believed that the additional unbalance is most likely due to the presence of additional (instrumental) noise; white noise would affect the variances, but not the covariances. This line of thought is confirmed by the experimental results in Table 3.5. In future work, additional noise can be accounted for by including the noise statistics in the model for the image covariance (see Sect. 3.7). Hence, the derived relation between the statistics of the estimated and actual image covariance remains unchanged. Further research on this topic is required.

Now, suppose this future work would enable us to predict the value of K . Then, through Eq. (3.93), it would perhaps also be possible to obtain reliability estimate of the measured displacement (i.e. without recourse to a comparison with measured displacements from neighbouring interrogation positions in a post-interrogation pro-

⁵A preliminary evaluation indicated that the difference between the results given by the exact expression in (3.34) and the approximation in (3.37) alone cannot account for the value of K found in the test experiments.

cedure; see Chapter 4). This would provide an alternative to the peak *detectability*⁶, which is commonly used to assess the reliability of the measured value of the displacement.

- The behaviour of the accuracy as function of the displacement that was found in the test measurement showed that it has the same character as the displacement bias: the error is practically constant for a uniform weight kernel, while it is directly proportional to the displacement for a Gaussian weight kernel. This implies that below a certain displacement the estimate obtained from the Gaussian weight kernel yields more accurate results than those obtained with the uniform weight function. It would be interesting to investigate this further in more detail; perhaps it is possible to find an *optimal* weight kernel for a given experiment, that is designed with respect to *a priori* knowledge of the observed flow field.
- The test measurements demonstrated that displacement measurements at low pixel resolution could be made with an accuracy that is better than 0.1 px. Suppose we have a mean displacement with a nominal value of 8 px, then measurements of the displacement with a relative accuracy that is better than 2% seem feasible. Our analytical and experimental results are in qualitative agreement with the experimental results obtained by Willert & Gharib (1991) at corresponding image density, and those obtained by Lourenço (1993). The quantitative differences between these experimental results can be ascribed to differences in particle-image diameter. (Again it is emphasized that both Willert & Gharib and Lourenço did not report the occurrence of a displacement bias, despite the fact that they claim an accuracy that is better than the present results.)

Willert & Gharib (1991) found that the accuracy of the estimated (uniform) displacement decreases with increasing image density. At first sight, this seems a feasible result; the more particle-image pairs per interrogation area the more accurate result for the estimated displacement. Yet, this conclusion is *not* confirmed by the present analytical results. How is this possible? Let us have a closer look at the role of the image density in our analysis.

The present analytical results show that the accuracy of estimating the peak centroid is *independent* of the image contrast, i.e. σ_I , which is the only term that depends on the image density. One should realize that σ_I does not only depend on the image density, but also on the intensity of the incident light sheet, the conversion of light into charge in the CCD, and the gain of the analog-to-digital converter in the frame grabber. So, we can always create a situation with the same value for σ_I but with different values of the image density, simply by adjusting the light intensity or the electronic gain. Now, *if* the accuracy would depend on σ_I *then* a simple rescaling, e.g. by changing the electronic gain, would yield a higher value of accuracy. This is rather odd, because the relative differences between the signal and

⁶The *detectability* is defined as the ratio of the maximum of the displacement-correlation peak and the maximum of the highest random correlation peak; see also Chapter 4.

noise peaks did not change⁷. This demonstrates that the estimation *accuracy* of the peak centroid does not depend on σ_I (viz., the image density). However, note that in our analytical model we assumed that the displacement-correlation peak has already been identified correctly (i.e. we are always dealing with a *valid* displacement). The *probability* to identify the valid displacement-correlation peak among the random-correlation peaks is proportional to the image density. Once we have identified the proper correlation peak, the estimation of its centroid only depends on its shape and diameter. Hence, the *probability* to find a valid displacement is determined by the image density, while the *accuracy* of the measured (valid) displacement depends only on the particle-image diameter. Alternatively, one may say for a *uniform* displacement that each particle-image pair that is added to the pairs already inside an interrogation area does *not* contribute to the information on the displacement, but only reduces the uncertainty with regard to the most probable displacement.

So, in the case of a uniform displacement the estimation accuracy does not depend on the number of particle images, given that the displacement-correlation peak is detected correctly. Then why did Willert & Gharib find a relation with the image density? A possible explanation is given below.

Willert & Gharib (1991) did not subtracted the mean image intensity prior to estimation of the image covariance, in correspondence to the covariance estimator investigated by Adrian (1988). As a result the correlation peaks are superimposed on a background level. This changes the relative differences between the estimated covariances that are used for estimating the fractional displacement (some thought shows that an increase in the background level affects the value of the parameter K ; as a result the rms random error depends on the mean background level, viz., image density).

To conclude this chapter, the following remarks should be made. The analytical investigation in this chapter has demonstrated that an interrogation analysis with a resolution that is substantially lower than used conventionally can yield in principle results with comparable accuracy. However, further research is required to improve the analytical model for the image covariance. The most important achievement of the results in this chapter is that we can now investigate and comprehend the behaviour of various (three-point) estimators and weight kernels analytically. This replaces the rather laborious empirical approach that was commonly employed in the past.

⁷A rescaling does not enhance the information content of the signal.

Chapter 4

Data Validation: Detection of Spurious Vectors¹

Abstract. *A statistical model is introduced that describes the occurrence of spurious vectors in PIV data. This model is used to investigate the performance of three different post-interrogation procedures: the global-mean, the local-mean and the local-median test. The model was also used to optimize the performance of these procedures. Predicted performances agree very well with those obtained from an artificially generated PIV record. It is demonstrated that the “detectability” as the conventional measure for the reliability of a measured displacement vector is very inefficient, compared to the three tests mentioned here. The local-median test has the highest efficiency.*

4.1 Introduction

In Particle Image Velocimetry (PIV) we often find that measurements results contain a number of “spurious” vectors, like e.g. in Figure 4.1. These vectors deviate unphysically in magnitude and direction from nearby “valid” vectors, and in general originate from interrogation spots that contain insufficient particle-image pairs. In practice the number of spurious vectors in a PIV data set is relatively low (typically less than 5%). However, their occurrence is more or less inevitable: Even in carefully designed experiments there remains a finite probability that an interrogation yields a spurious vector.

Generally, PIV measurement data are subject to a post-interrogation procedure in which spurious vectors are identified and subsequently discarded from the data set. It would be ideal to have a measure of reliability for each displacement vector that is directly obtained from the auto-correlation function of the interrogation spot itself, like e.g. the “detectability” D_0 (Keane & Adrian 1990). In practice it appears that these reliability estimates are not very robust (this will be demonstrated later on). Instead, each displacement vector is compared with nearby vectors and those that have an “unacceptably” large

¹WESTERWEEL, J. Efficient detection of spurious vectors in particle image velocimetry data. Accepted for publication in: *Exp. Fluids*.

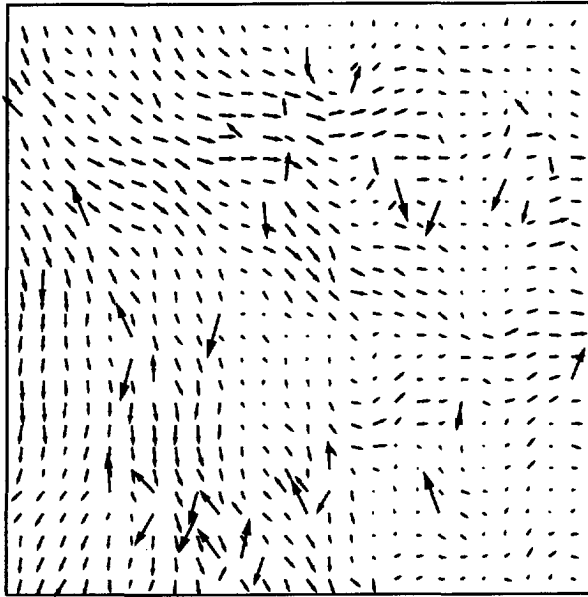


Figure 4.1: Arbitrary example of a PIV measurement result containing spurious displacement vectors.

deviation are labeled as “spurious”.

In a visual representation of a PIV data set (e.g. like in Figure 4.1) spurious vectors can be easily recognized as mismatches in the observed pattern. However, visual inspection of PIV measurement data is tedious and subjective, and therefore not reproducible and not optimal. A visual approach will certainly fail for large quantities of PIV data; The human operator will soon become fatigued and will become indifferent with respect to performing his task. This brings up the need for a purely statistical approach for the post-processing of PIV data. This does not only provide objective means to evaluate the data, but would also provide a basis for the development of automated procedures that are robust and optimally efficient. Although most authors report that they use some kind of statistical method to evaluate their PIV measurement data in a post-interrogation procedure, an account of the details of the procedure is rarely given. In this chapter first a statistical model is introduced that describes the occurrence of spurious data in PIV measurements. This model is subsequently employed to investigate the performance of three different tests for post-interrogation evaluation. Finally predictions from the model are tested against the results obtained from an artificially generated PIV image.

This chapter is dedicated to the statistical evaluation of PIV measurement data that is

contaminated with spurious data. The occurrence of spurious data—also called outliers—in measurement data is found in almost every field of experimental research. There is a variety of evaluation methods and statistical tests for the detection of outliers in statistical data (Barnett & Lewis 1979). The methods presented in this chapter were—in part—adapted from statistical consistency tests that have been applied successfully in neutron scattering experiments (Fredrikze 1985; Westerweel 1987). Similar procedures are also used in digital image processing to filter out binary noise (Jain 1989). To certain extent the contents of this chapter could be generalized to include also signals from other sources.

4.2 The PIV signal

We first give a more exact definition of what is called “valid” and “spurious”, instead of the qualitative definition given in the Introduction. Subsequently we will introduce a stochastic model of a PIV “signal” contaminated with spurious data. It is emphasized that we are not looking for a mathematically exact description of this signal, but merely a convenient model that allows us to examine different post-interrogation procedures.

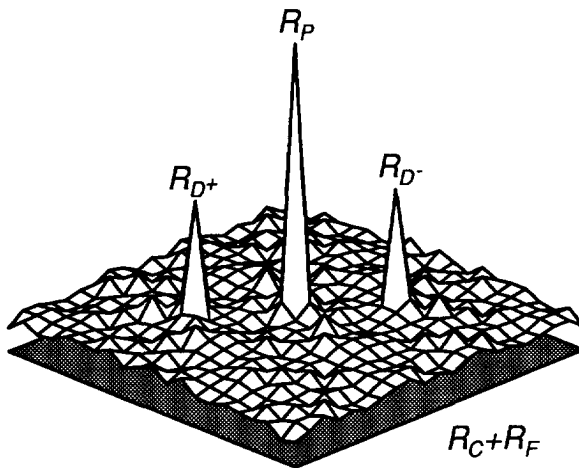


Figure 4.2: Typical example of the spatial auto-correlation function $R(\vec{s})$ of an interrogation spot in a double-exposure PIV record. The function $R(\vec{s})$ consists of five terms (see text): $R_P + R_{D+} + R_{D-} + R_F + R_C$ (Adrian 1988).

Today the most common method to analyze a PIV record is by computation of the spatial auto-correlation function $R(\vec{s})$ in a small interrogation spot (either directly or from its optically Fourier-transformed image). Figure 4.2 shows a typical example of $R(\vec{s})$ for a

double-exposure PIV record. Adrian (1988) showed that $R(\vec{s})$ can be separated into five terms, i.e. the particle-image self-correlation peak $R_P(\vec{s})$, the displacement correlation peaks $R_{D+}(\vec{s})$ and $R_{D-}(\vec{s})$, and a noise term $R_F(\vec{s})$ due to random particle correlations, superimposed on the mean background correlation $R_C(\vec{s})$. The two displacement peaks $R_{D+}(\vec{s})$ and $R_{D-}(\vec{s})$ are located on opposite sides of $R_P(\vec{s})$.

The particle-image displacement is taken equal to the centroid of the highest non-central peak of $R(\vec{s})$. When this peak corresponds to $R_{D+}(\vec{s})$ (or $R_{D-}(\vec{s})$) a valid estimate of the particle-image displacement is obtained. Otherwise, the peak that was detected is part of the noise term $R_F(\vec{s})$, and yields a spurious estimate of the displacement vector. Usually the search for the highest correlation peak is limited to a window that includes the range of displacements anticipated in the experiment. The *detectability* D_0 of the peak is defined as the ratio of the highest and second highest correlation peak in the search window (Keane & Adrian 1990). A high value of D_0 indicates that the detected peak is substantially larger than the other peaks in the search window. Thus, D_0 may be considered as a measure for the reliability that the peak centroid corresponds to a valid displacement.

The detection of either a valid or a spurious displacement depends on the number and spatial distribution of particle-image pairs inside the interrogation spot. In practice it appears that a minimum of four particle-image pairs is required to obtain an unambiguous measurement of the displacement. The number of particle images inside an interrogation spot is a stochastic variable with a Poisson probability distribution. Hence, an average of 10 particle-images per interrogation spot at an average in-plane displacement of $\frac{1}{4}D_I$ —where D_I is the diameter of the interrogation spot—yields a 95% probability to find at least four particle-image pairs (i.e. a 95% probability to obtain a valid displacement). Keane & Adrian (1990) made a detailed investigation of the yield of valid displacement vectors as function of seeding density, particle motion (parallel and perpendicular to the PIV light-sheet), and velocity-field gradients. They give an optimal design for PIV measurements with a valid-data yield, indicated here as Γ , of at least 95%.

By increasing the seeding density one can improve the valid-data yield, but this is not always desirable. By increasing the seeding density (at fixed particle size) we also increase the influence of the seeding on the flow itself (two-phase effects) and the optical opacity of the fluid (Adrian 1984). Thus, even in an optimally designed PIV experiment we will have to accept a certain fraction of spurious data.

Briefly summarized, the outcome of the analysis of an interrogation spot at (i, j) , indicated by $\vec{V}'_{i,j}$, is at random either a valid or spurious displacement vector, with a valid-data yield Γ . A *valid* outcome $\vec{V}'_{i,j}$ is equal to the local average $\vec{V}_{i,j}$ of the displacement field over the interrogation spot, apart from a small measurement error $\vec{\epsilon}_{i,j}$ (Adrian 1988). A *spurious* outcome for $\vec{V}'_{i,j}$ is equal to the centroid $\vec{U}_{i,j}$ of some random peak inside the search window. Based on this description we now propose the following expression for

$\vec{V}'_{i,j}$, in terms of a stochastic 'signal' or random field:

$$\vec{V}'_{i,j} = \gamma_{i,j} \cdot (\vec{V}_{i,j} + \vec{\varepsilon}_{i,j}) + (1 - \gamma_{i,j}) \cdot \vec{U}_{i,j} \quad (4.1)$$

where $\gamma_{i,j}$ is a binary random variable that takes a value of either 0 or 1. Let us further specify the random fields $\vec{V}_{i,j}$, $\vec{\varepsilon}_{i,j}$, $\vec{U}_{i,j}$ and $\gamma_{i,j}$:

- $\vec{V}_{i,j}$:

In practice, we do not have any *a priori* knowledge of the instantaneous displacement field $\vec{V}_{i,j}$ (e.g. measurements in turbulent flows). We therefore consider $\vec{V}_{i,j}$ as a random field, with statistics that are directly related to the statistics of the observed flow (taking into account that $\vec{V}_{i,j}$ is a low-pass filtered representation of the flow field observed in the PIV light sheet; see Adrian 1988). It is convenient to treat $\vec{V}'_{i,j}$ identically for all (i, j) , and deal with the components of $\vec{V}'_{i,j}$ individually. This implies that the statistics of $\vec{V}_{i,j}$ do not depend on (i, j) , and that the components in $\vec{V}_{i,j}$ are uncorrelated and have identical probability density functions (pdf's). In other words, $\vec{V}_{i,j}$ is a *homogeneous* random vector-field, with statistically *orthogonal* components:

$$E[\vec{V}_{i,j}] = \vec{\mu} \quad (4.2)$$

$$\text{cov}[\vec{V}_{i,j}, \vec{V}_{i+k,j+l}] = \sigma_V^2 \cdot \vec{1} \cdot \rho(k, l) \quad (4.3)$$

where $\vec{1}$ is the unit matrix, $\vec{\mu}$ the mean displacement, σ_V^2 the variance and $\rho(k, l)$ the spatial auto-correlation function of $\vec{V}_{i,j}$. This would correspond to a signal obtained from an isotropic homogeneous turbulent flow that is uniformly advected. Obviously, this does not represent a general situation: Most (turbulent) flows are not isotropic or even homogeneous. However, in most cases it will be possible to transform $\vec{V}_{i,j}$ into a signal that complies with (4.2–4.3). For more details refer to Appendix C.1. For an optimally designed PIV experiment the magnitude of the mean displacement $\|\vec{\mu}\|$ is equal to $\frac{1}{4}D_I$ (Keane & Adrian 1990). The displacement range—defined as the difference of the largest and smallest attainable absolute displacements—is maximally $\frac{1}{2}D_I$ (for double-exposure PIV records). This implies that the (equivalent) radius of the search window—denoted by R_I —is maximally $\frac{1}{4}D_I$. The size of the search window should match the expected range of displacements in the experiment. This imposes an upper limit for σ_V relative to R_I , i.e. $\sigma_V/R_I \approx^{max} \frac{1}{12}$, in which case the search window should contain about 99.8% of the displacements observed in the flow.

- $\vec{\varepsilon}_{i,j}$:

For non-overlapping interrogation regions the measurement errors $\vec{\varepsilon}_{i,j}$ in neighbouring interrogation positions are independent. Furthermore, we assume that the two components in $\vec{\varepsilon}_{i,j}$ are statistically orthogonal, and are identical homogeneous white normal random fields with zero mean and a variance equal to σ_ε^2 , i.e.:

$$E\{\vec{\varepsilon}_{i,j}\} = \vec{0} \quad (4.4)$$

$$\text{cov}[\vec{\varepsilon}_{i,j}, \vec{\varepsilon}_{k,l}] = \sigma_\varepsilon^2 \cdot \vec{1} \cdot \delta_{ik} \delta_{jl} \quad (4.5)$$

where δ_{ij} is the Kronecker delta symbol. For most PIV systems σ_ε is estimated to be less than 1% of the full displacement range, i.e. $\sigma_\varepsilon/D_I < 0.02$.

- $\vec{U}_{i,j}$:

A spurious vector corresponds to a random position within the area that is searched for the highest correlation peak. We assume that $\vec{U}_{i,j}$ is independent from $\vec{V}_{i,j}$, and has a uniform pdf over the search window. In general, the search window will have its center close to the expected mean displacement $\vec{\mu}$, with a diameter equal to $2R_I$, i.e.:

$$E[\vec{U}_{i,j}] \approx \vec{\mu} \quad (4.6)$$

$$\text{cov}[\vec{U}_{i,j}, \vec{U}_{k,l}] = \sigma_U^2 \cdot \vec{1} \cdot \delta_{ik} \delta_{jl} \quad (4.7)$$

with: $\sigma_U/R_I = \frac{1}{3}\sqrt{6} \approx 0.82$. For $\sigma_V/R_I \stackrel{\text{max}}{\approx} \frac{1}{3}$ this implies that $\sigma_U/\sigma_V > 2.5$. In other words, we can expect a significant contribution of $\vec{U}_{i,j}$ to the statistics of $\vec{V}'_{i,j}$. It may be expected that for larger σ_U/σ_V it becomes easier to distinguish between “valid” and “spurious” data. It does however not make sense to use a search window that is substantially larger than the expected range of displacements. In practice we will only have values of σ_U/σ_V close to 2.5. In the remainder of this chapter we consider $\sigma_U/\sigma_V=3$.

- $\gamma_{i,j}$:

For $\gamma_{i,j} = 1$ the process in (4.1) yields a valid vector for $\vec{V}'_{i,j}$. The probability $P(\gamma_{i,j} = 1)$ is equal to the valid-data yield Γ . We assume that the occurrence of a spurious vector is a purely random event that is not correlated with the displacement field $\vec{V}_{i,j}$. (Realize that this is only true in first approximation; see Keane & Adrian 1990.)

The expectation and variance of $\vec{V}'_{i,j}$ now become:

$$E[\vec{V}'_{i,j}] = \Gamma \cdot E[\vec{V}_{i,j} + \vec{\varepsilon}_{i,j}] + (1 - \Gamma) \cdot E[\vec{U}_{i,j}] \quad (4.8)$$

$$\text{cov}[\vec{V}'_{i,j}, \vec{V}'_{i,j}] = \Gamma (\sigma_V^2 + \sigma_\varepsilon^2) \vec{1} + (1 - \Gamma) \sigma_U^2 \vec{1} + \Gamma(1 - \Gamma) (E[\vec{V}_{i,j}] - E[\vec{U}_{i,j}])^2 \quad (4.9)$$

Note that $\vec{V}'_{i,j}$ for $E[\vec{V}_{i,j}] = E[\vec{U}_{i,j}]$ is an *unbiased* estimate of $\vec{V}_{i,j}$, independent of Γ , with a variance equal to $\Gamma(\sigma_\varepsilon^2 + \sigma_V^2) + (1 - \Gamma)\sigma_U^2$.

4.3 Detection methods

In the Introduction we already mentioned that spurious vectors are visually recognized as vectors that exhibit an “unexpectedly large” deviation with respect to nearby vectors. We

define the residual displacement vector $\vec{r}_{i,j}$ as the deviation of the observed displacement from the expected displacement, i.e.:

$$\vec{r}_{i,j} = \vec{V}'_{i,j} - \vec{V}_{i,j}. \tag{4.10}$$

To comply with existing evaluation techniques for scalar data we consider the squared magnitude of $\vec{r}_{i,j}$ as a *scalar* measure for the deviation of $\vec{V}'_{i,j}$ with respect to $\vec{V}_{i,j}$, i.e.:

$$r^2_{i,j} = \|\vec{V}'_{i,j} - \vec{V}_{i,j}\|^2. \tag{4.11}$$

The identification of spurious data is based on a statistical test on the residuals with respect to its statistics (mean and variance). For the signal in (4.1) this implies for each (i, j) a null hypothesis $H_0: \gamma_{i,j} = 1$ is tested against the alternative hypothesis $H_1: \gamma_{i,j} = 0$ for the residual defined in (4.11).

Under H_0 the residual vector $\vec{r}_{i,j}$ is equal to $\vec{\epsilon}_{i,j}$, which is a normal white random field, with statistics given in (4.4–4.5). Hence, $r^2_{i,j}$ has an *exponential* probability density function:

$$f(r^2|H_0) = \frac{1}{2\sigma_\epsilon^2} \exp\left(-\frac{r^2}{2\sigma_\epsilon^2}\right) \tag{4.12}$$

which has a mean value $E\{r^2|H_0\} = 2\sigma_\epsilon^2$. The pdf in (4.12) is an approximation valid for $r^2/R_I^2 \ll 1$. This condition is met in most practical situations, for which σ_ϵ^2/R_I^2 is usually less than 0.01.

On the other hand, under the alternative hypothesis H_1 the residual vector $\vec{r}_{i,j}$ is equal to $\vec{U}_{i,j} - \vec{V}_{i,j}$. For $\sigma_U^2/\sigma_V^2 \gg 1$ the squared scalar residual under H_1 has approximately a *uniform* pdf:

$$f(r^2|H_1) = U(0, R_I^2). \tag{4.13}$$

This is exact when $\vec{U}_{i,j}$ has a uniform distribution within a circular region of radius R_I centered at $\vec{V}_{i,j}$.

For a given reliability level we can compute a critical value r_c^2 above which H_0 is rejected. We now have obtained an objective decision criterion by which we can label a specific $\vec{V}'_{i,j}$ as either “valid” or “spurious”. There is however a finite probability that we label *valid* data erroneously as “spurious” and *vice versa*. These errors are commonly indicated as errors of the first and second kind respectively, i.e.:

$$E_1 = P(r^2 > r_c^2 | H_0) \cdot P(\gamma = 1), \tag{4.14}$$

$$E_2 = P(r^2 < r_c^2 | H_1) \cdot P(\gamma = 0). \tag{4.15}$$

In addition the *cost* function K is defined as:

$$K = C_1 \cdot E_1 + C_2 \cdot E_2 \tag{4.16}$$

where C_1 and C_2 are weights for E_1 and E_2 respectively. Minimizing K with respect to r_c^2 yields an optimal value of r_c^2 for a given set of (C_1, C_2) . For $C_1 = C_2$ the result for r_c^2 is

usually referred to as the *Bayes decision criterion*. Here we will consider only $C_1 = C_2 = 1$, although there may be situations where a different choice for (C_1, C_2) is more appropriate. If we apply (4.12) and (4.13) in (4.14) and (4.15) respectively, and subsequently minimize K in (4.16) for r^2 we obtain the following expression for r_c^2 (with $C_1 = C_2 = 1$):

$$\frac{r_c^2}{R_I^2} = -\frac{2\sigma^2}{R_I^2} \ln \left[\frac{1 - \Gamma \frac{2\sigma^2}{R_I^2}}{\Gamma \frac{2\sigma^2}{R_I^2}} \right] \tag{4.17}$$

(Note that minimizing K for $C_1 = C_2 = 1$ is equivalent to solving $\Gamma f(r^2|H_0) = (1 - \Gamma)f(r^2|H_1)$ with respect to r^2 .) The corresponding result for K yields:

$$K = (1 - \Gamma) \frac{2\sigma^2}{R_I^2} \left[1 - \ln \left(\frac{1 - \Gamma \frac{2\sigma^2}{R_I^2}}{\Gamma \frac{2\sigma^2}{R_I^2}} \right) \right] \tag{4.18}$$

In Figure 4.3 are plotted the results for K with respect to r_c^2 as function of $E\{r^2|H_0\}/2\sigma^2$ for three different values of Γ .

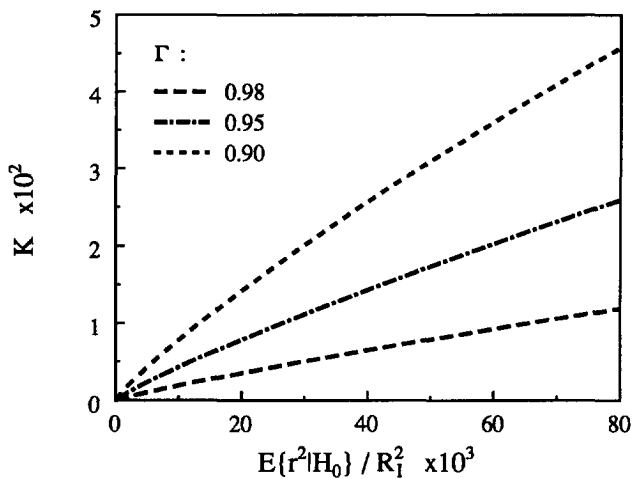


Figure 4.3: The total cost K as function of the mean squared residual $E\{r^2|H_0\} = 2\sigma^2$ for three different values of the valid-data yield Γ .

In practice $\vec{V}_{i,j}$ is not known *a priori*, and therefore has to be estimated from the measured signal itself. This yields an estimate $\hat{r}_{i,j}^2$ for the squared scalar residual:

$$\hat{r}_{i,j}^2 = \|\vec{V}'_{i,j} - \hat{\vec{V}}_{i,j}\|^2. \tag{4.19}$$

where $\hat{V}_{i,j}$ denotes an estimator for $\vec{V}_{i,j}$. A suitable estimator should be unbiased and have a variance that is substantially smaller than $\vec{V}'_{i,j}$. The remainder of this section deals with the description of three different tests, based on the global-mean, the local-mean and the local-median estimators respectively.

4.3.1 global-mean test

The global mean of $\vec{V}'_{i,j}$ is defined as the mean of $\vec{V}'_{i,j}$ taken over the entire data set:

$$\langle \vec{V}' \rangle = \frac{1}{N} \sum_{i,j} \vec{V}'_{i,j} \tag{4.20}$$

where N is the total number of vectors in the data set. The expectation value and variance of the global mean can be easily obtained from (4.8–4.9):

$$E[\langle \vec{V}' \rangle] \approx \vec{\mu} \tag{4.21}$$

$$\text{var}[\langle \vec{V}' \rangle] \approx \frac{1}{N'} [\Gamma(\sigma_\epsilon^2 + \sigma_V^2) + (1 - \Gamma)\sigma_U^2] \tag{4.22}$$

where N' is the effective number of independent samples in the PIV measurement data, given by:

$$\frac{1}{N'} = \frac{1}{N} \sum_{k,l} \rho(k,l) \tag{4.23}$$

The value of N' is inversely proportional to the integral length scale in $\vec{V}_{i,j}$. For flows that have a velocity correlation function with a long “tail” the value of N' may be reduced considerably with respect to N . In the limit $N' \rightarrow \infty$ the variance of $\langle \vec{V}' \rangle$ converges to zero. By substituting $\hat{V}_{i,j} = \langle \vec{V}' \rangle$ in (4.19) it is found that the lower bound for $E\{\hat{r}_{i,j}^2|H_0\}$ is equal to $2(\sigma_\epsilon^2 + \sigma_V^2)$. In practice, $\sigma_\epsilon^2 \ll \sigma_V^2$, and as a result the pdf for \hat{r}^2 under H_0 is much broader than the distribution given in (4.12), i.e.:

$$E\{\hat{r}^2|H_0\} = 2(\sigma_\epsilon^2 + \sigma_V^2). \tag{4.24}$$

Hence, using $\langle \vec{V}' \rangle$ as an estimate for $\vec{V}_{i,j}$ will lead to a relatively high value of $E\{\hat{r}^2|H_0\}/R_T^2$. From (4.18) and Figure 4.3 it is clear that we do not expect a high efficiency from this estimator.

4.3.2 local-mean test

Alternatively, one can use the local mean $\langle \vec{V}' \rangle_{i,j}$ over a small neighbourhood of $\vec{V}'_{i,j}$, i.e.:

$$\langle \vec{V}' \rangle_{i,j} = \frac{1}{N_M} \left(\sum_{k,l \in M} \vec{V}'_{i+k,j+l} - \vec{V}'_{i,j} \right) \tag{4.25}$$

where \mathbf{M} denotes the neighbourhood of (i, j) that includes N_M elements. The choice for the size of \mathbf{M} will depend on the correlation length of $\vec{V}_{i,j}$. Here we will only consider a 3×3 eight-connected neighbourhood with $N_M=8$. Note that in (4.25) we exclude $\vec{V}'_{i,j}$ itself from $\langle \vec{V}' \rangle_{i,j}$; In this way $\langle \vec{V}' \rangle_{i,j}$ is not correlated with $\vec{V}'_{i,j}$ for $\gamma_{i,j} = 0$, which simplifies the analysis.

In most cases neighbouring measurement data are highly correlated, as a result of a high spatial correlation of the velocity field over a short distance. Assume that the covariance for \vec{V}' in the neighbourhood \mathbf{M} is given by:

$$\text{cov}[\vec{V}'_{i,j}, \vec{V}'_{i+k,j+l}] = \eta \cdot \sigma_V^2 \tag{4.26}$$

for $(k, l) \in \mathbf{M}$ and where η is a constant that has a value slightly smaller than one. This assumption allows us to obtain a relatively simple expression for $E\{\hat{r}^2|H_0\}$.

First, we consider the case for $\Gamma = 1$. Substitution of $\hat{V}'_{i,j} = \langle \vec{V}' \rangle_{i,j}$ in (4.19) yields:

$$E\{\hat{r}^2|\Gamma = 1\} = 2 \left(1 + \frac{1}{N_M} \right) \left(\sigma_\epsilon^2 + (1 - \eta)\sigma_V^2 \right). \tag{4.27}$$

Here we find that $E\{\hat{r}^2|\Gamma=1\}$ for $\eta \rightarrow 1$ approaches $2\sigma_\epsilon^2(1 + \frac{1}{N_M})$. Clearly, the local-mean estimator for $\vec{V}'_{i,j}$ is much more precise than the global-mean estimator.

Let us consider the case for Γ less than one. Now we have a finite probability that one or more of the measurement data in \mathbf{M} is a spurious vector. The probability to find k spurious vectors in a set of N_M data points at a valid-data yield Γ is given by a binomial distribution $B(k; N_M, 1 - \Gamma)$. In Table 4.1 the probabilities are given to find up to four spurious vectors in a 3×3 eight-connected neighbourhood for different values of Γ . From this table it is clear that in general we have a relatively high probability to have at least one spurious vector (more than 30% at $\Gamma=0.95$). For $\eta < 1$ the covariance of $\vec{r}_{i,j}$ is given by:

$$\text{cov}\{\vec{r}_{i,j}, \vec{r}_{i,j}|H_0\} = \sum_{k=0}^{N_M} B(k; N_M, 1 - \Gamma) \cdot \text{cov}\{\vec{r}_{i,j}, \vec{r}_{i,j}|k\} \tag{4.28}$$

where $\text{cov}\{\vec{r}_{i,j}, \vec{r}_{i,j}|k\}$ is the covariance when \mathbf{M} contains exactly k spurious vectors.

The presence of one or more spurious vectors in the neighbourhood of (i, j) strongly affects the outcome of $\langle \vec{V}' \rangle_{i,j}$. Also, the occurrence of a single spurious vector in (i, j) will affect the evaluation of all vectors in its neighbourhood. In other words, the estimator $\langle \vec{V}' \rangle_{i,j}$ smoothes out spurious data, which increases the probability to reject valid data in the neighbourhood of a spurious vector. Obviously the estimator $\langle \vec{V}' \rangle_{i,j}$ is not very robust. This is reflected in the mean of \hat{r}^2 obtained in the local-mean test, which can be obtained from (4.28):

$$E\{\hat{r}^2|H_0\} = 2 \left[\Gamma \left(1 + \frac{1}{N_M} \right) \left(\sigma_\epsilon^2 + (1 - \eta)\sigma_V^2 \right) + \frac{1}{N_M} \cdot (1 - \Gamma) \cdot \sigma_U^2 \right]. \tag{4.29}$$

In Figure 4.4 $E\{\hat{r}^2|H_0\}$ is plotted as function of η for different values of Γ . We find a considerable increment of $E\{\hat{r}^2|H_0\}$ with respect to the case $\Gamma=1$ in (4.27). For example,

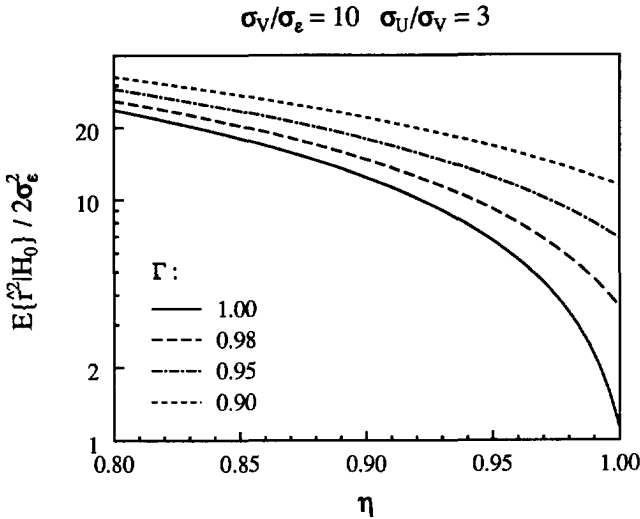


Figure 4.4: The mean of the squared estimated residual $E\{\hat{r}^2|H_0\}$ normalized by $2\sigma_\varepsilon^2$ as function of the local correlation η of the displacement data, for three different values of the valid-data yield Γ .

if we take $\sigma_U/\sigma_V = 3$ with $\eta = 0.95$ then $E\{\hat{r}^2|H_0\}$ for $\Gamma = 0.95$ is more than two times $E\{\hat{r}^2|\Gamma = 1\}$. This means that we can only obtain an accurate estimate for $\vec{V}_{i,j}$ provided that the neighbourhood is free from spurious vectors or, alternatively, that we have *a priori* knowledge on valid and spurious vectors. For example, we could first do a “rough” identification of spurious vectors by using the global-mean test and subsequently apply the local-mean test in which we only use those vectors that were labeled as “valid” in the preceding evaluation to compute $(\vec{V}')_{i,j}$. One may expect that this combination of the global-mean and local-mean tests should improve the overall performance, in comparison with their individual performances. It should be noted however that it is more complicated to optimize such a two-step procedure.

4.3.3 local-median test

The global-mean and local-mean are both *linear* estimators for $\vec{V}_{i,j}$. A nonlinear estimator that is often used in outlier identification is the *median* of the sample data (Barnett & Lewis 1979; Fredrikze 1985; Westerweel 1987). The median is the middle value (n^{th} element) of a sequence of $2n + 1$ scalar elements, that has been rearranged in increasing or decreasing order (for any even number of elements, the median is equal to the mean of the two middle elements). The outcome for the median is very robust with respect to contamination with spurious data. Let us illustrate this with an example.

Consider a sample of $2n+1$ elements, with a valid-data yield Γ . Spurious data will in general have large deviations from the expected value and, while computing the median, will end up at the begin or the end of the rearranged sequence. As a result, the outcome for the median is in general equal to the value of one of the valid elements in the sequence, and does not depend on the value of any spurious elements. This is in clear contrast to a linear estimate, such as the sample mean. Only for strongly contaminated data the outcome of the median yields a spurious value. The probability that a sample of 9 elements contains more than four spurious vectors is less than 0.2% for $\Gamma > 0.90$.

In digital image processing the local median is used as a nonlinear filter that efficiently removes binary noise ("salt & pepper noise") (Jain 1989). To some extent the characteristics of binary noise are similar to those of spurious vectors in PIV measurement data. Another property of the median filter (when used as a spatial filter) is that it is an "edge-preserving" filter, i.e. it does not smooth out strong gradients. There is however not a unique definition for the median of vector data. Here we obtain the "median displacement vector" by computing the median for each component individually:

$$[\vec{V}']_{i,j} = \begin{pmatrix} \text{median}\{v_{i+k,j+l}^x | k, l \in \mathbf{M} \cup \{0,0\}\} \\ \text{median}\{v_{i+k,j+l}^y | k, l \in \mathbf{M} \cup \{0,0\}\} \end{pmatrix} \quad (4.30)$$

where v^x and v^y denote the components of \vec{V}' . Note that we now include $\vec{V}'_{i,j}$ in computing $[\vec{V}']_{i,j}$; The main reason for this is that the analysis of the median statistics of an *odd* number (i.e. $N_M + 1$) of elements is less complicated. Let us consider the mean and variance of the estimator in (4.30). The median of a stochastic variable is equal to its mean when the probability density function is symmetric with respect to the mean. Correspondingly, $\hat{r}_{i,j}$ is unbiased with respect to $\vec{r}_{i,j}$ when $\vec{V}'_{i,j}$ has a symmetric pdf with respect to $\vec{V}_{i,j}$. This condition is met when $E[\vec{V}] = E[\vec{U}]$. Again we assume that the covariance of $\vec{V}'_{i,j}$ is given by (4.26). We also assume that the samples $\vec{V}'_{i+k,j+l} | k, l \in \mathbf{M} \cup \{0,0\}$ may be considered as independent and orthogonal with identical pdf's given by:

$$\Gamma N(\vec{V}_{i,j}, \sigma^2 \vec{1}) + (1 - \Gamma) U(\|\vec{V}'_{i+k,j+l} - \vec{V}_{i,j}\| < R_l) \quad (4.31)$$

with $\sigma^2 = \sigma_\epsilon^2 + (1 - \eta)\sigma_V^2$. An expression for the pdf of the median of a sample with $2n+1$ elements from a stochastic process is given in Appendix C.2. For samples that have a normal pdf with zero mean and variance σ^2 the pdf of the median is in good approximation a normal distribution $N(0, \sigma^2/N_{\text{eff}})$, with $N_M/N_{\text{eff}} \approx 1.47 + \mathcal{O}(\Gamma)$. Compare this with the pdf of the sample mean, which has a normal pdf $N(0, \sigma^2/N)$. If we substitute $\hat{V}_{i,j} = [\vec{V}']_{i,j}$ in (4.19) we obtain through (4.28):

$$E\{\hat{r}_{i,j}^2 | H_0\} = 2 \left(1 + \frac{1}{N_{\text{eff}}}\right) (\sigma_\epsilon^2 + (1 - \eta) \cdot \sigma_V^2). \quad (4.32)$$

Note the similarity with (4.27). The value of N_{eff} depends only weakly on Γ . In Figure 4.5 we compare $E\{\hat{r}^2 | H_0\}$ for the local-mean and local-median tests as function of Γ . The mean of \hat{r}^2 for the local-median estimator remains practically constant over a wide range

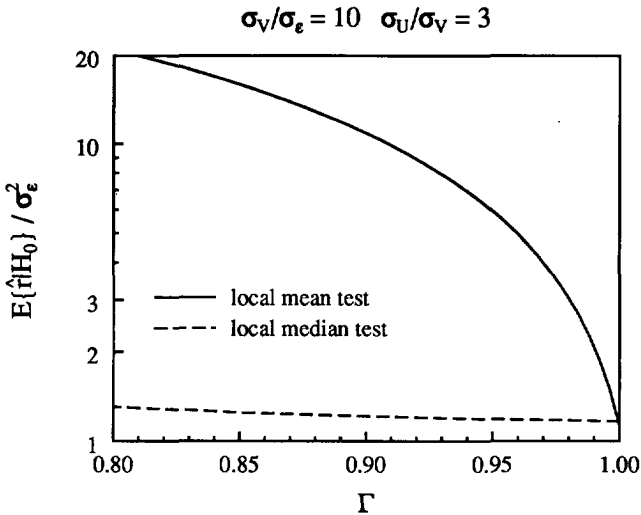


Figure 4.5: The mean of the squared estimated residual $E\{\hat{r}^2|H_0\}$ normalized by $2\sigma_\epsilon^2$ for the local mean and the local median as function of the valid-data yield Γ .

in Γ , while the mean of \hat{r}^2 for the local-mean estimator increases rapidly as Γ decreases. Thus, the local median estimator will yield the most accurate and robust estimate for $\vec{V}_{i,j}$ in the three tests described in this section.

In the analysis given here we have assumed that the data points (i, j) do not lie on one of the edges or corners of the data set. For the “bulk” data-points we have $N_M = 8$ for an eight-connected 3×3 neighbourhood \mathbf{M} . In principle this analysis also applies to edge and corner data-points, but with $N_M = 5$ and 3 respectively. Note that only a relatively small fraction of the data set consists of edge and corner data-points. It is therefore expected that their influence on the statistics of the (estimated) residuals is negligible.

4.4 Performance tests

To demonstrate the superior performance of the local median estimator for $\vec{V}_{i,j}$ in evaluating PIV measurement data a comparative test was carried out for the three estimators defined in the previous section. In the first part of Section 4.3 we defined the cost K to portray the performance of an evaluation procedure. Complementary to K we now define the *efficiency* of a procedure as $1 - K$, with $C_1 = C_2 = 1$, which indicates the fraction of displacement vectors that were properly identified as either valid or spurious data. In order to determine this quantity we need *a priori* knowledge of which vectors are valid

Table 4.1: The probability $B(k; N_M, 1 - \Gamma)$ to find k spurious vectors in a neighbourhood of $N_M = 8$ elements for three different values of Γ .

k	$B(k; 8, 1 - \Gamma)$ $\times 100$			
	$\Gamma =$	0.98	0.95	0.90
0		85.1	66.3	43.0
1		13.9	27.9	38.3
2		1.0	5.1	14.9
3		0.0	0.5	3.3
4		0.0	0.0	0.5

and which are spurious. This was established by generating an artificial PIV image from a given velocity field, and subsequently by comparing the displacement field after PIV analysis with the original displacement field.

A displacement field that has the kinematic characteristics of homogeneous turbulence was simulated with the method of random Fourier modes described by Fung *et al.* (1992). For this simulation 64 Fourier modes were used, with random phase and an amplitude that corresponds to the $-5/3$ power-law found in the inertial subrange. The modes were distributed over the wavenumber range such that each mode contributes an equal amount to the total energy. A constant advection velocity was added to obtain a displacement field with a degree of turbulence of 16%. This would correspond to a situation where $R_I = \frac{1}{4}D_I$ and $\sigma_U/\sigma_V=3$. The valid-data yield was determined by the average number of particles in the image. It was assumed that all particles have equal diameters. The intensity of each particle was determined according to its position in a light sheet with a Gaussian intensity profile perpendicular to the image plane. The PIV image that was generated complies with the optimization described by Keane & Adrian (1990), with respect to the in-plane and out-of-plane displacements. Thus, the expected valid-data yield Γ was equal to 0.95. The smallest spatial variation (wavelength) in this field was taken equal to twice the diameter of the interrogation spot in the PIV analysis. In that case the $-5/3$ decay in the spectrum yields a correlation value η in (4.26) of approximately 0.95 between nearest neighbours in the PIV data-set.

Interrogation analysis of the artificially generated PIV image yielded a test data-set that consisted of in total 5041 vectors. Additionally, the "detectability" D_0 was obtained for each vector. For each displacement vector \hat{r}^2 was computed according to each of the three tests described in the previous section.

A practical way to evaluate the pdf of \hat{r}^2 is by its cumulative histogram. Under the null hypothesis \hat{r}^2 has approximately an exponential distribution. Now, if we sort a total of N residuals in magnitude and subdivide them into M bins, each containing an equal fraction of $\Delta\theta = M/N$ residuals, the expectation value for the lowest residual r_m^2 in the

m -th bin is given by:

$$\theta_m \equiv m\Delta\theta = \int_0^{r_m^2} \frac{1}{2\sigma^2} \exp\left(-\frac{r^2}{2\sigma^2}\right) dr^2 \quad (4.33)$$

which is equivalent to:

$$r_m^2 = 2\sigma^2 \ln\left(\frac{1}{1-\theta_m}\right). \quad (4.34)$$

If we plot r_m^2 for each bin against the logarithm of $1/(1-\theta_m)$ we expect to find a straight line with a direction coefficient equal to $E\{\hat{r}^2|H_0\}$. In Figure 4.6 are given the cumulative histograms for the residuals from the test data-set obtained by the global mean, the local mean and the local median tests respectively. From (4.24), (4.29) and (4.29) we can predict the values of $E\{r^2|H_0\}$ for the three tests respectively. The solid lines in Figure 4.6 represent the expected histograms according to an exponential pdf. The predicted and observed results for $E\{r^2|H_0\}/R_0^2$ are given in Table 4.2. In this table are also given the predicted values for r_c^2 and $1-K$ according to (4.17) and (4.18) respectively, together with the corresponding results obtained from the test data-set. Note that the observed performances are very close to the predicted performances. This demonstrates that the model described in Section 2 gives an adequate description of the PIV “signal”.

In addition we also tested the performance of the “detectability” D_0 as a means to

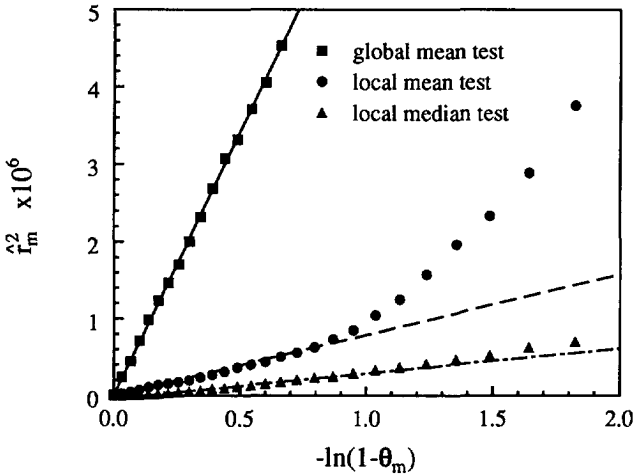


Figure 4.6: The cumulative histograms for the residuals in the test data-set for the global-mean, local-mean and local-median tests. The solid lines represent the expected histograms.

Table 4.2: The predicted and observed values for $E\{\hat{r}^2|H_0\}/R_I^2$, r_c^2/R_I^2 and $1-K$ for different tests applied to an artificial PIV record (see text).

test		predicted	observed
global mean	$E\{\hat{r}^2 H_0\}/R_I^2$	0.0448	0.0485
	r_c^2/R_I^2	0.271	0.238
	$1 - K$	0.9842	0.9867
local mean	$E\{\hat{r}^2 H_0\}/R_I^2$	0.00658	0.00702
	r_c^2/R_I^2	0.052	0.075
	$1 - K$	0.9970	0.9952
local median	$E\{\hat{r}^2 H_0\}/R_I^2$	0.00289	0.00298
	r_c^2/R_I^2	0.026	0.022
	$1 - K$	0.9985	0.9986
detectability	$1 - K$	-	0.9280

distinguish between valid and spurious displacement vectors. Since the original displacement field is known, we can easily determine E_1 and E_2 as function of a critical values for D_0 . It appeared that a cost function for D_0 does not have a *minimum* for $D_0 > 1$. This implies that $\Gamma f(D_0|H_0) > (1 - \Gamma)f(D_0|H_1)$ for all $D_0 > 1$. As decision criterion for the detectability test was used the $N \cdot \Gamma$ -largest observed value of D_0 . (This corresponds to $E_1 = E_2$.) Thus a critical value was found of 1.1, with $1 - K = 92.80\%$. Note that Keane & Adrian (1990) propose a slightly higher value between 1.2 and 1.5. If we compare the performances the different tests in Table 4.2 it is clear that the detectability test has a very poor performance, especially compared to the performance of the local-median test.

4.5 Conclusions

From the comparison of the predicted and observed performances in the previous section we conclude that the statistical model for $\vec{V}'_{i,j}$ described in Section 4.2 gives an adequate description of the PIV signal, and that it is capable to analyze and to predict the optimal performance of the post-interrogation procedures described in Section 4.3. In a practical situation we can estimate $E\{\hat{r}^2|H_0\}$ from the cumulative histogram of \hat{r}^2 . Figure 4.6 demonstrates that we can determine $E\{\hat{r}^2|H_0\}$ directly from its histogram by fitting a straight line to the cumulative histogram (for small values of \hat{r}^2). An *a priori* estimate of Γ can be obtained from the figures given by Keane & Adrian (1990) given the mean number of particle-images per interrogation spot, the mean in-plane and out-of-plane displacements and velocity gradient. (These parameters are required anyway to set up the PIV experiment.) For a given value of Γ one can directly determine the optimal (Bayes) decision criterion r_c^2 . For given values of $E\{\hat{r}^2|H_0\}$ and Γ we can also predict the

efficiency of the post-interrogation evaluation procedure.

The comparative test described in Section 4.4 pointed out that the detectability, which is the "conventional" quantity to characterize the reliability of a measured displacement vector, has the lowest efficiency of the tests described in this chapter. Comparison of the performances of the global-mean and local-mean tests pointed out that the evaluation of the deviations relative to the local displacement field yields a much higher efficiency than those relative to the global mean displacement. However, it appears that the local-mean test is very sensitive to the presence of spurious displacement vectors in the direct neighbourhood of an evaluated vector, and its performance decreases rapidly as Γ decreases. The highest efficiency was obtained by the local-median test. For the test data-set the number of erroneous identifications in the local-median test was almost 4 times smaller than in the local-mean test. The only difference in the evaluation algorithms is that a local median instead of a local mean is computed.

Chapter 5

Estimation of Vorticity and Deformation

Abstract. *The vorticity and deformation are flow properties that can be obtained by differentiation of the velocity field. The two-dimensional measurement data obtained from PIV measurements allow the evaluation of components of the vorticity vector and deformation tensor. The accuracy of these estimates is limited by the spatial resolution and noise level of the PIV data. It is shown that the accuracies encountered in data sets from digital PIV analyses can yield reliable estimates of the vorticity and deformation.*

5.1 Introduction

In the previous chapters we have seen how to extract velocity information from a flow seeded with small tracer particles. Now we have come to the point where we can estimate (elements of) flow quantities that relate to the dynamics of coherent flow structures. In the following we will identify these flow structures as areas where the value of the vorticity or the second invariant of the deformation tensor exceed a certain threshold. In this chapter we take a closer look at the estimation of these quantities from PIV data sets. Our point of departure in this chapter is a PIV data set that consists of the instantaneous measurement of the in-plane velocity field on a regular mesh of points. This data set is supposed to be free from spurious data (i.e. spurious vectors have been detected and subsequently removed from the data set with the procedure discussed in Chapter 4).

The vorticity and deformation have in common that they are obtained by *differentiation* of the velocity field. Since we have only measurement data in discrete points we have to estimate the spatial derivatives of the velocity field by *finite differences*. In addition the measurement data are disturbed by noise; in general the contribution of noise to the result is amplified by the differentiation of the data.

The methods described here will be used in the PIV applications described in Part II.

5.2 Vorticity

The vorticity vector is defined as the curl of the velocity field, viz.

$$\vec{\omega} = \nabla \times \vec{v} \tag{5.1}$$

(Batchelor 1967). With only two velocity components available we can only determine the out-of-plane component of $\vec{\omega}$, i.e.

$$\omega_z = \frac{\partial v}{\partial X} - \frac{\partial u}{\partial Y} \tag{5.2}$$

where u and v denote the velocity components in the X direction and Y direction respectively (see Fig. 2.5). This quantity can be estimated from central first-order differences of the measured velocity data, viz.

$$\omega_z \sim \frac{v_{i+1,j} - v_{i-1,j}}{2\Delta X} - \frac{u_{i,j+1} - u_{i,j-1}}{2\Delta Y} \tag{5.3}$$

where i and j are indices of a mesh point in the PIV data set in the X direction and Y direction respectively, and ΔX and ΔY the distances between mesh points. However, as we will see shortly after, the estimator in (5.3) strongly amplifies the noise in the PIV data set. To reduce the influence of the noise on the estimate for ω_z we have to apply some degree of smoothing to the velocity data. Landreth & Adrian (1990b) propose a spatial-averaging filter with a Gaussian weight kernel $w_{i,j}$, i.e.

$$w_{i,j} = \exp \left[-2(i^2 + j^2)/P^2 \right]. \tag{5.4}$$

An appropriate choice of P should strongly reduce the random noise, while it leaves the velocity signal virtually unaffected.

Another method to determine the vorticity, proposed by Reuss *et al.* (1989), is based on the application of the Stokes theorem on a small surface

$$\omega_z = \lim_{S \rightarrow 0} \oint_C \frac{\vec{v} \cdot d\vec{\ell}}{S} \tag{5.5}$$

where C denotes the contour that encloses the surface S . For the contour C taken along the 8-connected neighbourhood of a data point in (i, j) , as shown in Figure 5.1, the vorticity is estimated by (Landreth & Adrian 1990a)¹:

$$\begin{aligned} \omega_z \sim \frac{1}{4\Delta X \Delta Y} \left[\right. & \Delta Y v_{i+1,j} + \frac{1}{2} \Delta Y \{ v_{i+1,j-1} + v_{i+1,j+1} \} \\ & - \Delta X u_{i,j+1} - \frac{1}{2} \Delta X \{ u_{i-1,j+1} + u_{i+1,j+1} \} \\ & - \Delta Y v_{i-1,j} - \frac{1}{2} \Delta Y \{ v_{i-1,j-1} + v_{i-1,j+1} \} \\ & \left. + \Delta X u_{i,j-1} + \frac{1}{2} \Delta X \{ u_{i-1,j-1} + u_{i+1,j-1} \} \right]. \tag{5.6} \end{aligned}$$

¹The original formula given by Reuss *et al.* (1989) contained a few sign errors; the correct formula is given by Landreth & Adrian (1990a).

If we substitute

$$\tilde{u}_{m,n} = \frac{1}{2} \left[u_{m,n} + \frac{1}{2} \{ u_{m-1,n} + u_{m+1,n} \} \right] \quad \text{and} \quad \tilde{v}_{m,n} = \frac{1}{2} \left[v_{m,n} + \frac{1}{2} \{ v_{m,n-1} + v_{m,n+1} \} \right]$$

then (5.6) becomes:

$$\omega_Z \sim \frac{\tilde{v}_{i+1,j} - \tilde{v}_{i-1,j}}{2\Delta X} - \frac{\tilde{u}_{i,j+1} - \tilde{u}_{i,j-1}}{2\Delta Y} \tag{5.7}$$

cf. Eq. (5.3). So, (5.6) is equivalent to a (5.3) with a local (3-point) filtering of the velocity data.

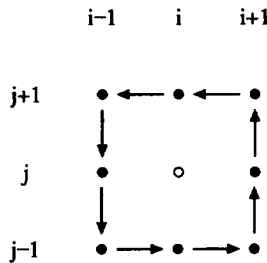


Figure 5.1: The contour along the 8-connected neighbourhood of a data point in (i, j) .

performance testing

To investigate the performances of the different methods to determine the vorticity from PIV data a simple test was carried out. In this test the performance of the estimators in (5.3), with and without the filtering in (5.4), and (5.6). We investigated the combined effect of the size and vorticity amplitude of the structure (“the strongest vorticity occurs at the smallest scales”; see Sect. 1.1), and the effect of random noise.

For this test we considered a one-dimensional shear layer aligned with the X -direction of the data set, with the following functional relationship

$$u = \frac{1}{2} - \frac{1}{\pi} \arctan \left(\frac{Y}{\sigma_\omega} \right) \quad \text{and} \quad v = 0 \tag{5.8}$$

where σ_ω is a parameter that determines the *width* of the shear layer. Note that u ranges from 0 to 1, and that the velocity and position are dimensionless. The corresponding vorticity is obtained by applying (5.2) to (5.8), which yields

$$\omega_Z = \frac{1}{\pi \sigma_\omega} \frac{1}{1 + (Y/\sigma_\omega)^2} \tag{5.9}$$

Note that the *maximum* vorticity (for $Y = 0$) is equal to $1/\pi\sigma_\omega$. PIV data sets for different values of σ_ω were generated by sampling the velocity field in (5.8) with intervals

$\Delta X = \Delta Y = 1$. The smallest value for σ_ω was chosen such that the steepest gradient of u over ΔY was less than about 20% of the mean velocity, i.e. $\sigma_\omega \geq 0.75$. (For gradients less than about 20% of the mean velocity we can neglect the gradient bias; see Sect. 2.9 and Adrian (1988).) To account for the measurement error white gaussian noise with levels from 0.5 to 5% of the full range velocity range were added to the data set. The total size of each data set was 20×20 data points (i.e. 20 data points across, and 20 data points along the shear layer). Subsequently the estimators for the vorticity in (5.3), with and without the filtering in (5.4), and (5.6) were applied to the artificially generated data sets. This is illustrated in Figure 5.2 where the actual (noise-free) data for the velocity and vorticity with $\sigma_\omega = 2$ are compared to the corresponding data with a noise level of 2% computed by (5.6). The rms differences between the estimated and actual vorticity in (5.9), relative to the *maximum* vorticity as function of σ_ω (viz., $1/\pi\sigma_\omega$) are given in Table 5.1.

The results in Table 5.1 show that even in a noise-free situation the vorticity is esti-

Table 5.1: The rms differences of estimated and actual vorticity relative to the maximum vorticity (in %) for three different methods, as function of the spatial resolution (indicated by σ_ω) and the relative noise level for a shear layer of finite width (see text).

<i>1st order central differences, without filtering</i>					
σ_ω	noise level				
	0.0%	0.5%	1.0%	2.5%	5.0%
0.75	7.10	7.13	7.27	7.36	8.22
1.00	7.28	7.31	7.28	7.64	8.61
2.00	4.54	4.79	4.81	7.01	10.34
4.00	1.92	2.37	4.74	8.81	19.72
<i>1st order central differences, with filtering (P=1)</i>					
σ_ω	noise level				
	0.0%	0.5%	1.0%	2.5%	5.0%
0.75	2.93	3.23	4.00	6.85	12.27
1.00	3.41	3.78	4.45	8.47	16.35
2.00	2.05	3.91	6.88	16.86	30.64
4.00	0.77	6.47	12.94	31.55	58.28
<i>circulation along 8-connected neighbourhood</i>					
σ_ω	noise level				
	0.0%	0.5%	1.0%	2.5%	5.0%
0.75	2.93	3.09	3.44	4.99	8.43
1.00	3.41	3.59	3.71	5.69	10.26
2.00	2.05	3.02	4.37	10.58	19.24
4.00	0.78	4.06	8.01	19.25	36.67

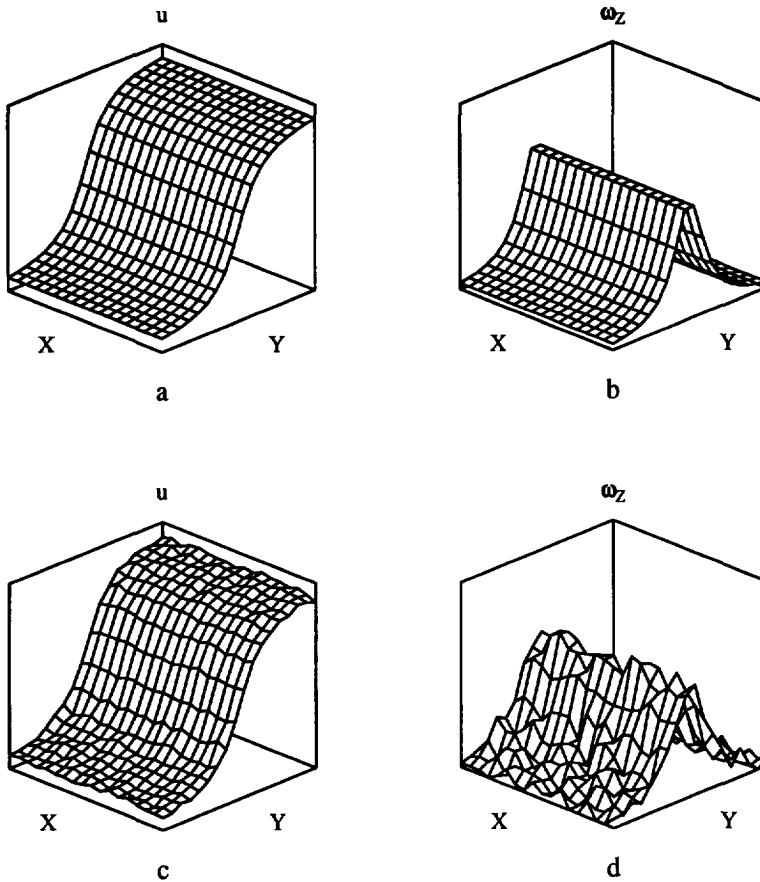


Figure 5.2: The velocity (a) and vorticity (b) profile of the shear-layer defined in (5.8) with $\sigma_\omega = 2$. The same velocity data are shown in (c) but now with a 2% noise superimposed on the original data. In (d) is shown the corresponding vorticity, computed according to (5.6).

mated with an error of a few percent. This is the result of estimating the derivatives in (5.2) with finite differences. Note that the performances for (5.3) with the filtering of (5.4) with $P = 1$ for the zero-noise case yields practically the same results as for (5.6). This shows that the two methods are practically identical (in the absence of random noise); see the remark after Eq. (5.6). Noise in the data set considerably increases the error for all three methods. Although sharp gradients (viz., low σ_ω) can be resolved quite accurately, weaker gradients (viz., high σ_ω) can only be barely distinguished from the noise at higher

noise levels. Rather unexpected is that these results show that the estimator (5.3) *without* filtering at high noise levels performs better than the same estimator *with* filtering. A possible explanation is that the filtering removes not only part of the noise but also a substantial part of the velocity signal. The estimator in (5.6) also implies a spatial filtering of the data, but apparently the loss of velocity information is not as strong as for (5.4) with $P=1$. Roughly, the noise level in the vorticity data is an order of magnitude higher than in the PIV velocity data.

As a general conclusion from this test we can say that the noise in the PIV data set causes that large regions with a relatively low amplitude of the vorticity are attenuated more strongly than small regions with high values of the vorticity. We will therefore observe only the vorticity fluctuations at a certain scale. It is likely that this scale is directly related to the spatial resolution (viz., ΔX , ΔY) of the data set. This should be borne into one's mind when interpreting PIV results. Of course, the test carried out here is very limited, and further investigation on this matter is required. Currently the estimator given in Eq. (5.6) appears to have the best overall performance of the three estimators considered here, and is therefore preferable to the other two methods. The results of this test confirm our initial thought that the noise is amplified by the differentiation of the PIV data. This implies that if we want to yield significant results on the vorticity, say a noise level in the vorticity of 10–20%, we should measure the velocity with an accuracy of 1–2%. We have seen in the previous chapters that such high accuracy is within reach of the digital PIV method.

5.3 Deformation

Our interest is to study the relation between different regions of a flow, and how kinetic energy and shear-stress is exchanged between these regions. A convenient way to describe the processes that take place in a flow is through its *topology*; the flow can be represented by a collection of saddle-points, repelling and attracting foci that correspond to critical points in the Jacobian of the velocity field (Hesselink & Helman 1987). Here we review a method due to Hunt *et al.* (1988) to break down a flow field into three generic flow types, characterized by its *deformation*. This classification is based on the value of the second invariant of the deformation tensor and the pressure. The second invariant of the deformation tensor is given by²

$$II = \frac{\partial v_i}{\partial X_j} \frac{\partial v_j}{\partial X_i} = E_{ij}^2 - \frac{1}{2}\omega_i^2 \quad (5.10)$$

with $\vec{v}=(v_1, v_2, v_3)$ and $\vec{X}=(X_1, X_2, X_3)$, and where E_{ij} is the symmetric strain tensor

$$E_{ij} = \frac{1}{2} \left(\frac{\partial v_i}{\partial X_j} + \frac{\partial v_j}{\partial X_i} \right)$$

²Here we use the suffix notation for vector and tensor components, with the usual convention that terms containing a repeated suffix are to be regarded as summed over all three possible values of the suffix.

(Batchelor 1967) and ω_i is the vorticity vector. The root-mean-square values of II , and the fluctuating pressure p and absolute velocity $\|\vec{v}\|$ are denoted by the subscript *rms*. Hunt *et al.* (1988) propose the following classification:

E: eddies

These zones are defined by a strong swirling motion *with* vorticity (thus excluding irrotational swirling motion). However, strong vorticity can also be connected to shear layers. To exclude shear layers we have to look at the local pressure; vortices are characterized by a local minimum in the fluctuating pressure (Hunt *et al.* 1988; Robinson 1991a). Therefore, two criteria are applied to define E zones: (a) the second invariant of the deformation tensor is less than $-2II_{rms}$ (viz., the vorticity is much larger than the rate of strain), and (b) the pressure is less than $-0.2p_{rms}$.

C: convergence zones

These zones are defined as regions with irrotational straining motion i.e. with a strong convergence or divergence of streamlines. This region contains a stagnation point (defined in a suitable frame of reference). The criteria for the C zone are: (a) the straining is large compared with the vorticity, i.e. $II > II_{rms}$, and (b) the pressure in the interior of a C region is larger than p_{rms} . The pressure criterion excludes the classification as C regions of irrotational swirling flow.

S: streaming zones

In these zones the flow velocity deviates strongly from the mean velocity, and with low deformation of the streamlines. These regions are defined by: (a) $v^2 > v_{rms}^2$ (viz., high speed), and (b) $|II| < II_{rms}$ (viz., low deformation).

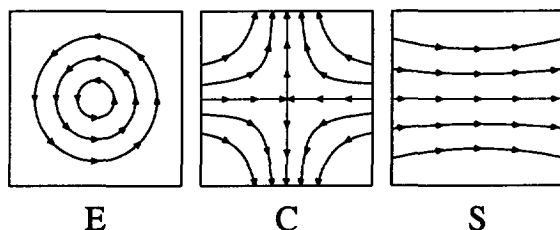


Figure 5.3: The generic flow types associated with *eddies* (E), *convergence zones* (C) and *streaming zones* (S); Hunt *et al.* (1988).

The generic flow patterns associated with the E, C and S zones are depicted in Figure 5.3. It is conjectured by Hunt *et al.* (1988) that each of these three regions has its own contribution to the transport processes in the flow. Let us consider for example *mixing*. The eddy (E) zones lack a strong mixing of the flow, while on the other hand strong mixing occurs in the convergence (C) zones. The streaming (S) zones have a low deformation,

but the velocity in this region is high with respect to other regions. So, streaming zones transport fluid between different flow regions. Hence, these zones make different contributions to mixing processes in flows. A similar distribution over these three flow types may also apply to other processes and flow quantities.

The method of Hunt *et al.* (1988) has been applied mainly to three-dimensional fully-resolved numerically simulated flows. In PIV we only have two-dimensional information of the velocity field in a planar cross section of the flow. Although this information is incomplete, and besides is contaminated with noise, we attempt to apply similar methods to describe the observed flow field. Presently there is very little knowledge with respect to the robustness of these methods and to the *interpretation* of the results for two-dimensional experimental (PIV) data. Nonetheless, our present aim was to acquire experimental data that would enable us to investigate coherent flow structures. Of course it will be necessary in a subsequent study to investigate in more detail the interpretation of these data. We will return to this point in the conclusion of this thesis; see Chapter 10. For now we will just use the information provided by PIV measurements to compute the second invariant of the deformation tensor, and apply the classification suggested by Hunt *et al.* (1988). With only two velocity components available on a regular mesh of point II is approximately given by first-order differences in $u_{i,j}$ and $v_{i,j}$, i.e.

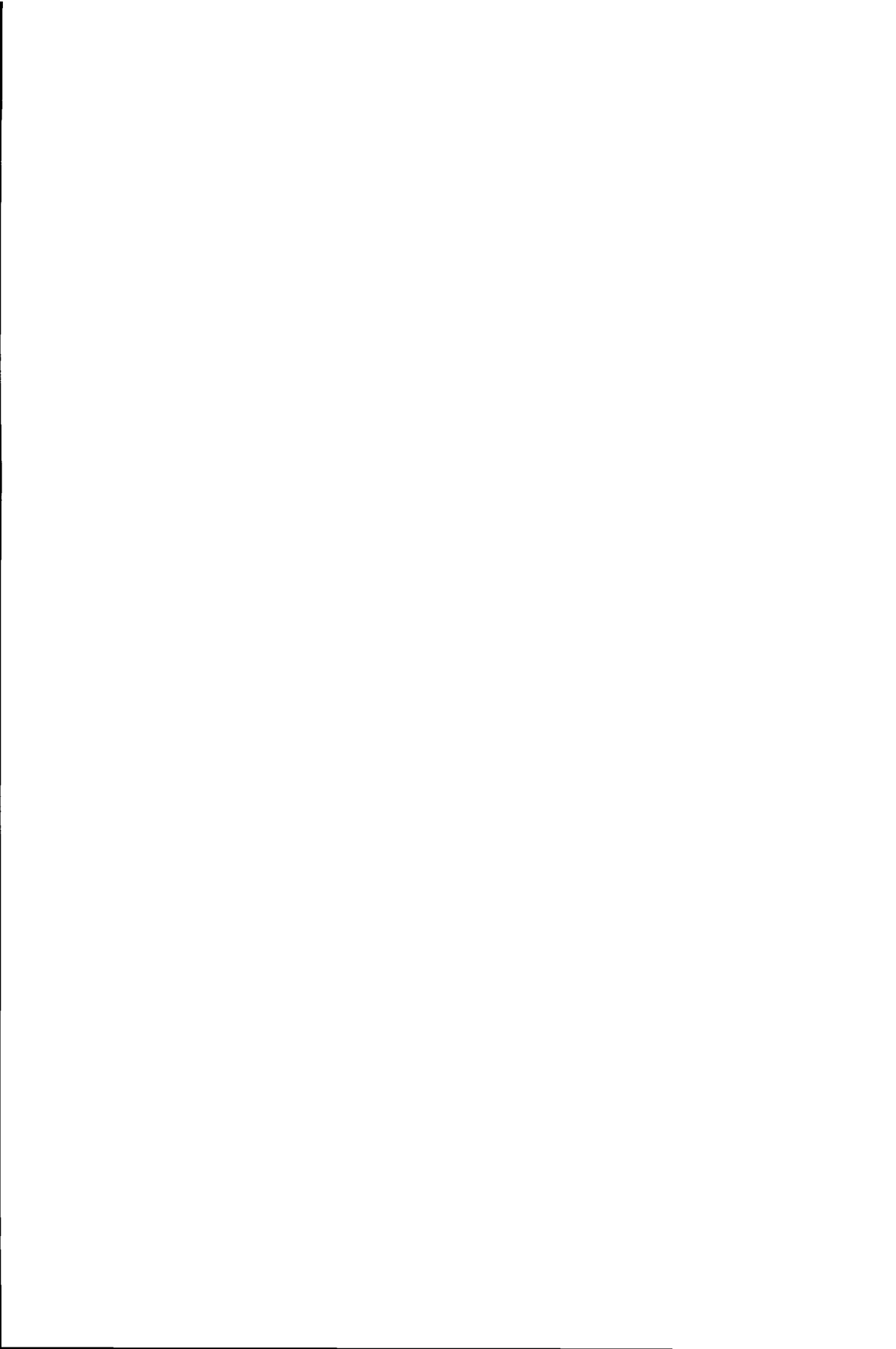
$$II_{i,j} \sim \left(\frac{u_{i+1,j} - u_{i,j}}{\Delta X} \right)^2 + \left(\frac{v_{i,j+1} - v_{i,j}}{\Delta Y} \right)^2 + 2 \left(\frac{v_{i+1,j} - v_{i,j}}{\Delta X} \right) \left(\frac{u_{i,j+1} - u_{i,j}}{\Delta Y} \right). \quad (5.11)$$

We have seen in the previous section that first-order differences tend to be very sensitive to the noise in the velocity data. For ω_Z we used an alternative method, given in (5.6), based on Stokes' theorem; see (5.5). We did not look for a similar alternative for II . Instead we used the expression in (5.11). To reduce the effect of noise we filtered the velocity data prior to applying (5.11) according to the method by Landreth & Adrian (1990b).

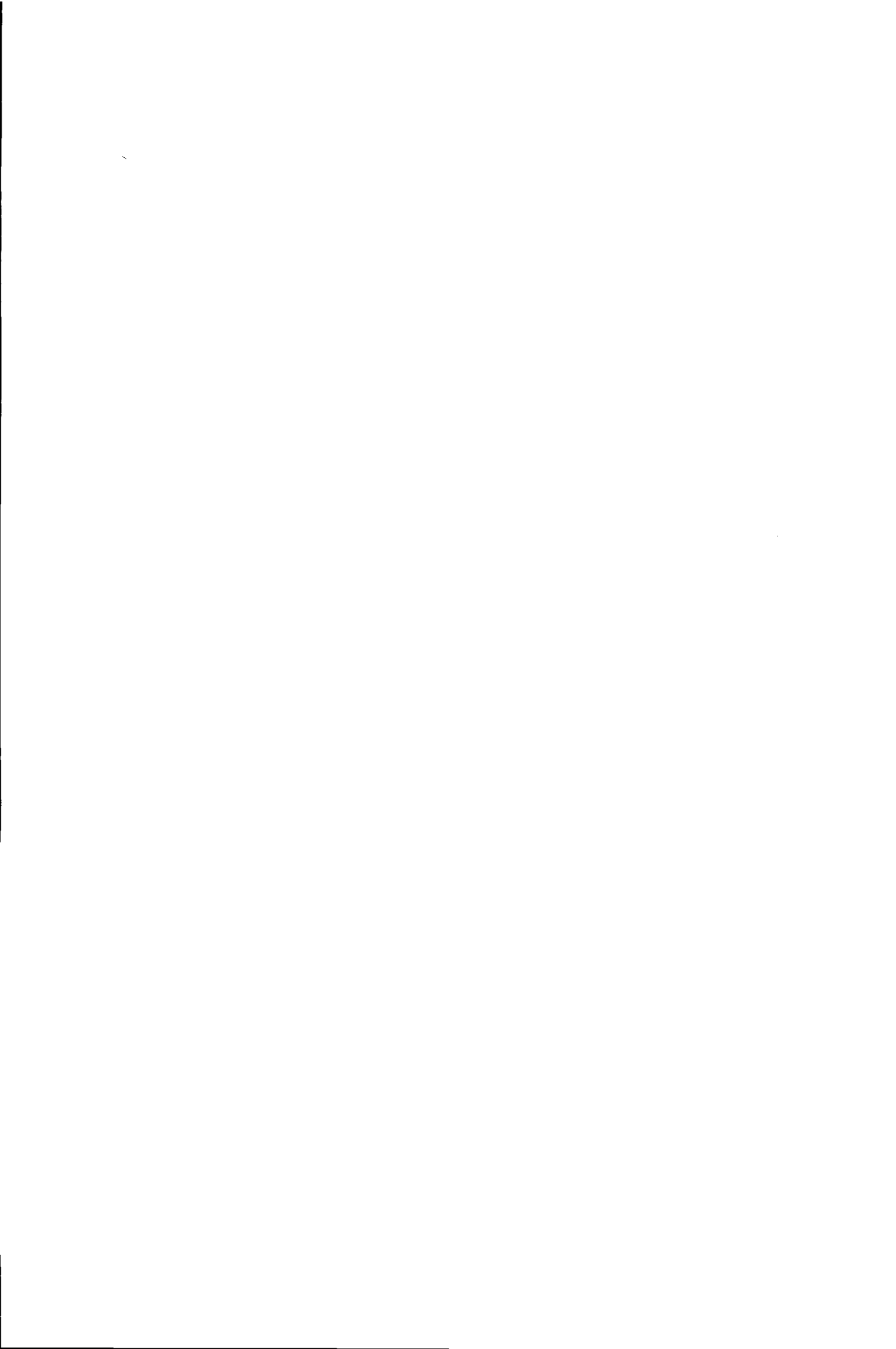
5.4 Conclusion

In this chapter we have described the methods to compute the vorticity and the second invariant of the deformation tensor. These quantities allow us to deduce the structures that are present in the flow. The main problem is that the PIV data are contaminated by noise. This has a strong influence on the estimation of these quantities. Besides that, the PIV data only provide two-dimensional information from a planar cross-section of the flow, so that we can only estimate a sub-set of the components of the vorticity vector and deformation tensor. This makes it more difficult to interpret the data.

In order to yield significant estimates of the vorticity and deformation the noise in the PIV data should at least be smaller than 5%. In Chapter 3 we have seen that for DPIV an accuracy of 1–2% should be feasible. In the next chapter we discuss the results of a measurement with DPIV applied to turbulent flow behind a grid. These data were subsequently used to demonstrate the methods discussed in this chapter.



Part II
application



Chapter 6

Application of Digital Particle Image Velocimetry to Turbulent Flow¹

Abstract. *The spatial resolution and measurement accuracy in digital PIV are lower than those in conventional or optical PIV. The question is raised whether this prevents significant measurements of turbulent flow structures with digital PIV. To assess the feasibility of digital PIV with respect to turbulent flow measurements a test experiment is carried out. Data from a digital PIV measurement of homogeneous grid turbulence are used to estimate the vorticity and deformation of the flow field. The results demonstrate that consistent detection of flow structures by these flow quantities is possible for digital PIV data.*

6.1 Introduction

Traditionally PIV images are recorded on photographic film. The film negative is interrogated optically in a point-by-point manner by the Young's fringes method. The fringe pattern is digitized and analyzed by a computer (Adrian 1986b). We refer to this method as *optical PIV*, or OPIV. Digital particle image velocimetry (DPIV) is an alternative interrogation method in which the entire image is digitized. This image is subsequently analyzed by direct computation of the auto-correlation of small sub-images. The basic principles of OPIV and DPIV are equal; the main difference between these techniques is that DPIV provides high processing speed compared with OPIV. The processing of 1,000 in DPIV can be carried out in less than a minute (Westerweel *et al.* 1992), while in OPIV the same amount of interrogations is carried out in 15–60 minutes (Adrian 1986b; Lourenço & Krothapalli 1988a). This gain in processing speed is at the expense of accuracy and resolution. The relative measurement error in OPIV is estimated at less than

¹WESTERWEEL, J., ELGAARD, C. & NIEUWSTADT, F.T.M. 1991 Presented at: *EuroMech Colloquium 279 "Image Analysis as a Measuring Technique in Flows"* (Delft) July 2–5 (*unpublished*).

1%, whereas the error in DPIV is estimated at 1–2%. The high processing speed of the DPIV method allows the analysis of a large number of images (say 100–1000 images) within an acceptable amount of time. The analysis of a large set of images is required for the analysis of time sequences or the statistical investigation of coherent flow structures². Up to now DPIV was applied to relatively simple flows, such as the wake flow behind a cylinder (Westerweel *et al.* 1992) and the evolution of a vortex ring (Willert & Gharib 1991). In these applications the decrease in resolution and accuracy were acceptable. However, these limitations may not be acceptable in the application of DPIV to turbulent flows. It was therefore decided to carry out a test measurement. For this purpose PIV photographs were used that were taken in a PIV facility at the Fluid Dynamics Unit at the Department of Physics of the University of Edinburgh. This facility is used for investigation of homogeneous turbulent flow generated by a grid (*grid turbulence*) (McCluskey *et al.* 1993). The PIV photographs were digitized and subsequently analyzed with DPIV.

6.2 Experimental set-up

The measurements were carried out in an air flow behind a grid in a small wind tunnel. The cross section of the tunnel was $50 \times 50 \text{ mm}^2$. The turbulence was generated by a square grid with a distance of 2 mm between the grid cells. The grid had a solidity of 3 (the solidity is defined here as the ratio of the area covered by the grid bars and the area of the grid maze.) The mean flow velocity was 2.3 m/s. The Reynolds number of the flow—based on the mean flow velocity and mesh distance—was equal to 300. The flow was seeded with corn-oil droplets with a diameter of 1–2 μm . The number density of the seeding particles was estimated at 3 mm^{-3} . The flow was illuminated with a scanning-beam light sheet from a 15 W cw Ar⁺ laser. The thickness of the light sheet was approximately 1 mm. To create a scanning beam an 18-sided polygon mirror rotating at 300 Hz was used. In this configuration the exposure time-delay is 185.2 μs . Photographs were taken with a 35 mm photographic camera equipped with a 50 mm focal length lens with an numerical aperture of 2.8. The optical axis of the camera was normal to the plane of the light sheet. The image magnification was equal to 0.5. The area in the light sheet that was recorded was 70 mm in the streamwise direction and 50 mm in the spanwise direction. The center of the viewing area was located at a distance of 150 mm downstream of the grid. We used ASA 400 Kodak black-and-white film (which has a resolution of 80 line-pairs/mm). The focal depth is about the thickness of the light sheet. The camera shutter was set to 1/1000 s; with an exposure time-delay of 185.2 μs this yields an average of 5.4 exposures on a single photograph. In this configuration the estimated particle-image displacement between two exposures was about 0.24 mm on the film negative. In total three negatives were selected for further analysis. Here we discuss in detail the analysis and results for one particular negative.

²see Chapter 1

6.3 Digital analysis

The negative was projected on a white sheet of paper, and a selected area in the negative was recorded by a CCD-video camera. The size of the area was chosen as follows. The (nominal) particle-image displacement on the negative was equal to 0.24. Following the recommendations by Keane & Adrian (1990) this implies that the diameter of the interrogation area should be four times the in-plane displacement. We therefore chose an interrogation area of 1 mm². The digital image consisted of 512×512 pixels, and was analyzed with 32×32-pixel interrogation regions. This implies that the area covered by the digital image is 256 mm² (the digital image consists of 16×16 contiguous 32×32-pixel interrogation areas). The CCD-array that was used has a 3:2 aspect ratio, so that we selected an analysis area on the film negative of 20×14 mm².

The image was digitized to 512×512 pixels, with 256 grey-levels. The digital analysis with 32×32-pixel interrogation regions, with a 50% overlap, yielded a total of 31×31 interrogations. The interrogation analysis was carried out on a Hewlett-Packard HP9000/835S, which takes 36 seconds³ for one image. It should be emphasized that this processing time is obtained *without* the use of any dedicated hardware (such as an array processor). The analysis of the digital image without any preprocessing appeared to contain a large number of spurious vectors (about 16%). This was most likely caused by the non-uniform illumination in the digitization of the negative. We therefore subtracted the image background and normalized the image contrast prior to the DPIV analysis⁴. This reduced the number of spurious vectors considerably to within an acceptable amount (to about 5%). The result is shown in Figure 6.1. Before we can extract any quantitative information from the PIV data set we had to remove the spurious vectors. The detection of a spurious vector was based on the deviation of a vector from the median displacement of its 8 neighbours⁵. Vectors with large deviations from the estimated local median displacement are discarded from the data sets. The discarded vectors are replaced by linear interpolation.

In Table 1 are given the mean, rms, minimum and maximum values for the streamwise (u) and spanwise (v) velocities, and the velocity amplitude ($\sqrt{u^2+v^2}$). The turbulence intensity is defined as the ratio of the rms value and the mean value of $\sqrt{u^2+v^2}$. From the values listed in Table 1 we find that the turbulence intensity in the present data set is 14%. (This is a rather high value for grid turbulence. Apparently, a distance of 75 times the grid spacing downstream the grid was not sufficient for the flow to develop. We suspect that this is related to the high value of the solidity of the grid.) In Figure 6.2 is given the vector map of the displacement field after subtraction of the mean flow velocity given in Table 1. This figure shows that the vector map contains several large eddy structures. These structures will be further analyzed in the following section.

³On the later model HP9000/720 the analysis time for the same image is only 8 seconds.

⁴see Appendix B.1

⁵see Chapter 4

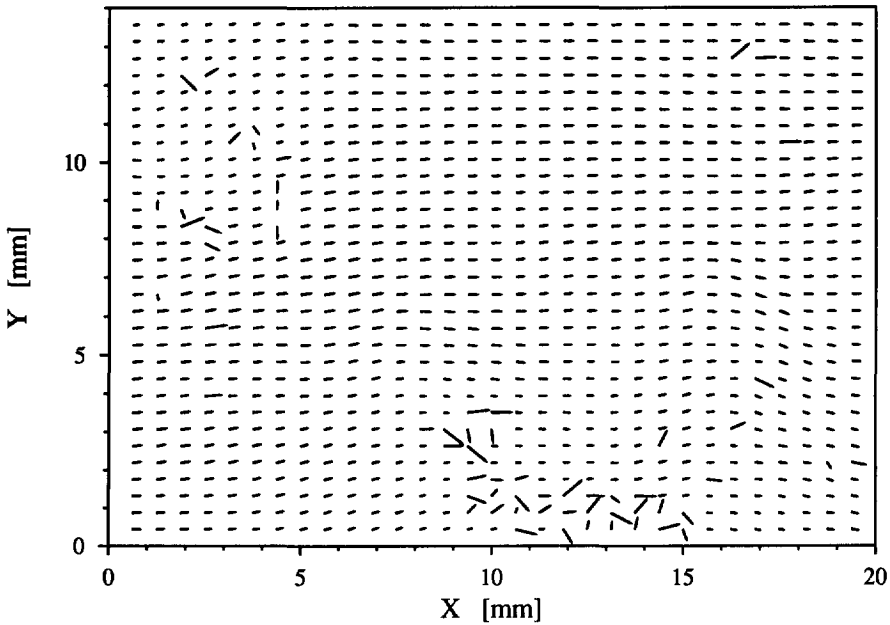


Figure 6.1: The vector map of the raw output from the interrogation analysis of a digital PIV image of a turbulent flow behind a grid. See text for further details.

Table 1 The statistics for the streamwise (u) and spanwise (v) velocity components, the velocity amplitude ($\sqrt{u^2+v^2}$) and the out-of-plane vorticity (ω_z).

		mean	rms	min.	max.
u	m/s	2.46	0.39	1.53	3.24
v	m/s	0.17	0.29	-1.04	0.76
$\sqrt{u^2+v^2}$	m/s	2.47	0.38	1.60	3.30
ω_z	10^3 s^{-1}	-0.05	0.31	-1.14	0.90
II	10^6 s^{-2}	0.07	0.21	-0.92	3.09

6.4 Vorticity and deformation

In order to make a quantitative evaluation of the structures observed in Fig. 6.2 we used the experimental PIV data to compute the out-of-plane component of the vorticity and

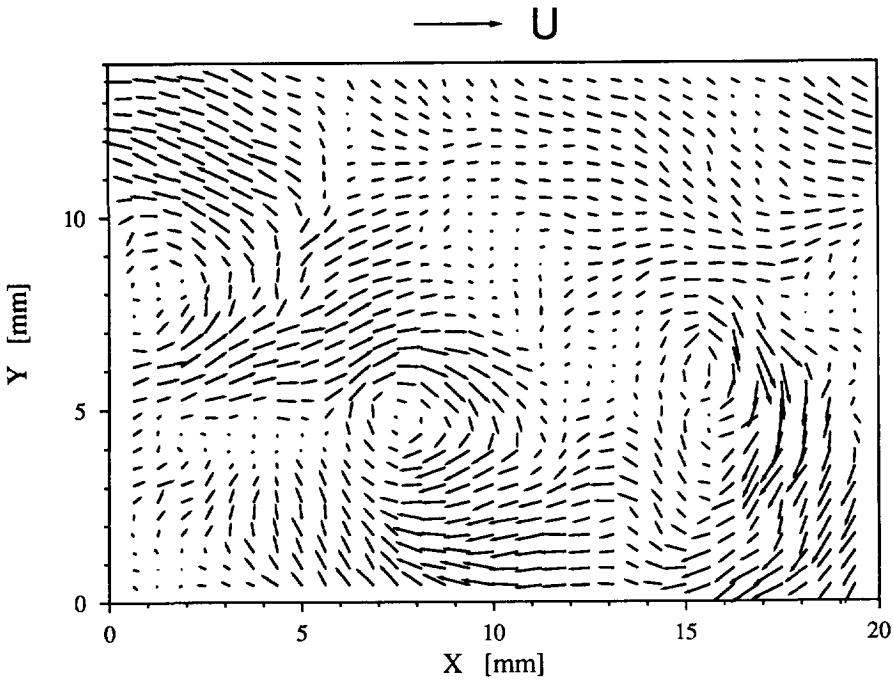


Figure 6.2: The vector map of Fig. 6.1 after replacing spurious vectors and subtraction of the mean velocity (represented by the arrow at the top of the figure).

the second invariant of the deformation tensor⁶.

The out-of-plane vorticity component $\omega_z (= \partial v / \partial x - \partial u / \partial y)$ can be expressed as:

$$\omega_z = \lim_{A \rightarrow 0} \frac{\oint_C \vec{u} \cdot d\vec{l}}{A} \quad (6.1)$$

where C is a contour enclosing the area A . This expression was used to compute the vorticity (Landreth & Adrian 1990a), by taking the contour C over the eight-connected neighbourhood of a point in the velocity data sets. This procedure yields less noisy results compared with estimating ω_z from first-order differences in u and v . The mean, standard deviation, minimum and maximum of ω_z are given in Table 1. In Figure 6.3 we indicated regions with a high magnitude of the vorticity (i.e. fluctuations that deviate more than one time the rms value of the vorticity). One can clearly see large regions with positive and negative vorticity. Elongated regions correspond to structures that seem to correspond to shear-layer structures. Note how high momentum fluid is found between adjacent regions

⁶see Chapter 5.

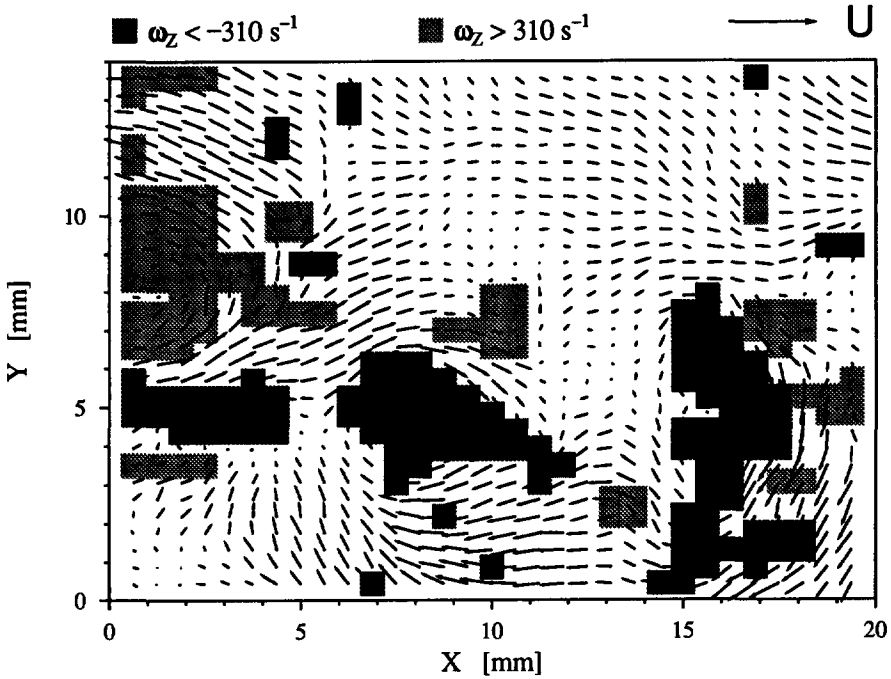


Figure 6.3: The (out-of-plane component of the) vorticity corresponding to the vector map in Fig. 6.2.

of positive and negative vorticity. The regions that cover only one or two data points probably arise due to a large fluctuation of the random measurement error.

Another way to characterize the structures observed in Fig. 6.2 is through the value of the second invariant of the deformation tensor, given by

$$II = \frac{\partial u_i}{\partial x_j} \frac{\partial u_j}{\partial x_i} \quad (6.2)$$

with $\vec{u} = (u_1, u_2, u_3)$ and $\vec{x} = (x_1, x_2, x_3)$. (Here we use the suffix notation for tensor components; terms containing a repeated suffix are summed over the suffix variable.) Hunt *et al.* (1988) describe a method to divide a flow map into three zones: eddy zones (E), convergence zones (C) and streaming zones (S). This is done according to the value of the second invariant of the deformation tensor II , namely

$$\text{E: } II < -2 \cdot II_{\text{rms}}$$

$$\text{C: } II > II_{\text{rms}}$$

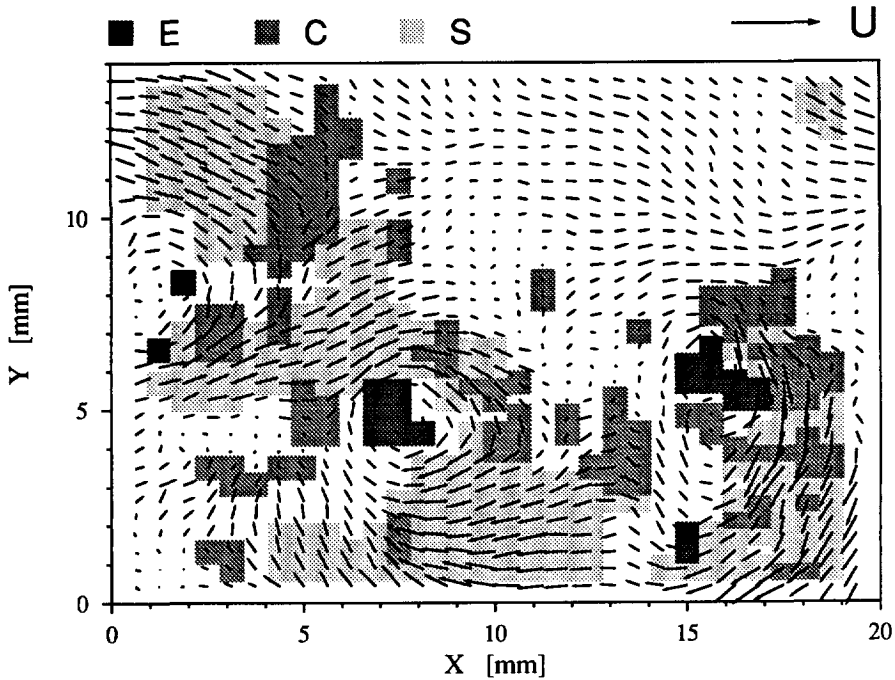


Figure 6.4: The classification of the vector map of Fig. 6.2 in eddy (E), convergence (C) and streaming (S) zones, based on the value of the second invariant of the deformation tensor and magnitude of the fluctuating velocity.

$$S: -2 \cdot II_{\text{rms}} \leq II \leq II_{\text{rms}} \text{ and } \sqrt{u^2 + v^2} \geq u_{\text{rms}}$$

where II_{rms} is the rms value of II , and u_{rms} the rms value of $\sqrt{u^2 + v^2}$. The division into E, C and S zones is a convenient way to detect coherent structures in turbulent flows⁷. However, to do this properly for a three dimensional flow it would also require fully three dimensional flow data (velocity and pressure; see Hunt *et al.* (1988)). Because PIV measurements yield only two velocity components in a planar cross section of the flow the division has been made as if the flow was two-dimensional. II was computed by first-order differences. This procedure is quite sensitive to measurement errors. Therefore, prior to differentiation a mild low-pass filter was applied (Landreth & Adrian 1990b). The statistics of II are given in Table 1. The subdivision of the flow map in Fig. 6.2 in E, C and S zones is given in Figure 6.4.

At present we want to refrain from linking the detected E, C and S regions to any interpretation of the flow dynamics. Instead we use the result shown in Fig. 6.4 to verify whether the observed flow patterns match the detected regions. The map in Fig. 6.4 is

⁷Further details are given in Sect. 5.3.

dominated by large S zones that clearly match parts of the flow map with high velocity and low deformation. At the edges of the S zones, and at places where different S zones meet, we find C zones. In some of the C zones the vector map displays a flow pattern that resembles a stagnation point. The vector map also contains a few distinct eddy structures. Note that only the cores of the eddy structures are detected as E regions; this is in correspondence to what we would expect, i.e. the eddy consists mainly of irrotational swirling flow (except for its core). However, since we have no information about the pressure field we cannot distinguish between irrotational swirling flow and shear-layer. We therefore also detect some other regions with a shearing motion at the edges of S zones as E zones.

6.5 Conclusions

The present results demonstrate that DPIV can be applied to turbulent flows to yield quantitative information of the (coherent) motions present in the flow. Coherent flow structures were detected by applying a threshold value to the local value of the (out-of-plane component of the) vorticity and the second-invariant of the (two-dimensional) deformation tensor. The image analysis in DPIV requires only a fraction of the time that would be needed for the analysis of the same image with the traditional PIV method (OPIV). In the measurement described here we had a flow with a turbulence intensity of 14%. Although this is a rather high value for grid turbulence it is about the turbulence intensity anticipated in the near-wall region of a turbulent boundary layer; this flow type will be the object of study with DPIV in the near future. The present results provide a picture of the quality of the results we can expect in this future study. In the present application the fluctuations of the velocity with respect to the mean are relatively large compared to the estimated relative measurement error in DPIV (i.e. 14% and 1-2% respectively). One can expect that the quality of the results obtained with DPIV decreases with decreasing turbulence intensity. Cornelisse *et al.* (1991) carried out an experiment similar to the one presented here. They took measurements with OPIV, DPIV and LDA of turbulent flow generated behind a grid, but at lower turbulence intensities (down to 3%). They compared the OPIV and DPIV data obtained from corresponding interrogation regions in the same negative. This comparison showed that even at a turbulence level of only 3% DPIV could still yield significant velocity data.

Chapter 7

Measurements with Particle Image Velocimetry of Fully Developed Turbulent Pipe Flow at Low Reynolds Number¹

Abstract. *Measurements with particle image velocimetry were carried out in fully developed turbulent pipe flow at a Reynolds number of 5,277. Data were obtained in a plane through the centerline of the pipe, across the full diameter. Statistical properties of the flow obtained by ensemble averaging photographs and averaging the data along the axial direction were in good agreement with direct numerical simulation. Maps of instantaneous tangential vorticity reveal spatial structures near the pipe wall that resemble coherent flow structures predicted by direct numerical simulation and observed in earlier experimental studies.*

7.1 Introduction

Fully developed turbulent pipe flow has been the subject of experimental studies for decades (see e.g. Schlichting (1979)), and it is very well suited for testing and exploring new experimental techniques and numerical codes such as direct numerical simulation. From a numerical point of view, the development of codes for other standard turbulent wall-flows such as channel flow and boundary-layer flow is less complicated than for a pipe flow because they can be implemented in rectangular grids. Pipe flow, on the other hand, is most naturally considered in cylindrical coordinates. To test the implementation of the equations of motion in a cylindrical coordinate system, a combined study was initiated in which a code for direct numerical simulation (DNS) of turbulent pipe flow was developed. Following an earlier DNS study on turbulent channel flow (Kim *et al.*

¹WESTERWEEL, J., ADRIAN, R.J., EGGELS, J.G.M. & NIEUWSTADT, F.T.M. 1993 In: *Applications of Laser Techniques to Fluid Mechanics* (ed. R.J. Adrian *et al.*) Springer-Verlag, Berlin.

1987) the Reynolds number based on the friction velocity u_* and the pipe diameter D was chosen to be $Re_* = 360$. Concurrently, experiments on fully developed pipe flow were carried out with hot-wire anemometry and particle image velocimetry (PIV) at the same Reynolds number. This paper describes the experimental details and the results of the measurements with PIV. A paper that includes all numerical and experimental results obtained in this study is in preparation (Eggels *et al.* 1993a).

Particle image velocimetry (PIV) is an optical measurement technique that allows the acquisition of instantaneous flow fields in a planar cross section of a flow. The technique is a two-stage process. First, the flow is seeded with small particles which are able to follow the motion of the fluid. A thin sheet of light illuminates a plane in the flow. The motion of the particles is usually recorded by taking a double-exposure photograph. The displacement of particle images during the time-delay between the two exposures is directly proportional to the local fluid velocity. Second, the image on the photograph is analyzed ("interrogated") on a regular grid of points, where each point yields the local in-plane displacement of the particle images. Given the image magnification and the time delay between the exposures one obtains the instantaneous in-plane velocity of the fluid. For further details on PIV refer to a review by Adrian (1991) and a paper by Keane & Adrian (1990).

PIV is a multi-point technique, and it is therefore very well suited to investigation of coherent flow patterns. These patterns have been observed in flow visualization and more recently in numerical simulations. Traditional single-point measurement probes like the hot-wire and laser-Doppler anemometer cannot reveal these structures in a straightforward way. By spatial differentiation of PIV velocity data one can obtain the out-of-plane component of the vorticity. It is generally believed that the patterns observed in the vorticity hold the key to understanding the dynamics of coherent structures in turbulence. Thus, the PIV measurements in turbulent pipe flow can not only provide experimental results on traditional quantities such as turbulence statistics, but also quantitative results on instantaneous vortical structures. Recently, Liu *et al.* (1991) performed PIV experiments on turbulent channel flow, in which they were able to identify these flow patterns. The flow conditions in their experiment were comparable to the DNS performed by Kim *et al.* (1987). The aim of the present experiment was to perform similar measurements for conditions at which a DNS of the pipe flow exists.

The PIV measurements were made near the end of a 17 m long smooth pipe with an inner diameter of 127 mm and a Reynolds number of 5,277 based on the bulk velocity and the diameter of the pipe. Measurements with laser-Doppler anemometry (LDA) were carried out to verify that the flow at the test section was fully developed. The PIV laser sheet illuminated a plane through the centerline of the pipe, and a view area that included the full diameter of the pipe was photographed. In total 33 photographs were taken. Each photograph yielded instantaneous two-dimensional data sets of the axial (x -coordinate) and radial (r -coordinate) velocities at 8,500 points. (We will use (u,v) to denote the components in the (x,r) directions, and z to denote the direction normal

the PIV light sheet. In some cases we will use y to denote the distance from the wall.) From the PIV velocity data conventional turbulence statistics like the mean and the RMS fluctuation, the Reynolds stress and the power spectrum have been determined. These are compared with the results from the LDA measurements, and with results obtained from the numerical simulation. Subsequently, the instantaneous tangential component of the vorticity computed from the PIV data and the associated vortical structures will be evaluated qualitatively.

7.2 Experiments

7.2.1 pipe flow facility

The pipe flow facility was previously used for accurate hot-wire measurements on fully developed turbulent flow at a Reynolds number of 50,000 (Lekakis 1988). The air flow through the pipe was driven by a blower, powered by a d.c. motor with a variable transmission. The air passed a settling chamber, a honeycomb, and a grid before it entered the pipe. The grid introduced an initial disturbance, which reduced the inlet length that was required before the flow became fully turbulent. The pipe had a total length of 17 m, equal to 134 diameters. At high Reynolds numbers an inlet length of 40 to 50 pipe diameters is considered sufficient length to produce a fully developed flow (Schlichting 1979), but at low Reynolds numbers the development of the flow depends on the flow condition at the pipe inlet (Wyganski & Champagne 1973). Measurements conducted with LDA, which will be discussed later, indicated that the flow was fully developed at the location of the PIV measurements.

The flow rate through the pipe was set and monitored by measuring the pressure drop over a length of 11.88 m. (The high pressure tap was located 2.74 m downstream from the pipe inlet.) For a Reynolds number of 5,300 the expected value for the pressure drop is about 0.80 Pa, corresponding to a water column of 76 μm . The pressure drop was measured with a micro-manometer, which had an absolute reading error of 0.04 Pa.

The test section at the end of the pipe had a transparent wall of 80 μm thick acetate, designed to eliminate serious aberrations caused by light rays passing through the pipe wall at shallow angles. This made it possible to photograph particle images located less than 0.7 mm from the wall.

7.2.2 seeding

For both LDA and PIV measurements the flow was seeded with 1–2 μm diameter oil droplets generated by two atomizers. The droplets were small enough to follow the motions of the air flow very accurately. The density of the seeding was controlled by the flow rate of air through the atomizers. Injection into the pipe flow was by means of a small L-shaped pipe located at the centerline, about 14 diameters downstream from the pipe inlet, and orientated in the direction of the flow. In this way the injection of seeding did

not introduce swirl into the flow, and the seeding was well mixed across the pipe by the time it reached the test section.

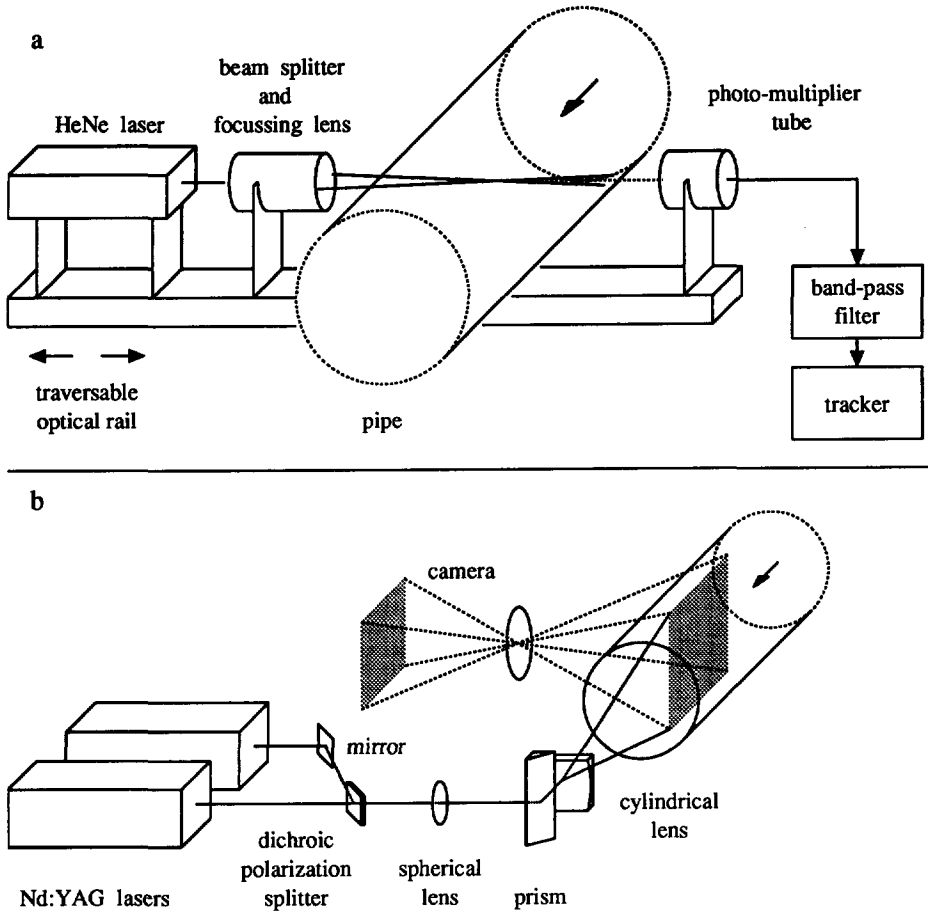


Figure 7.1: Optical configuration for the LDA (a) and PIV (b) measurements.

7.2.3 LDA measurements

LDA measurements of the axial component of the velocity were carried out with a 5 mW HeNe laser in a dual-beam configuration, with a photo-multiplier in the forward scattering direction (see Figure 7.1a). The laser beam was split into two parallel beams

with a separation of 48 mm, and these two beams were focussed to a measurement spot with a 249.7 mm focal length lens. The measurement volume defined by the e^{-2} optical intensity was 250 μm in diameter and 2.59 mm long. The output signal from a TSI 1090 frequency tracker was sampled at 10 Hz (0.1 s roughly corresponds to an Eulerian time scale, estimated by dividing the pipe diameter by centerline velocity) and integrated over 300 s to determine the mean value of the velocity. The root-mean-square (RMS) fluctuating velocity was measured with a digital RMS voltmeter, with an integration time-constant of 100 s. The estimated statistical sampling errors for the measured velocities were about 0.3% for the mean and 1–2% for the RMS.

7.2.4 PIV measurements

The optical system for the PIV measurements is sketched in Figure 7.1b. Light pulses were provided by two frequency-doubled Nd:YAG pulsed lasers with an energy of 130 mJ per pulse at a repetition rate of 20 Hz. The firing of the lasers was accurately synchronized with a time delay of 0.30000 ms. The orthogonally polarized laser beams were combined into a double-pulsed beam by a polarization splitter plate. A prism at the pipe outlet reflected the beam 90 degrees into the pipe. A spherical lens (1000 mm focal length) combined with a cylindrical lens (–100 mm focal length) transformed the beam into a thin, vertical light sheet that spanned the entire diameter of the pipe with a thickness of 0.4 mm. The light sheet had a non-uniform light distribution, with a maximum intensity near the centerline and gradually lower intensity towards the pipe wall.

A camera with a 300 mm focal length $f/5.6$ lens recorded double-exposure photographs on 5"×4" T-max 400 film, with a magnification of 0.70. The field of view was 127 mm (one pipe diameter) in the radial direction, by 141 mm in the axial direction, with a focal depth of 0.4 mm (comparable to the thickness of the light sheet). In total, 33 photographs were taken and developed.

7.2.5 interrogation of the PIV photographs

The negatives were analyzed in the interrogation system described by Landreth & Adrian (1990). Figure 7.2 shows a schematic of this interrogation system, which consists of a computer-controlled translation stage that holds the negative, a 256×256 pixel (px) CCD array (Reticon) with a frame grabber (Poynting Products), and a micro-computer (MicroVax II) with an array processor (Mercury Computers Numerix-432). The system was operated in "image mode", i.e. the particle image displacement is computed directly from the image observed in the interrogation spot, in contrast to the "fringe mode" in which the particle image displacement is computed from the optical Fourier transform of the illuminated spot. A condensed mathematical description of the analysis is given by Keane & Adrian (1990). The analysis in the "image mode" involves digitization of an interrogation area by a video camera trained on the film and computation of the two-dimensional auto-correlation of the image. The particle displacement in the interrogation spot is obtained from the centroid of the largest non-central peak in the auto-correlation.

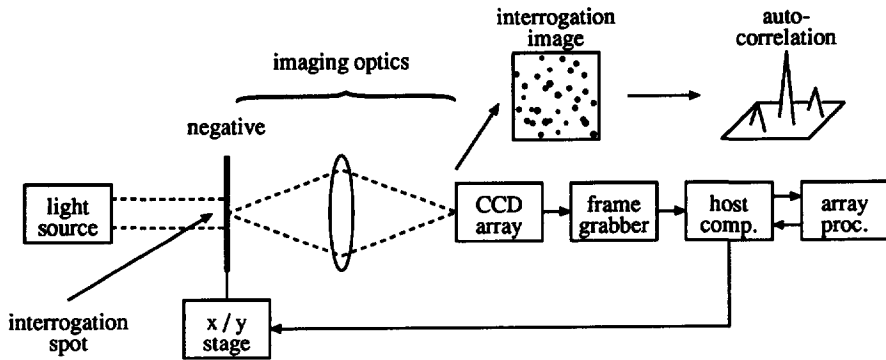


Figure 7.2: Schematic diagram of the interrogation system using the direct correlation method ("image mode").

After the analysis of one interrogation spot is complete, the negative is translated to the next interrogation position, and the procedure is repeated until the entire negative is analyzed.

We interrogated each negative with non-overlapping spots having a size of $0.98 \times 0.98 \text{ mm}^2$, with a spacing of 1 mm between subsequent interrogations in both directions. The corresponding measurement volume and spatial resolution in the flow are 0.78 mm^3 and 1.43 mm respectively. A single interrogation (in "image mode") was performed in 0.9 s. The analysis of one negative (8,500 interrogation positions) took about $2\frac{1}{2}$ hours. The maximum particle-image displacement was about 0.2 mm, and the average number of particle-image pairs in the interrogation spot was 25. Both figures are in accordance with the recommendations given by Keane and Adrian (1990) for optimal results. The particle images had a diameter of about $30 \mu\text{m}$. The RMS error in the displacement was estimated at 0.3 px (Prasad *et al.* 1992), which corresponds to 0.7% of the maximum particle-image displacement (0.2 mm) in the present experiment.

Reliable measurements were obtained down to a distance of 3.57 mm from the pipe wall. Closer to the wall pairing images overlap, and it was no longer possible to separate the displacement peaks from the central peak. If an image shifting technique had been used, reliable measurements could have been obtained at even smaller distances from the wall. Even so, the present results extend from the centerline down to 10 viscous wall units from the pipe wall (which is near the transition of the viscous sub-layer into the buffer layer).

The interrogation of each negative yielded a data set of 8,500 vectors (85 rows in the axial direction of 100 vectors each). The data sets contained a small number of spurious vectors (less than 2%). Spurious vectors are usually associated to signal "drop-out" due to an insufficient number of particle-image pairs or high velocity gradients within the

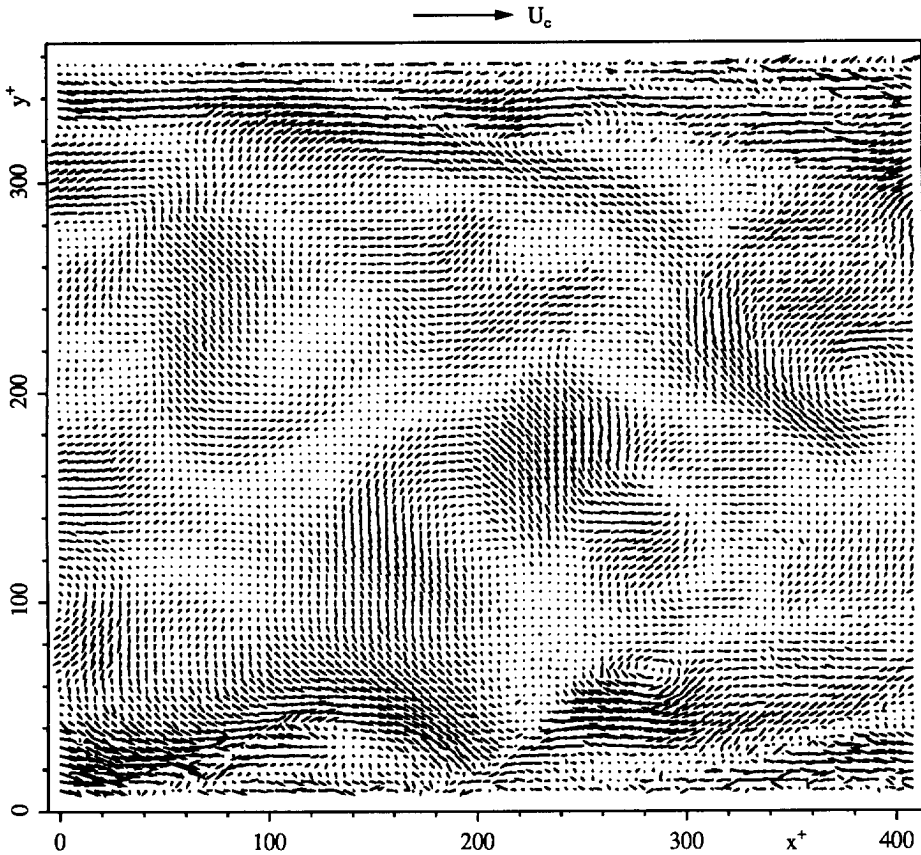


Figure 7.3: Vector map of the instantaneous fluctuating velocity obtained from the interrogation of a PIV photograph.

interrogation spot (Keane & Adrian 1990). In the present case most of the spurious vectors occurred near the pipe wall where the image contrast was low, the velocity gradients were high and pairs of images were likely to overlap. In a post-interrogation procedure each vector was compared with an estimate computed from its 8-connected neighbourhood. A vector was labeled as an outlier if the deviation from this estimate was statistically unacceptable (based on a 99% reliability interval). These outliers were discarded from the data set, and the gaps were filled by linear interpolation.

The vector map of one of the instantaneous fluctuating velocity fields (i.e. the total minus the mean velocity profile) is shown in Figure 7.3. The turbulent character of the flow is obvious, and regions of high activity near the wall are very clear.

7.3 Results

7.3.1 fully developed flow

The best way to verify that the flow was fully developed would have been comparison of the flow characteristics at several locations along the pipe. However, this would be a time-consuming operation. Instead with the LDA optics positioned near the test section, measurements were performed on (1) the mean centerline velocity as function of the measured pressure drop, and (2) the radial profile of the mean axial velocity component, at a Reynolds number close to 5,300. A substantial deviation of these quantities from the values expected for fully developed flow would have indicated that the flow at the test section is not fully developed (Patel & Head 1969).

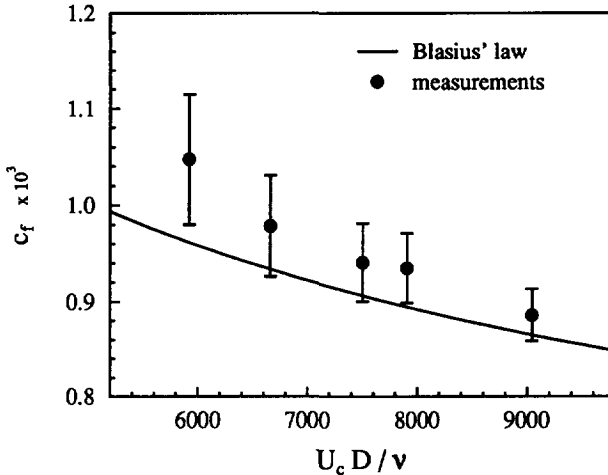


Figure 7.4: The skin-friction coefficient c_f as function of the Reynolds number $U_c D / \nu$ based on centerline velocity.

The skin-friction coefficient c_f was computed from the measured pressure drop ΔP and centerline velocity U_c according to (Schlichting 1979):

$$c_f = \frac{\tau_0}{\frac{1}{2}\rho U_b^2} = \frac{D}{2\rho L} \frac{\Delta P}{0.59U_c^2} \quad (7.1)$$

where ρ is the density of the fluid, L the length over which ΔP is measured and D the pipe diameter. We used $U_c/U_b = 1.30$ to express c_f in terms of centerline velocity rather than bulk velocity (This relation is valid for $Re \approx 4,000 - 7,000$; Patel & Head 1969). Figure 7.4 compares the present results with Blasius' semi-empirical law for a fully

developed pipe flow (Patel & Head 1969; Schlichting 1979): $c_f = 0.07910 \cdot (U_b D/\nu)^{-1/4}$. The error bars represent the reading error of the manometer. The present results are slightly higher than Blasius' law, but this is not unexpected, in view of the fact that the high-pressure tap is located only 22 diameters downstream of the pipe inlet where the flow was apparently in a developing state. LDA measurements of the mean velocity profile were made at a Reynolds number close to 5,300 along a line normal to the plane of the PIV light sheet, from the centerline of the pipe down to 3 mm from the wall. To test the velocity data for fully developed flow the results were compared to the profile for pipe flow given by Reichardt (1951):

$$U^+ = \frac{1}{\kappa} \ln(1 + \kappa y^+) + c \left(1 - e^{-y^+/\eta} - \frac{y^+}{\eta} e^{-by^+} \right) + \frac{1}{\kappa} \ln \frac{\frac{3}{2} \left(1 + \frac{2r}{D} \right)}{1 + 2 \left(\frac{2r}{D} \right)^2} \quad (7.2)$$

where y^+ ($= y u_* / \nu$) is the dimensionless distance from the wall and r/D the distance from the centerline relative to the pipe diameter, with the constants: $\kappa = 0.40$ (the Von-Kármán constant), $c = 7.8$, $\eta = 11.0$ and $b = 0.33$. The third term on the right-hand side is a correction that accounts for the wake region in the central part of the flow. The remaining terms correspond the logarithmic profile for turbulent wall flows ($U^+ = \kappa^{-1} \ln y^+ + 5.5$). Reichardt obtained the profile in Eq. (7.2) partially from a fit to experimental data. For a quantitative comparison with this profile the velocity data had to be normalized with friction velocity. Ideally, the friction velocity should be obtained independently, e.g. from the measured pressure drop (Schlichting 1979):

$$u_* = \sqrt{\frac{\Delta P D}{4 \rho L}} \quad (7.3)$$

However, measurement of ΔP (with an estimated error of 5%) would have yielded an estimate for u_* with an estimated error of 2.5%. The LDA data for the mean axial velocity have an accuracy of 0.3%; Using an estimate for u_* with an error that is substantially larger than 0.3% could lead to systematic errors in the normalized profiles. Alternatively, one could estimate the friction velocity from Blasius' law (using: $c_f = 2(u_*/U_b)^2$). Then the error in u_* would be (mainly) determined by the error in U_b . However, it appeared that an estimate of U_b (by numerical integration) from the experimental data had an estimated RMS error of 0.6%. Again, this would have yielded an estimate of u_* that was not accurate enough. It was therefore decided to determine u_* from a fit of the experimental data to Reichardt's profile, from which a least-squares value of $u_* = 44.0 \pm 0.2$ mm/s was obtained. This value was consistent with the value directly obtained from the pressure drop (44.2 ± 1.1 mm/s) and Blasius' law (43.7 ± 0.4 mm/s). The weighted residual sum of squares was equal to 45, about 40% larger than the upper critical value of the 99% reliability interval (31.3). Taking into account that Eq. (7.2) in its turn is a result of a fit to experimental data (we will return to this point in the next section), it was decided to accept the hypothesis that the flow was fully developed.

Table 7.1: Some experimental conditions and data in the LDA and PIV measurements and the computer simulation.

	LDA	PIV	DNS
Re	5,427	5,277	5,300
Re_*	370.6	366.3	360.0
U_b (mm/s)	644.4	626.6	—
U_c (mm/s)	853.2	842.9	—
U_c/U_b	1.324	1.345	1.312
u_* (mm/s)	44.0	43.5	—
U_b/u_*	14.65	14.40	14.72
U_c/u_*	19.39	19.38	19.31
c_f	9.32×10^{-3}	9.64×10^{-3}	9.23×10^{-3}
ν/u_* (mm)	0.3427	0.3467	—
$\frac{1}{2}D^+$	185.3	183.2	180.0
Δr^+	7.56	4.12	1.88
Δx^+	0.73	4.12	7.03
Δz^+	0.73	1.15	8.84 ^a

^a Tangential resolution at the pipe wall ($\frac{1}{2}D^+ \Delta\theta$).

7.3.2 turbulence statistics

Turbulence statistics were obtained from the PIV velocity fields by averaging data along lines of constant r in each field, and then ensemble averaging the line averages over the full set of 33 fields. The results are compared with those from the LDA measurements, and direct numerical simulation. The flow conditions in the experiments and the numerical simulation are summarized in Table 7.1.

The fitting procedure described above was applied to the mean velocity profile given by the PIV data to determine the friction velocity from which it was found that $u_* = 43.5 \pm 0.2$ mm/s. This value is within the estimated error of the value for u_* obtained from Blasius' law (42.7 ± 1.0 mm/s). Figure 7.5 shows the velocity profiles obtained from opposite sides of the centerline. For comparison the results obtained by the LDA measurements and the numerical simulation are also plotted. The profile obtained from the PIV data is slightly skewed (the data from the upper half of the pipe are smaller than those from the lower half), and in some locations it deviates significantly from the LDA and DNS data. Since the PIV data were obtained along a line normal to the plane of the light sheet, the results in Figure 7.5 could be interpreted as an indication of an azimuthal variation of the mean velocity profile (with a period of 2π). However, it should be noted that the PIV data roughly correspond to a total measurement time of only 7 seconds. (This value was obtained by multiplying the number of photographs (33) with the length of the measurement domain in axial direction (141 mm), divided by the mean axial ve-

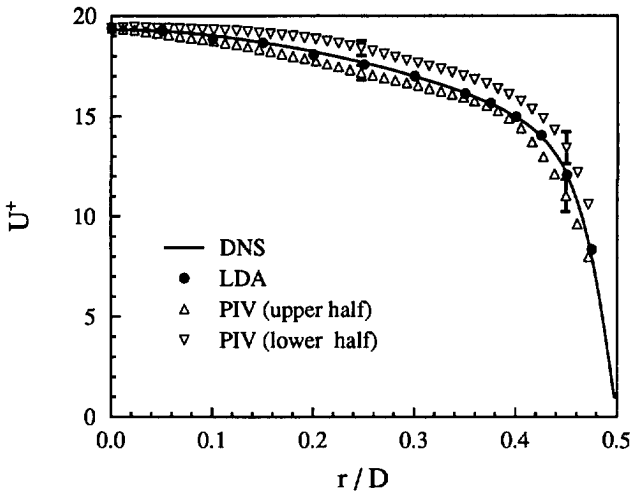


Figure 7.5: Axial mean velocity, normalized by friction velocity, as function of the distance from the centerline.

locity (626 mm/s.) This is very short in comparison with the measurement time for the LDA data (300 s). We therefore did not immediately accept a physical cause for the skew in Figure 7.5, but first investigated whether it could be related to the finite sample size of the PIV data.

It is important to realize that there is a difference in the way velocity data is acquired in PIV with respect to LDA. In LDA the velocity profile is obtained *sequentially*, at different r -locations. Thus in LDA the data points at different distances from the wall are statistically independent. On the other hand, in PIV the velocity data are obtained simultaneously at many r -locations (by acquisition of instantaneous velocity maps) and therefore the PIV data for the mean axial velocity profile are correlated along the radial direction. Random fluctuations in correlated data from a stochastic process appear as smooth variations over a *length* that is determined by the width of the correlation function, and with an *amplitude* that is related to the (sample) variance. To assess the extent of correlation in the radial direction the two-point correlation function of the axial velocity fluctuations, defined as

$$\rho_{uu}(r_1, r_2) = \frac{\text{cov}\{u(r_1), u(r_2)\}}{\sqrt{\text{var}\{u(r_1)\}\text{var}\{u(r_2)\}}} \quad (7.4)$$

was computed, and the results at $r_2/D = 0.45, 0.25$ and 0.00 are shown in Figure 7.6. It is clear that the PIV data are correlated over a considerable distance in radial direction. The width of each of the curves in Figure 7.6 is approximately $0.1-0.2 D$, which roughly corresponds to the integral length scale. However, correlation over larger lengths also

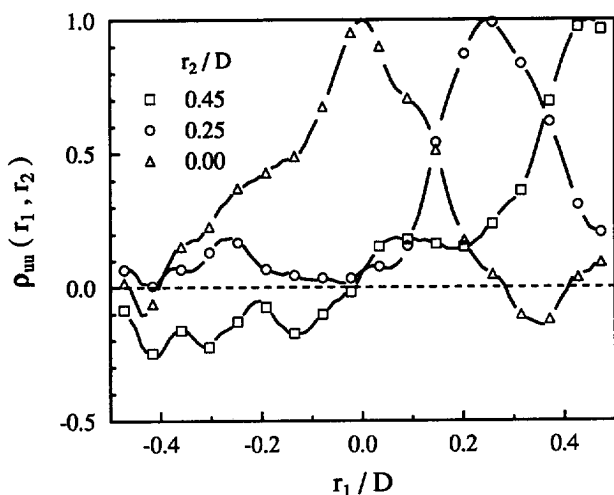


Figure 7.6: Two-point correlation $\rho_{uu}(r_1, r_2)$ of axial velocity fluctuations as function of the distance r_1/D from the centerline, for three values of r_2/D .

seem to be present: fluctuations of the axial velocity component near the pipe wall ($r_2/D = 0.45$) on opposite sides of the centerline are *negatively* correlated *across* the pipe. This can be related to large-scale coherent motion (see e.g. Townsend 1956). Hence, the PIV velocity profiles in Figure 7.5 are not statistically independent. Near the pipe wall fluctuations are negatively correlated, which enhances the skewness of the profile. It therefore seems plausible that the skew observed in Figure 7.5 is due to the limited sample size.

Figure 7.7 compares the mean velocity profile obtained by averaging the PIV data in Figure 7.5 to the LDA data, the DNS data, and Reichardt's velocity profile (Eq. (7.2)) *without* the wake correction (this corresponds to the limit $Re \rightarrow \infty$). The wake correction is also shown. To emphasize the differences between the data and Reichardt's profile Figure 7.8 plots the difference between the data from LDA, PIV and DNS and the profile in Eq. (7.2). The experimental results (normalized with the friction velocity) deviate systematically from Reichardt's formula. Note that the numerical results carry the same systematic deviation. Obviously, Reichardt's formula (which was obtained from a fit to experimental data) merely gives a description of the velocity profile and is not completely exact. Nevertheless, the agreement of the experimental data with the numerical data indicates that the value obtained for the friction velocity is accurate.

Figure 7.9 shows the RMS of the fluctuating axial (u'^+) and radial (v'^+) velocity components computed from the PIV data, and normalized with u_* , and Figure 7.10 shows the Reynolds-stress profile ($\langle u^+ v^+ \rangle$), normalized with u_*^2 . The corresponding results obtained by DNS are shown for comparison. Figure 7.9 also contains the values of u'^+ measured

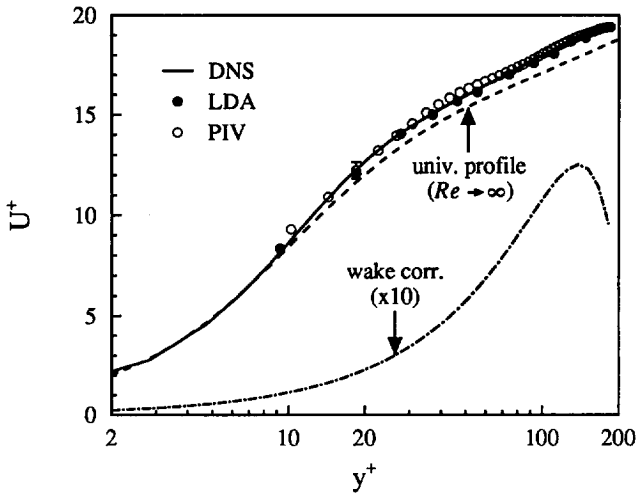


Figure 7.7: Axial mean velocity, normalized by friction velocity, as function of the distance from the pipe wall in wall units, in semi-log scale.

by LDA. The error bars represent the 95% reliability intervals based on the estimated sampling covariance. The measurements of u^{+} agree very well with the numerical results. Near the pipe wall the measurements of v^{+} deviate significantly from the DNS results due to noise in the PIV data. The noise also affects the axial velocity component, but the contribution is relatively small because the amplitude of u^{+} near the pipe wall is relatively large. The result for the Reynolds stress also agrees with the numerical result (taking into account the estimated sampling error). The smooth variations of the PIV data relative to the DNS data in Figures 7.9–7.10 are directly related to the correlation of the data along the radial direction, which was discussed in the previous paragraph.

One-dimensional power spectra of the fluctuating axial and radial components of the velocity (denoted by F_{uu} and F_{vv} respectively) normalized by turbulent intensity squared were also computed at three distances from the centerline ($r/D = 0.00, 0.25$ and 0.45). Figure 7.11 compares the spectra as functions of the dimensionless wavenumber κD to the (normalized) spectra obtained from numerical simulation. The deviation of the numerical result for $F_{uu}(\kappa)$ at $r/D = 0.45$ from the corresponding experimental results is most likely related to the fact that the velocity auto-correlation at 2.5 pipe diameters in the axial direction (this is halfway the domain in the DNS in axial direction) is still 0.09. As a result, the spectrum $F_{uu}(\kappa)$ at $r/D = 0.45$ in the DNS is smaller than in the PIV data over the wavenumber range shown in Figure 7.11. For $F_{uu}(\kappa)$ at $r/D = 0.25$ and 0.00 and $F_{vv}(\kappa)$ at $r/D = 0.45, 0.25$ and 0.00 the PIV results agree with the DNS results within statistical accuracy up to a dimensionless wavenumber of $\kappa D = 50$. This is almost two decades of wavenumber. For larger wavenumbers the velocity signal is obscured by

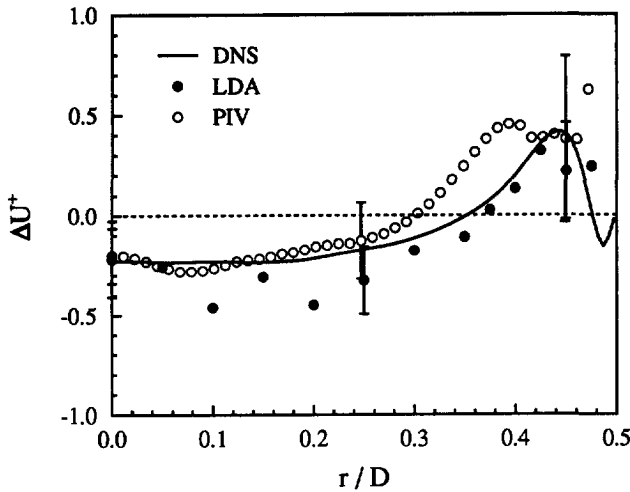


Figure 7.8: Residuals of the axial mean velocity, normalized by friction velocity, with respect to the velocity profile in Eq. (7.2).

noise in the PIV signal. The highest noise level, with a signal-to-noise ratio² (SNR) of 1.4, was found in the radial velocity component at $r/D = 0.45$ (A relatively high RMS of the fluctuating radial velocity component has already been noted at this location). In the other spectra the signal-to-noise ratio is about 30. At the centerline ($r/D = 0.00$) this corresponds to an error of 0.4 px, which is in close agreement with the accuracy that was estimated from calibration measurements (Prasad *et al.* 1992).

7.3.3 vortical structures

Until now only ensemble averaged results have been presented. By averaging the data the detailed structure that can be found in the instantaneous flow maps such as Figure 7.3 is lost. A detail from Figure 7.3 is shown in Figure 7.12. The flow pattern in this figure resembles that of a hair-pin vortex that has been cut in its plane of symmetry.

The instantaneous tangential vorticity component $\omega_z (= \partial v / \partial x - \partial u / \partial y)$ has been calculated for each vector field by computing the circulation along a line that connects the eight neighbours of a data point, and dividing the result by the enclosed area. This method, due to Reuss *et al.* (1989), is equivalent to spatially smoothing of the data with a filter whose length is two times the spatial grid of the data set prior to differentiation. In this way amplification of noise in the vorticity data is restricted at the cost of a small

²We defined the signal-to-noise ratio as the total energy in the signal divided by the total energy in the noise.

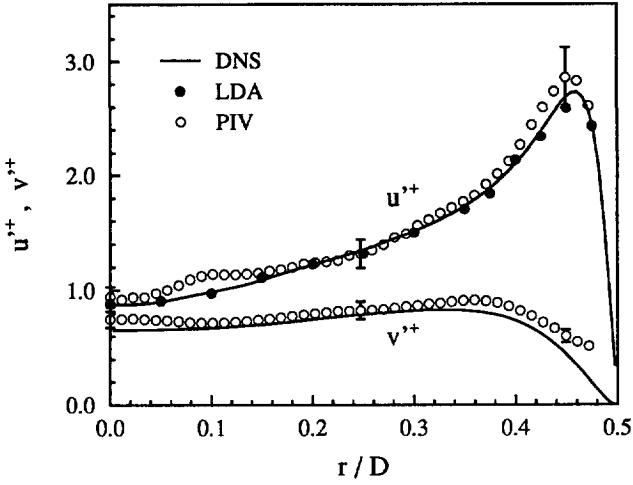


Figure 7.9: Axial (u'^+) and radial (v'^+) turbulent intensities, normalized by friction velocity, as function of the distance from the centerline.

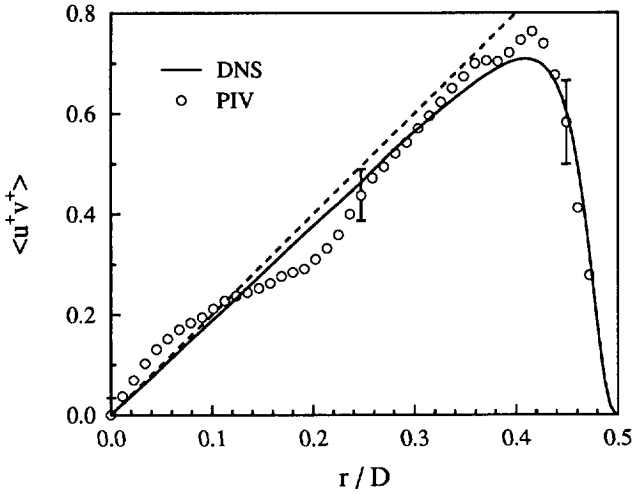


Figure 7.10: Reynolds stress, normalized by friction velocity squared, as function of the distance from the centerline (the dashed line represents the total shear stress).

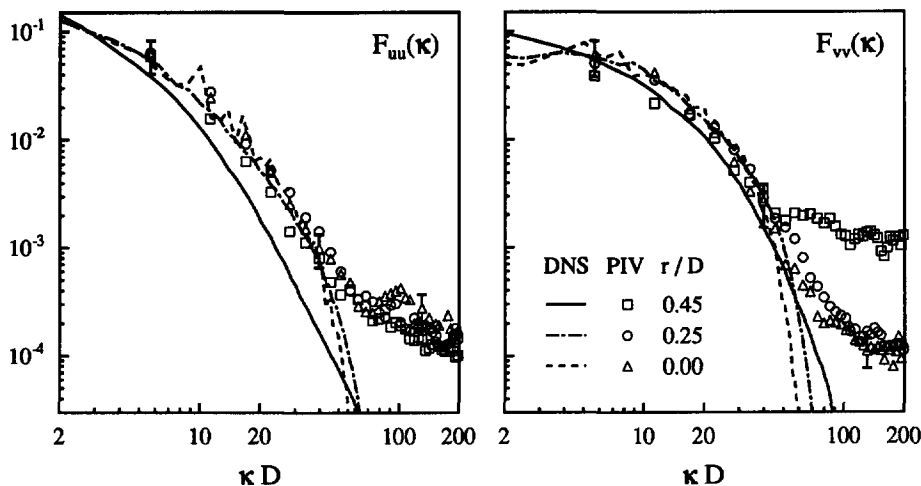


Figure 7.11: Power spectra of the axial (F_{uu}) and radial (F_{vv}) fluctuating velocity, normalized with turbulence intensity squared, at three distances from the centerline.

loss in spatial resolution.

The vorticity maps show structures inclined to the pipe wall at an angle between 8 and 16 degrees. The structures have a length of 100^+ – 350^+ in the axial direction, and intrude about 100^+ into the flow. Most of the observed DNS structures can be classified as one of the following types:

1. “plain” shear layers: These are straight shear layers at an oblique angle to the pipe wall. These structures are the most common.
2. “kinked” shear layers: These structures resemble plain shear layers but they have a distinctive kink.
3. “hair pin” vortices: These are strong vortices at the end of a shear layer. This suggests that these structures are related to hair-pin vortices.
4. “isolated” vortices: usually found in the continuation of a straight line through a shear layer. Isolated vortices only seem to appear at a distance from the wall of more than 90 viscous length scales.

Figure 7.13 shows examples of these structures, found in different PIV data sets. Shear layers and vortices were also found in vorticity maps obtained by Liu *et al.* (1991) in a turbulent channel flow at approximately the same Reynolds number. We noted a strong resemblance between these structures with the different states in the temporal evolution

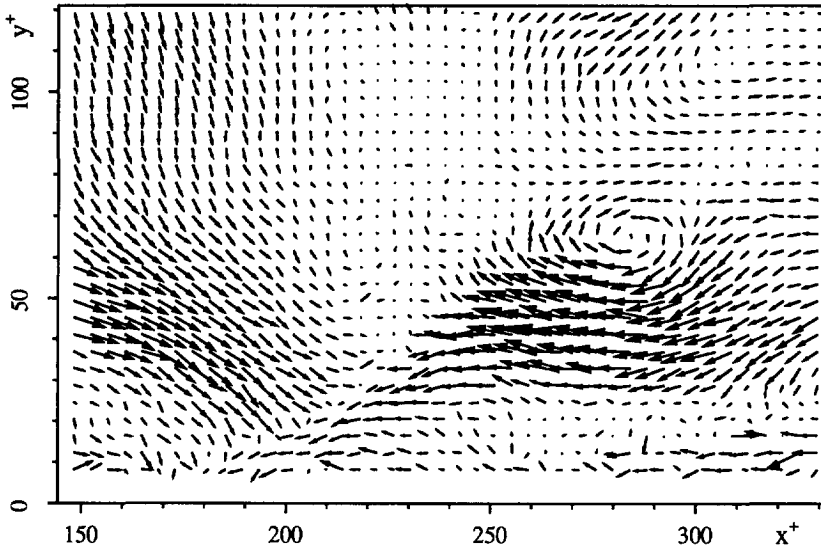


Figure 7.12: Detail near the pipe wall from the vector map in Fig. 7.3.

of a hairpin vortex found in a direct numerical simulation on a turbulent boundary layer studied by Robinson (1991).

7.4 Summary and conclusions

Experimental data were obtained from a turbulent pipe flow at a Reynolds number close to 5,300 with LDA and PIV. The results of the LDA measurements (which preceded the PIV measurements) verified that the observed flow was fully developed at the test section. Using PIV, instantaneous velocity maps were obtained of the axial and radial velocity components in a planar cross section through the centerline of the pipe. The spatial resolution was 1.43 mm in both the axial and radial direction.

Ensemble averaging the PIV data yielded turbulence statistics of the pipe flow as function of the radial distance from the centerline. Results were obtained for the mean axial velocity, the axial and radial turbulent intensities and the Reynolds stress. Also, true wavenumber spectra of the fluctuating axial and radial velocity components were computed at three radial positions without recourse to the use of Taylor's frozen field hypothesis. The PIV results for the axial mean and turbulent intensity profiles agree with the results obtained with LDA, within the estimated statistical error. The profiles of the axial mean velocity, axial and radial turbulent intensities and Reynolds stress,

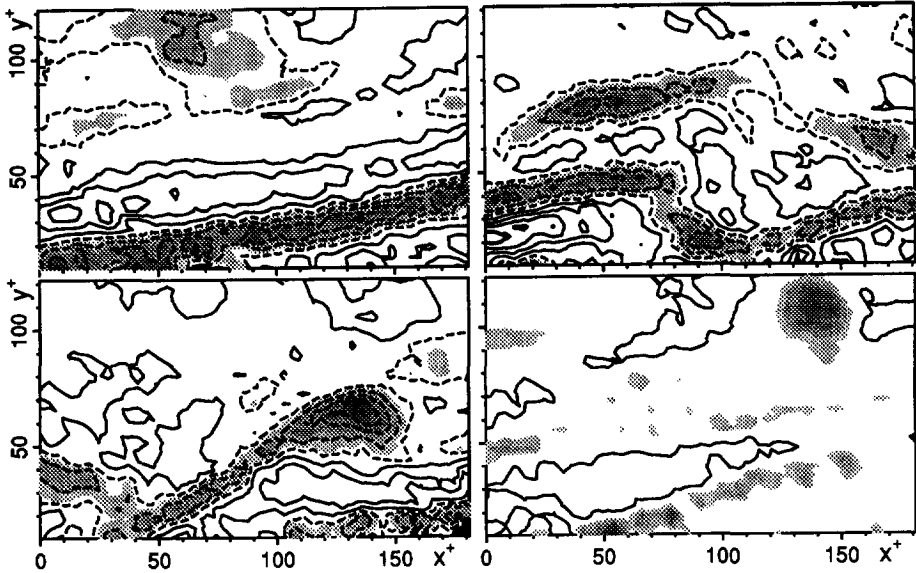


Figure 7.13: Contour maps of vortical structures near the pipe wall found in the maps of tangential vorticity (ω_z) computed from the PIV data sets: “plain” (top left) and “kinked” (top right) shear layers, and “hair-pin” (bottom left) and “isolated” (bottom right) vortices. The flow is from left to right. Shaded regions correspond to: $\omega_z < -7.5 \text{ s}^{-1}$.

together with the power spectra, were compared with results from a numerical simulation of turbulent pipe flow. In general, the PIV and numerical results are quite consistent, and apparent differences appeared to be a result of the finite accuracy of the experimental data. It is important to normalize experimental data with an independent and accurate estimate of the friction velocity.

Maps of the tangential component of the vorticity were computed from the instantaneous flow maps obtained with PIV. Strong vortical structures were found in the near-wall region of the flow, at an oblique angle of 8–16°, which intrude about 100 viscous wall-units into the flow. Four generic planar structures were identified in a qualitative comparison of the vorticity maps: “plain” and “kinked” shear layers, and “hair-pin” and “isolated” vortices. These structures may be elements of a more complex three-dimensional structure. For example, Liu *et al.* (1991) suggest that the shear layer is an interface between a wallward sweep and second quadrant fluid that is pumped upward by a hairpin, so that it usually lays behind a hairpin vortex. Some of the structures may however be different stages of evolution of a hair-pin, as suggested by Robinson (1991).

Since velocity fluctuations are correlated over considerable distances in the axial and radial direction, large numbers of photographs are required in PIV experiments to ob-

tain accurate results on turbulence statistics. We expect results with high accuracy from hot-wire measurements carried out elsewhere. The major contribution of the PIV measurements to the comparative study mentioned in the Introduction will be the generation of experimental data that allow a quantitative identification and comparison of vortical structures found in numerical data sets. Presently, we are preparing a comparison of the vorticity patterns shown in Figure 7.13 with the DNS results. The results will be presented in the near future (Eggels *et al.* 1993b)³.

³See Chapter 8.

Chapter 8

Comparison of Vortical Flow Structures in DNS and PIV Studies of Turbulent Pipe Flow¹

Abstract. Fully developed turbulent pipe flow at $Re = U_c D / \nu = 7000$ is studied numerically by means of Direct Numerical Simulation (DNS) and experimentally by means of Particle Image Velocimetry (PIV). Several mean properties of vortical flow structures, defined as regions of the flow where the fluctuating tangential vorticity component exceeds a threshold value, are computed from the DNS and PIV data and compared quantitatively. Reasonable agreement is obtained illustrating that DNS can provide quantitative information on turbulence flow structures although the vortical structures in the near-wall region observed in DNS are approximately twice as large as those in PIV.

8.1 Introduction

Direct numerical simulation is an established numerical technique to study the details of turbulent flows. Beside providing turbulence flow statistics, the data generated by DNS can be used to study flow structures e.g. in the near-wall region of low Re-number turbulent flows (see e.g. Robinson 1991a). In this paper, numerically generated turbulent flow structures obtained from DNS are compared with experimental results obtained from particle image velocimetry. Using DNS and PIV, fully developed turbulent pipe flow is considered at a Reynolds number, based on centerline velocity and pipe diameter, equal to 7000. The present work is part of a broader joint study in which, beside the DNS and PIV studies, results of hot-wire and laser-Doppler measurements are also included for comparison of numerical simulation with experiment. The results of a second DNS using a different numerical code are also presented in this joint study. The details and statistical results are described by Eggels *et al.* (1993a). In general, the agreement between

¹EGGELS, J.G.M., WESTERWEEL, J., NIEUWSTADT, F.T.M. & ADRIAN, R.J. 1993 In: *Near-Wall Turbulent Flows*. (eds. R.M.C. So *et al.*) Elsevier. pp. 413-422.

numerical and experimental statistical results is excellent. For a description of the PIV experimental setup, we refer to Chapter 7.

In the present paper, we focus on a quantitative comparison of properties related to turbulent flow structures obtained from DNS and PIV. Experimentally, the 2-D velocity distribution is measured instantaneously in a planar cross-section of the flow. This cross-section extends over the complete pipe diameter D in radial direction and over approximately $1.1D$ in the streamwise direction. By spatial differentiation of this instantaneous velocity field, the spatial distribution of the out-of-plane component of the vorticity vector is obtained. In Fig. 7.13 examples of the 2-D distribution of the vorticity fluctuations are shown as found in different PIV data sets. The shaded regions correspond to flow regimes where the instantaneous negative vorticity fluctuations exceed a negative threshold value. Clearly, these vorticity fluctuations are organized in what is called here “vortical flow structures”. The observed structures can be classified in different types as indicated in Fig. 7.13. A major distinction is made between elongated flow structures (“shear layers”) on one hand and more compact structures (“vortices”) on the other hand. Several statistical properties of these vortical flow structures are computed and compared quantitatively with the corresponding results obtained from the DNS data. First, we computed some properties of the near-wall vortical flow structures mainly, including the mean angle of inclination of these structures with respect to the pipe wall. Secondly, the mean shape-parameter (defined as the ratio of the perimeter squared to the area of a structure) is computed as function of the distance to the pipe wall. The details of the techniques used for these computations and the corresponding results are described in Section 8.2. Although the physical interpretation of the present results might perhaps not always be precise and clear, one should keep in mind that the aim of the present study is only focussed on a quantitative comparison of flow structure properties obtained from DNS and PIV rather than on a detailed interpretation of the observed phenomena. To get an impression of the relevance of the vortical flow structures to the turbulence flow statistics, conditionally sampled data are presented in Section 8.3. Finally, in Section 8.4 a summary and the conclusions of the present work are given.

8.2 Computational technique and results

8.2.1 Introduction

All present analyses of turbulent flow structures are based on the spatial distribution of the out-of-plane component ω_θ of the vorticity vector, i.e. the vorticity component aligned with the azimuthal direction. This is certainly the most obvious flow parameter available in PIV which can also be related directly to flow structures as indicated in Fig. 7.13. Furthermore, ω_θ can be computed easily from the DNS data. Alternatively, one could use a different parameter like pressure or enstrophy (see Robinson (1991a) for an overview of possible parameters and their usefulness in analyzing turbulent flow structures) to quantify some properties of flow structures but these alternative parameters cannot be obtained from the PIV data. Since the present analysis is based on ω_θ , the RMS of its

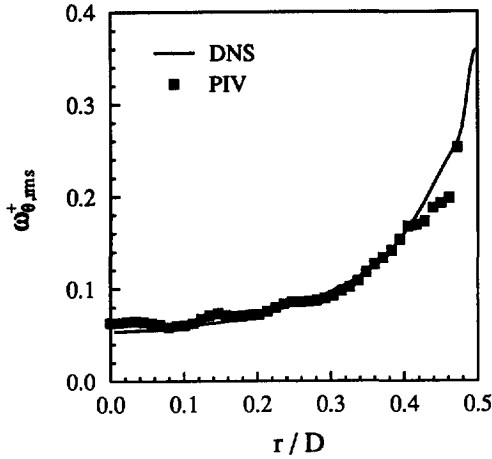


Figure 8.1: Root-mean-square values of the vorticity component ω'_θ as function of the distance r/D from the centerline. $\omega_{\theta,rms}^+$ denotes $\omega_{\theta,rms}$ normalized by ν/u_*^2 .

fluctuation (ω'^2) is computed first and shown in Fig. 8.1. The agreement between DNS and PIV is excellent in view of the measurement error in PIV which is largest near the wall. Therefore, only close to the wall ($r/D > 0.4$) the vorticity fluctuations found in PIV deviate from those obtained from DNS.

The analyses are carried out by means of the image processing system TCL-Image. Within TCL-Image, the 2-D vorticity distributions can be processed easily and quickly using standard procedures for image processing and pattern recognition. In the present study, the negative vorticity fluctuations are considered only which means that regions with positive vorticity fluctuations have been neglected. This is done because the negative vorticity fluctuations tend to be more organized in flow structures as observed in the PIV measurements. Furthermore, by omitting the positive fluctuations, the vortical flow structures formed by regions of negative vorticity are identified more easily. Of course, similar analyses can be carried out using a different range of vorticity fluctuations. For the purpose of the present study this is of minor importance as long as the DNS and PIV data are processed exactly in the same way.

8.2.2 Computation of near-wall structure properties

To quantify mean properties of the vortical flow structures in the near-wall region of the pipe, the 2-D covariance function has been determined for each 2-D plane. This covariance

²From hereinafter, the vorticity ω'_θ is normalized by wall units, i.e. by ν/u_*^2 in which u_* is the wall shear velocity defined as $\sqrt{\tau_w/\rho}$ and ν the kinematic viscosity.

function is defined as:

$$\text{cov}(r_x, r_r) = \frac{1}{N_x N_r} \sum_{i=1}^{N_x} \sum_{j=1}^{N_r} \omega'_\theta(i\Delta x, j\Delta r) \omega'_\theta(i\Delta x + r_x, j\Delta r + r_r). \quad (8.1)$$

in which $\vec{r} = (r_x, r_r)$ represents the displacement vector. N_x and N_r denote the number of data points in axial and radial direction respectively, Δx and Δr the corresponding grid spacing. Zero padding is used at the edges of each plane, except for the streamwise direction in DNS. As in the actual simulation, periodic boundary conditions are adopted here.

Both the DNS and PIV vorticity distributions have *not* been normalized with their RMS profiles to obtain a 2-D homogeneous distribution. The reason for this is that such a normalization would enhance weak vortical flow structures in regimes with low RMS vorticity in favour of strong vortical flow structures in the near-wall region where the RMS vorticity is much larger (see Fig. 8.1). Since we are mainly interested in properties of the latter structures here, normalization is not applied. The DNS data at dimensionless distances to the wall (y^+) smaller than 10.4 viscous wall units, have been omitted because the corresponding PIV data are not available. In the DNS data, the 2-D covariance distributions are averaged over all planes in azimuthal direction to yield only one 2-D covariance function per data field. During the simulation 43 data fields are stored, so 43 independent covariance functions are available from the DNS data. From the PIV data, 64 covariance distributions are computed using 32 PIV recordings (each recording was split in an upper and lower part of $\frac{1}{2}D \times 1.1D$ size each). The PIV data have been reduced to 8 independent covariance functions each of which is obtained by averaging 8 covariance distributions.

The 2-D covariance function which is finally obtained and normalized to unity using its maximum value, resembles an elliptical pattern of contour lines shown in Fig. 8.2 as an example of the DNS data. This distribution can be characterized by several parameters, i.e. by the length scales L_1 and L_2 corresponding to the size of the ellipse along its principal axes, by the mean angle α between the direction of the major principal axis and the pipe wall and by ρ characterizing the “2-D shape” of the ellipse (ρ is the correlation coefficient between r_x and r_r ; $\rho = 0$ corresponds to a circle, $\rho = 1$ to a line). All four parameters are computed using linear regression theory. Beside its mean value, the 95% reliability interval, based on the variance of the parameter considered, the number of independent functions N_p and the student-t distribution, is determined for each parameter. The results are listed in Table 8.1.

Obviously, the mean length scales L_1 and L_2 are significantly smaller in PIV in comparison with DNS. The mean angle of inclination α obtained from DNS agrees rather well with PIV. On average, the vortical flow structures in DNS and PIV are inclined at a nearly similar angle despite the significantly different proportions L_1 and L_2 . The “2-D shape” parameter ρ obtained from the PIV data is also found to be much smaller than ρ obtained from DNS. This indicates that the PIV covariance function tends to be more circular (or less elongated) than the DNS covariance distribution. In general, the 95% reliability intervals of the PIV results are larger than those of the DNS results because

Table 8.1: Mean properties of near-wall vortical flow structures. L_1 and L_2 are given in arbitrary units, α in degrees. ρ is a correlation coefficient, whereas N_p represents the number of independent data sets.

	PIV ($N_p = 8$)		DNS ($N_p = 43$)	
	mean	95% reliability interval	mean	95% reliability interval
L_1	14.00	$11.72 \leq L_1 \leq 16.28$	L_1 21.65	$20.98 \leq L_1 \leq 22.32$
L_2	2.18	$1.81 \leq L_2 \leq 2.53$	L_2 2.98	$2.95 \leq L_2 \leq 3.01$
α	8.9	$7.6 \leq \alpha \leq 10.3$	α 7.9	$7.7 \leq \alpha \leq 8.1$
ρ	0.549	$0.377 \leq \rho \leq 0.721$	ρ 0.715	$0.710 \leq \rho \leq 0.720$

of the rather small number of available data sets and the presence of noise. This experimental noise might explain why L_1 , L_2 and ρ are smaller in PIV than in DNS. Due to the noise, the elongated structures near the wall can be subdivided into several smaller, less elongated, structures (see e.g. the “shear layer” shown in the contour map at the bottom right position of Fig. 7.13). As a result of this subdivision, the mean values of L_1 , L_2 and ρ might become smaller in PIV. We will return to this point also in the next section.

8.2.3 Computation of mean shape-parameter

In Fig. 7.13, the vortical flow structures shown as shaded regions differ in shape and size. From an earlier PIV study, the vortical flow structures in the core region of the flow seemed to be more compact than those close to the wall which appeared to be more elongated. To quantify this qualitative observation, a dimensionless shape-parameter S , defined as the perimeter squared of a structure divided by 4π times its area, is computed

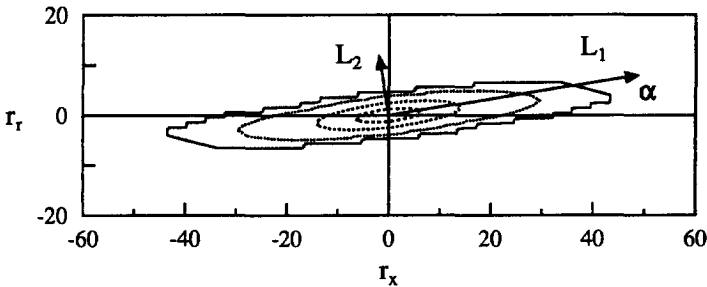


Figure 8.2: Contour map of the 2-D covariance function as an example of the DNS data. The maximum value of the covariance function is normalized to unity. The step size between two sequential contour lines equals 0.2. L_1 and L_2 represent the principal axes of the best fit ellipse, α denotes the angle between the direction of L_1 and the r_r -axis. r_x and r_r are in arbitrary units.

as a function of the radial distance r/D from the centerline. For a circular and square structure, S equals 1 and $4/\pi$ respectively.

In contrast to the procedure described in the previous section, the DNS and PIV 2-D vorticity distributions are now normalized by the RMS vorticity profiles to yield a 2-D homogeneous distribution. At each position of the flow field, ρ_ω representing the ratio of the vorticity magnitude $-\omega'_\theta$ to the corresponding RMS value $\omega'_{\theta,rms}$ is thus available. Rather arbitrarily, a threshold value $\rho_\omega = 2$ is imposed to select the regions with largest vorticity fluctuations. Each particular region is denoted as a vortical flow structure of which several shape-parameters are computed within TCL-image. The details of the numerical procedures involved in the latter computation are described in the TCL-Image manual and by Dorst & Smeulders (1985).

In Fig. 8.3 the mean shape-parameter S is shown as a function of r/D . Beside the mean values obtained from DNS and PIV, the spreading in the DNS data is indicated by the two additional lines denoted with 10% and 90%. The region in between these two lines captures 80% of all computed values of S . Obviously, the mean value of S increases towards the wall in both DNS and PIV. On average, the vortical flow structures close to the wall are elongated more than those close to the centerline, confirming the qualitative observation mentioned earlier. The mean values obtained from PIV show some scatter which is again due to the small number of available data sets. Close to the wall, S obtained from PIV decreases whereas S from the DNS remains nearly constant. The subdivision of elongated structures into smaller structures due to the noise in PIV, as discussed in the previous section, is the main reason for this decrease of S . Towards the wall, the spreading of S also increases which indicates that compact vortical flow structures ($S \approx 1.5 \dots 2.0$) are present at all radial positions whereas strongly elongated structures ($S > 5$) are only observed near the wall ($r/D > 0.3$). These quantitative results must depend on the imposed threshold $\rho_\omega = 2$ but we expect that the observed general tendency discussed above will be qualitatively similar for other threshold values.

8.3 Conditionally sampled flow statistics

In Sect. 8.2, the 2-D vorticity distributions were subdivided into regions of the flow where $\omega'_\theta \leq -\rho_\omega \omega'_{\theta,rms}$ and where $\omega'_\theta > -\rho_\omega \omega'_{\theta,rms}$ with ρ_ω and $\omega'_{\theta,rms} > 0$. The former regions are referred to as vortical flow structures. In this section the relevance of these vortical flow structures to the turbulence flow statistics is studied by means of conditional sampling. Therefore, each mean turbulent flow quantity $\langle \phi \rangle$ is assumed to consist of two contributions:

$$\langle \phi \rangle = \langle \phi \rangle_{vfs} + \langle \phi \rangle_r \tag{8.2}$$

with

$$\langle \phi \rangle = \frac{1}{N} \sum_{i=1}^N \phi(i) \quad , \quad \langle \phi \rangle_{vfs} = \frac{1}{N_{vfs}} \sum_{i=1}^{N_{vfs}} \phi(i) \quad \text{and} \quad \langle \phi \rangle_r = \frac{1}{N_r} \sum_{i=1}^{N_r} \phi(i) \tag{8.3}$$

in which $\langle \phi \rangle_{\text{vfs}}$ denotes the average sampled over the vortical flow structures only, $\langle \phi \rangle_r$ the average sampled over all other regions of the flow, N the total number of samples, N_{vfs} the number of samples which satisfy the sampling condition and N_r the number of samples equal to $N - N_{\text{vfs}}$. Since the flow field is subdivided into two complementary regions only, the following relation holds:

$$1 = n_{\text{vfs}} + n_r \quad \text{with} \quad n_{\text{vfs}} = \frac{N_{\text{vfs}}}{N} \quad \text{and} \quad n_r = \frac{N_r}{N}. \quad (8.4)$$

Here n_{vfs} denotes the fraction of the flow field occupied by the vortical flow structures and n_r the fraction of all other regions. To investigate whether the conditional average over the vortical flow structures contributes significantly more or less to the turbulence flow statistics in comparison with the average over all other regions, the relative importance is expressed in terms of $F_{\langle \phi \rangle}$:

$$F_{\langle \phi \rangle} = \frac{\frac{\langle \phi \rangle_{\text{vfs}}}{n_{\text{vfs}}}}{\frac{\langle \phi \rangle_r}{n_r}} = \frac{\frac{1}{N_{\text{vfs}}} \sum_{i=1}^{N_{\text{vfs}}} \phi(i)}{\frac{1}{N_r} \sum_{i=1}^{N_r} \phi(i)} \quad (8.5)$$

If $F_{\langle \phi \rangle}$ equals 1, the vortical flow structures contribute just as much to the turbulence flow statistics as the averaged contribution over all other regions of the flow field. For $F_{\langle \phi \rangle} > 1$ or $F_{\langle \phi \rangle} < 1$, their contribution is significantly more or less respectively. This conditional sampling on vortical flow structures of the flow field has been applied to several turbulence flow quantities for DNS and PIV using $\rho_\omega = 0, 1$ and 2. In Fig. 8.4, $F_{\langle \phi \rangle}$ is shown as function of r/D where $\langle \phi \rangle$ represents the mean axial velocity $\langle W \rangle$. In the middle of the pipe ($r/D < 0.4$), $F_{\langle W \rangle}$ approximately equals 1 indicating that the vortical flow structures travel with a velocity similar to the mean velocity $\langle W \rangle$ corresponding to the position r/D . Towards the wall, $F_{\langle W \rangle}$ obtained from DNS increases up to 2. This increase could be a numerical artifact of $\langle W \rangle_r$ or n_{vfs} tending to zero close to the wall. However, this is not very likely to be the case here because at $r/D = 0.497$ ($y^+ = 0.937$) we obtain $\langle W \rangle_{\text{vfs}} = 0.533u_*$, $\langle W \rangle_r = 0.401u_*$, $n_{\text{vfs}} = 0.43$ and $n_r = 0.57$ for $\rho_\omega = 0$. Furthermore, n_{vfs} and thus also n_r are fairly constant for all r/D . The radially averaged values of n_{vfs} for $\rho_\omega = 0, 1$ and 2 respectively equal 0.456, 0.133 and 0.036 for the DNS data. The PIV data provide almost the same result: 0.460, 0.133 and 0.036 respectively. Close to the wall, it thus appears that the vortical flow structures travel with a velocity larger than the mean velocity.

In Fig. 8.5, $F_{\langle \phi \rangle}$ is shown with $\langle \phi \rangle$ representing the mean Reynolds shear stress $\langle u'w' \rangle$. For $r/D < 0.3$ the vortical flow structures seem to contribute more to the Reynolds shear stress than the total over all other regions. However, the PIV results do not confirm the DNS results here. Despite the large scatter in the PIV data, $F_{\langle u'w' \rangle}$ becomes smaller than 1 at $r/D \approx 0.1$ in contrast to the DNS data. Near the wall at $r/D \approx 0.46$ (which exactly matches the location of maximum shear-production and maximum turbulence intensity of the streamwise velocity component), the averaged Reynolds shear

stress is larger outside regions which satisfy the sample condition. Both DNS and PIV yield $F_{\langle u'w' \rangle} < 1$, even for $\rho_\omega = 0$. It has not been investigated yet whether this also implies that the turbulence shear-production is largest in regions where $\omega'_\theta > 0$. Near the wall and the centerline, $\langle u'w' \rangle_{\nu fs}$ and $\langle u'w' \rangle_r$ decrease to zero, but since $\langle u'w' \rangle_{\nu fs}$ is larger here than $\langle u'w' \rangle_r$, $F_{\langle u'w' \rangle}$ increases.

$F_{\langle \phi \rangle}$ has also been computed for the velocity fluctuations. Since the observed tendency for all three components is similar, only $F_{\langle w'w' \rangle}$ is shown in Fig. 8.6. The agreement between DNS and PIV is encouraging in particular for $\rho_\omega = 0$. Similar as in Fig. 8.5 for $F_{\langle u'w' \rangle}$, $F_{\langle w'w' \rangle}$ becomes smaller than 1 at $r/D \approx 0.46$. This illustrates that the velocity fluctuations are also larger in flow regions where $\omega'_\theta > 0$ than in regions where $\omega'_\theta < 0$. If the mean shear-production in the former regions is indeed larger than in the latter because of the larger averaged Reynolds shear stress, then the observed tendency here can be explained by the larger mean shear-production.

8.4 Summary and discussion

Direct numerical simulation and particle image velocimetry are used to study fully developed turbulent pipe flow at $Re = 7000$. Several DNS and PIV turbulence flow statistics have been compared in earlier work and provided an excellent agreement. In the present work, some mean properties of vortical flow structures observed in DNS and PIV have been compared quantitatively. No attempt has been made to interpret the observed phe-

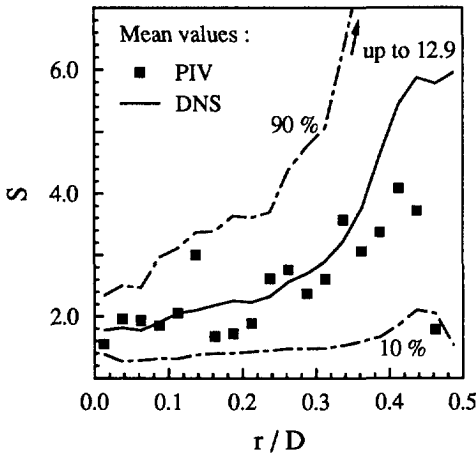


Figure 8.3: Mean shape-parameter S as function of the distance r/D from the centerline. The imposed threshold value ρ_ω equals 2. The lines denoted with 10% and 90% illustrate the spreading in the DNS data.

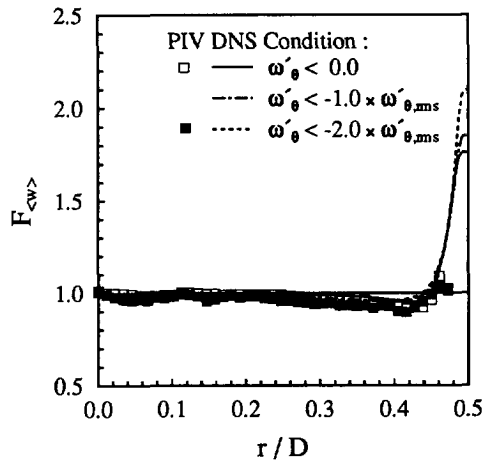


Figure 8.4: Relative importance of the vortical flow structures to the turbulence flow statistics expressed in terms of the ratio $F_{\langle \phi \rangle}$ as function of r/D . Here $\langle \phi \rangle$ represents the mean axial velocity $\langle W \rangle$.

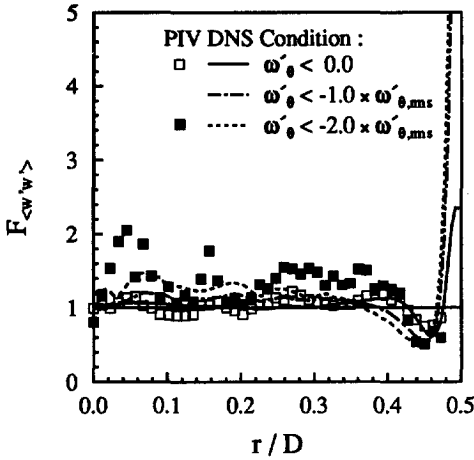


Figure 8.5: As in Fig. 8.4, but with $\langle \phi \rangle$ representing the mean Reynolds shear stress $\langle u'w' \rangle$.

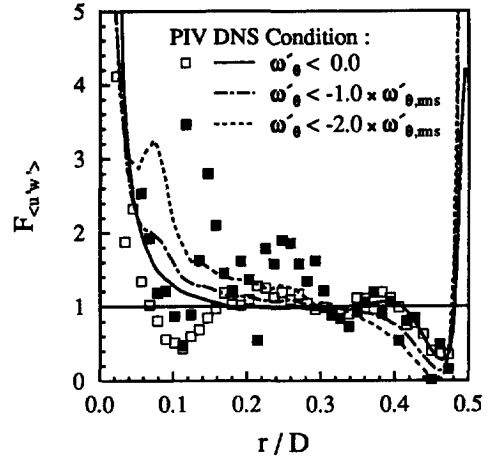


Figure 8.6: As in Fig. 8.4, but with $\langle \phi \rangle$ representing the streamwise velocity fluctuations $\langle w'w' \rangle$.

nomena and presented results e.g. in terms of flow dynamics.

A vortical flow structure referred to in this paper is defined as a region of the flow where the ratio $\rho_\omega = -\omega'_\theta/\omega'_{\theta,rms}$ exceeds a threshold value. The analyses of the present comparison are based on the spatial distribution of ω'_θ because this is one of the most obvious parameters which is available in both DNS and PIV.

First, some mean properties of vortical flow structures in the near-wall region have been computed. A qualitative observation of the PIV data indicated that the vortical flow structures in the near-wall region are elongated and inclined with respect to the pipe wall. Quantitatively, we obtained a mean angle α of inclination equal to 8.9 degrees for the PIV data. The 95% reliability interval ($7.6 < \alpha < 10.3$), however, is rather large due to the presence of noise and the small number of available PIV data sets. From the DNS data, we obtained $7.7 < \alpha < 8.1$ with 95% reliability and a mean angle $\alpha = 7.9$ degrees. The PIV and DNS results are in reasonable agreement. Other mean properties obtained from PIV, like the averaged length scales of the near-wall vortical flow structures, differ significantly from DNS which is most probably due to noise in the PIV data.

Secondly, a dimensionless shape-parameter S has been computed as function of the distance r/D from the centerline. In general, the present analyses showed that for both DNS and PIV the vortical flow structures near the centerline of the pipe are more compact than those close to the wall which are more elongated. In particular, it is found that compact flow structures are present at all r/D whereas strongly elongated structures only appear close to the wall.

Furthermore, a quantitative analysis has been made in which the flow statistics conditionally sampled over the vortical flow structures have been compared with flow statistics

sampled over all other regions in the flow in order to study the relevance of the vortical flow structures to the flow statistics. It was found that the vortical structures in the middle of the pipe ($r/D < 0.4$) travel with the mean velocity corresponding to the radial position r/D . Close to the wall, the vortical structures travel with a velocity larger than the mean velocity. At $y^+ \approx 15$ ($r/D \approx 0.46$), it appeared that the averaged Reynolds shear stress and the velocity fluctuations are larger in regions where $\omega'_\theta > 0$ in comparison with regions where $\omega'_\theta < 0$.

The present work illustrates that DNS can provide quantitative information on turbulence flow structures and that these DNS results are in reasonable agreement with PIV. However, some uncertainties remain involved in the DNS. Possible influences on the flow structures caused by the numerical procedures used in the simulation, the applied numerical resolution and/or the size of the computational domain still need to be investigated. None of these uncertainties have been mentioned here although they may be of importance for studies of flow structures using DNS. In the present paper a first explorative quantitative comparison of numerical and experimental results is presented, but there is also an unmistakable need for a comparison of the present DNS and PIV results with other experimental, numerical and in particular theoretical results regarding turbulence flow structures.

Chapter 9

Application of Digital Particle Image Velocimetry to a Turbulent Pipe Flow¹

Abstract. *The results are presented of probably the first successful application of digital particle image velocimetry (DPIV) in a fully developed turbulent flow. The flow under study was a small region close to the wall (ranging from $40 < y^+ < 90$) in a smooth pipe flow, at a relatively low Reynolds number of 5,300, based on the bulk velocity and the diameter of the pipe. The advantage of DPIV in comparison with the traditional implemented PIV method is the enormous reduction in analysis time. The time needed for 1000 interrogations with the conventional PIV analysis is typically 1000 seconds, whereas for DPIV about 60 seconds are needed. This reduction in analysis time is achieved at the cost of a small reduction in accuracy. The present DPIV experiments were carried out with a simple video camera with an effective resolution of 256×512 pixels. Despite this rather poor resolution, the results demonstrate that DPIV is sufficiently accurate to yield statistically significant results. The accuracy is estimated at $0.2\text{--}0.4 u^+$, which corresponds to a measured particle image displacement of $0.1\text{--}0.2$ pixel. The turbulent statistics show satisfactory agreement in comparison with data obtained with the conventional PIV method. Visual comparison of vector maps representing instantaneous fluctuating velocity fields obtained from the present DPIV measurements and conventional PIV experiments previously carried out in the same facility, show that both techniques are able to capture similar flow patterns. A first investigation to detect flow structures gives promising results.*

9.1 Introduction

It is generally accepted that turbulent flow is not random, but consists of spatially and temporal coherent structures. These flow patterns can be observed e.g. in flow visualiza-

¹VAN DER HOEVEN, J.G.TH., WESTERWEEL, J., NIEUWSTADT, F.T.M. & ADRIAN, R.J. 1993 In: *Proc. of IUTAM Symp. "Eddy Structure Identification in Free Turbulent Shear Flows"* (Poitiers) 12-14 Oct. 1992. Kluwer Academic, Dordrecht.

tion. With traditional single-point measurement techniques, like hot-wire and the laser-Doppler anemometry, it is difficult to observe the spatial character of these structures. Therefore, additional multi-point techniques are required.

Particle Image Velocimetry (PIV) is such a technique. With PIV one can obtain quantitative information on the instantaneous flow pattern in a plane. This yields direct information on the spatial coherence of structures. In addition, the spatial distribution of derived quantities can be computed, such as the out-of-plane vorticity component and the second invariant of the 2D deformation tensor. It is believed that these quantities may be relevant for the dynamics of coherent structures.

The technique of PIV starts with a flow which is seeded with small particles that accurately follow the flow. The particles are usually illuminated with a laser sheet. Traditionally, doubly or multiple-exposure images of the particles are recorded on photographic film. The film negative is then analyzed by means of scanning it with an optical/electronic interrogation technique. The principle of this technique is as follows. A small interrogation spot in the negative is illuminated with a laser beam. This results in a Young's fringes interference pattern in the far field of the transmitted light beam. The distance of these fringes is directly proportional to the local fluid velocity. Their orientation is perpendicular to the displacement of the particle-image pairs on the negative (Adrian 1986). This pattern is subsequently digitized with a typical resolution of 256×256 pixels, for analysis with a computer. The fringe pattern is equivalent to the Fourier transform of the auto-correlation of the interrogation image. Hence, one can alternatively carry out the analysis by direct observation of the interrogation image and by computation of the auto-correlation directly.

This method, based on the analysis of either the fringe pattern or the direct computation of the correlation function, yields accurate local velocity measurements, usually better than 1%. In addition, the spatial resolution is rather high, up to 100×100 interrogation spots per photograph. However, this technique is rather slow, up to several hours per photograph are needed. This rather large analysis time is due, partly to the developing of the film, and partly to the scanning process, which requires the traversing of the camera and laser beam across the negative. Therefore, the conventional PIV technique is only appropriate to treat a small set of images.

For the study of the dynamics of coherent structures, like e.g. in turbulent boundary layer flows, one is interested in the time evolution of the flow or in the statistics of the observed flow patterns. In this case analysis of large numbers of images is essential. A slow analysis method is then unacceptable. Therefore, we have developed an alternative PIV technique based on a digital analysis of the images instead of the optical (fringe) analysis. (From hereafter we will denote the alternative digital method as DPIV and the conventional method as OPIV.) First, instead of using photographic film, the complete image of the particles is recorded digitally with a CCD-array, with a typical resolution of 512×512 pixels. Second, the digitized image is then analyzed by interrogating small regions, usually 32×32 pixels or 64×64 . In such an interrogation window the distance

between particle images is obtained from the correlation function calculated by FFT's. For further details on this alternative analysis for large numbers of images we refer to Chapter 7.

Using this technique the analysis time per complete image is now reduced to seconds rather than hours. Therefore, sequences of images (100–1000 frames) can be analyzed within reasonable time. However, there is a small reduction in the measuring accuracy, which is now 1–3%, and a somewhat lower spatial resolution, i.e. 1,000–4,000 interrogations/image.

Some additional advantages arise due to the digitization of the complete image before analyzing. First, standard image processing techniques can be applied, e.g. to correct for noise or non-uniform background lighting. Second, series of *single-exposure* images can be analyzed using the *cross-correlation* technique on two successive images to obtain the velocity information (Willert & Gharib 1991). In this way, one gets rid of the velocity direction ambiguity present using the *auto-correlation* technique on *double-exposure* images. In addition, cross correlation allows a more accurate determination of the displacement of the correlation peak.

The results are presented of the application of DPIV in a fully developed turbulent air flow. The flow under study was a smooth pipe flow at a relatively low Reynolds number. Recently PIV measurements using the conventional analysis technique were carried out in the same pipe flow facility under the same flow conditions. In that case a total of 33 photographs was taken in a plane through the centerline of the pipe, across the full diameter. For these measurements the negatives of the PIV photographs were analyzed in the interrogation system described by Landreth & Adrian (1990). The results of these experiments were presented together with the results of LDA measurements and DNS calculations for comparison in Chapter 7. Some experimental conditions and data of the PIV measurements are summarized in Table 1. This will be the set of measurement data, with which we will compare our present DPIV data.

The main reason for doing these experiments was the opportunity to compare the results of the, probably, first application of DPIV measurements in a fully turbulent flow with the results of measurements with the conventional implemented PIV carried out in the same flow facility and under the same flow conditions. To investigate the statistical quantities of flow properties, like vorticity, which are associated with flow structures a larger number of images is required. Therefore, under the same flow conditions, a set of 501 double-exposure images was taken using a simple video camera. The data was analyzed in terms of statistics, such as mean and rms profiles. Subsequently, conditional sampling was applied.

9.2 Experimental set-up

A schematic of the experimental set-up is given in Figure 9.1. Except for the image acquisition, the experimental set-up and flow conditions are the same as described in

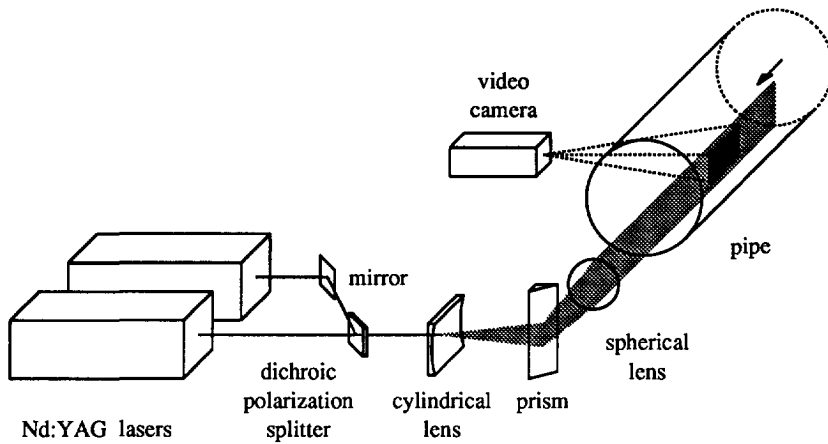


Figure 9.1: Schematic diagram of the experimental set-up (cf. Fig. 7.1b).

more detail in Chapter 7.

turbulent pipe flow

The images were taken near the end of a 17 m long smooth pipe with an inner diameter of 127 mm. The Reynolds number was 5,277, based on the bulk velocity and the diameter of the pipe. To verify if the air flow was fully developed at the test section LDA measurements were carried out. For the results, which confirmed that the velocity profile was fully developed, and a description of these experiments we refer to Chapter 7. The flow was seeded with 1–2 μm diameter oil droplets generated by two atomizers. Injection was about 14 pipe diameters downstream of the flow inlet.

The optical set-up for the pulsed laser light sheet is given in Fig. 9.1. Two Nd:YAG pulsed lasers with a repetition rate of 20 Hz were accurately synchronized with a time delay of 0.50000 ms². The orthogonally polarized laser beams were combined into a double pulsed beam by a polarization splitter plate. A prism at the pipe outlet reflected the beam 90 degrees into the pipe. A spherical lens combined with a cylindrical lens transformed the beam into a thin, vertical light sheet. The thickness of the light sheet was about 1–2 mm.

image acquisition

The image acquisition system was built up with commercially available components. A simple video camera (Panasonic GP-MF702) with 649×491 (non-square) pixels was used in the interlaced mode, with a low cost Data Translation frame grabber in a PC-AT. The frame rate of the video camera was 30 Hz. The camera was synchronized with the two

²Note that a different value of the time delay was used in the OPIV measurements; see page 147.

lasers to obtain double-exposure images. The memory of the frame grabber could store 4 images. To empty its memory took about 1–2 minutes per 4 frames. Therefore, the 501 taken images are not a “continuous” time series.

Limited by the number of pixels of the video camera (because the camera was operated in interlaced mode only 256 lines in y-direction are available), the overall image size was chosen rather small, $20 \times 15 \text{ mm}^2$. Expressed in viscous units the length and height of the image was 60^+ and 50^+ , respectively. The camera was focused on a small part of the wall boundary layer, 15 to 30 mm distance from the wall, which corresponds to y^+ ranging from 40 to 90. This particular location was chosen, based on the previous OPIV measurements, which revealed it as an interesting area.

9.3 Results

First, the results of the different steps of the image analysis are presented and discussed. Next, the results of turbulence statistics are presented in comparison with the results of the OPIV experiments in the full pipe diameter. In addition, some results of conditionally sampled statistics are presented, compared with the results from the OPIV data and a direct numerical simulation (DNS) carried out at the same Reynolds number (Eggels *et al.* 1993b).

preprocessing

The digitally recorded video images can be enhanced relatively easy using standard image processing routines. The camera was used in the interlaced mode. Therefore, as a first step, the black lines were removed and we interpolated the remaining 256 lines to 512 lines. Next, the images were normalized to correct for possible non-uniform background lighting. For these operations we used the software package TCL-image.

interrogation analysis

In general, PIV data sets contain erroneous vectors. These are due to an insufficient local density of particle-images, or to a non-uniform particle displacement distribution within the interrogation area (Keane & Adrian 1990). After a test analysis of a small number of images it turned out that the particle density was too low for the analysis with 32×32 pixel interrogation areas. Therefore, we increased the size of the interrogation window to 64×64 pixels. This corresponds to a spatial averaging over an area of $7.5^+ \times 8.2^+$. The overlap of neighbouring interrogation areas was 75%. The combination of the used camera ($649 \times 491 \text{ px}$) and frame grabber ($512 \times 512 \text{ px}$) yielded images with $506 \times 480 \text{ px}$ exposed pixels. This yielded a set of 501 instantaneous velocity fields of 27×27 nodes each. A vector map of one of the obtained instantaneous velocity fields is shown in Figure 9.2.

The mean displacement of the particle images, as a function of distance from the wall, varied from 7.5 to 8.5 pixels. This means a relative particle displacement compared

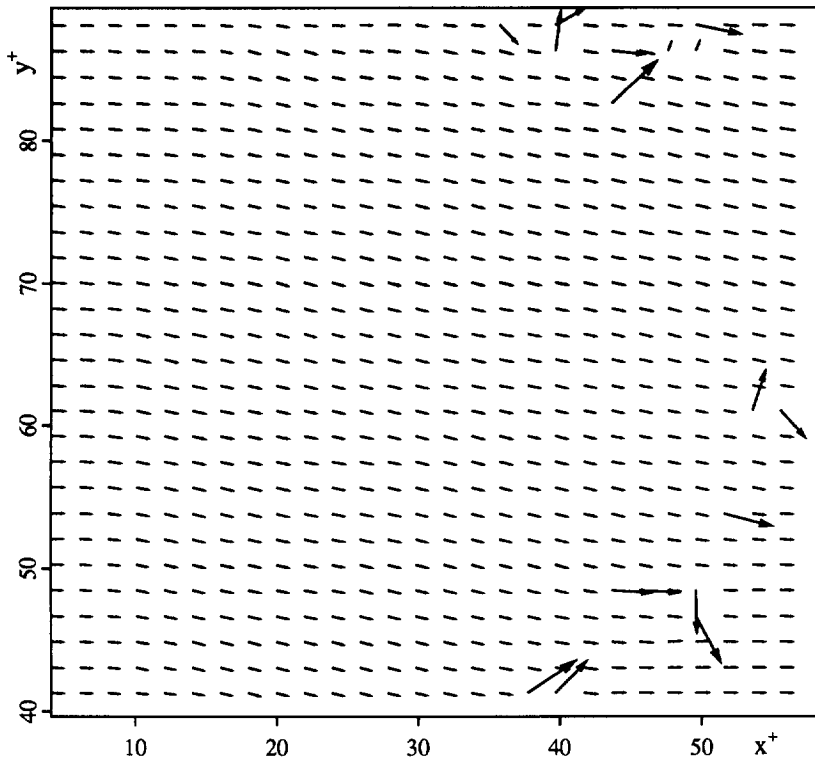


Figure 9.2: Vector map of the instantaneous velocity field obtained from the interrogation of a DPIV image. The map contains about 2% spurious vectors.

to the length of the interrogation area of $8/64$. This value is in agreement with the recommendations by Keane & Adrian (1990).

The analysis of one frame took less than 45 seconds (on our laboratory computer HP9000/720). That is, 60 seconds per 1000 vectors. For comparison only we mention here that for the analysis of an OPIV negative 1000 seconds per 1000 interrogations were needed (disregarding the time needed for the development of the film).

postprocessing: erroneous vectors

As the example of a raw DPIV vector map shows there are some erroneous vectors (see Fig. 9.2). For large numbers of images it would be an enormous laborious task to detect and replace these spurious vectors manually. In addition, visual inspection of PIV measurement data is subjective, and therefore not reproducible and not optimal. Therefore,

an algorithm has been written, which rejects vectors as spurious based on a deviation from the local median. An account of the details of this procedure and its efficiency is described in Chapter 4. After rejection, vectors are automatically replaced by a new velocity vector which value is computed by means of the interpolation of the eight neighbouring vectors.

Counting the number of detected outliers per image we found that about two third contained less than 1% of spurious vectors (for one third of the images the number of detected outliers was zero). We disregarded all the images which contained more than 5% of spurious vectors. This yielded that 93% of the images (i.e. 464) was used for further analysis.

turbulence statistics: mean and rms profiles

The turbulent flow statistics were obtained from the remaining 464 instantaneous velocity fields by averaging the data along lines of constant y in each field and then calculating the line averages over the full set. To normalize the flow quantities with the viscous length scale, ν/u_* , and the friction velocity, u_* , we used the results obtained previously with the OPIV measurements (see Table 7.1). The results are presented in the Figures 9.3–9.5. The

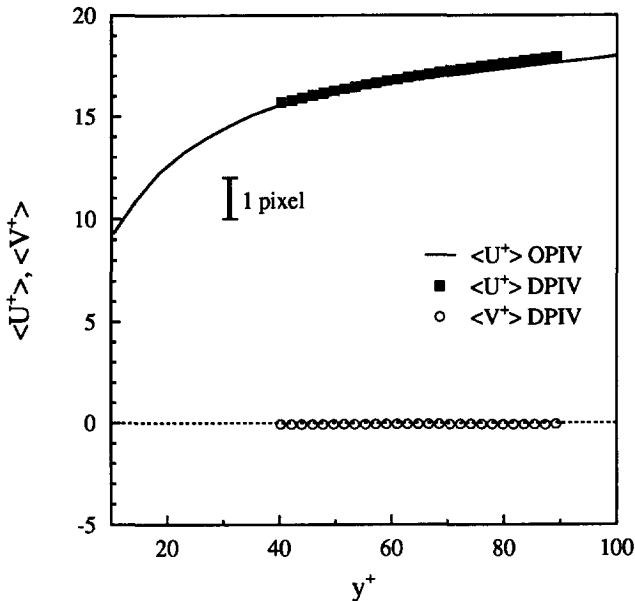


Figure 9.3: Mean axial (U) and radial (V) velocity profiles, normalized by friction velocity. The solid line represents the result from the OPIV measurement (see Chapter 7). The bar denotes the velocity corresponding to a particle-image displacement of 1 pixel.

normalized mean velocity profile (Fig. 9.3) and the normalized rms fluctuating velocity profiles (Fig. 9.4) are compared with the results from the OPIV data. As mentioned before, we used the results obtained with OPIV to normalize the DPIV data. Therefore, the agreement between the two mean profiles is rather good. In Fig. 9.3 the bar represents the velocity corresponding to a measured particle image displacement of 1 pixel.

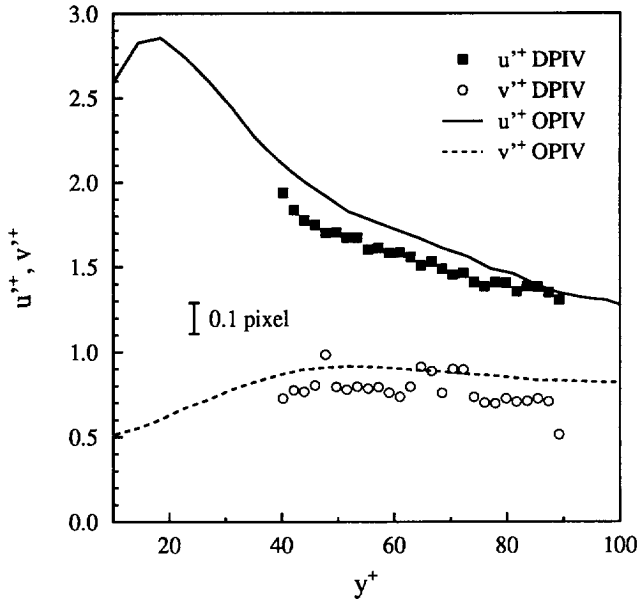


Figure 9.4: RMS profiles, normalized by friction velocity. The line represents the results from the OPIV measurement (see Chapter 7). The bar denotes the velocity corresponding to a particle-image displacement of 0.1 pixel.

In the rms profiles we see a difference of about 10%. This can be explained in terms of the differences in size of the interrogation windows between the two experiments. One should be aware of the fact that because of the finite size of the interrogation window the measured velocity field is a low-pass filtered representation of the observed flow field. The filter length is proportional to the size of the interrogation window. In the OPIV measurement the diameter of the interrogation window was about 4 viscous units, while in the DPIV measurement it was about 8 viscous units. Therefore, the turbulent fluctuations in the DPIV measurements are not fully resolved, which results in a slightly smaller value of rms fluctuating velocities. The bar in Fig. 9.4 shows the accuracy in the velocity, corresponding to 0.1 pixel. This indicates that the particle image displacement is estimated within sub-pixel accuracy.

We subsequently computed the out-of-plane component of the vorticity, given by

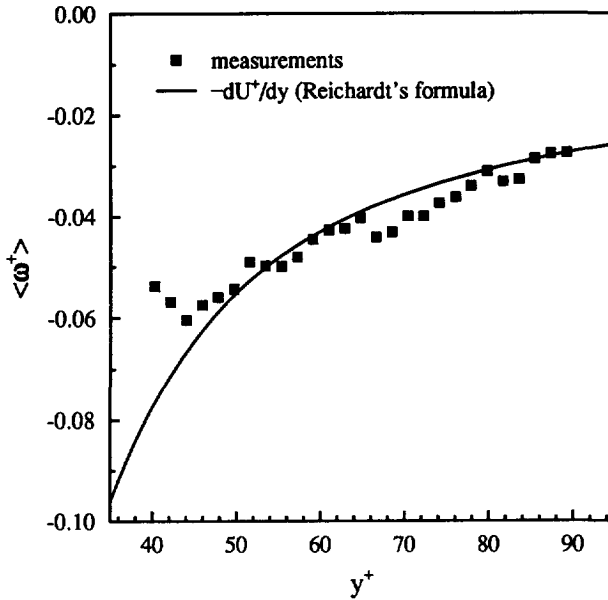


Figure 9.5: Mean vorticity profile, in viscous units. The line represents the computed profile obtained with Reichardt's formula for a fully developed turbulent pipe flow; see Eq. (7.2).

$\omega_z = \partial v / \partial x - \partial u / \partial y$. As an additional check of the accuracy of the measured data we compared the mean out-of-plane vorticity component with the derivative of Reichardt's formula for the universal profile for fully developed pipe flow (Reichardt 1951). This is shown in Figure 9.5. Except for the scattering in the measurements the agreement is good. Landreth & Adrian (1990) suggest to apply a careful smoothing prior to estimation of the vorticity, which suppresses the amplification of noise in the vorticity data due to differentiation of the velocity data. Since this would imply a further loss of spatial resolution we computed the vorticity directly from the measured displacement field. The agreement between the experimental and expected result in Fig. 9.5 demonstrates that the vorticity—without the additional smoothing—yields significant results.

turbulence statistics: structures

Visual inspection of the instantaneous fluctuating velocity fields reveals “structure-like” features. As an illustration two fields are shown in Figures 9.6 and 9.7. The fluctuating fields are obtained after subtraction of the local mean velocity. For demonstration reasons only, the result was multiplied with a factor of 10. When this procedure is carried out on the vector field shown in Fig. 9.2 we obtain the result shown in Fig. 9.6. The

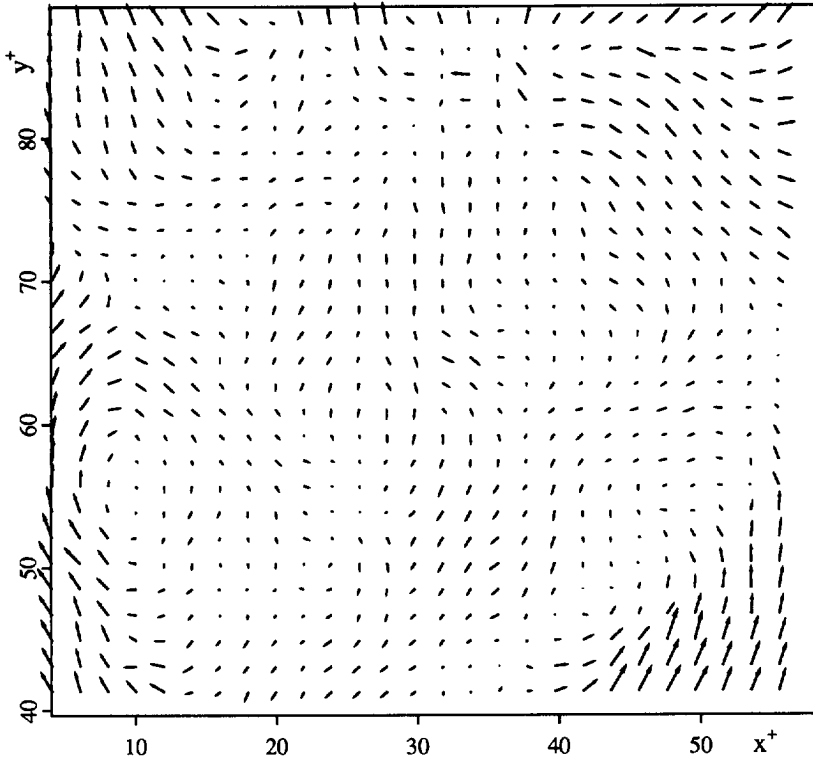


Figure 9.6: Vector map of the instantaneous fluctuating velocity field as obtained after replacing spurious vectors and after subtraction of the local mean velocity from the field shown in Fig. 9.2. The vectors have been magnified by a factor of 10 with respect to the vectors in Fig. 9.2.

fluctuating velocity components are rather small, especially if seen in comparison with the instantaneous fluctuating field shown in Fig. 9.7. This field reveals a dominant coherent movement in the flow. Compare this with the detail of an instantaneous fluctuating velocity field obtained with OPIV shown in Fig. 7.12. The similarity between the large patterns is striking! We emphasize that these flow patterns were found in the same pipe flow facility at equal flow conditions, but in different experiments. It should be repeated that the OPIV experiments covered the full pipe diameter instantaneously with sufficient spatial resolution. Whereas for the DPIV experiments we focused on a relatively small region of the pipe flow, due to the relatively low spatial resolution of the image acquisition components. However, visual comparison of the two instantaneous fluctuating fields (Figs. 9.6 and 9.7) demonstrates that both techniques are able to capture similar structures. Despite the lower spatial resolution and measurement accuracy of DPIV in

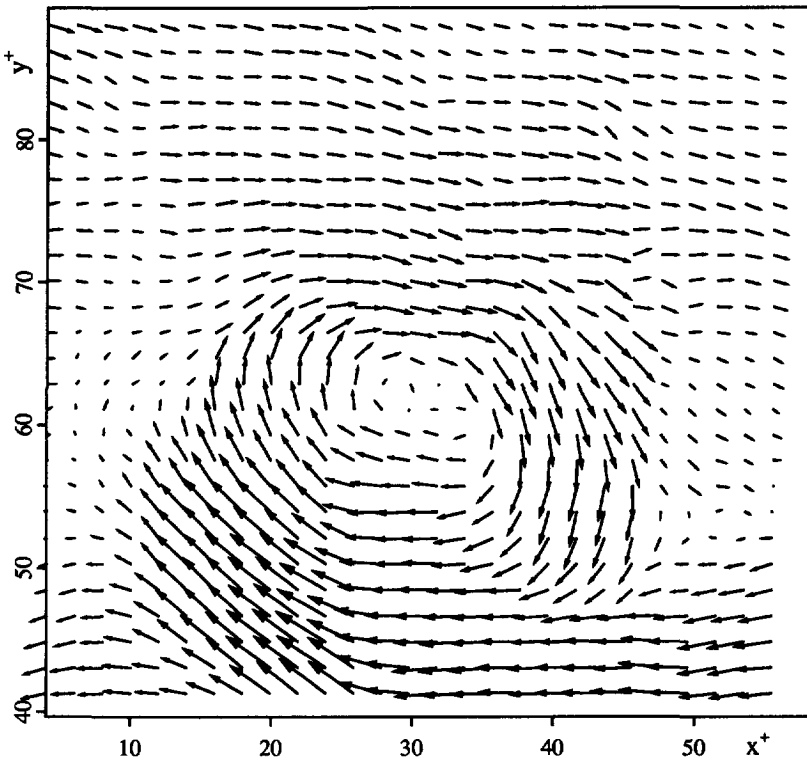


Figure 9.7: As in Fig. 9.6, but obtained from another DPIV image; cf. Fig. 7.12.

comparison with OPIV it is possible with DPIV to resolve coherent flow structures in turbulent flows. The obvious advantage of DPIV is that the time needed to record and process the digital image to yield the result shown in Fig. 9.7 is only a fraction of the time needed for the analysis of an image with OPIV.

Dealing with large numbers of images, fully automatic algorithms are needed to search for flow structures. Recently, Eggels *et al.* (1993b)³ presented some results of a quantitative comparison study of vortical flow structures generated by a direct numerical simulation (DNS) in the same geometry (*viz.*, a smooth pipe) and flow conditions as the OPIV measurements presented in Chapter 7 and the DPIV measurements presented here. For obvious reasons of comparison, our data has been processed exactly in the same way.

The assumption underlying their conditional sampling criterion is based on observa-

³see Chapter 8

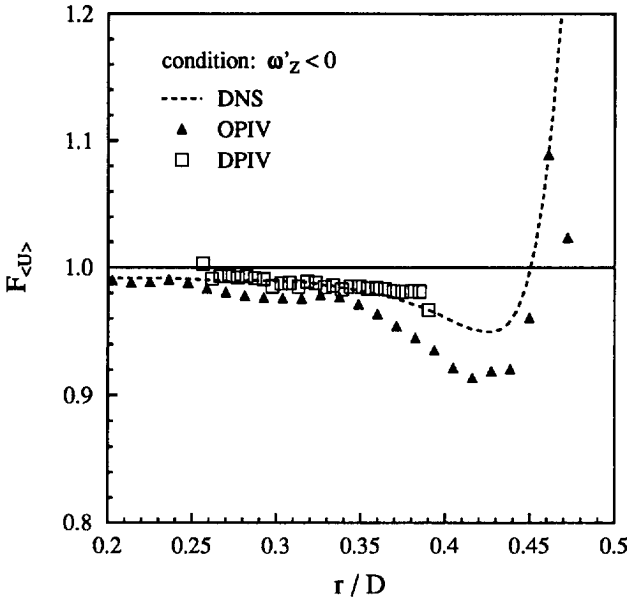


Figure 9.8: Relative importance of the vortical flow structures to the mean velocity as function of the dimensionless distance from the centerline.

tions of the instantaneous 2-D fluctuating vorticity distributions as obtained with OPIV. It seems that the regions with negative vorticity fluctuations, $\omega'_z < 0$, tend to be more organized in flow structures. Therefore, the regions where $\omega'_z > 0$ were neglected. The former regions are referred to as vortical flow structures. To investigate the relevance of these vortical flow structures to the turbulence flow statistics conditional sampling is used. Therefore, each mean turbulent flow quantity $\langle \phi \rangle$ is assumed to consist of two contributions: $\langle \phi \rangle = \langle \phi \rangle_{\text{vfs}} + \langle \phi \rangle_r$, with the conditionally sampled averages over the vortical flow structures $\langle \phi \rangle_{\text{vfs}}$ and over the remaining flow regions, $\langle \phi \rangle_r$, i.e.

$$\langle \phi \rangle_{\text{vfs}} = \frac{1}{N} \sum_{i=1}^{N_{\text{vfs}}} \phi(i) \quad \langle \phi \rangle_r = \frac{1}{N} \sum_{i=1}^{N_r} \phi(i) \quad (9.1)$$

respectively, where N is the total number of data samples, N_{vfs} the number of samples which, according to the conditioning criterion, correspond to vortical flow structures, and N_r the number of samples corresponding to all other flow regions. The fraction of samples corresponding to either of the flow types are denoted with n_{vfs} or n_r , with $n_{\text{vfs}} + n_r = 1$. To investigate the relevance of the vortical flow structures to the mean turbulence statistics the averaged contribution of both vortical flow structures and all the other flow regions

are compared, expressed in the following parameter⁴:

$$F_{\langle\phi\rangle} = \frac{\frac{\langle\phi\rangle_{vfs}}{n_{vfs}}}{\frac{\langle\phi\rangle_r}{n_r}} = \frac{\frac{1}{N_{vfs}} \sum_{i=1}^{N_{vfs}} \phi(i)}{\frac{1}{N_r} \sum_{i=1}^{N_r} \phi(i)}. \tag{9.2}$$

If $F_{\langle\phi\rangle}$ equals one, the averaged contribution of both flow regions is equal. For a more detailed description and for a discussion of the results obtained from the DNS and the OPIV data we refer to the paper by Eggels *et al.* (1993b).

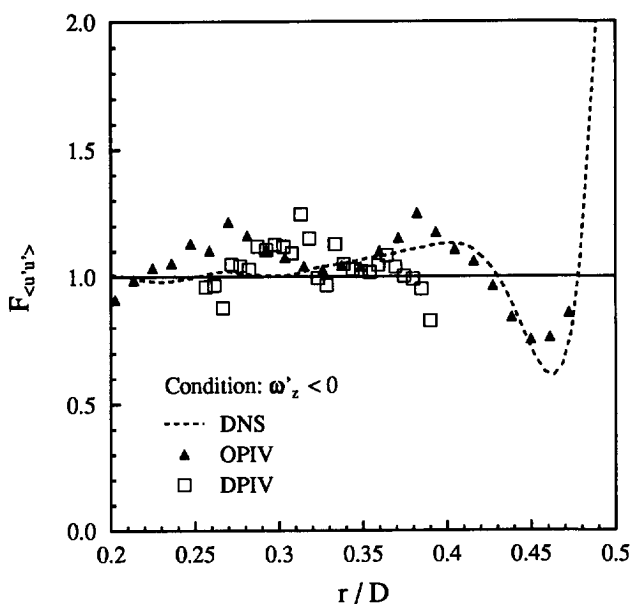


Figure 9.9: Relative importance of the vortical flow structures to the root mean square of the streamwise velocity fluctuations, as function of the dimensionless distance from the centerline.

The results of this conditional sampling are given in the Figures 9.8–9.10 in comparison with the results obtained from the OPIV and DNS data sets. In these figures the relative contribution to the mean flow velocity, $\langle U \rangle$, the mean Reynolds stress, $\langle u'v' \rangle$, and the turbulence intensity in flow direction, $\langle u'u' \rangle$ are shown. In the investigated area, $40 < y^+ < 90$, the value of $F_{\langle\phi\rangle}$ for all three mean quantities is approximately equal to one. $F_{\langle U \rangle}$ approximately equal to one is indicating, that the vortical flow structures travel with a velocity similar to the local mean flow velocity. The scattering in the DPIV results for $F_{\langle u'v' \rangle}$ and $F_{\langle u'u' \rangle}$ is relatively large compared with the results obtained with OPIV.

⁴see Eq. (8.5)

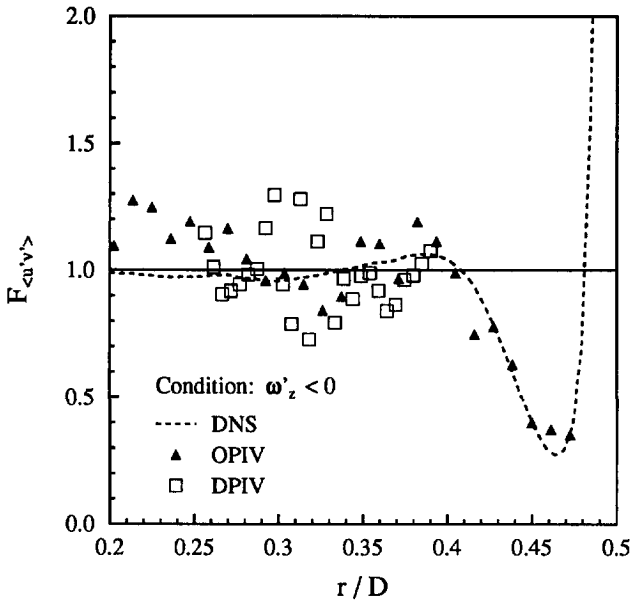


Figure 9.10: Relative importance of the vortical flow structures to the Reynolds shear stress, as function of the dimensionless distance from the centerline.

9.4 Conclusions

The measurements presented here are probably the first successful application of DPIV in a fully developed turbulent flow. The flow under study was a relatively small area close to the wall in a pipe flow, at a Reynolds number of 5,300. The dimensions of the flow region, ranging from $40 < y^+ < 90$, were defined by the resolution of the camera and the frame grabber. A set of 501 directly recorded digital images were analyzed. The analysis time of each image in 730 interrogation positions took less than 45 seconds. This is a considerable improvement in processing speed in comparison with the conventional method applied in OPIV. Hence, we could easily analyze this large amount of images in a very short time. The turbulence statistics of first and second order quantities, calculated from the data are in fair agreement to previously carried out OPIV measurements spanning the full diameter of the same pipe flow. The accuracy is estimated at $0.2-0.4 u^+$, which corresponds to a measured particle image displacement of $0.1-0.2$ pixel. Visual inspection of the instantaneous fluctuating velocity fields shows that both techniques are able to capture similar dominant structures. In addition, some results of a numerical comparison of structures found in the two data sets (DPIV and OPIV) were presented. Summarizing, the results of the application of DPIV in a turbulent flow are encouraging.

Chapter 10

Conclusions

In this final chapter we summarize the main results and conclusions presented in this thesis. We review to which extent the problems put forward in the first chapter of this thesis have been clarified. In addition we will consider some general aspects of the application of PIV to turbulent flow research. This chapter concludes with the author's view on the future developments in (digital) PIV.

recapitulation of the problem

In the first chapter of this thesis we have argued that for the investigation of coherent flow structures in turbulent flow we need a (new) measurement technique that yields quantitative spatial information of the instantaneous flow velocity field. A very promising technique is particle image velocimetry (PIV) which is an optical measurement technique that yields the instantaneous velocity field in a planar cross section of the flow. The data obtained from PIV measurements enable us to compute flow quantities, such as (components of) the vorticity and the deformation; these quantities are very useful in the study of coherent flow structures, since vorticity and deformation are closely related to the dynamics of coherent structures. The fundamental differences of PIV with classical visualization should be emphasized here. First, classical visualization yields only a *qualitative* picture of the flow structures, while PIV yields *quantitative* information. Secondly, in classical flow visualization the tracer material (dye, smoke or particles) is applied in such a way that the flow structure of interest becomes directly visible, while in PIV the tracer material (particles) is applied homogeneously and the flow structure is deduced through physical quantities of the flow field (viz., vorticity).

In conventional PIV, images are recorded on photographic film, which—after development—is interrogated in small interrogation areas by an optical read-out system. We therefore refer to this conventional method as OPIV. The interrogation area is analyzed with a high *pixel* resolution, which yields accurate results (better than 1%). By using a large film format we can also obtain a high *spatial* resolution. However, the analysis in OPIV is (inherently) slow due to (a) the development of the film and (b) the mechanical manipulation of the negative in the interrogation system. As a result the analysis of a single negative takes several hours. This implies a bottleneck in the processing of a

sequence of PIV images, which is a serious obstacle in the application of PIV to the investigation of coherent structures in turbulent flow, where one is especially interested in the time evolution of structures; see Example 1 on page 20.

In this thesis an alternative digital implementation of the PIV method is presented—referred to as DPIV—that processes the data in less than about 1% of the time needed for the OPIV analysis. The price to pay for this improvement is a somewhat lower spatial resolution and a slight loss of accuracy. A test measurement of the vortex street in the wake of a circular cylinder described in Sect. 1.3.2 demonstrated that with low pixel resolution we can still extract significant information of the dynamics of coherent structures in a flow. The digital analysis of a PIV photograph taken from a turbulent flow behind a grid demonstrated that digital PIV, despite its somewhat lower resolution and accuracy, can provide significant information of coherent structures in turbulent flow.

There are no fundamental differences between the traditional and digital OPIV methods. However, in the traditional PIV analysis the interrogation images are digitized and processed with a high pixel resolution, while for digital PIV a low pixel resolution is used. For analysis with high pixel resolution we can neglect the fact that we are dealing with images of discrete pixels, but this approach can no longer be maintained at low pixel resolution. Also there seemed to be a kind of controversy reported in literature; the accuracy claimed at low pixel resolution appeared to be better than was expected on the base of extrapolation of the accuracy at high pixel resolution; see Sect. 1.3.3. The estimates of the measurement accuracies were all obtained from simple calibration measurements, which did not provide much insight or explanation of this controversy. In addition, there was no clear picture of the limitations of the DPIV method with respect to the pixel resolution in the interrogation analysis; in other words, what is the minimum required pixel resolution that would still yield significant results? In this thesis an analytical investigation of the measurement accuracy for digital interrogation of PIV images was carried out. In Fig. 1.10 the subsequent stages are given in the PIV image acquisition and analysis that were investigated. The results of this investigation are given in Part I of this thesis.

10.1 Theory (Part I)

In this section we will discuss the major results of the analysis derived in Part I, namely: digital PIV analysis (image statistics, bandwidth, accuracy), data-validation (spurious data) and the estimation of vorticity and deformation.

image statistics

The measurement of the velocity field from tracer displacements implies that the *measured* flow field is a low-pass filtered representation of the *actual* flow field; see Sect. 2.3. It was shown that a dense seeding of the flow (i.e. the average distance of the tracer particles is less than their displacement) can in principle fully resolve the observed displacement field. Additionally we argued that, if we want to obtain a measurement that is not biased in favour or against a certain flow structure, a homogeneous seeding is required

with particles that follow the motion of the fluid exactly (*ideal tracer particles*) in an incompressible flow. Under this condition the spatial image statistics are *homogeneous*; see Sect. 2.7. This was the point of departure for our analytical investigation, where we partially followed the procedure as put forward by Adrian (1988) for continuous images. It was necessary to re-derive and extend his results in order to include also the digitization of PIV images; see Sect. 2.9. In the theoretical analysis given in Part I of this thesis we obtained expressions for the (ensemble) statistics of the digital images and subsequent estimation of these statistics from a single realization of a PIV image; see Eq. (3.10) in Sect. 3.2.

bandwidth

One of the most important aspects of digitization of images is the choice of an appropriate sampling rate. In Sect. 3.5 we took a closer look at the (minimum) required sampling rate that would be needed for the interrogation analysis. It appeared that the high pixel resolution used in conventional OPIV analysis corresponds to a sampling rate that matches the optical bandwidth of the PIV imaging system, i.e. the original picture can in principle be reconstructed from the discrete image. We argued, however, that for the determination of the displacement it is not necessary to have complete optical information of the picture. Alternatively we estimated the bandwidth of the PIV image according to Parzen's definition, which yielded a value that is about a factor 4^2 lower than the optical bandwidth; see Eq. (3.16). It was subsequently demonstrated that the information content of the PIV signal does not further improve for sampling rates above the Parzen bandwidth. In a practical situation this implies that a pixel resolution of 64×64 is already sufficient, while the optical bandwidth would prescribe a resolution of 256×256 pixels.

accuracy of interrogation analysis

The actual accuracy of the measurement as function of the pixel resolution is not only determined by the image bandwidth, but also by the performance of the estimator that is used to determine the centroid of the displacement-correlation peak. We have tested the performance (mean and variance) of three different estimators.

We further employed the results obtained for the statistical properties of the image statistics to investigate the performance of three different estimators for the centroid of the displacement-correlation peak, namely the center-of-mass, parabolic peak-fit and Gaussian peak-fit estimators; see Sect. 3.8.1. The accuracy of center-of-mass estimator improves slightly with increasing pixel resolution. Hence, although the information content of the signal does not improve for a resolution that is higher than the bandwidth, the estimation of the displacement at high pixel resolution is somewhat better than at low pixel resolution. The investigation also revealed that other estimators, i.e. the parabolic and Gaussian peak-fit estimators, loose accuracy when the pixel resolution is increased; these estimators appear to have an optimal performance at a pixel resolution that matches the minimum required sampling rate of the PIV image. This explains the controversy that

was observed in calibration measurements with different estimators at different pixel resolutions; see Sect. 1.3.3. As was already discussed in the previous paragraph, it was shown in Sect. 3.7 that the information content of the displacement-correlation peak at a resolution above the image bandwidth (by Parzen's definition) changes marginally. This implies that with the use of optimally efficient estimators—given the pixel resolution—the relative accuracy as function of the pixel resolution changes marginally. Let us illustrate the implication of these results with respect to the differences between OPIV (i.e. analysis with high pixel resolution) and DPIV (i.e. analysis with low pixel resolution): by reducing the pixel resolution with a factor of 8 (viz., from 256×256 to 32×32 pixels) the processing speed is increased by a factor of 100, while the relative accuracy deteriorates with only a factor 2–4.

Not only the *choice* of the estimators was discussed, but also the influence of two important *properties*: the mean and the variance. First, we showed that even for uniform displacements there is a small bias towards the zero displacement. Secondly, we could predict the behaviour of the random measurement error as function of the displacement. Let us review the consequences of these results.

We found in Sect. 3.9.1 that the bias is inversely proportional to the pixel resolution and proportional to the width of the displacement-correlation peak. In other words, the magnitude of the bias is determined by the width of the displacement peak with respect to the size of the interrogation area. Thus, a bias will occur for all influences that tend to increase the width of the displacement-correlation peak, i.e. the increase of the particle-image diameter due to the finite size of the tracer particles, but also unresolved motion at scales below the size of the interrogation area and strong velocity gradients over the interrogation area. (It should be noted here that Adrian (1988) reports that a such bias would occur only for non-uniform displacements.)

For particle-images with a diameter of 4 px and a 32×32 pixel interrogation region with a uniform weight kernel this bias is about 0.06 px. This was also verified in a test experiment. Markedly this bias was not reported by others (Willert & Gharib 1991; Lourenço 1993), although it should have made a significant contribution to the total measurement error in their calibration measurements.

Hence, we obtained a general explanation of biases in the measured displacement with respect to the actual displacement. Our theoretical analysis also provided a simple correction procedure in order to compensate for this bias. It is important to note that this correction is applied prior to the actual estimation of the displacement; the correction does not require any parameter (since the bias is proportional to the correlation-peak width, an *a posteriori* correction would require the width of the correlation peak as a parameter).

In Sect. 3.9.2 we have shown analytically that the accuracy of estimating the peak centroid does not depend on the image density of the PIV image, but only on the width of the peak. However, the probability to detect the displacement-correlation peak amongst the random correlation peaks is determined by the image density. (The combination of these two effects determines the overall performance of the PIV analysis). We investi-

gated the behaviour of the measurement accuracy as function of the displacement. The expression for the variance of the estimator (Eq. 3.93) can be split up in three terms: (a) a *partial-derivative* term that only depends on the applied estimator, (b) a *balance* term that depends on the weight kernel, and (c) a *variance* term that depends on the bandwidth of the PIV image. It appeared that the qualitative behaviour of the accuracy as function of the displacement is determined by the choice for the weight kernel in the interrogation analysis; for a *uniform* weight kernel the accuracy is approximately constant as function of the displacement, while for a *Gaussian* kernel the accuracy is directly proportional to the displacement. The behaviour for different weight kernels could be understood qualitatively. However, it was necessary to introduce a free parameter (probably related to instrumental noise) to obtain also a quantitative agreement between the analytically predicted and observed accuracies. It is conjectured that a more realistic model for the statistics of the PIV signal (i.e. one that includes also the presence of instrumental noise) would make it possible to predict also this free parameter.

It was demonstrated that in a practical situation the accuracy for the measurement of the displacement at low pixel resolution is less than 0.1 px. This value is based on rather large particle-images (with a diameter of about 4 px). Calibration experiments by Willert & Gharib (1991) suggest that accuracies up to 0.02 px are feasible.

spurious data

The probability that the highest correlation peak is indeed the displacement-correlation peak is determined by the number of particle images in the interrogation image. A simple model, based on the principle that at least five particle-images are required to yield a valid displacement (Sect. 3.6.4), seemed to explain qualitatively the behaviour as function of the displacement of spurious vectors in a test experiment; see Sect. 3.10. Still, this is somewhat unsatisfactory, because we concluded earlier that the fact that a PIV image consists of *particle-images* is not significant with respect to the analysis. Instead, one would expect a model that relates the valid-detection probability to the image *contrast*¹. This model would then perhaps also apply to images with high source density (viz., speckle images). Further investigation on this matter is required.

In principle it would be possible to reduce the probability of detecting a spurious displacement peak to an arbitrarily small value by increasing the image density. However, in practice there are a few complications. First, at a certain density the particle images will start to overlap. From that point we can insert more particles to the flow, but this no longer improves the image quality (which is now determined by the contrast of the speckle pattern). Secondly, the application of a high density of tracer particles may have undesirable influence on the flow or may considerably reduce the transparency of the fluid. Therefore a strategy that aims at a maximal reduction of the spurious-data probability may not always prove to be effective. Instead, it is more practical to allow a (predefined) fraction of spurious data (say 5%) and subsequently remove these data in a

¹The image contrast is defined as the rms fluctuating image intensity divided by the mean image intensity.

post-interrogation data-validation procedure.

An argument against such a strategy is that in this way one may perhaps filter out interesting flow phenomena. This argument may have some relevance, but it is not necessarily true. Let us explain this. In Appendix A.2 it was described that under the conditions of a homogeneous distribution of ideal tracer particles in an incompressible flow the distribution of these particles over the flow is *not* determined by the flow velocity field. So, the local density of the tracer particles is not determined by the presence of any flow structure. Thus, from *first principles*, we do not expect to find a higher signal “drop-out” (i.e. the occurrence of insufficient particle-images in the interrogation area that results in the detection of a spurious displacement) correlated with certain flow structures. However, the amplitude of the displacement-correlation peak is determined by the out-of-plane motion of the tracer particles (see Eq. (2.49)) and the local variations in the displacement field. Likely, these effects may be correlated with the presence of certain structures. Therefore to assure that the spurious data is independent from the flow field we must satisfy two additional requirements, namely: (a) the out-of-plane displacement is small with respect to the thickness of the light sheet and (b) the local variations of the displacement field are small with respect to the local mean displacement; see the discussion in Sect. 2.9.

Following the second strategy we developed a new method, based on the local-median filter. In Chapter 4 we used a statistical model of a PIV data set to test this method against other (existing) data validation procedures. We thus demonstrated that the local-median method is the most efficient and robust of the considered procedures. In addition the statistical model was used to optimize the procedures. Subsequently the method was successfully applied to all the experimental data described in Part II of this thesis. The most important achievement of the data validation methods presented in Chapter 4 is that they can be fully automated (the optimal decision criterion for accepting or rejection of data can—in principle—be determined automatically). This is especially beneficial to the processing of large amounts of PIV data sets.

vorticity and deformation

The validated data sets (after detection and removal of spurious data, and subsequently filling up “open” spaces in the data set by (linear) interpolation) can be used to determine contributions to the vorticity vector and deformation tensor. We applied existing methods, that are described in detail in Chapter 5. There we have shown that for significant results of the vorticity the (random) error in the measurement should be maximally a few percent of the accessible displacement range in the interrogation analysis. With the conventional OPIV analysis the relative error is commonly less than 1%; for digital PIV the relative measurement error is about 1–2%. Although not as accurate as with the conventional PIV method, we may still expect significant results for the estimated vorticity (and concurrently the estimated deformation). This was confirmed by the analysis of the PIV image taken from the turbulent flow behind a grid which demonstrated that digital PIV could provide significant information of the vorticity and deformation from a

turbulent flow; see Chapter 6.

To distinguish between different flow regions Hunt *et al.* (1988) suggested a method to subdivide a flow into eddies (E), convergence (C) regions and streaming (S) regions, based primarily on the value of the second invariant of the deformation tensor. In PIV we have only access to two velocity components from which we can evaluate only 4 out of 9 tensor components². Despite the fact that we have only an incomplete set of components (see Sect. 5.3) it appeared still possible to apply the concept of E, C and S regions to PIV data sets. The PIV measurement data obtained from the turbulent flow behind a grid demonstrated that we could detect flow patterns that match the patterns associated with these E, C and S regions; see Chapter 6. However, it is currently not known how to interpret the results from this type of classification when applied to planar cross section of a three-dimensional flow. In addition, in the case of experimental data the results may also be affected by noise. It was therefore decided, for the moment, not to apply these methods to the other experimental data³.

However, one of the general problems that we face in evaluating the PIV measurement results is how the computed vorticity and deformation are related to the actual instantaneous vorticity of the flow. Since we have a limited spatial resolution we have to estimate derivatives of the velocity field by finite differences. In doing this we will always make a (small) error, and subsequently we cannot always fully resolve all length scales (the same problem occurs in numerical simulation). On the other hand, we have seen in Sect. 5.2 that the noise in the PIV data set prevents the measurement of weak, large scale gradients. So, we conclude that we can only assess the derivatives of the velocity field over a limited range of scales. We will return to this point in Section 10.3.

10.2 Application (Part II)

The second part of this thesis consists of four papers that report on the application of PIV to turbulent flow, namely:

- DPIV measurements of a turbulent flow behind a grid (see Chapter 6),
- OPIV measurements of a fully developed turbulent pipe flow (see Chapter 7),
- numerical comparison of vortical flow structures in DNS and OPIV studies of turbulent pipe flow (see Chapter 8), and
- DPIV measurements of a fully developed pipe flow (see Chapter 9).

²Actually, we can evaluate even 5 components if we make use of the relation $\text{div } \vec{v} = 0$ for incompressible flows.

³With regard to the pipe flow data we have the additional complication that the radial flow direction is not homogeneous; the original definition by Hunt *et al.* (1988) applies to homogeneous and isotropic turbulence.

The first experiment was intended to assess the quality of velocity data from digital PIV measurements of turbulent flow with respect to the computation of vorticity and deformation. It has been mentioned in the introduction of this chapter and will not further be discussed here. The second paper describes OPIV measurements carried out as part of a joint study on fully developed turbulent pipe flow with both numerical and experimental techniques (a complete overview of all numerical and experimental results obtained in this study is given by Eggels *et al.* (1993a)). The aim was to compare the results from a direct numerical simulation (DNS) implemented in cylindrical coordinates, with experimental data obtained with hot-wire and laser-Doppler anemometry and PIV of the same flow geometry (*viz.*, a pipe flow) and at the same flow condition (*i.e.* $Re \sim 5,300$). In extension to this comparative study between numerical and experimental data an attempt was made, described in the third paper, to compare the structures observed in the OPIV data set with those observed in the DNS data set. The aim of the experiment described in the fourth paper was to find out if we could obtain with digital PIV the same kind of information as was obtained with the conventional PIV method.

A comparison was made of two different aspects of the flow: (a) the statistics of the flow velocity field and (b) the vortical structures observed in the numerical and experimental data sets.

statistics

The OPIV data sets were used to compute several turbulence statistics, like the mean and fluctuating rms velocity profiles and the shear stress profile. These results indicated that the observed flow could be considered as a fully developed turbulent pipe flow. The results from the OPIV data—though obtained from only 33 photographs—were in good agreement with the LDA data and with the results obtained from the DNS. The OPIV data were also used to estimate the spatial energy spectra of the axial and radial velocity components. The agreement with the spectra obtained with the DNS, taking into account the relatively small sample size of the OPIV data set, was quite good. It should be noted that these experimental spectra are truly spatial spectra, that were computed without recourse to use of Taylor's hypothesis of frozen turbulence. The flow statistics obtained with DPIV (500 images) agreed fairly well with those obtained with OPIV, even though the equipment was not optimally suited for this type of experiment. It should be emphasized that the time needed for the interrogation of 10^3 positions took 1,000 seconds with OPIV whereas it took only 60 seconds with DPIV.

vortical structures

A qualitative investigation of the vorticity maps computed from the OPIV data sets yielded four generic flow structures; see Fig. 5.3. These structures were found on more than one occasion on different photographs. Sometimes these structures were found in close proximity of one another; as if they belonged to a single, larger structure. The representation of these four generic structures in Fig. 7.13, suggests that they may be

related. These structures suggest correspondence with the temporal evolution of a hair-pin or horseshoe vortex found by Robinson (1991) in a direct numerical simulation of a turbulent boundary layer by Spalart (1988). Conversely, the structures in Fig. 7.13, could also represent the same (three-dimensional) structure, but seen in different lateral cuts. For example, the "vortex" structures could be found near the plane of symmetry of the structure in Fig. 1.3, while the "shear-layer" structures could correspond to cuts through the "legs" of the structure. The structures in Fig. 7.13 also seem to fit in with the conceptual model for the evolution of a hair-pin vortex in a boundary-layer flow, as suggested by Smith (1984). The occurrence of elongated and kinked shear layers resembles the structures observed and investigated by Kim *et al.* (1971). Summarizing, it can be said that we presently do not know exactly how to interpret these results. A further analysis of the numerical simulation data together with PIV data should bring more results.

Since we wanted to carry out an unbiased comparison (i.e. we did not want to pin us down to a specific structure observed in the OPIV data) we only investigated whether the *statistics* of the observed structures found in both data sets agreed or not. The results showed that the vortical structures in both the DNS and OPIV data have the same aspect ratio and inclination to the pipe wall. A logical next step would be the identification of the structures in Fig. 7.13 in the DNS data, and use the (fully resolved) DNS data to determine the mutual relationship between these structures. A preliminary investigation, in which a cross-correlation method between the two data sets was applied, revealed that a sophisticated procedure is needed to make a robust identification.

In the DPIV data set it was also possible to detect an eddy structure similar to one of the structures found in the OPIV measurements, see Figs. 7.12 and 9.7. This experiment demonstrated that it is possible to make direct (digital) recordings of small tracer particles in a turbulent flow. To the knowledge of the author this has been so far the *only successful* application of digital PIV to turbulent flow.

10.3 Future developments

theory of digital PIV

As was already concluded in Sect. 10.1 the theoretical approach presented in Chapters 3 and 2 only applies to an idealized situation. The two most common non-ideal situations are (a) inhomogeneous seeding (in the case of seeding with non-ideal tracer particles or compressible flow) and (b) the analysis of flow regions with strong velocity gradients. In these situations the (local) seeding density is linked to the (local) velocity field; see Appendix A.2. A logical next step would be to extend this analytical description to include also non-ideal situations. The main problem here is not the image analysis itself; provided that a sufficient number of particle-image pairs are present we will generally detect a displacement-correlation peak. The question is how to *interpret* the measured displacement. In the case of non-ideal tracer particles we may be able to account for the dynamical behaviour of the tracers with respect to accelerations or decelerations of

the fluid. In a sense the tracer particles can be considered as part of the *instrument*, with a “given” dynamical response. It may be possible to use a deconvolution approach for reconstruction of the actual displacement field. With regard to velocity gradients Adrian (1988) demonstrated that the measured displacement in the presence of a strong velocity gradient is biased towards low velocity. In that case we cannot simply interpret the measured displacement as a local (uniform) average over the displacement field. In the analytical description presented here we only consider the *translation* of the tracer pattern. An obvious—but non-trivial—extension would be to consider also the *rotation* and the *straining* motion of the pattern.

optimization

The analytical description of the image analysis allowed us to investigate the behaviour of different estimators for the fractional displacement, and the effect of applying different weight kernels. Conversely, we may apply this theoretical approach to “design” optimally efficient estimators and weight kernels, based on *a priori* knowledge of the observed flow field.

new imaging techniques

Although the development of the PIV technique has proven to be a substantial improvement in the experimental investigation of coherent flow structures, it only yields only the two in-plane velocity components in a planar cross section of the flow. The next step would be to develop techniques that would enable us to determine all three velocity components in a plane. Eventually these techniques may be extended to yield fully resolved three dimensional measurements of the flow field⁴.

Gauthier & Riethmuller (1988) and Arroyo & Greated (1993) demonstrated that the out-of-plane velocity component can be reconstructed from simultaneously recorded images in a two-camera stereoscopic imaging system. The reconstruction requires accurate measurement of the displacement, and the applications mentioned here used *photographic* recording. Westerweel & Nieuwstadt (1991) demonstrated with a simple test measurement and by the analysis of artificially generated PIV images that the accuracy of a stereoscopic *digital* PIV system is sufficient to yield significant measurements of the out-of-plane component. This has yet not been verified in any actual experiment.

Fully resolved three-dimensional measurement would require also different recording techniques, such as holography, tomography or volume imaging with a scanning light sheet (Dahm *et al.* 1992). One of the drawbacks of holographic recording is that it is difficult to acquire large sequences (time series) of densely seeded flows. The application

⁴With multiple-camera particle-tracking velocimetry (PTV) it is already possible to measure the three components of the fluid velocity in space; see e.g. Papantoniou & Maas (1990). However, this is only for a limited number of particles, distributed randomly over the flow. Besides, we have seen in Sect. 2.3 that PTV does not fully resolve the observed displacement field

of tomography and scanning light sheets in quantitative flow visualization is as yet mainly untouched.

interpretation of PIV data

In Chapter 5 it was already mentioned that the vorticity and deformation computed from PIV data sets yield a representation of the actual vorticity and deformation of the observed flow with respect to certain length scales only. Presently we do not exactly know how the *measured* vorticity is related to the *actual* vorticity in the flow. This implies that we should be somewhat careful in the interpretation of the results. This of course also holds for the deformation. With respect to the classification of E, C and S regions we have the additional problem that we can only determine 4 out of 9 tensor components. A detailed investigation of the relation between the classification of E, C and S zones based on a subset of the deformation tensor and the full deformation tensor was not included in this study, but should eventually be carried out in order to interpret the measured PIV data. Such a study could be carried out by generation of artificial PIV images from computer simulation data (so that we have access to all velocity components and pressure), and subsequently relate the results obtained from the PIV data to particular features of coherent flow structures. In this way we can learn from the numerical simulations, carried out at low Reynolds number, how to interpret PIV measurement data at high Reynolds numbers or complex flow geometries that are currently not accessible to numerical investigation.

The problem described above deals with the estimation of the three-dimensional features of objects derived from a two-dimensional representation (i.e. a "slice" or planar cross-section—of finite thickness—of the flow); in a sense there is a parallel with *stereology* (Russ 1986). In that respect the following should be remarked. It was demonstrated by Young (1988) that the measurement of simple object features (like the object perimeter and area) requires a sampling rate (viz., interrogation density) that is higher than the bandwidth of the picture (viz., measured velocity data). PIV images are usually interrogated with contiguous or partially overlapping interrogation regions. It is generally believed that an overlap of more than 50% does not yield substantially more information. This is based on two considerations⁵: (a) for an overlap of more than 50% the measurement errors for consecutive data become strongly correlated, and (b) only motions with a wavelength that is at least twice the diameter of the interrogation area can be resolved (by analogy of the Nyquist sampling criterion). Young's conclusion implies that for the determination of object features of coherent structures we must resolve the data by more than two points per smallest wavelength (i.e. an overlap of more than 50%). A preliminary test using the data in Sect. 3.10 indicated that the correlation between measurement errors remains small with overlaps up to 80%. This promising conjecture would imply that the amount of information that can be retrieved from a PIV image is substantially larger than generally believed. However, if we increase the overlap from 50 to 75%, the number of interrogations increases by a factor of four. This implies an even stronger demand

⁵A systematical investigation of these considerations has so far not been carried out.

on the processing speed (see Example 1 on page 20) with respect to the investigation of coherent flow structures. Nonetheless, in DPIV it is easy to extract the maximum amount of information from a image, because the processing time is not the limiting factor, as opposed to OPIV. It would therefore be useful to continue investigations along this line.

applications

The aim of the study presented in this thesis was to adapt PIV to the application to turbulent flow research, with special emphasis to coherent flow structures. The motivation for this study was that further developments in turbulent flow research (as a sequel to some notable breakthroughs obtained with computational methods) can only be achieved by experiments.

Both the DPIV measurements of grid turbulence (Chapter 6) and turbulent pipe flow (Chapter 9) demonstrated that DPIV is a feasible alternative to OPIV; see Sect. 1.4. It is expected that with appropriate equipment (i.e. high-resolution cameras with digital image storage) a higher spatial resolution and measurement accuracy can be achieved. This type of equipment was recently installed and is currently deployed in a pilot experiment on turbulent pipe flow.

To resolve both the macroscale and the microscale of the turbulent flow requires a very high spatial resolution (this problem is also faced by the direct numerical simulation of turbulent flow). Currently the spatial resolution of electronic imaging devices does not allow us to fully resolve all scales of turbulent flow at high Reynolds number. In the previous paragraph and in Chapter 5 we discussed how this may affect the estimation (and subsequently the interpretation) of flow quantities that are associated with the turbulent microscale. Anyway, we will not always be interested in the full range of scales. With PIV we are now able to investigate the flow at different scales in different experiments. We can observe the large-scale motion while neglecting the microscale (like in large-eddy simulation), or zoom in and study only the detailed structure of the flow⁶. This is an obvious advantage of PIV—as an experimental technique—with respect to most simulation methods. Let us illustrate this with an example.

Suppose we like to study the inner layer and logarithmic wall-layer of the turbulent boundary layer in a pipe flow. With PIV we can simply zoom in to the relevant section of the flow. On the other hand, with DNS or LES we have to simulate the *entire* flow volume; note that only 20% of the pipe volume is occupied by the inner and logarithmic wall-layers. Besides that, the use of periodic boundary conditions implies that the simulation domain should be at least twice the largest (anticipated) length scale in the flow. Hence, only about 10% of the simulated data is of interest! With PIV we can obtain relevant data more selectively than by numerical methods.

In the introduction of this thesis (Sect. 1.1.4) it was argued that for the measurement of coherent flow structures it is necessary to acquire a large set of PIV images. Apart from developing fast and automatic image acquisition and analysis procedures, we should also

⁶In this mode PIV would allow us to investigate sub-grid modelling in large eddy simulation.

consider alternative experimental techniques that yield the desired results from a smaller set of images. We may for example combine DPIV with LDA in such a way that an image or sequence of images is only acquired when a certain criterion for the LDA signal is met (*viz.*, the detection of a *sweep of ejection*). To achieve fast response times we need an electronic image acquisition and image storage system. We could use the conditional event detected by the LDA signal to trigger the image acquisition, either as a conditional *start* or conditional *stop*. Such a set-up would allow us to study transient phenomena, like the transition of high Reynolds-number laminar flow to turbulent flow. Another method to reduce the set of images is to subject the flow under study to a (repetitive) artificial disturbance, as was put forward by Brand (1992). This type of measurement requires electronic imaging and storing devices to achieve fast responses, initiated by an external triggering. Digital PIV is ideally suited for the analysis of this type of experiments.

10.4 Concluding remarks

With respect to traditional single-point measurement probes and classical flow visualization, particle image velocimetry has proven to be a fundamental step forward in the way we can observe flows under experimental conditions. Now flow properties such as vorticity and deformation, that previously belonged only to the domain of theoreticians and numerical codes, have reached the scope of experimentalists. Somewhat surprising is that—since the first pioneering experiments in the late 70's—there have been very few applications that make explicit use of this new and unique way of fluid flow measurement. In the view of the author this is partially related to the fact that in practice the conventional implementation of the PIV method does not allow the analysis of large sets of images, which is required to collect significant and reliable information of the flow under study. This thesis demonstrated that the distribution of the performance over accuracy, spatial resolution and processing speed (see Table 1.2) in digital PIV provides an alternative, and likely more suitable solution to the measurement of coherent flow structures in turbulent flows than the conventional implementation of the PIV method. It is the author's view that (digital) PIV can become an important tool in turbulent flow research, since it can provide necessary information of turbulent flows in geometries and at conditions that are (currently) not accessible to simulation methods. In the near future we can expect further improvements in computer and sensor technology, *i.e.* faster digital processors and sensors with higher resolution. Digital PIV will mostly benefit from these innovations, as there is a direct relation between performance and resolution, while the traditional PIV method remains with the inherently slow processing and manipulation of photographic material.

Appendix A

A.1 Linear system analysis

Consider a continuous parameter, linear—but not necessarily time-invariant—system with an impulse response $\mathcal{H}(t, s)$, shown schematically in Figure A.1. The output signal $\mathcal{Y}(t)$ for a given input signal $\mathcal{X}(t)$ is given by

$$\mathcal{Y}(t) = \int \mathcal{H}(t, s)\mathcal{X}(s)ds. \quad (\text{A.1})$$

Suppose that $\mathcal{X}(t)$ is a homogeneous zero-mean white random process, i.e.

$$\left. \begin{aligned} \langle \mathcal{X}(t) \rangle &= 0 \\ \langle \mathcal{X}(t)\mathcal{X}(t + \tau) \rangle &= \delta(\tau) \end{aligned} \right\} \forall t \quad (\text{A.2})$$

where $\langle \dots \rangle$ denotes the mean and $\delta(\tau)$ is the Dirac δ -function, then the impulse response is given by the *cross-covariance function* of the input and output processes, viz.

$$R_{\mathcal{X}\mathcal{Y}}(t, s) = \langle \mathcal{Y}(t)\mathcal{X}(s) \rangle \sim \mathcal{H}(t, s). \quad (\text{A.3})$$

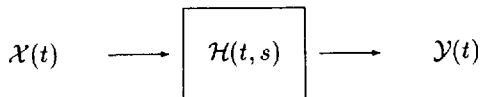


Figure A.1: Schematic representation of a linear system.

A.2 The tracer ensemble

Consider the ensemble of \mathcal{N} particles in a volume V . The position of a particle with index i at time t is given by $\vec{X}_i(t)$. The *state* of the ensemble at time t is represented by a vector

$$\vec{\Gamma}(t) = \begin{pmatrix} \vec{X}_1(t) \\ \vec{X}_2(t) \\ \vdots \\ \vec{X}_{\mathcal{N}}(t) \end{pmatrix} \quad (\text{A.4})$$

in a $3\mathcal{N}$ -dimensional phase space. For *ideal* tracer particles the trajectory of $\vec{\Gamma}$ is given by

$$\frac{d\vec{\Gamma}}{dt} = \vec{v}(\vec{\Gamma}, t) \quad (\text{A.5})$$

with

$$\vec{v}(\vec{\Gamma}, t) = \begin{pmatrix} \vec{v}(\vec{X}_1, t) \\ \vec{v}(\vec{X}_2, t) \\ \vdots \\ \vec{v}(\vec{X}_{\mathcal{N}}, t) \end{pmatrix}. \quad (\text{A.6})$$

In addition, we define the *displacement* $\vec{\mathcal{D}}(\vec{\Gamma}; t', t'')$ of $\vec{\Gamma}$ by $\vec{v}(t)$ during the time interval (t', t'') :

$$\vec{\mathcal{D}}(\vec{\Gamma}; t', t'') = \int_{t'}^{t''} \vec{v}[\vec{\Gamma}(t), t] dt \quad (\text{A.7})$$

cf. Eq. (2.1).

The ensemble mean of a quantity $A(\vec{X}, t)$ for a given flow field $\vec{v}(\vec{X}, t)$ is given by (for brevity of notation we omit the coordinates \vec{X} and t):

$$\langle A \rangle = \int_{[V]^{\mathcal{N}}} A(\vec{\Gamma}) \rho(\vec{\Gamma}) d\vec{\Gamma} \quad (\text{A.8})$$

where $\rho(\vec{\Gamma}, t)$ is the probability density function to find the ensemble in a state $\vec{\Gamma}$ at time t , with

$$\int_{[V]^{\mathcal{N}}} \rho(\vec{\Gamma}, t) d\vec{\Gamma} = 1. \quad (\text{A.9})$$

Note that the ensemble average defined in (A.8) is *linear* in A .

The second order statistic $\langle A(\vec{X}', t') A(\vec{X}'', t'') \rangle$ is given by (again we drop the coordinates \vec{X} and t in order to keep a concise notation):

$$\langle A' A'' \rangle = \iint A(\vec{\Gamma}') A(\vec{\Gamma}'') \rho(\vec{\Gamma}', \vec{\Gamma}'') d\vec{\Gamma}' d\vec{\Gamma}'' \quad (\text{A.10})$$

where $\rho(\vec{\Gamma}', \vec{\Gamma}'')$ is the joint probability density function to find the ensemble in a state $\vec{\Gamma}'$ at time t' and in a state $\vec{\Gamma}''$ at time t'' . We may write this function as

$$\rho(\vec{\Gamma}', \vec{\Gamma}'') = \rho(\vec{\Gamma}'' | \vec{\Gamma}') \cdot \rho(\vec{\Gamma}') \tag{A.11}$$

where $\rho(\vec{\Gamma}'' | \vec{\Gamma}')$ is the conditional pdf for $\vec{\Gamma}''$ given the initial state $\vec{\Gamma}'$. For a given flow field \vec{v} the state $\vec{\Gamma}''$ is uniquely given by the equation for the trajectory in (A.5), given the initial state $\vec{\Gamma}'$. We may therefore write

$$\rho(\vec{\Gamma}'' | \vec{\Gamma}') = \delta[\vec{\Gamma}'' - \vec{\Gamma}' - \vec{D}(\vec{\Gamma}')] \tag{A.12}$$

As a direct consequence Eq. (A.10) now reduces to

$$\langle A' A'' \rangle = \int A(\vec{\Gamma}) A(\vec{\Gamma} + \vec{D}) \rho(\vec{\Gamma}) d\vec{\Gamma} \tag{A.13}$$

Thus, for *ideal* tracer particles in a given flow field both first and second order ensemble statistics are described by $\rho(\vec{\Gamma}, t)$. In the remainder of this section we will evaluate $\rho(\vec{\Gamma}, t)$ for the special case of ideal tracer particles in a homogeneously seeded, incompressible flow.

Since there are no particles that appear into or disappear from the ensemble $\rho(\vec{\Gamma}, t)$ satisfies the continuity equation (for brevity of notation we omit from here on the coordinates $\vec{\Gamma}$ and t):

$$\frac{\partial \rho}{\partial t} + \vec{v} \cdot \text{grad } \rho + \rho \text{ div } \vec{v} = 0 \tag{A.14}$$

(cf. Liouville's theorem) where \vec{v} has been defined in (A.6). We now consider the special case of Eq. (A.14) for an *incompressible* flow with spatially *homogeneous* seeding, viz.

$$\text{div } \vec{v} = 0 \quad \text{and} \quad \text{grad } \rho = \vec{0} \tag{A.15}$$

Inserting this in (A.14) yields immediately that

$$\frac{\partial \rho}{\partial t} = 0 \tag{A.16}$$

which implies that $\rho(\vec{\Gamma}, t)$ is stationary and does not depend on the flow field. This considerably simplifies the evaluation of the first and second order ensemble statistics defined in (A.8) and (A.13). Hence, for a volume V with \mathcal{N} *ideal* tracer particles that are *homogeneously* distributed in an *incompressible* flow, we have, cf. Eq. (A.9):

$$\rho(\vec{\Gamma}, t) = V^{-\mathcal{N}} \tag{A.17}$$

With this result we can evaluate the first and second order statistics of the tracer pattern, defined in (2.3)

A.3 Ensemble statistics of the tracer pattern

We now apply the results from Appendix A.2 to find the first and second order statistics of the tracer pattern defined in (2.3). The first order statistic of G yields:

$$\begin{aligned}
 \langle G(\vec{X}, t) \rangle &= \int \cdots \int d\vec{X}_1 \cdots d\vec{X}_N \sum_{i=1}^N \delta[\vec{X} - \vec{X}_i] V^{-N} \\
 &= \frac{N}{VN} \int d\vec{X}_1 \delta[\vec{X} - \vec{X}_1] \int \cdots \int d\vec{X}_2 \cdots d\vec{X}_N \\
 &= \frac{N}{VN} V^{N-1} = \frac{N}{V}
 \end{aligned}
 \tag{A.18}$$

and subsequently the second order statistic:

$$\begin{aligned}
 &\langle G(\vec{X}', t') G(\vec{X}'', t'') \rangle \\
 &= \int \cdots \int d\vec{X}_1 \cdots d\vec{X}_N \sum_{i=1}^N \delta[\vec{X}' - \vec{X}_i] \sum_{j=1}^N \delta[\vec{X}'' - \vec{X}_j - \vec{D}(\vec{X}_j)] V^{-N} \\
 &= \int \cdots \int d\vec{X}_1 \cdots d\vec{X}_N \sum_{i=j} \delta[\vec{X}' - \vec{X}_i] \delta[\vec{X}'' - \vec{X}_i - \vec{D}(\vec{X}_i)] V^{-N} + \\
 &\quad \int \cdots \int d\vec{X}_1 \cdots d\vec{X}_N \sum \sum_{i \neq j} \delta[\vec{X}' - \vec{X}_i] \delta[\vec{X}'' - \vec{X}_j - \vec{D}(\vec{X}_j)] V^{-N} \\
 &= \frac{N}{VN} \int d\vec{X}_1 \delta[\vec{X}' - \vec{X}_1] \delta[\vec{X}'' - \vec{X}_1 - \vec{D}(\vec{X}_1)] \int \cdots \int d\vec{X}_2 \cdots d\vec{X}_N + \\
 &\quad \frac{N^2 - N}{VN} \int d\vec{X}_1 \int d\vec{X}_2 \delta[\vec{X}' - \vec{X}_1] \delta[\vec{X}'' - \vec{X}_2 - \vec{D}(\vec{X}_1)] \int \cdots \int d\vec{X}_3 \cdots d\vec{X}_N \\
 &= \frac{N}{V} \delta[\vec{X}'' - \vec{X}' - \vec{D}(\vec{X}'; t', t'')] + \frac{N^2 - N}{V^2}.
 \end{aligned}
 \tag{A.19}$$

where $\vec{D}(\vec{X}'; t', t'')$ is the displacement field, defined in Eq. (2.1). In the limit for $V \rightarrow \infty$ and $N \rightarrow \infty$ with $N/V = C$ constant, where C is the number density of the seeding, (A.18) and (A.19) yield

$$\langle G(\vec{X}, t) \rangle = C \tag{A.20}$$

$$\langle G(\vec{X}', t') G(\vec{X}'', t'') \rangle = C \delta[\vec{X}'' - \vec{X}' - \vec{D}(\vec{X}'; t', t'')] + C^2. \tag{A.21}$$

A.4 Diffraction limited spot of an optical system

The impulse response $h(x, y)$ of the optical system in Sect. 2.5 is given by the Fraunhofer diffraction pattern of the lens aperture (Goodman 1968). The intensity $|h|^2$ for a circular lens and coherent illumination is better known as the *Airy pattern*, which is a circularly symmetric function with a radial distribution given by

$$|h(r)|^2 = \left(\frac{\pi D}{4r_0} \right)^2 \left[2 \frac{J_1(\pi r/r_0)}{\pi r/r_0} \right]^2 \quad \text{with} \quad r_0 = \frac{\lambda z_0}{D} \tag{A.22}$$

where $J_1(x)$ is the Bessel function of the first kind and first order, and r the radial coordinate in the image plane (Goodman 1968). The first zero of the function in (A.22) is found in $r \approx 1.22r_0$ (see Fig. A.2). We can approximate (A.22) by a Gaussian curve, defined in (A.24):

$$\begin{aligned} |h(r)|^2 &\approx \left(\frac{\pi D}{4r_0}\right)^2 \exp\left[-(\pi r/2r_0)^2\right] \\ &\approx \frac{1}{4}\pi D^2 \mathcal{G}(r; \sigma_h) \end{aligned} \tag{A.23}$$

with $\sigma_h = r_0\sqrt{2}/\pi$. The functions (A.22) and (A.23) and their Fourier-Bessel transforms

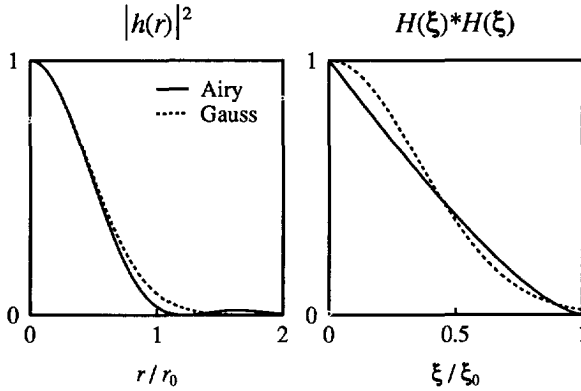


Figure A.2: The radial intensity profile of the Airy pattern and its Gaussian approximation (left) and their Fourier-Bessel transforms (right).

are plotted in Figure A.2. The approximation is very useful because it allows a considerable simplification of some of the mathematics encountered in this thesis. (Appendix A.5 summarizes relevant properties of Gaussian curves.)

A.5 Relevant properties of Gaussian curves

Consider the set of two-dimensional, circularly symmetric Gaussian curves $G(x, y; \sigma)$ in Cartesian coordinates:

$$\mathcal{G}(x, y; \sigma) = \exp\left[-\frac{x^2 + y^2}{2\sigma^2}\right] \tag{A.24}$$

where σ determines the *width* of the Gaussian curve. The total volume under $\mathcal{G}(x, y; \sigma)$ is equal to

$$\int_{-\infty}^{\infty} \int_{-\infty}^{\infty} \mathcal{G}(x, y; \sigma) dx dy = 2\pi\sigma^2. \tag{A.25}$$

This set of curves has several very convenient properties, given below, which considerably simplify some of the mathematics encountered in this thesis.

Fourier transformation:

$$\mathcal{G}(x, y; \sigma) \xleftrightarrow{\mathcal{F}} 2\pi\sigma^2 \mathcal{G}(\chi, \psi; 1/2\pi\sigma) \quad (\text{A.26})$$

multiplication:

$$\mathcal{G}(x, y; \sigma_1) \cdot \mathcal{G}(x, y; \sigma_2) = \mathcal{G}\left(x, y; \frac{\sigma_1\sigma_2}{\sqrt{\sigma_1^2 + \sigma_2^2}}\right). \quad (\text{A.27})$$

convolution:

$$\left(\frac{\mathcal{G}(x, y; \sigma_1)}{2\pi\sigma_1^2}\right) * \left(\frac{\mathcal{G}(x, y; \sigma_2)}{2\pi\sigma_2^2}\right) = \frac{\mathcal{G}\left(x, y; \sqrt{\sigma_1^2 + \sigma_2^2}\right)}{2\pi(\sigma_1^2 + \sigma_2^2)} \quad (\text{A.28})$$

Appendix B

B.1 Image enhancement

In high-resolution direct interrogation or Young's fringe analysis we only observe a single interrogation image at a time. Unique to the processing of digital PIV images is that we have the possibility to pre-process the entire image prior to analysis. Digital image processing has an enormous flexibility (although it should be said here that some image processing, like for example Fourier transformation, is much simpler and faster when implemented optically). For reviews of digital image processing methods refer to e.g. Rosenfeld & Kak (1982) or Jain (1989).

Image pre-processing can compensate for non-ideal aspects of our imaging system. For example, we can subtract a background image, correct for non-uniform illumination, enhance the image contrast or correct for perspective distortion or defocussing effects. This of course does not relieve us of carefully designing and implementing the imaging set-up described Sect. 2.5. Let us consider here one example of how digital image processing can improve the quality of our analysis.

B.1.1 correction for non-uniform illumination

Probably one of the most often encountered deviations from the ideal situation in PIV image recording is that of non-uniform illumination. In Sect. 2.5 we have assumed that the intensity of the light sheet is uniform in X and Y . However, if we use a *diverging* light sheet then the particle-images at the side of the light source are (slightly) brighter than those at the opposite side. In many situations this does not need to be a real problem (provided that the length scale over which the intensity changes is large compared to the equivalent size of the interrogation area in the object plane). However, our present analysis is based on the assumption that the PIV image is illuminated homogeneously. In order to compare our analytical results with those from an experiment it is essential that we meet this demand.

In Figure B.1 is given an example of a PIV image that suffers from non-uniform illumination. This is probably only visible to the observer who has been provided with the

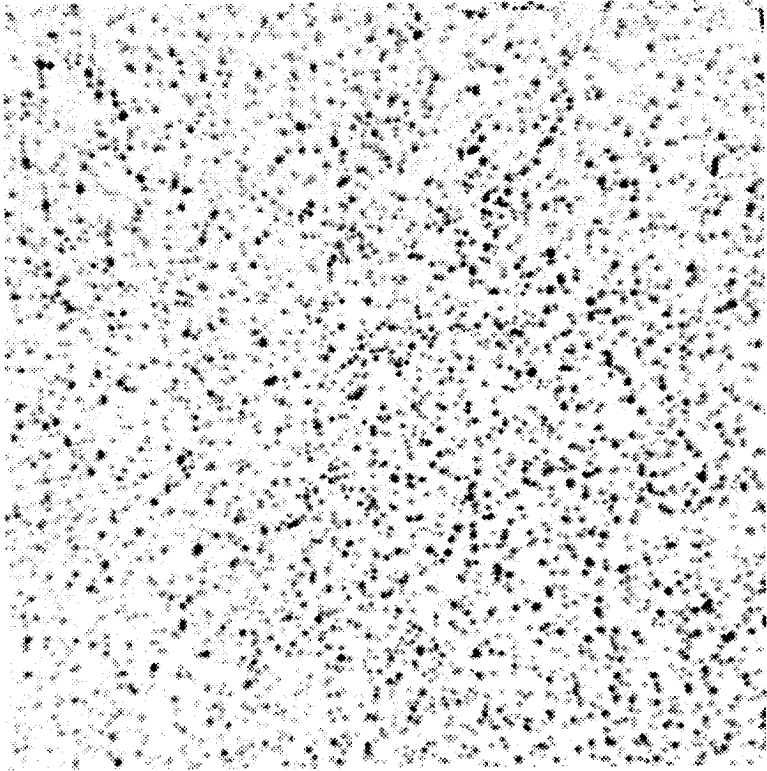


Figure B.1: PIV picture with non-uniform illumination; see text. (The grey values have been inverted.)

a priori knowledge that the right half of the image is slightly brighter than the left half. This becomes more readily visible by averaging along vertical lines. In Figure B.2a is plotted the average over groups of ten consecutive vertical lines, normalized by the global image mean, applied to the image in Fig. B.1. Now it is clearly visible that the left half of the image is on average 20% darker than the global-mean image intensity, while the right half is 20% brighter. Given that the global-mean grey value is equal to 42 we find that the difference in average grey level between the right and left halves is only about 14 grey levels in a total range of 256 grey. The human vision can only distinguish about 60 grey levels (Rosenfeld & Kak 1982), so that we can expect that the difference is barely visible. In the remainder of this section we deal with a technique to remove the effect of non-uniform illumination in digital images.

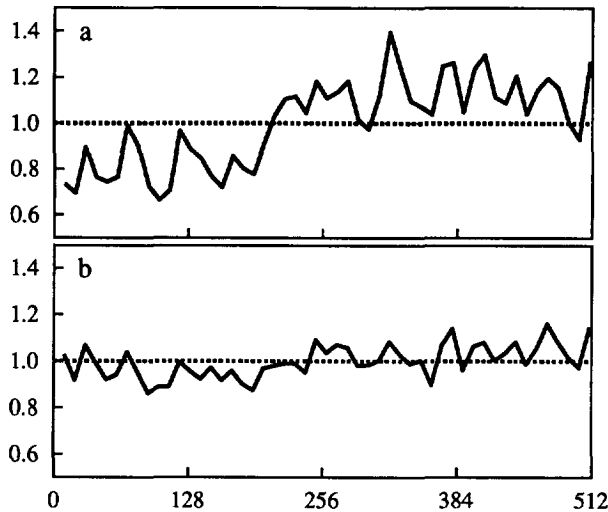


Figure B.2: The mean image intensity along columns relative to the global mean intensity for (a) the original image in Fig. B.1 and (b) after contrast normalization and background subtraction, shown in Fig. B.4.

There exist many different operations to correct for non-uniform illumination. In the following example we discuss one of them that proved to be very beneficial to PIV image analysis. Its principle is based on the fact that the image consists of a collection of objects that are all smaller than a certain area, superimposed on a slowly varying background. We want to remain with these objects only, and then subsequently normalize the local fluctuations in intensity so that the contrast over the image is (practically) constant.

Example 6 (*Contrast normalization*)

The operation that we discuss here is part of the TCL-Image software package¹ and is based on so-called min/max operations. To understand its principle it is more convenient to consider a one-dimensional signal. The solid line in Figure B.3a is a signal from a fourth-order moving-average process of a negative-exponential random variable. Hence the characteristic length scale of the signal fluctuations is five samples. We decide to remove all fluctuations that occur over a length scale greater than nine samples. The dashed lines in Fig. B.3a that enclose the solid line represent the local maximum (top) and the

¹TCL-Image has been developed by the TNO Institute of Applied Physics, the Netherlands.

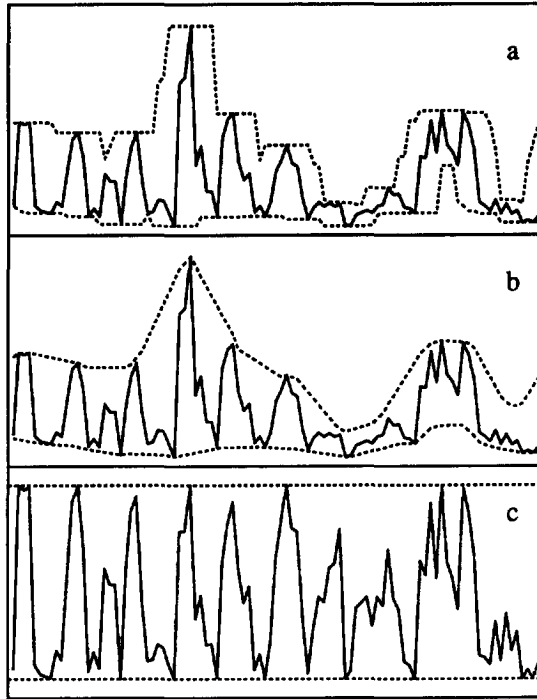


Figure B.3: Example of contrast normalization using min/max filtering on a one-dimensional signal. The solid line is the signal; the dashed lines are upper and lower envelopes. (a) The original signal with local maximum and local minimum envelopes. (b) The envelopes after smoothing with a uniform filter. (c) The signal after subtraction of the lower envelope in (b) and normalized by the difference between the upper and lower envelopes in (b).

local minimum (bottom) over nine samples. Figure B.3b shows the same signal, but now the local maximum and local minimum have been smoothed with a uniform filter, again over nine samples. The dashed lines may be considered to represent the upper and lower envelopes (over a length scale of nine samples) of the original signal. The lower envelope represents the “local background” signal, and the difference between the upper and lower envelopes the “local contrast”. The lower envelope is subtracted from the original signal, and subsequently divided by the difference between the upper and lower envelopes. The result is shown in Figure B.3c. All fluctuations with length scales larger than the filter length (viz., 9 samples) have been removed from the original signal. What remains is a signal that may be considered homogeneous over a length scale larger than the selected filter length.

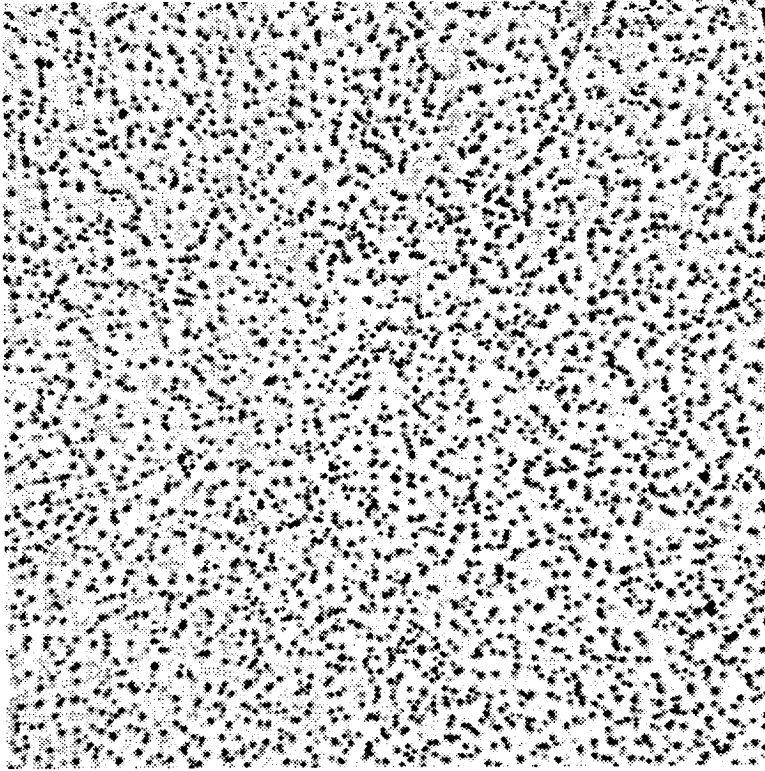


Figure B.4: The picture of Fig. B.1 after contrast normalization.

The image in Figure B.1 consists of particle images with an area of about 4×4 pixels. In Figure B.4 is given the image of Fig. B.1 but now after the contrast normalization procedure described above, with a filter size of 15×15 pixels. The filter size should be larger than the size of the particle images. If we use a filter size that is very close to the particle image size then we alter the statistics of the PIV image (i.e. the intensity statistics have no longer a negative-exponential pdf). On the other hand, the filter size should be smaller than the spatial variations in the image background. In this particular example a filter size of 15×15 pixels yielded satisfactory results. Figure B.2b shows again the average pixel intensity over groups of ten consecutive vertical lines, normalized by the global image mean, but now for the image in Fig. B.4. Here the effect of unequal illumination in the original image has been removed. In this way we assure that the mean

and variance of the pixel intensity of the digital images subjected to the PIV analysis are (approximately) homogeneous.

B.2 Computation of the cross-covariance

Although we may compute the interrogation covariance defined in Eq. (3.27) directly, there exists an alternative way by using discrete Fourier transformation. This is a very attractive method, since we can make use of a fast algorithm, called the *fast Fourier transform* (FFT). In the first part of this section we will show how the covariance can be computed using discrete Fourier transformation. The main difference with the direct computation of the covariance is that the FFT computation considers the image as *periodic*. Therefore certain precautions, like zero-padding and windowing, are usually made to assure that the computation yields a reliable estimate of the covariance. We will deal with these in two additional subsections.

Wold's theorem² (Priestley 1992) states that the spectral density function and covariance function of a discrete-parameter random process are Fourier transform pairs. This theorem also applies to two-dimensional random fields (Rosenfeld & Kak 1982). This property is commonly used for computation of the estimated covariance function from a given set of observations.

Consider a square interrogation image $\Delta I_{r,s}$ of $N \times N$ pixels. We may consider $\Delta I_{r,s}$ as an infinitely large image with

$$\Delta I_{r,s} = 0, \text{ outside } 1 \leq r \leq N, 1 \leq s \leq N. \tag{B.1}$$

Let $\Delta \tilde{I}_{r,s}$ be a periodic image with a period $M \geq N$ in both r and s and such that:

$$\Delta \tilde{I}_{r,s} = \Delta I_{r,s}, \text{ for } 1 \leq r \leq M, 1 \leq s \leq M. \tag{B.2}$$

The discrete Fourier-transform (DFT) of $\Delta \tilde{I}_{r,s}$ is given by (Oppenheim *et al.* 1983; Rosenfeld & Kak 1982):

$$\tilde{F}[u, v] = \frac{1}{M^2} \sum_{r=\langle M \rangle} \sum_{s=\langle M \rangle} \Delta \tilde{I}_{r,s} \exp \left[-\frac{2\pi i}{M}(ru + sv) \right] \tag{B.3}$$

where $r=\langle M \rangle$ and $s=\langle M \rangle$ denote that the summations are taken over one period in r and s . Note that $\tilde{F}[u, v]$ is also periodic in u and v , with period M . If we take the summations over an area for which $\Delta \tilde{I}_{r,s} = \Delta I_{r,s}$, we obtain

$$\tilde{F}[u, v] = \frac{1}{M^2} \sum_{s=1}^M \sum_{t=1}^M \Delta I_{r,s} \exp \left[-\frac{2\pi i}{M}(su + tv) \right]. \tag{B.4}$$

Let $\Delta \tilde{I}'_{r,s}$ and $\Delta \tilde{I}''_{r,s}$ be the periodic images associated with the interrogation images $\Delta I'_{r,s}$ and $\Delta I''_{r,s}$ respectively, constructed according to Eqs. (B.1–B.2). For each of these two

²This is the discrete-parameter equivalent of the Wiener-Khinchine theorem

signals the discrete Fourier transform given in (B.4) is computed, denoted by $\tilde{F}'[u, v]$ and $\tilde{F}''[u, v]$ respectively. The cross-spectral density of these two images is given by

$$\tilde{S}_{II}[u, v] = \tilde{F}'[u, v] \tilde{F}''[u, v]^* \quad (\text{B.5})$$

where * denotes the complex conjugate. Substitution of (B.4) in (B.5) yields

$$\begin{aligned} \tilde{S}_{II}[u, v] &= \left\{ \frac{1}{M^2} \sum_{k=1}^M \sum_{l=1}^M \Delta \tilde{I}'_{k,l} \exp \left[-\frac{2\pi i}{M} (ku+lv) \right] \right\} \left\{ \frac{1}{M^2} \sum_{m=1}^M \sum_{n=1}^M \Delta \tilde{I}''_{m,n} \exp \left[-\frac{2\pi i}{M} (mu+nv) \right] \right\}^* \\ &= \frac{1}{M^4} \sum_{k=1}^M \sum_{l=1}^M \sum_{m=1}^M \sum_{n=1}^M \Delta \tilde{I}'_{k,l} \Delta \tilde{I}''_{m,n} \exp \left[-\frac{2\pi i}{M} \{ (k-m)u + (l-n)v \} \right] \\ &= \frac{1}{M^4} \sum_{r=-(M-1)}^{M-1} \sum_{s=-(M-1)}^{M-1} \left\{ \sum_{m=1}^M \sum_{n=1}^M \Delta \tilde{I}'_{m,n} \Delta \tilde{I}''_{m+|r|,n+|s|} \right\} \exp \left[-\frac{2\pi i}{M} (ru+sv) \right] \\ &= \frac{N^2}{M^4} \sum_{r=-(M-1)}^{M-1} \sum_{s=-(M-1)}^{M-1} \left\{ \frac{1}{N^2} \sum_{m=1}^{N-|r|} \sum_{n=1}^{N-|s|} \Delta \tilde{I}'_{m,n} \Delta \tilde{I}''_{m+|r|,n+|s|} \right\} \exp \left[-\frac{2\pi i}{M} (ru+sv) \right] \quad (\text{B.6}) \end{aligned}$$

by substitution of $r = k - m$ and $s = l - n$, and Eq. (B.1). The term between the braces is recognized as the (biased) cross-covariance estimator $\hat{R}_{II}[k, m]$ defined in Eq. (3.27):

$$\tilde{S}_{II}[u, v] = \frac{N^2}{M^4} \sum_{r=-(M-1)}^{M-1} \sum_{s=-(M-1)}^{M-1} \hat{R}_{II}[r, s] \exp \left[-\frac{2\pi i}{M} (ru+sv) \right] \quad (\text{B.7})$$

Since $\hat{R}_{II}[r, s] = 0$ for $|r|, |s| \geq N$ this result shows that for $M \geq 2N$ the inverse discrete Fourier transform of the cross-spectral density of $\Delta \tilde{I}'_{s,t}$ and $\Delta \tilde{I}''_{s,t}$ yields exactly $\hat{R}_{II}[r, s]$. The same result also applies to multiple exposure frames.

The main advantage behind using DFT's is that it can be implemented using the efficient FFT algorithm. Whereas the direct computation of $\hat{R}_{II}[u, v]$ requires $\mathcal{O}(N^4)$ multiplications, the same result is obtained by using FFT's with only $\mathcal{O}(N^2 \log N)$ multiplications.

B.2.1 zero-padding

In the procedure described previously we transformed the interrogation images of finite size $N \times N$ into a periodic image with a period $M \geq N$ in the orthogonal coordinates. In order to ensure that $\hat{R}_{II}[u, v]$ fits the domain we should use $M \geq 2N$.

Zero-padding (as the adding of extra zeroes around the image is commonly referred) implies that 3/4 of the image consists of zeroes. In practice the particle-image displacement should be less than about $N/4$ pixels, in order to have a sufficient data yield. This implies that the cross-covariance vanishes for $|r|, |s| > N/4$. In that case we may even

choose $M=N$. Thus, for the computation of $\hat{R}_{II}[r, s]$ using DFT zero-padding is not required in practice. Without zero-padding of the interrogation area we further reduce the processing time for the image analysis. For example, the time required to compute the FFT of a 32×32 -pixel interrogation area is about 1/5 of the time required for a 64×64 -pixel interrogation area.

However, computation of the $\hat{R}_{II}[r, s]$ without zero-padding has some consequences for the expectation and (co)variance of the estimated cross-covariance. For $M=N$ Eq. (B.7) becomes:

$$\tilde{S}[u, v] = \frac{1}{N^2} \sum_{r=0}^{N-1} \sum_{s=0}^{N-1} \left\{ \hat{R}_{II}[r, s] + \hat{R}_{II}[N-r, N-s] \right\} \exp \left[-\frac{2\pi i}{N}(ru + sv) \right]. \quad (\text{B.8})$$

Let us denote the inverse discrete Fourier transform of $\tilde{S}[u, v]$ by $\tilde{R}_{II}[r, s]$, viz.

$$\tilde{R}_{II}[r, s] = \hat{R}_{II}[r, s] + \hat{R}_{II}[N-r, N-s]. \quad (\text{B.9})$$

Provided that the particle-image displacement is less than $N/2$ and $d_t/\Delta \ll N$, we have

$$E \left\{ \tilde{R}_{II}[r, s] \right\} = E \left\{ \hat{R}_{II}[r, s] \right\} \quad (\text{B.10})$$

by $E \left\{ \hat{R}_{II}[r, s] \right\} \sim 0$ for $|r|, |s| > N/2$. Consider the (co)variance of $\tilde{R}_{II}[r, s]$ near the maximum of $\hat{R}_{II}[r, s]$ in $\{m_0, n_0\}$. In that case we find

$$\text{var} \left\{ \tilde{R}_{II}[r, s] \right\} \approx \text{var} \left\{ \hat{R}_{II}[r, s] \right\} + \text{var} \left\{ \hat{R}_{II}[N-r, N-s] \right\} \quad (\text{B.11})$$

and

$$\text{cov} \left\{ \tilde{R}_{II}[r, s], \tilde{R}_{II}[r+t, s+u] \right\} \approx \text{cov} \left\{ \hat{R}_{II}[r, s], \hat{R}_{II}[r+t, s+u] \right\} \quad (\text{B.12})$$

by Eqs. (3.37) and (3.38). Thus, without zero-padding of the variance of $\hat{R}_{II}[r, s]$ is increased by an amount proportional to the noise in the estimated cross-covariance for large displacements. Taking a closer look at (3.36) tells us that $\text{var} \left\{ \hat{R}_{II}[N-r, N-s] \right\}$ is in general much smaller than $\text{var} \left\{ \hat{R}_{II}[r, s] \right\}$ for $|r|, |s| \ll N/2$.

B.2.2 window functions

By extracting only a finite interrogation area from the complete PIV record we may introduce abrupt steps at the edges of the interrogation image. This may be caused by a non-uniform background intensity, or by particle images that fall only partially inside the interrogation area. As a result artefacts may appear in the estimated cross-covariance that have a direct influence on the analysis result. The usual procedure to overcome this problem is to multiply the sample data with a window function that puts a lower weight to the sample data close to the edges of the domain. In Sect. 3.6.3 we already discussed the effect of weight kernels on the estimation of the cross-covariance. Here we discuss the use of window functions with respect to the periodic continuation of interrogation area in

FFT analysis.

We know that the PIV image consists of a collection of particle-images with approximately equal size. For small particle images (say with a diameter of 2–4 pixels) the image intensity already strongly fluctuates over the interrogation image. The occurrence of a particle image that falls only partially inside the interrogation area is proportional to the ratio of the boundary pixels and the total number of pixels N . So, first of all we are only dealing with a small, and likely negligible, fraction of the total number of particle images. Furthermore, we may view these fractional particle-images as contributing to the noise in the estimated cross-covariance. By the fact that these fractional particle-images are always *smaller* than the “fully” present particle-images, it is plausible to accept that the length scale of this noise is negligible with respect to that of the noise due to correlation between random particle images (see Eq. 3.40). Therefore the presence of particles at the boundary is not expected to have a strong effect on the analysis result.

A more serious problem is the presence of a non-uniform background. Our total analysis has been based on the principle of a *homogeneous* random field. This was mainly done to ensure an unbiased sampling of the observed flow field. Here we find another reason to have homogeneous images (i.e. the estimation of $\hat{R}_{II}[u, v]$ that is free from artefacts). It is however not always possible to ensure a uniform background at the image recording stage. We know that the diameter of the particle-images is small with respect to the size of the interrogation area. In that case we can use a high-pass filtering operation to remove intensity fluctuations with a length scale of the order of the interrogation area, while preserving the particle images that have a diameter less than the characteristic filter length.

We have thus seen that it is not necessary to use window functions in order to avoid boundary effects in DFT processing of interrogation images.

Appendix C

C.1 Non-homogeneous random fields

In order to treat all residuals in an equal manner—in other words, to have identical pdf's for $\hat{r}_{i,j}^2$ for all (i, j) —the PIV 'signal' in the post-interrogation evaluation should be statistically homogeneous, with components that are statistically homogeneous. In general however $\vec{V}_{i,j}$ does not satisfy this condition (e.g. turbulent channel flow or turbulent jet flow). Provided that (1) the pdf of $\vec{V}'_{i,j}$ in each point (i, j) is (approximately) normal, and (2) the first and second statistical moments are known *a priori*, then $\vec{V}'_{i,j}$ can be projected onto a new random field $\vec{V}'_{i,j}$ that is (at least in first approximation) homogeneous and orthogonal. This will be illustrated with an example.

Consider a random field $\vec{X}_{i,j}$ that is homogeneous in only one direction (here taken equal to the direction associated with the i -coordinate). This random field would e.g. describe the PIV signal from a turbulent pipe or channel flow. The statistics of this random field are given by:

$$E[\vec{X}_{i,j}] = \vec{\mu}(j) \quad (\text{C.1})$$

$$\text{cov}[\vec{X}_{i,j}, \vec{X}_{i+k,j+l}] = \begin{pmatrix} \sigma_{ii}^2(j) & \sigma_{ij}^2(j) \\ \sigma_{ji}^2(j) & \sigma_{jj}^2(j) \end{pmatrix} \vec{\rho}(k; j, j+l) \quad (\text{C.2})$$

where $\vec{\mu}_j$, σ_{ii} , σ_{jj} and $\sigma_{ij} = \sigma_{ji}$ represent the 'profiles' of the mean displacement, root-mean-square fluctuating displacement in i and j direction, and mean Reynolds stress respectively, and $\vec{\rho}$ the spatial correlation tensor. For the evaluation procedures described here only the nearest-neighbour correlations are involved. In general nearest-neighbour data will be highly correlated, and differ only by small amounts (this is closely related to the demand that spatial variations in the displacement field should be small over a length scale equal to the diameter of the interrogation spot). Thus, the assumption made in (4.26) is also valid for PIV data obtained from non-homogeneous flows.

Provided that we have *a priori* knowledge of the statistics of the observed flow field¹

¹These statistics would usually be obtained from preceding single-point measurements, e.g. by laser-Doppler anemometry

the random field in (C.1-C.2) can be projected onto a homogeneous and orthogonal random field. This is achieved by applying the following (linear) transformations:

$$\vec{X}'_{i,j} = (\vec{X}_{i,j} - \vec{\mu}(j)) \cdot \begin{pmatrix} \sigma_{ii}^{-1}(j) \\ \sigma_{jj}^{-1}(j) \end{pmatrix} \tag{C.3}$$

In the new random field \vec{X}' the components have a normal pdf with zero mean and unit variance for all (i, j) . The two components in \vec{X}' are correlated by an amount: $\rho' = \sigma_{ij}^2 / \sigma_{ii} \sigma_{jj}$ (this is related to the mean shear). This is subsequently removed by redistribution of the two displacement components:

$$\vec{X}'' = \begin{pmatrix} \frac{1}{\sqrt{2+2\rho'}} & 0 \\ 0 & \frac{1}{\sqrt{2-2\rho'}} \end{pmatrix} \begin{pmatrix} 1 & 1 \\ -1 & 1 \end{pmatrix} \vec{X}' \tag{C.4}$$

We now have a new random field \vec{X}'' with statistically orthogonal components with identical normal pdf's with zero mean and unit variance for all (i, j) .

C.2 The pdf of the mean and the median

Consider a sample $\{x_1, x_2, \dots, x_N\}$ of N elements from a white stochastic process with a pdf $f(x)$. The pdf of the sample mean $\langle x \rangle$ is given by the N -fold convolution of $f(x)$:

$$f(N\langle x \rangle) = \int_{-\infty}^{\infty} \dots \int_{-\infty}^{\infty} dx_1 \dots dx_{N-1} f(x_1) \dots f(x_{N-1}) f(N\langle x \rangle - x_1 - \dots - x_{N-1}). \tag{C.5}$$

For a white process with a normal pdf $N(0, \sigma^2)$ the mean $\langle x \rangle$ has a normal pdf $N(0, \sigma^2/N)$.

Consider the sorted array of the sample $\{x_1, x_2, \dots, x_N\}$, i.e.

$$\{x_1, x_2, \dots, x_N\} \rightarrow \{x'_1, x'_2, \dots, x'_N\} \quad \text{with} \quad x'_1 \leq x'_2 \leq \dots \leq x'_N. \tag{C.6}$$

The sample median, denoted by $[x]$, for odd $N (=2n+1)$ is defined as the $(n+1)$ -th element of the sorted array, i.e. $[x] = x'_{n+1}$. The pdf of $[x]$ for N independent samples is given by:

$$\begin{aligned} f([x]) &= P([x]|x'_1, \dots, x'_n \leq [x]; x'_{n+1} = [x]; x'_{n+2} \dots x'_N \geq [x]) \frac{(2n+1)!}{n!n!} \\ &= f(x) \left(\int_{-\infty}^{[x]} f(x) dx \right)^n \left(\int_{[x]}^{\infty} f(x) dx \right)^n \frac{(2n+1)!}{n!n!}. \end{aligned} \tag{C.7}$$

(Note that $(2n+1)!/n!n!$ is the number of permutations for $[x]$ in the *unsorted* array of samples.) If $f(x)$ is normal, then $f([x])$ fits to a normal pdf with a variance that is approximately $1.47\sigma^2/N$ for $N \gg 1$.

References

- ADRIAN, R.J. 1983 Laser Velocimetry. In: *Fluid Mechanics Measurement*. (ed. R.J. Goldstein) Springer, Berlin.
- ADRIAN, R.J. 1984 Scattering particle characteristics and their effect on pulsed laser measurements of fluid flow: speckle velocimetry vs particle image velocimetry *Appl. Opt.* **23**, 1690.
- ADRIAN, R.J. & YAO, C.-S. 1984 Development of pulsed laser velocimetry (PLV) for measurement of turbulent flow. In: *Proc. Symp. Turbul.* (ed. X. Reed *et al.*) University of Missouri, Rolla.
- ADRIAN, R.J. & YAO, C.-S. 1985 Pulsed laser technique application to liquid and gaseous flows and the scattering power of seed materials. *Appl. Opt.* **24**, 44.
- ADRIAN, R.J. 1986a Image shifting technique to resolve directional ambiguity in double-pulsed velocimetry *Appl. Opt.* **25**, 3855.
- ADRIAN, R.J. 1986b Multi-point optical measurements of simultaneous vectors in unsteady flow—a review. *Int. J. Heat & Fluid Flow* **7**, 127–145.
- ADRIAN, R.J. 1988 Statistical properties of particle image velocimetry measurements in turbulent flow. In *Laser Anemometry in Fluid Mechanics - III* (ed. R.J. Adrian *et al.*) LADOAN Instituto Superior Tecnico, Lisbon, pp. 115-129
- ADRIAN, R.J., OFFUTT, P.W., LANDRETH, C.C., LIU, Z.-C. & HANRATTY, T.J. 1990 Studies of liquid turbulence using double-pulsed particle correlation. *Proc. 5th Int. Symp. Appl. Laser Techn. Fluid Mech.* (Lisbon) 9–12 July, 15.4
- ADRIAN, R.J. 1991 Particle-imaging techniques for experimental fluid mechanics. *Annu. Rev. Fluid Mech.* **22**, 261–304.
- ARROYO, M.P., YONTE, T., QUINTANILLA, M. & SAVIRON, J.M. 1988 Particle image velocimetry in Rayleigh-Benard convection: Photographs with a high number of exposures *Opt. Lasers Eng.* **9**, 295.
- AUBRY, N., HOLMES, P., LUMLEY, J.L. & STONE, E. 1988 The dynamics of coherent structures in the wall region of a turbulent boundary layer. *J. Fluid Mech.* **192**, 115–173.
- BARNETT, V. & LEWIS, T. 1979 *Outliers In Statistical Data* Wiley, New York.
- BATCHELOR, G.K. 1967 *An introduction to fluid dynamics*. University Press, Cambridge (UK).
- BERGÉ, P., POMEAU, Y. & VIDAL, CH. 1987 *Order within Chaos*. Wiley, New York.
- BLACKWELDER, R.F. & KAPLAN, R.E. 1976 On the wall structure of the turbulent boundary layer. *J. Fluid Mech.* **76**, 89–112.
- BRAND, A.J. 1992 *The turbulent boundary layer: spanwise structure, evolution of low-velocity regions and response to artificial disturbances*. Ph.D. thesis, Delft University

of Technology..

- BROWN, G.L. & ROSHKO, A. 1974 On density effects and large structure in turbulent mixing layers. *J. Fluid Mech.* **64**, 775-816.
- BURCH, J.M. & TOKARSKI, J.M.J. 1968 Production of multiple beam fringes from photographic scatters. *Optica Acta* **15**, 101-111.
- CANTWELL, B.J. 1981 Organized motion in turbulent flow. *Annu. Rev. Fluid Mech.* **13**, 457.
- CHO, Y.-C. 1989 Digital image velocimetry. *Appl. Opt.* **28**, 740.
- CORNELISSE, J.M., GODEFROY, H.W.H.E., KOOPMANS, F., UITTENBOGAARD, R.E. & WESTERWEEL, J. 1991 An experimental comparison between optical and digital particle velocimetry. Presented at: *EuroMech 279 "Image Analysis as Measuring Technique in Flows"* (Delft) 2-5 July
- COUPLAND, J.M., PICKERING, C.J.D. & HALLIWELL, N.A. 1987 Particle image velocimetry: The ambiguity problem. *Proc. SPIE Vol. 814 Photomechanics and Speckle Metrology* August 1987 (San Diego), p. 738
- COUPLAND, J.M. & HALLIWELL, N.A. 1988 Particle image velocimetry: rapid transparency analysis using optical correlation. *Appl. Opt.* **27**, 1919.
- COUPLAND, J.M. & PICKERING, C.J.D. 1988 Particle image velocimetry: estimation of measurement confidence at low seeding densities *Opt. Lasers Eng.* **9**, 201-210.
- DAHM, W.J.A., SOUTHERLAND, K.B. & BUCH, K.A. 1992 Four-dimensional laser induced fluorescence measurements of conserved scalar mixing in turbulent flows. In: *Applications of Laser Techniques in Fluid Mechanics.* (ed. R.J. Adrian et al.) Springer, Berlin.
- DORST, L. & SMEULDERS, A.W.M. 1985 Length estimators compared. In: *Proc. pattern recognition in practice II.* June 19-21, Amsterdam, The Netherlands.
- EGGELS, J.G.M., UNGER, F., WEISS, M.H., WESTERWEEL, J., ADRIAN, R.J., FRIEDRICH, R. & NIEUWSTADT, F.T.M. 1993a Fully developed turbulent pipe flow. A comparison between direct numerical simulation and experiment. (in preparation)
- EGGELS, J.G.M., WESTERWEEL, J., ADRIAN, R.J. & NIEUWSTADT, F.T.M. 1993b Comparison of flow structures in DNS & PIV studies of turbulent pipe flow. In: *Proc. Int. Conf. on near-wall turbulent flows*, Tempe (AZ) 15-18 March (see Chapter 8)
- EMRICH, R.J. 1981 *Methods of experimental physics.* Part 18A: Fluid Dynamics. Academic, New York. pp. 6-64.
- FINGERSON, L.M. & FREYMUTH, P. 1983 Thermal Anemometers. In: *Fluid Mechanics Measurement.* (ed. R.J. Goldstein) Springer, Berlin.
- FREDRIKZE, H. 1985 *Neutron diffraction on sub- and supercritical krypton.* Ph.D. the-

- sis Delft University of Technology, pp. 74-77.
- FUNG, J.C.H., HUNT, J.C.R., MALIK, N.A. & PERKINS R.J. 1992 Kinematic simulation of homogeneous turbulence by unsteady random Fourier modes *J. Fluid Mech.* **236**, 281-318.
- GAUTHIER, V. & RIETHMULLER, M.L. 1988 Application of DPIV to complex flows: measurement of the third component. In: *VKI-LS 1988-06 "Particle Image Displacement Velocimetry,"* Von-Kármán Institute for Fluid Mechanics, Rhode-Saint-Genèse.
- GOODMAN, J.W. 1968 *Introduction to Fourier Optics.* McGraw-Hill, New York.
- GOODMAN, J.W. 1984 Statistical properties of laser speckle patterns. In *Laser Speckle and Related Phenomena* (ed. J.C. Dainty) Springer, Berlin. pp. 9-75.
- GRAY, C. & GREATED C.A. 1988 The application of particle image velocimetry to the study of water waves. *Opt. Lasers Eng.* **9**, 265.
- GUPTA, A.K., LAUFER, J. & KAPLAN, R.E. 1971 Spatial structure in the viscous sublayer. *J. Fluid Mech.* **50**, 493-512.
- HARDER, K. & TIEDERMAN, W.G., 1991 Drag reduction and turbulent structure in two-dimensional channel flows. *Phil. trans. Roy. Soc.* **336**, 1640.
- HE, Z.H., SUTTON, M.A., RANSON, W.F. & PETERS, W.H. 1984 Two-dimensional fluid-velocity measurements by use of digital-speckle correlation techniques. *Exp. Mech.* **24**, 117.
- HEAD, M.R. & BANDYOPADYAY, P. 1981 New aspects of turbulent boundary layer structure. *J. Fluid Mech.* **107**, 297-338.
- HESELINK, L. & HELMAN J. 1987 Evaluation of flow topology from Numerical Data. *AIAA Invited Pap.* 87-1181-CP
- HESELINK, L. 1988 Digital image processing in flow visualization. *Annu. Rev. Fluid Mech.* **20**, 421-485.
- HINZE, J.O. 1975 *Turbulence.* (2nd Ed.) McGraw-Hill, New York.
- HUNT, J.C.R., WRAY, A.A. & MOIN, P. 1988 Eddies, streams, and convergence zones in turbulent flows. *Proc. of the Summer Program 1988*, Center for Turbulence Research, Stanford. pp. 193-208.
- HUSSAIN, A.K.M.F. 1986 Coherent structures and turbulence. *J. Fluid Mech.* **173**, 303-356.
- ISSERLIS, L. 1918 On a formula for the product moment coefficient of any order of a normal frequency distribution in any number of variables *Biometrika* **12**, 134-139.
- JAIN, A.K. 1989 *Fundamentals Of Digital Image Processing* Prentice-Hall, Englewood Cliffs (NJ), pp. 246-249
- KAUFMANN, W. 1963 *Fluid Mechanics* McGraw-Hill, New York. pp. 216-222.
- KEANE, R.D. & ADRIAN, R.J. 1990 Optimization of particle image velocimeters.

- Part I: Double-pulsed systems. *Meas. Sci. Technol.* **1**, 1202–1215.
- KEANE, R.D. & ADRIAN, R.J. 1991 Optimization of particle image velocimeters. Part II: Multiple-pulsed systems. *Meas. Sci. Technol.* **2**, 963–974.
- KEANE, R.D. & ADRIAN, R.J. 1993 Theory of cross-correlation of PIV images. In: *Flow Visualization and Image Analysis*. (ed. F.T.M. Nieuwstadt) Kluwer Academic, Dordrecht. pp. 1–25
- KERKER, M. 1969 *The Scattering of Light* Academic, New York
- KIM, H.T., KLINE, S.J. & REYNOLDS, W.C. 1971 The production of turbulence near a smooth wall in a turbulent boundary layer. *J. Fluid Mech.* **50**, 133–160.
- KIM, J., MOIN, P. & MOSER, R. 1987 Turbulence statistics in fully developed channel flow at low Reynolds number. *J. Fluid Mech.* **177**, 133–166.
- KIMURA, I. & TAKAMORI, T. 1986 Image processing of flow around a circular cylinder by using correlation technique. In: *Flow Visualization IV* Proc. 4th Int. Symp. on Flow Visualization, 26–29 August 1986, Paris. pp. 221–226
- KLINE, S.J., REYNOLDS, W.C., SCHRAUB, F.A. & RUNDSTADTLER, P.W. 1967 The structure of turbulent boundary layers. *J. Fluid Mech.* **30**, 741–773.
- KLINE, S.J. 1978 The role of visualization in the study of the structure of the turbulent boundary layer. *Workshop on coherent structure of turbulent boundary layers*. (eds. C.R. Smith & D.E. Abbott) Lehigh University, Bethlehem (PA)
- LAMB, H. 1932 *Hydrodynamics* University Press, Cambridge (UK).
- LANDRETH, C.C. & ADRIAN R.J. 1988 Electrooptical image shifting for particle image velocimetry *Appl. Opt.* **27**, 4216.
- LANDRETH, C.C. & ADRIAN, R.J. 1990a Impingement of a low Reynolds number turbulent circular jet onto a flat plate at normal incidence. *Exp. Fluids* **9**, 74–84.
- LANDRETH, C.C. & ADRIAN R.J. 1990b Measurement and refinement of velocity data using high image density analysis in particle image velocimetry. In *Applications of Laser Anemometry to Fluid Mechanics* (ed. R.J. Adrian *et al.*) Springer, Berlin. pp. 484–497.
- LEKAKIS, I.C. 1988 *Coherent structures in fully developed turbulent pipe flow*. Thesis University of Illinois.
- LIU, Z.-C., LANDRETH, C.C., ADRIAN, R.J. & HANRATTY, T.J. 1991 High resolution measurement of turbulent structure in a channel with particle image velocimetry. *Exp. Fluids* **10**, 301–312.
- LOURENÇO, L.M. 1988 Some comments on particle image displacement velocimetry. In *VKI-LS 1988-06 "Particle image displacement velocimetry"* Von-Kármán Institute for Fluid Mechanics, Rhode-Saint-Genève.
- LOURENÇO, L.M. & KROTHAPALLI, A. 1988a Particle image displacement velocime-

- try measurements of a three dimensional jet. *Exp. Fluids* **31**, 1835-1837.
- LOURENÇO, L.M. & KROTHAPALLI, A. 1988b Application of PIDV to the study of the temporal evolution of the flow past a circular cylinder. In: *Laser Anemometry in Fluid Mechanics III* (eds. R.J. Adrian *et al.*) LADOAN-Instituto Superior Tecnico, Lisbon. pp. 161-177
- LOURENÇO, L. 1993 Recent advances in LSV, PIV and PTV. In: *Flow Visualization and Image Analysis* (ed. F.T.M. Nieuwstadt) Kluwer Academic, Dordrecht. pp. 81-99
- LUCHINI, P., MANZO, F. & POZZI, A. 1991 Resistance of a grooved surface to a parallel flow and cross flow. *J. Fluid Mech.* **228**, 87-109.
- MANSOUR, N.N., KIM, J. & MOIN, P. 1988 Reynolds-stress and dissipation-rate budgets in a turbulent channel flow. *J. Fluid Mech.* **194**, 15-44.
- MCCCLUSKEY, D.R., ELGAARD, C., EASSON, W.J. & GREATED, C.A. 1993 The application of PIV to turbulent two-phase flows. In: *Flow Visualization and Image Analysis* (ed. F.T.M. Nieuwstadt) Kluwer, Dordrecht.
- MERZKIRCH, W. 1987 *Flow Visualization*. 2nd Ed. Academic, New York.
- MEYNART, R. 1983 Speckle velocimetry study of vortex pairing in a low-Re unexcited jet. *Phys. Fluids* **26**, 2074-2079.
- MEYNART, R. 1991 Past and future of PIV. Invited lecture at *EuroMech 279 "Image analysis as measuring technique in flows"* (Delft) 2-5 July
- OERTEL, H. SEN. & OERTEL, H. JUN. 1989 *Optische Strömungsmesstechnik*. G. Braun, Karlsruhe.
- OPPENHEIM, A.V., WILLSKY, A.S. & YOUNG, I.T. 1983 *Signals and Systems*. Prentice-Hall, Englewood Cliffs (NJ).
- PAPANTONIOU, D. & MAAS, H.-G. 1990 Recent advances in 3-D particle tracking velocimetry. *Proc. 5th Int. Symp. Appl. Laser Techn. Fluid Mech.* (Lisbon) 9-12 July, 18.4
- PARZEN, E. 1957 On choosing an estimate of the spectral density function of a stationary time series. *Ann. Math. Statist.* **28**, 921-932.
- PATEL, V.C. & HEAD, M.R. 1969 Some observations on skin friction and velocity profiles in fully developed pipe and channel flows. *J. Fluid Mech.* **38**, 181-201.
- PRASAD, A.K., ADRIAN, R.J., LANDRETH, C.C. & OFFUTT, P.W. 1992 Effect of resolution on the speed and accuracy of particle image velocimetry interrogation. *Exp. Fluids* **13**, 105-116.
- PRIESTLEY, M.B. 1992 *Spectral Analysis and Time Series*. (7th Ed.) Academic, San Diego (CA).
- REICHARDT, H. 1951 Vollständige Darstellung der turbulenten Geschwindigkeitsverteilung.

- lung in glatten Leitungen. *Z. angew. Math. Mech.* **31**, 208–219.
- REUSS, D.L., ADRIAN, R.J., LANDRETH, C.C., FRENCH, D.T. & FANSLER T.D. 1989 Instantaneous planar measurements of velocity and large-scale vorticity and strain rate in an engine using particle-image velocimetry. *SAE Technical Paper Series* 890616
- ROBINSON, S.K. 1991a The kinematics of turbulent boundary layer structure. *NASA TM-103859*
- ROBINSON, S.K. 1991b Coherent motions in the turbulent boundary layer. *Annu. Rev. Fluid Mech.* **23**, 601–639.
- ROSENFELD, A. & KAK, A.C. 1982 *Digital Picture Processing* (2nd Ed.) Academic, Orlando.
- ROSHKO, A. 1954 On the development of turbulent wakes from vortex streets *NACA Report* 1191.
- RUSS, J.C. 1986 *Practical Stereology*. Plenum, New York.
- SCHLICHTING, H. 1979 *Boundary-Layer Theory* 7th Ed. McGraw-Hill, New York..
- SCHWARZ-VAN MANEN, A.D. 1992 *Coherent structures over grooved surfaces*. Ph.D. thesis, Eindhoven University of Technology..
- SIMPKINS, P.G. & DUDDERAR, T.D. 1978 Laser speckle measurements of transient Benard convection. *J. Fluid Mech.* **89**, 665–671.
- SMALLWOOD, G.J. 1992 *A Technique for Two-Colour Particle Image Velocimetry*. M.Sc. thesis, University of Ottawa.
- SMITH, C.R. 1984 A synthesized model of the near-wall behaviour in turbulent boundary layers. *Proc. 8th Symp. on Turbulence* (eds. G.K. Patterson & J.L. Zakin) University of Missouri (Rolla)
- SPALART, P.R. 1988 Direct simulation of a turbulent boundary layer up to $Re_\theta=1410$. *J. Fluid Mech.* **187**, 61–98.
- TENNEKES, H. & LUMLEY, J.L. 1972 *A first course in turbulence*. MIT Press, Cambridge (MA).
- TOWNSEND, A.A. 1956 *The Structure of Turbulent Shear Flow*. University Press, Cambridge..
- VAN DYKE, M. 1982 *An Album of Fluid Motion*. Parabolic, Stanford.
- VASSILICOS, C. 1992 Multispiral turbulent structure. *Proc. 4th European Turb. Conf.* (Delft) 30 June – 3 July.
- WALLACE, J.M., ECKELMANN, H. & BRODKEY, R.S. 1972 The wall region in turbulent shear flow. *J. Fluid Mech.* **54**, 39–48.
- WALSH, M.J. & LINDEMANN, A.M. 1984 Optimization and application of riblets for

- turbulent drag reduction. *AIAA paper* 84-0347
- WESTERWEEL, J. 1987 Statistical tests for time-of-flight spectra in neutron scattering experiments *Report 132-87-02* Interfaculty Reactor Institute, Delft. (in Dutch)
- WESTERWEEL, J., NIEUWSTADT, F.T.M. 1991 Performance tests on three-dimensional velocity measurements with a two-camera digital particle image velocimeter. In: *Laser Anemometry: Advances and Applications*. (ed. A. Dybbs & B. Ghorashi) ASME, New York. Vol. I, pp. 349-355.
- WESTERWEEL, J., FLÖR, J.B. & NIEUWSTADT, F.T.M. 1992 Measurement of dynamics of coherent flow structures using particle image velocimetry. In: *Applications of Laser Techniques in Fluid Mechanics* (ed. R.J. Adrian *et al.*) Springer, Berlin.
- WILLERT, C.E. 1989 High resolution correlation peak detection. *ECE 251 C* UCSD, La Jolla
- WILLERT, C.E. & GHARIB, M. 1991 Digital particle image velocimetry. *Exp. Fluids* **10**, 181-193.
- WILLMARTH, W.W. & LU, S.S. 1972 Structure of the Reynolds stress near the wall. *J. Fluid Mech.* **55**, 65-92.
- WYGNANSKI, I.J. & CHAMPAGNE, F.H. 1973 On transition in a pipe. Part 1. The origin of puffs and slugs and the flow in a turbulent slug. *J. Fluid Mech.* **59**, 281-335.
- YAO, C.S. & ADRIAN, R.J. 1984 Orthogonal compression and 1-D analysis technique for measurement of particle displacements in pulsed laser velocimetry. *Appl. Opt.* **23**, 1687-1689.
- YOUNG, I.T. 1988 Sampling density and quantitative microscopy. *Analyt. Quant. Cytol. Histol.* **10**, 269-275.

List of Symbols

Chapters 1 to 3, Appendices A and B

Roman capitals and calligraphic

$A_k(x, y)$	light amplitude field due to a particle with index k	(2.22)
C	number density of the tracer particles in the flow	(2.5)
D	lens aperture	p. 38
$\vec{D}(\vec{X}; t', t'')$	displacement field	(2.1)
\vec{D}'	mean displacement over measurement volume	(2.9)
$\vec{D}(\vec{\Gamma}; t_1, t_2)$	displacement of $\vec{\Gamma}$ by $\vec{V}(t)$ during time interval (t_1, t_2)	(A.7)
$F(\chi, \psi)$	Fourier transform	(3.13)
$\tilde{F}[u, v]$	discrete Fourier-transform of a periodic image $\Delta\tilde{I}_{r,s}$	(B.3)
$F_I[r, s]$	loss of correlation due to in-plane motion of tracer particles	(3.45)
F_m	$F_I[m_o + m, 0]$	(3.70)
$F_O(D'_Z)$	loss of correlation due to out-of-plane motion of tracer particles	(2.47)
$F_i(x, y)$	structure function of the tracer image	(2.41)
$G(\vec{X}, t)$	tracer pattern	(2.3)
$G'(\vec{X})$	realization of the tracer pattern at time t'	(2.4)
$G''(\vec{X})$	realization of the tracer pattern at time t''	(2.4)
$\mathcal{G}(x, y; \sigma)$	circularly symmetric Gaussian curve	(A.24)
$I(x, y)$	image intensity field	(2.19)
$I'(x, y)$	realizations of $I(x, y)$ at time t'	(2.43)
$I''(x, y)$	realizations of $I(x, y)$ at time t''	(2.43)
$I_{i,j}$	discrete image intensity	(3.1)
I^\bullet	quantized image intensity	(3.11)
\bar{I}	mean image intensity	(3.22)
$\Delta I_{i,j}$	fluctuating image intensity	(3.21)
$\Delta\tilde{I}_{i,j}$	periodically extended interrogation image	(B.1)
$I_o(\vec{X}, Y, Z)$	intensity of the light sheet	(2.15)
$I_o(Z)$	light sheet intensity profile	(2.16)
I_Z	maximum of $I_o(Z)$	(2.16)
$J_1(x)$	Bessel function of the first kind and the first order	(A.22)
K	decorrelation constant for \hat{R}_{-1} and \hat{R}_{+1}	(3.92)
\mathcal{L}	characteristic length scale of the flow	p. 6
\mathcal{L}_o	integral length scale of $\hat{R}_{II}[r, s]$	(3.66)
M	image magnification	(2.13)
M	total image diameter in pixels	(B.2)
N	diameter of the interrogation image in pixels	p. 213
N_I	image density	(3.50)
N_S	source density	(2.25)

\mathcal{N}	number of particles	(2.3)
P	number of exposures	(2.54)
P	filter length for spatial smoothing of velocity data	(5.4)
$P(n)$	Poisson probability distribution	(3.51)
Re	Reynolds number	p. 6
$R_f(x, y)$	ensemble auto-covariance of $f(x, y)$	(2.52)
R_{GG}	ensemble covariance function of the tracer pattern	(2.7)
$R_I(x, y)$	ensemble auto-covariance of $I(x, y)$	(2.35)
$R_{II}(x, y)$	ensemble cross covariance of $I'(x, y)$ and $I''(x, y)$	(2.43)
$R_I[i, j]$	auto-covariance of the discrete image field	(3.4)
$R_{II}[m, n]$	discrete cross-covariance function of $I'_{i,j}$ and $I''_{i+m,j+l}$	(3.7)
$\hat{R}_{II}[r, s]$	inverse discrete Fourier transform of $\hat{S}[u, v]$	(B.9)
$\hat{R}_{II}[m, n]$	(biased) estimator of $R_{II}[m, n]$	(3.27)
$R_{II}^*[r, s]$	unbiased estimate of the image cross-covariance	(3.87)
\hat{R}_m	$\hat{R}_{II}[m_o + m, 0]$	(3.70)
$S(\chi, \psi)$	image spectral density	(3.15)
$\hat{S}_{II}[u, v]$	cross-spectral density of the interrogation images $\Delta I'_{r,s}$ and $\Delta I''_{r,s}$	(B.5)
T_B	time scale of the "bursting" process	p. 10
$U_g(x, y)$	geometrical optics prediction of $U_i(x, y)$	(2.18)
$U_i(x, y)$	complex amplitude of the light wave in the image plane	(2.17)
$U_o(X, Y)$	complex amplitude of the light wave in the object plane	(2.18)
U	characteristic velocity scale of the flow	p. 6
V	volume	p. 200
$\delta V(\vec{X}')$	measurement volume around \vec{X}'	p. 36
$\vec{V}(\vec{\Gamma}, t)$	velocity of the ensemble state variable $\vec{\Gamma}$ at time t	(A.5)
W	bandwidth	(3.13)
W_P	bandwidth (Parzen's definition)	(3.16)
$W_{i,j}$	weight kernel	(3.43)
\vec{X}	position vector	(2.1)
$\vec{X}_i(t)$	position vector of particle with index i at time t	(2.3)
$\Delta X, \Delta Y$	distance between mesh points in PIV data set	(5.3)
Z_0	object distance	(2.12)
ΔZ_0	light sheet thickness	p. 38
$\Delta Z'$	light-sheet thickness based on first moment of $I_o(Z)$	(2.32)
$\Delta Z''$	light-sheet thickness based on second moment of $I_o(Z)$	(2.39)
δZ	focal depth	(2.14)

lower-case Roman

a	model parameter proportional to volume under displacement-correlation peak	(3.54)
a_1	model parameter proportional to the width of the displacement-correlation peak	(3.74)

d_R	diameter of the displacement-correlation peak	(3.59)
d_p	diameter of a particle	(2.20)
d_s	diameter of the Airy pattern	(2.21)
d_i	diameter of a particle image	(2.20)
f	lens focal length	(2.12)
$f(x, y)$	(multiple-exposure) image frame	(2.50)
$g(x, y)$	particle-image pattern	(2.28)
$h(x, y)$	amplitude impulse response of the diffraction-limited optical system	(2.18)
$ h ^2$	Airy pattern	(A.22)
$[m_0, n_0]$	position of the displacement-correlation peak in integer pixel units	p. 212
$p(x, y)$	sampling function	(3.2)
q	difference between two consecutive quantization levels	(3.12)
(r_D, s_D)	in-plane particle-image displacement	(3.67)
$t(x, y)$	particle image for unit incident-light intensity	(2.26)
t_0	integrated intensity of $t(x, y)$	(2.34)
Δt	exposure time delay	(2.1)
u, v	in-plane components of the velocity	(5.2)
u_*	friction velocity of a boundary layer	(1.2)
u^+	velocity scaled with u_*	(1.3)
$\vec{v}(\vec{X}, t)$	flow velocity field	(2.1)
z_0	image distance	(2.12)

Greek

Γ	valid-data yield	(3.53)
$\vec{\Gamma}(t)$	state of the tracer ensemble at time t	(A.4)
Δ	diameter of a pixel	(3.1)
ϵ	fractional displacement	(3.67)
$\partial\hat{\epsilon}/\partial R_{\pm 1}^*$	sensitivity of the fractional displacement estimator with respect to the unbiased covariance estimator	(3.93)
$\hat{\epsilon}_C$	center-of-mass estimator of ϵ	(3.71)
$\hat{\epsilon}_G$	Gaussian-fit estimator of ϵ	(3.73)
$\hat{\epsilon}_P$	parabolic-fit estimator of ϵ	(3.72)
ϵ	error between the velocity field and the displacement field	(2.2)
ϵ_b	tracking error of a fractional-displacement estimator	(3.102)
ζ	quantizer noise	(3.11)
η	Kolmogorov length scale of the turbulent microstructure	p. 6
κ_4	fourth order cumulant	(3.32)
λ	wavelength of light	(2.14)
μ	average number of particle pairs	(3.51)
ν	kinematic viscosity	p. 6
ρ	fluid density	p. 8
$\rho(\vec{\Gamma}, t)$	pdf to find an ensemble in a state $\vec{\Gamma}$	(A.8)

$\rho'(\vec{X})$	spatial distribution function of \vec{D} in $\delta V(\vec{X}')$	(2.8)
$\varrho[t, u]$	correlation of $\vec{R}_{II}[m_o, n_o]$ with $\vec{R}_{II}[m_o \pm t, n_o \pm u]$	(3.65)
σ	width parameter for Gaussian curve $\mathcal{G}(x, y)$	(A.24)
σ_I^2	variance of image intensity	(3.54)
τ_*	wall shear stress	p. 8
$\Phi_{pp}(s, t)$	self-correlation of the pixel sampling function	(3.6)
$\phi_k(x, y)$	phase of the amplitude field due to a particle with index k	(2.23)
χ, ψ	spatial frequencies	(3.13)
$\vec{\omega}$	vorticity vector	(5.1)
ω_Z	out-of-plane component of the vorticity	(5.2)

special symbols

*	convolution integral	(2.18)
*	complex conjugate	(B.5)
$\langle \dots \rangle$	the ensemble mean of a quantity	(A.8)

Chapter 4

Roman capitals

$B(k)$	binomial distribution	(4.28)
C_1	weight factor for error of the first kind	(4.16)
C_2	weight factor for error of the second kind	(4.16)
D_I	diameter of the interrogation spot	p. 110
D_0	detectability	p. 110
E_1	error of the first kind	(4.14)
E_2	error of the second kind	(4.15)
H_0	null hypothesis	p. 113
H_1	alternative hypothesis	p. 113
K	cost function	(4.16)
\mathbf{M}	neighbourhood of (i, j) that includes N_M elements	(4.25)
N	total number of vectors in the data set	(4.20)
N'	effective number of independent samples in the data set	(4.23)
N_{eff}	effective number of independent samples for the median	p. 118
$R(\vec{s})$	spatial auto-correlation function	p. 109
$R_P(\vec{s})$	particle image self correlation peak	p. 110
$R_{D^+}(\vec{s})$	displacement correlation peak	p. 110
$R_{D^-}(\vec{s})$	displacement correlation peak	p. 110
$R_F(\vec{s})$	noise term due to random particle correlations	p. 110
$R_C(\vec{s})$	mean background correlation	p. 110
R_I	equivalent radius of the search window	p. 111
$\vec{U}_{i,j}$	position of the highest random correlation peak	(4.1)

$\vec{V}'_{i,j}$	measured displacement	(4.1)
$\vec{V}_{i,j}$	local average of the displacement	(4.1)
$\langle \vec{V}' \rangle$	global mean of $\vec{V}'_{i,j}$	(4.20)
$\langle \vec{V}'_{i,j} \rangle$	local mean of $\vec{V}'_{i,j}$	(4.25)
$[\vec{V}'^*]_{i,j}$	local median of $\vec{V}'_{i,j}$	(4.30)

lower-case Roman

$f(r^2 H_0)$	pdf of $r^2_{i,j}$ under H_0	(4.12)
i, j	coordinates of the data point in the PIV data set	
$\vec{r}_{i,j}$	residual displacement vector	(4.10)
$\hat{r}^2_{i,j}$	estimate for the squared scalar residual	(4.19)
r^2_c	critical value of the displacement vector	(4.14)
r^2_m	lowest residual in the m -th bin	(4.33)
v^x, v^y	x and y-components of \vec{V}'	(4.30)

Greek

$\gamma_{i,j}$	binary random variable	(4.1)
$\delta_{i,j}$	Kronecker delta symbol	(4.5)
$\vec{\epsilon}_{i,j}$	measurement error	(4.1)
η	local correlation of the velocity field	(4.26)
θ_m	expectation value for the lowest residual r^2_m in the m -th bin	(4.33)
$\Delta\theta$	fraction of the total data in each bin of the histogram	(4.33)
$\vec{\mu}$	mean displacement	(4.2)
$\rho(k, l)$	spatial auto-correlation function of $\vec{V}'_{i,j}$	(4.3)
σ^2	variance	(4.31)
σ^2_V	variance of the fluctuating velocity	(4.3)
σ_ϵ	variance of measurement error	(4.5)
σ_U	variance of the position of the highest random correlation peak	(4.7)

special symbol

$\vec{1}$	unit matrix	(4.3)
-----------	-------------	-------

List of Abbreviations

CCD	charge coupled device
DFT	discrete Fourier transformation
DPIV	digital particle image velocimetry
DNS	direct numerical simulation
FFT	fast Fourier transformation
HWA	hot-wire anemometry
LDA	laser-Doppler anemometry
LSV	laser speckle velocimetry
OPIV	optical particle image velocimetry
PIV	particle image velocimetry
PTV	particle tracking velocimetry
SNR	signal-to-noise ratio
pdf	probability density function
px	pixel (picture element)
rms	root-mean-square

Digital Particle Image Velocimetry : Theory and Application

Summary

Flow visualizations clearly show that turbulence is not a random process, but consists of so-called *coherent flow structures*. An interpretation in terms of coherent structures plays an important role in many turbulent phenomena. With traditional flow visualization we only obtain a *qualitative* picture of these structures. On the other hand, traditional instruments like the hot-wire and laser-Doppler anemometers are one-point measurement techniques, and therefore not able to reveal the instantaneous spatial structure of a flow. With the aid of a new observation technique, called "particle image velocimetry" (PIV), *quantitative*, two-dimensional information of the flow velocity field is obtained. The basic principle of this method is to determine the fluid velocity in a thin light sheet from the motion of small tracer particles that are added to fluid. Images of the tracer particles are recorded. The recording is subsequently analyzed on a point-by-point basis in small interrogation areas by means of a correlation method. The results of PIV measurements enable us to compute (components of) other flow quantities, such as the *vorticity* or the *deformation*; these quantities have a close relationship to the dynamics of coherent flow structures.

The conventional method for the analysis of PIV images (photographs) yields accurate results with a high spatial resolution, but is very time-consuming. This is a major problem in the application of PIV to study the statistical properties and the dynamics of coherent structures in turbulent flows, which requires the analysis of a large number of images. This was about the situation at the beginning of the study described in this thesis. To overcome this problem a digital implementation of the PIV method—referred to as digital PIV or DPIV—is proposed in this thesis. DPIV considerably reduces the processing time, at the cost of a slight reduction in measurement accuracy. In DPIV the pixel resolution in the interrogation analysis is reduced by a factor 8^2 with respect to the pixel resolution used in conventional PIV interrogation analysis; this reduces the processing time by a factor of 100, while the loss of relative measurement accuracy is only a factor 2–4. In a practical situation a single image is interrogated in 1,000 positions in less than 10 seconds, with a relative measurement accuracy of 1–3%. Hence, DPIV was expected to provide a feasible solution to process large quantities of PIV images. So, the main aim of this thesis can be more specifically defined as to establish the necessary theoretical basis and practical verification to justify this expectation.

The remainder of the thesis consists of two parts. Part I deals with the necessary theoretical aspects of (digital) PIV, related to image acquisition, interrogation analysis, data validation and data analysis. Part II describes the application of the traditional PIV method and the new digital PIV method to turbulent flow.

In Part I a relation between the statistics of the tracer particles and the statistics of the

digital PIV pictures is established. Based on this result an estimation is made of the minimum required sampling rate for PIV pictures. It is derived that the required bandwidth for PIV analysis is a factor 3-4 lower than the optical bandwidth. This explains why the reduction in pixel resolution in DPIV analysis with respect to the conventional PIV analysis (in which the pixel resolution matches the optical bandwidth) has little effect on the relative measurement accuracy. The derived analytical results are subsequently used to investigate the performance of different estimators for the particle-image displacement. This demonstrates that interrogation with high pixel resolution (conventional PIV) and with low pixel resolution (digital PIV) need different optimal estimators for the particle-image displacement. The analytical predictions are in good quantitative agreement with measurement results obtained from a linearly displaced test image.

Under certain circumstances the measured displacement in an interrogation area is spurious as a result of insufficient particle-images within the interrogation area. It is therefore necessary to validate the measurement data prior to the evaluation of flow properties from PIV data sets. A statistical model is introduced that describes the occurrence of spurious vectors in PIV data. This model is used to investigate and optimize the performance of different post-interrogation procedures for detection of spurious vectors.

The vorticity and deformation are flow properties that can be obtained by differentiation of the velocity field. The two-dimensional measurement data obtained from PIV measurements allow the evaluation of components of the vorticity vector and deformation tensor. The accuracy of these estimates is limited by the spatial resolution and noise level of the PIV data. It is shown that the accuracies encountered in data sets from digital PIV analyses can yield reliable estimates of the vorticity and deformation. This is demonstrated in Part II with the results of a test measurement of homogeneous turbulent flow behind a grid.

Part II describes the application of the conventional PIV method and the new digital PIV method to turbulent flow. (The application to grid turbulence was already mentioned in the previous paragraph.) The main subject of Part II is the application of PIV to fully developed turbulent pipe flow. First the measurement of this flow with the conventional PIV method is described. In total 33 photographs were recorded, of a plane through the centerline of the pipe across the full diameter. The observed structures closely resemble the structures found in numerical simulations and the structures proposed in conceptual models of the boundary-layer flow structure. The flow structures found in the vorticity computed from the velocity data of the PIV measurements are compared with those found in the results of a numerical simulation, carried out at the same flow condition and in the same flow geometry as the PIV measurements. This comparison shows that the statistical properties of the structures found in the experimental and numerical data sets agree *quantitatively*. (It is beyond the scope of this thesis to pursue a further interpretation of the observed flow patterns.) To assess the feasibility of the alternative DPIV method, measurements are carried out with DPIV in the same facility. About 500 pictures are recorded and analyzed. The view area in the DPIV measurements is now smaller, and the final results exhibit slightly higher scatter. However, the total processing time for

the analysis of the DPIV pictures was only a fraction of the time required to analyze the PIV photographs. The agreement of the flow data obtained with digital PIV agree reasonably well with those obtained with the conventional PIV method. (The digital PIV pictures were recorded with moderate video equipment; it is expected that the quality of the results will improve when the PIV pictures will be recorded with high-quality digital instruments.)

In this thesis it is demonstrated that digital PIV is a feasible alternative to the conventional PIV method, and is capable of analyzing large amounts of PIV pictures at an acceptable computational effort. The logical next step is to apply digital PIV to turbulent flows with the aim to investigate the statistical properties and dynamics of coherent flow structures. It is expected that experimental PIV data will provide necessary information of turbulent flows in geometries and at flow conditions that are (currently) not accessible to computer simulations. However, one of the next problems that needs to be solved is how to *interpret* the observed two-dimensional patterns in terms of evolutionary three-dimensional flow structures. In that respect it can be expected that experimental PIV data en numerical simulation data will complement each other.

Digitale Particle Image Velocimetry : Theorie en Toepassing

Samenvatting

Met behulp van klassieke stromingsvisualisaties is in het verleden aangetoond dat turbulentie niet als een puur stochastisch proces moet worden opgevat, maar ook zogenaamde *coherente structuren* bevat. Een interpretatie in termen van coherente structuren speelt een belangrijke rol bij verschillende turbulente verschijnselen. Met klassieke visualisatie verkrijgen we slechts een *kwalitatief* beeld van deze structuren. De traditionele meettechnieken zoals hitte-draad anemometrie en laser-Doppler anemometrie daarentegen zijn één-punts methoden die niet in staat zijn om de instantane, ruimtelijke structuur van de stroming te bepalen. Met behulp van een nieuwe, optische meettechniek, genaamd "Particle Image Velocimetry" (PIV), kan *kwantitatieve* twee-dimensionale informatie over het instantane snelheidsveld worden verkregen. Het basisprincipe van deze techniek bestaat uit het toevoegen van kleine deeltjes aan het fluidum, waarbij de snelheid wordt bepaald uit de beweging van deze deeltjes in een lichtvlak in de stroming. Van deze deeltjes wordt een opname gemaakt die vervolgens puntsgewijs in kleine interrogatie-gebieden wordt geanalyseerd door middel van een correlatie-methode. De resultaten van PIV-metingen stellen ons in staat om (componenten van) andere stromingsgrootheden te bepalen, zoals de vortciteit en de vervorming; deze grootheden hangen nauw samen met de dynamica van coherente structuren.

De conventionele methode die wordt gebruikt voor de analyse van PIV-opnames (foto's) heeft een hoge nauwkeurigheid en een hoge ruimtelijke resolutie, maar is erg traag. Dit is met name een probleem bij toepassingen waarbij een groot aantal opnames moet worden geanalyseerd, zoals bij het onderzoek naar de statistische eigenschappen of de dynamica van coherente structuren. Dit was de situatie bij de aanvang van de studie die staat beschreven in dit proefschrift. Als oplossing voor dit probleem wordt in dit proefschrift een *digitale* implementatie van de PIV-methode—oftewel DPIV—voorgesteld. DPIV geeft een aanzienlijke versnelling van de verwerkingstijd, die echter een kleine verslechtering in ruimtelijke resolutie en meetnauwkeurigheid tot gevolg heeft. Bij DPIV is de pixel-resolutie in de beeldanalyse een factor 8^2 lager dan bij de conventionele PIV-methode; dit geeft een versnelling van de beeldanalyse met een factor 100, terwijl de relatieve meetnauwkeurigheid met slechts een factor 2-4 afneemt. In de praktijk kan een digitale opname in 1.000 posities worden geanalyseerd in minder dan 10 seconden. De relatieve meetnauwkeurigheid bedraagt 1-3%. Op basis hiervan was de verwachting dat DPIV een haalbaar alternatief is voor toepassingen waarbij het noodzakelijk is om grote aantallen opnames te analyseren. Het hoofddoel van dit proefschrift kan daarom preciezer worden omschreven als het theoretisch onderbouwen en vervolgens verifiëren van deze verwachting.

Het resterende deel van dit proefschrift bestaat uit twee delen. Deel I behandelt de benodigde theoretische aspecten van DPIV met betrekking tot de beeldopname, beeld-

analyse, data-validatie en data-analyse. Deel II beschrijft de toepassing van de conventionele en nieuwe digitale PIV-methoden op turbulente stromingen.

In Deel I wordt eerst een relatie afgeleid tussen de statistiek van willekeurig over de stroming verdeelde deeltjes en de statistische eigenschappen van de digitale opnames. Aan de hand van dit resultaat wordt de minimale bemonsteringsfrequentie voor PIV-opnames bepaald. Er wordt aangetoond dat de bandbreedte van PIV-opnames een factor 3-4 lager is dan de optische bandbreedte. Dit verklaart waarom de afname in pixel-resolutie bij DPIV in vergelijking met de conventionele PIV-methode (waarbij de bemonsteringsfrequentie is afgestemd op de optische bandbreedte) nauwelijks effect heeft op de relatieve meetnauwkeurigheid. De afgeleide theoretische relaties worden vervolgens gebruikt om de eigenschappen van verschillende schatters van de verplaatsing van de deeltjes in de opnames. Hiermee wordt aangetoond dat de analyse met hoge pixel-resolutie (conventionele PIV) en lage pixel-resolutie (DPIV) verschillende optimale schatters vereisen. De theoretische voorspellingen blijken goed overeen te komen met resultaten uit metingen aan een testbeeld dat lineair wordt verplaatst.

Onder bepaalde omstandigheden kan het voorkomen dat in een bepaald interrogatiegebied onvoldoende deeltjes aanwezig zijn om de snelheid te kunnen bepalen. De gevonden verplaatsing is dan onjuist. Daarom is het nodig de individuele meetdata te valideren, voordat de verschillende stromingsgrootheden geschat kunnen worden uit PIV-data. Van verschillende validatie-methoden zijn de eigenschappen bepaald met behulp van een statistisch model, dat het optreden van onjuiste meetdata beschrijft. Dit model is ook gebruikt om de methoden te optimaliseren.

De vortciteit en deformatie zijn stromingsgrootheden die worden verkregen door het snelheidsveld te differentiëren. Componenten van de vortciteitsvector en deformatietensor kunnen worden geschat uit de twee-dimensionale meetdata verkregen uit PIV-metingen. De nauwkeurigheid van deze schattingen wordt bepaald door de ruimtelijke resolutie van de meetdata en door de aanwezige ruis. Er wordt aangetoond dat de nauwkeurigheid van meetdata verkregen uit digitale PIV-metingen nog voldoende is om betrouwbare schattingen te maken van de vortciteit en deformatie. Ter demonstratie worden in Deel II de experimentele data van een turbulente stroming achter een rooster geanalyseerd.

Deel II beschrijft de toepassing van de conventionele PIV-methode en de nieuwe digitale PIV-methode op turbulente stromingen. (De toepassing van digitale PIV op rooster-turbulentie werd al in de vorige paragraaf genoemd.) Het hoofdonderwerp van Deel II is de meting met PIV aan een volledig ontwikkelde turbulente pijpstroming. Eerst worden metingen met de conventionele PIV-methode beschreven. Daarbij zijn in totaal 33 foto's genomen van een vlak door de as van de pijp, over de gehele pijpdiameter. De structuren in de meetresultaten vertonen een sterke gelijkenis met structuren zoals die worden voorgesteld door conceptuele modellen en zoals die zijn gevonden in resultaten van computersimulaties. De statistische eigenschappen van de experimenteel gevonden structuren blijken kwantitatief overeen te stemmen met die van structuren in de resultaten van een computersimulatie, uitgevoerd in dezelfde stromingsgeometrie en bij vrijwel dezelfde

stromingscondities. Hieruit blijkt dat de statistische eigenschappen van structuren in de experimentele en numerieke resultaten kwantitatief met elkaar overeenkomen. (Een verdere interpretatie van de gevonden structuren valt buiten het bestek van het onderzoek beschreven in dit proefschrift.) Om een indruk te krijgen van de bruikbaarheid van de alternatieve, digitale PIV-methode zijn digitale opnames gemaakt van dezelfde stroming. Ongeveer 500 opnames zijn geanalyseerd, waarbij de beeldgrootte echter kleiner is dan bij de metingen met de traditionele PIV-methode. Daar staat tegenover dat dit grote aantal opnames werd geanalyseerd in slechts een fractie van de tijd die nodig was voor het analyseren van de conventionele PIV-opnames. De fouten in de DPIV-metingen vertonen een wat grotere spreiding dan die in de conventionele PIV-metingen. Desondanks komen de resultaten redelijk goed overeen. (De digitale PIV-opnames zijn gemaakt met eenvoudige video-apparatuur. Het is te verwachten dat de kwaliteit van de resultaten zal verbeteren bij gebruik van apparatuur van betere kwaliteit.)

In dit proefschrift is aangetoond dat digitale PIV een haalbaar alternatief is voor de conventionele PIV-methode, en dat deze in staat blijkt om grote aantallen opnames te analyseren in een relatief zeer korte tijd, terwijl de meetresultaten nog steeds een acceptabele nauwkeurigheid hebben. Een logische volgende stap is om deze techniek daadwerkelijk in te zetten bij onderzoek naar de dynamica van coherente structuren. Naar wordt verwacht zullen experimentele PIV-resultaten met name informatie verschaffen over stromingen in geometrieën en bij condities die (vooralsnog) niet toegankelijk zijn voor computersimulaties. Daarbij dient aandacht te worden besteed aan de vertaling van twee-dimensionale patronen in de meetdata naar tijdsafhankelijke, drie-dimensionale verschijnselen in de stroming. Hierbij zullen computer-simulaties en PIV—als experimentele techniek—elkaar wederzijds aanvullen.

Acknowledgements

At this point I would like to thank all people and organizations that contributed to the work described in this thesis. In particular I would like to acknowledge the following people:

In the first place I would like to thank my promotor Frans Nieuwstadt for giving me the opportunity to carry out this research project at the Laboratory for Aero & Hydrodynamics (A&H), and for his guidance and suggestions. I greatly appreciate that he encouraged me to arrange working visits to other laboratories, and that he draw my attention to the KNAW research fellowships.

I enjoyed working with my fellow Ph.D. colleagues at A&H. Especially I wish to thank Jack Eggels and Jacobiene van der Hoeven for their cooperation and for their contributions to this research project. Maarten Dirkzwager is acknowledged for providing the kinematic-simulation software, while Arno Brand is thanked for introducing me to the world of coherent flow structures.

Furthermore I wish to express my gratitude to all members of the permanent staff of A&H. In particular I would like to thank Jaap van der Zanden for his remarks and suggestions concerning the theoretical part of the manuscript. Also I enjoyed the cooperation with Hans Bessem in our "quest" for suitable image acquisition hardware. Bert van der Velden is appreciated for his support in the computer hardware and software, and Cor Gerritsen for his support in dealing with the video and laser equipment.

Next I would like to thank the laboratories I visited for their hospitality and cooperation. I am thankful to Prof. C.A. Greated, Charlotte Elgaard and their colleagues at Edinburgh University for providing the opportunity to carry out PIV measurements in their facilities. It was furthermore my privilege to work at the University of Illinois at Urbana-Champaign (UIUC) under the supervision of Prof. R.J. Adrian. I especially wish to thank Peter Offutt and Ajay Prasad for their valuable advise and assistance during the experiments at UIUC. Besides that, I highly appreciated the companionship of my UIUC colleagues. I enjoyed the cooperation and discussions with Rob Uittenbogaard and his colleagues at Delft Hydraulics and it was a pleasure to work with Jan-Bert Flör and Casper Williams at the Eindhoven University of Technology.

Finally I would like to express my warmest thanks and respect to my wife, Jacorien Wouters, who supported and helped me in completing this thesis, in addition to her own demanding job. Besides that I appreciate her for bearing 4 months of loneliness during my stay at UIUC. Thanks are also due to Jacorien's colleagues at KEMA for tolerating my intermittent visits.

The work described in this thesis was financially supported by the "Commissie Beek" and the "3TU-Vernieuwingsruimte." My conference and working visits were financially supported by the Netherlands Organization of Scientific Research (NWO), the Royal Institute of Engineers (KIvI) and the University of Illinois. Portions of the research at UIUC were supported by Grant N000 14-90-J-1415 from the Office of Naval Research.

Curriculum Vitae

Jerry Westerweel was born on December 4, 1964 in Rotterdam, the Netherlands. In 1983 he graduated from pre-university education (VWO) at the *Scholengemeenschap Libanon* in Rotterdam. From 1983 till 1988 he studied Applied Physics at the Delft University of Technology, the Netherlands. The work described in his Master's thesis was carried out at the Radiation Physics group of Prof. J.J. van Loef at the Interfaculty Reactor Institute in Delft. The subject of his Master's thesis was *inelastic neutron scattering by dense hydrogen gas*. In 1989 he started to work as *assistent-in-opleiding* (AIO) towards his Ph.D. at the Laboratory for Aero & Hydrodynamics, under supervision of Prof. F.T.M. Nieuwstadt, of the Faculty of Mechanical Engineering and Marine Technology, Delft University of Technology. His assignment was to develop an optical whole-field measurement method for turbulence applications, and the results of this work are described in this thesis. He also presented these results at several international symposia and conferences. In the winter of 1991 he paid a short working visit to the Fluid Dynamics Unit of Prof. C.A. Greated of the University of Edinburgh (U.K.). He was furthermore member of the organizing committee for the EuroMech Colloquium 279 "Image Analysis as a Measurement Technique in Flows," July 2-5, 1991, Delft. In the fall of 1991 he spent four months as a visiting scholar in the group of Prof. R.J. Adrian at the Department of Theoretical & Applied Mechanics, University of Illinois at Urbana-Champaign (U.S.A.). In 1992 he gave an invited lecture on the subject of this thesis at the IAHR short-course on "Flow Visualization and Flow Structures" at the ETH in Zürich. Since July 1, 1993, he has accepted a research fellowship of the Royal Dutch Academy of Sciences (K.N.A.W.), by which he is associated with the Laboratory for Aero & Hydrodynamics for another three years. For the main part of this period he will work at the group of Prof. L. Hesselink at the Aeronautics & Astronautics Department of Stanford University (U.S.A.).